INVESTIGATION OF TWO-PHASE FLOW STRUCTURES IN THE PIPEWORK OF WET CENTRAL HEATING SYSTEMS

A thesis submitted for the degree of Doctor of Philosophy

by

Ali Shefik

College of Engineering, Design and Physical Sciences

Brunel University

Oct 2015

ABSTRACT

Wet central heating systems account for a very large portion of energy consumption in the UK and recent figures indicate that its usage in households will be increasing even further. Under such circumstances, it is desirable to use these systems in the most efficient way possible. However, dissolved gases that penetrate into central heating systems are later released as bubbles due to local supersaturated conditions occurring on the primary heat exchanger wall of the boiler. This leads to a two-phase flow throughout the pipework, causing microbubbles to escape to the upper parts of the system and creating cold spots in the radiators, thus, reducing its efficiency. There is an increasing trend in building services to install devices that remove these unwanted gases. Therefore, investigation of two-phase structures throughout different pipe installations will facilitate companies in enhancing their deaerator designs.

In this regard, extensive experimental and computational investigations of two-phase flow structures were conducted within this study. Two-phase flow structures were measured by a photographic technique and investigated in means of void fractions, bubble sizes, and velocities. Fluid velocities in the range of 0.5 to 1.1 m/s at typical wet central heating temperature (60 to 80 °C) and pressures (2.2 to 27 bar) were utilized.

Results show that that bubble production increases as temperature, boiler heating load, and saturation ratio escalate. On the other hand, it reduces when the pressure and flow rate of the system gets higher. A clear relationship between bubble sizes and system parameters was non-existent, except for the system flow rate (where bubble diameters decrease as the flow rate increases). Moreover, bubbles were evenly distributed during vertical flow when compared to horizontal flow, where bubbles tend to flow at the upper parts of the pipe. Furthermore, it was shown that bubble distributions were highly affected by obstacles like the 90 degree bend,

thermocouple or pressure sensors. In addition, it was observed that axial flow development of bubbly flow was a continuous process and void fraction at the upper part of the pipe increased as the flow travelled through horizontal pipeline.

Regarding the bubble velocity measurements, it was concluded that, bubble velocity profiles show development along both vertical and horizontal flows and approach to profiles which can be expressed with the power-law. Moreover, coalescence of two bubbles during horizontal flow was captured, emphasizing that the effect of coalescences should not be neglected at low void fractions. It was also found that bubbly flow in central heating systems was in a coalescences dominant regime and maximum bubble diameter observed at most positions were higher than theoretically defined values. Moreover, bubble dissolution effect was not observed at any of the test rig conditions. The reasons were thought to be the variation saturation ratio and axial flow development of two-phase flow, which supress the effect of dissolution and favour coalescence phenomenon.

Finally, after evaluating conclusions from the experimental results and computational study regarding the effect of the 90 degree bend on void fraction distributions, it was concluded that the employed physical model and solver settings in ANSYS Fluent 14.5, can be utilized to predict bubble distribution developments throughout the central heating systems' pipework.

Keywords: Central heating systems, two-phase flow, bubbly flow, bubble distributions, bubble sizes, bubble velocities, coalescence, image processing, experimental fluid measurements.

AUTHOR'S DECLARATION

This research was conducted at Brunel University London, under the supervision of Dr. Yunting Ge. The research presented in this thesis, unless otherwise stated or referenced, is the work of the author.

The work has not been submitted for another degree or award to any other institution.

Ali Shefik

Date: 26th October, 2015

ACKNOWLEDGEMENTS

I would like to express my great gratitude to Dr. Yunting Ge, my supervisor, for his patience and encouragement throughout this research. I am very grateful to him for giving me this opportunity.

I would also like to express my appreciation to Ing. Anton Lamers, who has provided me with constructive inputs and invaluable advices for the maturation of my thesis. The time he has allocated to me is greatly appreciated.

I extend my thanks to Mr. Costas Xanthos as well, who lent his assistance to me whenever I asked for it.

I am equally very thankful to my dear friends, Serkan Mesutoglu, Hakki Ozer, Erdogan Kaygan, and Fuat Uyguroglu, for their never-ending support to always keep me enthusiastic.

I would like to use this opportunity to deliver a deep sense of gratitude towards my beloved companion, Dr. Gizem Caner. Her encouraging attitude and belief in me, provides me with appreciation and self-confidence. I feel fortunate to know that she will always be by my side.

Lastly, my deepest thanks go to my family, my mother Dr. Ayla Gurel, my brother Macit Sefik, and my second mother Narin Ferdi Sefik, for always being there for me and making my life meaningful. Nevertheless, special thanks goes to my dearest, mother, who has been alongside me for all my life like a close friend, as well as an academic inspiration. Her generosity in answering my endless questions, her intellectual capacity and her motivational support has helped me tremendously throughout the completion of my thesis.

On a final note, I feel extensively obliged to my father, Mehmet Ali Sefik, who has made me become who I am today. If he was alive, I am certain that he would be very proud of me today.

Ali Shefik October 2015

CONTENTS

LIST OF FIGURES

LIST OF TABLES

LIST OF EQUATIONS

LIST OF APPENDICES

NOMENCLATURE

a	Distance between camera and sight glass	[mm]
b	Distance between light guide and sight glass	[mm]
B	London-van der Waals constant	[J. m]
C	Concentration of dissolved gas	[kg/m^3]
D	Diameter of the pipe	[m or mm]
D	Mass diffusivity of dissolved gas	[m^2/s]
D_{nM}	Median diameter of bubbles in the sample	[mm]
d	Diameter	[m or mm]
E	Dimensionless curvature radius	[-]
ΔH	Heat absorption of the solute	[kJ/k.mol]
He	Henry's law constant expressed in the units of	[atm.cm^3/g.mole]
H	Height/Depth	[mm]
h	System head loss	[bar or atm]
K_H	Proportionality constant for Henry's law	[atm]
K	System resistance	[mbar.h^2/L^2]
k	Coefficient of mass transfer	[m/s]
L	Characteristic length	[m or mm]
l	Length	[m or mm]
L	Length of the pipe	[m or mm]
M	Interface mobility coefficient	[-]
n	Refractive index	[-]

N	Count number	[-]
P	Pressure	[bar or atm]
p_i	Partial pressure of component i	[bar or atm]
Q	Volume flow rate	[LPH or m^3/s]
q	Mass flux	[$kg/m^2.s$]
$\mathcal{R}$	Gas constant	[J/mol.K]
R	Radius of the pipe	[m or mm]
r	Radius	[m or mm]
t	Time	[s]
T	Temperature	[K or °C]
U	Average fluid velocity	[m/s]
u	Velocity	[m/s]
V	Volume	[m^3]
w	Width	[mm]
x_i	Mole fraction of component i	[-]
y	Distance to the centre of the pipe	[m or mm]

Subscripts

A	apparent
a	air
avg	average
abs	absolute
act	actual
b	bubble
bpf	bubbles per frame
cum	cumulative

c	continues
d	dispersed
f	frame
g	gas
g	glass
i	component i
l	local
m	total number of frames recorded
max	maximum
min	minimum
n	total number of bubbles counted
pix	pixel
R	real
rel	relative
s	sample
sat	saturation
T	total
v	vapour
v	volumetric
w	water

Greek Symbols

α	Saturation ratio	[-]
$\Gamma_{\emptyset}$	Diffusion coefficient	[m^2/s]
γ	Surface tension	[N/m]
ε	Void fraction	[-]

ϵ	Turbulence dissipation rate	[m^2/s^3]
θ	Angle	[°]
μ	Dynamic viscosity	[kg/m.s]
v	Kinematic viscosity	[m^2/s]
π	Ratio of a circle's perimeter to its diameter	[-]
ρ	Density	[kg/m^3]
σ	Supersaturation level	[-]
σ_o	Standard deviation	[-]

ABBREVIATIONS

AAV	Automatic air vent
atm	Atmospheric pressure
CAD	Computer aided design
CFD	Computational fluid dynamics
DOF	Depth of field
EPSRC	Engineering and physical sciences research council
fps	Frames per second
HSG	Horizontal sight glass
LPH	Litres per hour
SR	Saturation ratio
TGM	Total gas measurement
VSG	Vertical sight glass
WD	Working distance

DIMENSIONLESS NUMBERS

Re	Reynolds Number	$\left(\frac{Inertial\ forces}{Viscous\ forces} = \rho \mathrm{u} L / \mu = \frac{\mathrm{u} L}{v}\right)$
Sc	Schmidt number	$\left(\frac{Momentum\ diffusivity}{Mass\ diffusivity} = v / D\right)$
Sh	Sherwood number	$\left(\frac{Mass\ transfer\ rate}{Diffusion\ rate} = kL / D\right)$
We	Weber Number	$\left(\frac{Inertial\ forces}{Surface\ tension\ forces} = \rho \mathrm{u}^2 L / \gamma\right)$

CHAPTER 1 INTRODUCTION

1.1 Background

Bubble nucleation in supersaturated solutions is a common phenomenon that can be observed in everyday life. For instance, when you open a can of carbonated drink, bubble formation starts instantly and the drink turns into a medium that has two different phases, liquid and gas. Similarly, two-phase flow in wet central heating systems appears mainly because of bubble nucleation at supersaturated conditions occurring on the primary heat exchanger wall of the boiler (Fsadni 2012). Dissolved gases are released as bubbles when they encounter high temperatures and low pressures inside the heat exchanger. These condition gradients inside the heat exchanger result in local supersaturated positions on the wall and lead to heterogeneous nucleation. In flowing systems, nucleating bubble detach from the nucleation surface when the drag forces acting on a bubble overcome the surface tension forces parallel to the nucleation surface, and then they flow through the system pipework resulting in two-phase flow (Fsadni et al. 2011b).

Multi-phase flow phenomenon is met with great interest in all branches of natural sciences, as well as engineering and industrial applications, and since it is a popular topic for a wide range of different fields, extensive research has been conducted on the subject (Brennen 2005; Crowe 2006; Crowe et al. 2012). Multi-phase flow phenomenon can be used as an advantage or it can produce negative effects. For example, in flotation separation technique, bubbles are used to separate solid particles from aqueous solutions (Lemlich 1972). However, bubble formation in central heating systems result in undesirable consequences. Microbubbles flowing through system pipework tend to escape to the upper parts of the system (low

pressure) causing cold spots in radiators, and/or maintenance or noise problems. This results in loss of energy and time, thus, a reduction in efficiency (Ge et al. 2013).

Recent energy reports point out that housing usage accounts for the highest percentage in the UK's energy consumption where more than 60% of household energy is utilized for space heating. In 2011, 90% of the households were already heated with central heating systems and graphs indicate that central heating usage in households would increase further and reach to 100% in near future (Department of Energy and Climate 2011). Under these circumstances, any improvement to the efficiency of central heating systems would gain prominence. There is an increasing trend in building services to install devices in the pipeline of the central heating systems to remove dissolved gases from the working fluid to prevent unwanted events, and therefore, save time and energy. There is a lack of data in the literature for two-phase flow characteristics, particularly for central heating systems, to assist companies in improving such devices. Most of the micro bubble deaerators are buoyancy driven devices, therefore, investigation of two-phase structures throughout different pipe installations will be useful for companies which aim to enhance their deaerator designs.

For this purpose, experimental facility was established at Brunel University London, UK to represent an ordinary wet domestic central heating system and a series of experiments were conducted in order to obtain a better understanding of two-phase flow phenomenon in such systems. Current project is taken over from an earlier researcher who gathered useful data on typical bubble sizes, volumetric void fractions, and nucleation and dissolution rates (Fsadni et al. 2011a; Fsadni et al. 2011b; Fsadni & Ge 2012; Fsadni et al. 2012; Fsadni 2012; Ge et al. 2013; Fsadni & Ge 2013; Fsadni & Ge 2014). Flow velocities investigated by the previous researcher were lower than 0.5 m/s inside the pipeline of the test rig. However, Curry (2001) suggests that water velocity throughout the system pipe work should be between 0.5 m/s to 1.5 m/s in order to avoid sludge settling occurring at lower velocities, as well as noise disruption resulting from higher velocities. Therefore, an external pump was installed to the test rig and flow velocities in the range of 0.5 to 1.1 m/s were investigated throughout the present project.

1.2 Research Objectives

As stated in the previous section, investigation of two-phase flow structures will assist deaerator manufacturers either to improve their designs or it will provide further understanding to make better suggestions for their installation and usage. Such an endeavour will advance the efficiency of bubble removal from typical central heating systems, and thus, help in saving energy and time. In this regard, objectives of the research project can be summarized as follows:

- To carry out detailed depth of field measurements to improve accuracy of experimentally measured and calculated void fractions.
- To improve previously developed photographic measurement technique and image processing routine in means of repeatability and accuracy.
- To investigate the effect of system parameters on bubble void fractions and sizes at boiler exit for higher flow rates than the previous project.
- To investigate bubble volume distributions at vertical and horizontal pipeline at higher flow rates than the previous project.
- To investigate bubble size distributions at vertical and horizontal pipeline at different locations throughout the pipework.
- To investigate possible effect of obstacles—such as pressure sensors, thermocouple and 90 degree bends—on bubble distribution.
- To employ a bubble measurement technique to investigate bubble velocity profiles across the pipe section at vertical and horizontal pipes.
- To investigate possible dissolution phenomenon for both vertical and horizontal pipelines at higher flow rates, which was previously reported for merely horizontal pipeline of the test rig at relatively low velocities.
- To investigate possible break-up and coalescence phenomena that may occur throughout the vertical and horizontal pipelines of the system.
- To carry out a computational study that can be used later to predict bubble distribution profiles throughout a typical wet central heating system.

1.3 Layout of the Thesis

Following this introduction, the research proceeds with a literature review in CHAPTER 2 where topics related to the two-phase flow phenomenon in central heating systems are presented. Relevant topics are: solubility of gases, supersaturated gas-liquid solutions, bubble nucleation in supersaturated solutions, and two-phase flow behaviours at vertical and horizontal pipes.

In CHAPTER 3, experimental design and methodology employed for the current study to investigate two-phase flow structures are provided. This chapter includes a comprehensive description of the conducted experiments with the main intention of providing information and knowledge for future studies that desire to replicate comparable experiments with similar equipment.

Results and discussions of these experiments are presented in CHAPTER 4. This chapter includes the following headings: effects of system parameters on two-phase flows at boiler exit, bubble volume and size distributions across the bubble section, bubble velocity profiles, and bubble sizes.

In CHAPTER 5, detailed information on the physical model and results of the computational study are outlined. Computational study is conducted to investigate bubble distributions at the horizontal pipeline, in order to contribute to the subject of experimental studies outlined in previous chapters. Finally, main conclusions and recommendations for future work are summarized in CHAPTER 6.

CHAPTER 2 LITERATURE REVIEW

2.1 Introduction

The following chapter presents the literature survey related to background information for the two-phase phenomenon which occurs in the pipeline of the wet central heating systems. Dissolved gases in the system liquid are responsible for the two-phase flow. Dissolved gases in the system liquid nucleate from the heat exchanger wall and detach from the surface, leading to two-phase bubbly flow through the system. In this framework, **Section 2.2** introduces the concept of solubility of gases in the liquid. Secondly, fundamentals of bubble formation, particularly for wet central heating systems, are explained in **Section 2.3** and then **Section 2.4** summarises the literature related to patterns and characteristics of two-phase flow in the pipes. Lastly, a brief summary of the whole chapter is delivered in **Section 2.5**.

2.2 Solubility of Gases in Liquids

In the Oxford Dictionary of Physics (2009), solubility is defined as the amount of solute that dissolves in a known amount of solvent to reach the equilibrium state called ‘saturated solution’. In the present study solvent and solute are represented by liquid and gas state, respectively. An impressive description of the physics of the dissolution process using the concept of motion of atoms can be found in Feynman (1994). Engineering applications of course look for practical prediction of solubilities; therefore, developing appropriate experiments and empirical equations is a necessity.

As reported in the chemical literature, experimental study of solubility of different substances has been on-going for more than 200 years. Reid et al. (1986) have

pointed out that the available data is extensive, but needs to be reorganised. In this book, they have provided a table of useful data sources regarding solubility of gases in liquids. Historically, several different ways and units have been in use for expressing solubility and, confusingly, different scientists have published their work with different units. However, explanations of different solubility units of gases in liquids helpfully exist in chemical literature, e.g., Markham & Kobe (1941), Battino & Clever (1966), Gerrard (1976) etc.

Two of the most popular units used to express solubility in older scientific articles are Bunsen and Ostwald coefficients. Bunsen coefficient is the volume of gas dissolved per unit volume of solvent at system temperature when the partial pressure of the solute is 1 atm, whereas Ostwald coefficient is the volume of gas dissolved per unit volume of solvent at system temperature and partial pressure. The relationship between these two coefficients can be simplified and expressed with **Equation (2-1)** if the solubility is small and the gas phase is ideal (Reid et al. 1986):

$$Ostwald\ coefficient = \frac{T}{273} \times (Bunsen\ coefficient) \quad \textbf{(2-1)}$$

It has been reported in Reid et al. (1986) that using a mole fraction or the Henry's law constant as a solubility unit has become more common than other units in recent years. In order to be up-to-date and consistent with recent studies, mole fraction (the amount of gas dissolved in the liquid in moles divided by amount of solution in moles) or the Henry's law constant is going to be used as a solubility unit in the present study.

The most notable study on solubility of gases in liquids was done by William Henry (1802) in the early 19th century. Gerrard (1976) summarized the details of his experiments and observations on the amount of gas absorbed by water which led to one of the gas laws known as Henry's Law. The main conclusion of Henry's experiments was that the amount of absorbed gas by water at 2 and 3 atm was equal to twice and thrice the amount dissolved under 1 atm pressure at a specific temperature. In other words, the concentration of dissolved gas in the liquid is proportional to its partial pressure over the aqueous phase. Gerrard (1976) stated that

there is inadequacy in Henry's statement about the effect of pressure because he did not provide a mathematical form and he also pointed out that one should not forget that the observations were only for five gases (CO_2, H_2S, N_2O, O_2 and N_2) in contact with water as a solvent.

At ordinary pressures, solubility of gases in liquids is very small if there is no chemical reaction between the solute and solvent. For example, at 20°C and a partial pressure of 1 atm, nitrogen has solubility value (mole fraction) of 1.24×10^{-5} in water (Reid et al. 1986). Gerrard (1976) has given a table of solubility values of several substances in water to show the effect of chemical reaction on solubility values. The solubility values show sharp increases for CO_2 and H_2S because of the chemical reaction between the gases and water (see **Table 2-1**).

Table 2-1. Bunsen coefficient of some gases in water at 25°C

Gas	N_2	H_2	CO	O_2	CO_2	H_2S
Solubility	0.01434	0.01754	0.02142	0.02831	0.759	2.282

**Source: Gerrard (1976)*

In general, Henry's law can be used to calculate the concentration of dissolved gas in the solution if the following three statements are valid (Danckwerts 1970):

- The dissolved gas amount is small.
- There is no reaction between the solvent and solute.
- The temperature and pressure of the system are not close to the critical temperature and pressure of the solvent.

Prausnitz et al. (1999) have provided some real values for two of the restrictions mentioned above when considering the validity of Henry's law. They noted that partial pressures should not exceed the range of 5 to 10 bars depending on the gas-liquid pair and dissolved gas amount should not exceed about 3 mol %. Temperature (15 to 85 °C) and pressure (1 to 3 atm) ranges in the present study are far less than the limitation given by Prausnitz et al. (1999) and the critical temperature (374 °C) and pressure (217.7 atm) of the solvent. Moreover, solubility of ordinary gases in water is far less than 3 mol % in the region of the temperature and pressure

conditions that exist in wet central heating systems. Therefore, Henry's law provides a very good approximation for calculating solubility in such systems.

Equation (2-2) is the most common way of expressing Henry's law in mathematical form (Perry et al. 1997):

$$p_i = K_H x_{\mathrm{i}} \tag{2-2}$$

Here p_i is defined as partial pressure of the solute in the gas phase (atm); K_H is the proportionality constant, expressed in units of atmospheres of solute pressure in the gas phase per unit concentration of the solute in the liquid phase (atm); and x_1 is the mole fraction of solute in the liquid phase (dimensionless).

Table 2-2 illustrates the change of the proportionality constant of nitrogen in water at different temperatures. Values in the table are from the "International Critics Tables" as cited in Perry et al. (1997) and can be used in **Equation (2-2)** to find either dissolved mole fraction of the nitrogen in the liquid or partial pressure of the nitrogen above the solution at moderate pressures and temperatures depending on which one is known.

Table 2-2. Proportionality constant (K_H) of nitrogen in water

Temperature (°C)	$\boldsymbol{K_h \times 10^{-4}}$ **(atm)**	**Temperature (°C)**	$\boldsymbol{K_h \times 10^{-4}}$ **(atm)**
0	5.29	40	10.4
5	5.97	45	10.9
10	6.68	50	11.3
15	7.38	60	12
20	8.04	70	12.5
25	8.65	80	12.6
30	9.24	90	12.6
35	9.85	100	12.6

**Source: Perry et al. (1997)*

Figures in the following sections (**Figures 2-1** to **2-4**) that show dissolved mole fraction of the gases in the water are calculated with **Equation (2-2)** by using the proportionality constant provided in the reference underneath each figure.

2.2.1 Effect of temperature on solubility of gases in liquids

As mentioned in Danckwerts (1970), the Henry's law constant depends on the temperature of the system and increases as the temperature increases as shown in the **Table 2-2**. This leads to the conclusion that solubility of gases decreases with increasing temperature. Danckwerts has formulated the relationship of the Henry's law constant dependence on temperature as in **Equation (2-3)**.

$$\frac{d \ln He}{d\left({}^{1}/_{T}\right)} = \frac{\Delta H}{\mathcal{R}} \qquad \textbf{(2-3)}$$

Where T represents the absolute temperature, $\mathcal{R}$ is the gas constant and ΔH is the heat absorption of the solute at a given temperatures. For moderate temperatures, values of ΔH are very small and therefore the plot of $\log He$ against ${}^{1}/_{T}$ is a straight line. This relationship has also been used for predicting the solubility at various temperatures (Danckwerts 1970).

In contrast to Danckwerts (1970), Prausnitz et al. (1999) have given the variation of the Henry's law constant with temperature for nine binary systems (see **Appendix 1** for the graph that has been provided in their book) and pointed out that the effect of temperature on the solubility of gases cannot be simply generalized as Danckwerts (1970) did. According to Prausnitz et al. (1999), the proportionality constant that is used in Henry's law depends not only on temperature, but on the nature of liquid-gas combination and property of the specific system as well. They have reported that it is more common to observe a reduction in the Henry's constant at high temperatures.

Also, Holmes (1996), as cited in Wisniak et al. (2006), has questioned the fact stated in most chemistry textbooks that dissolution of gases in liquids is an exothermic process and solubility of gases in liquids reduces with increasing temperature as a general rule, and argued that this generalization is not always true. For instance,

solubility of hydrogen (H_2) in water reduces as the temperature rises until it reaches 50 °C. After that temperature, hydrogen starts to dissolve in the water easier when one continues to increase the temperature of the gas-liquid system (see **Figure 2-1**).

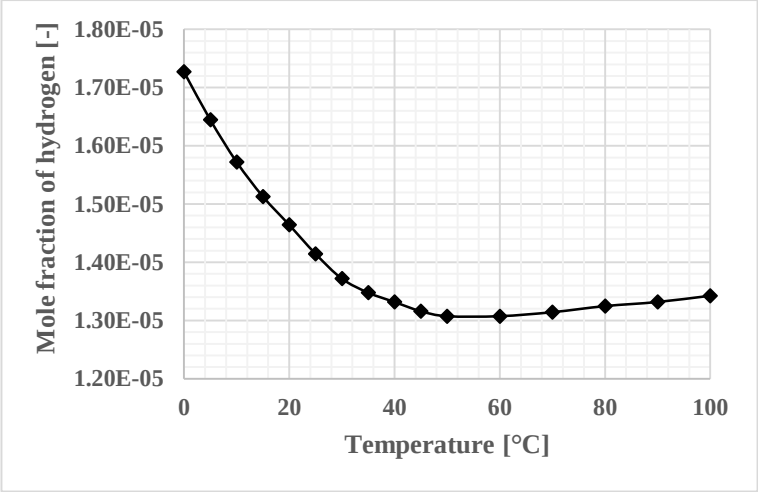

Figure 2-1. Solubility of hydrogen in water at partial pressure of 1 atm.

**Source: Perry et al. (1997)*

Even though there are some exceptions (notably hydrogen and helium), the solubility of ordinary gases in water often decreases with increasing temperature at a moderate temperature range as illustrated by **Figure 2-2**. At temperatures close to the critical temperature of the liquid, the solubility of gases increases with rise in system temperature (Reid et al. 1986).

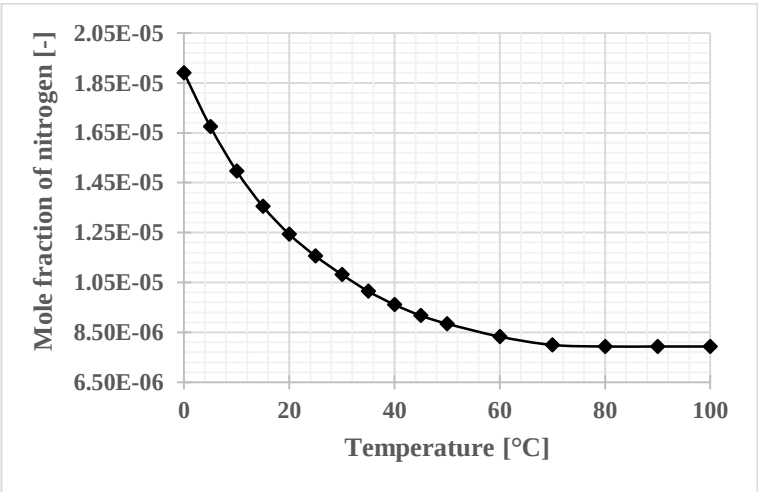

Figure 2-2. Solubility of nitrogen in water at partial pressure of 1 atm.

For those who are interested in predicting the solubilities at high temperatures, Harvey (1996) has investigated gas solubilities over large temperature ranges and defined a typical pattern of the Henry's law constant for a solute-solvent pair. He has found that the Henry's law constant increases as temperature rises and reaches its maximum value and then starts to decrease. His work provides a semi-empirical correlation for predicting the Henry's law constant over a large temperature range for more than ten gases in water and *n*-hexadecane with high precision.

2.2.2 Effect of pressure on solubility of gases in liquids

As mentioned in **Section 2.2**, the effect of pressure on solubility was first rigorously investigated by Henry (1802). He observed the linear relationship between the dissolved gas amount in the liquid and partial pressure of the gas over the liquid at a particular temperature. The effect of pressure on Henry's proportionality constant can be neglected unless the pressures are not high (Prausnitz et al. 1999). **Figure 2-3** illustrates how the amount of dissolved nitrogen in water changes at moderate partial pressures when the temperature is constant, and the linear dependence of solubility of nitrogen in water on partial pressure at constant temperature can be seen clearly.

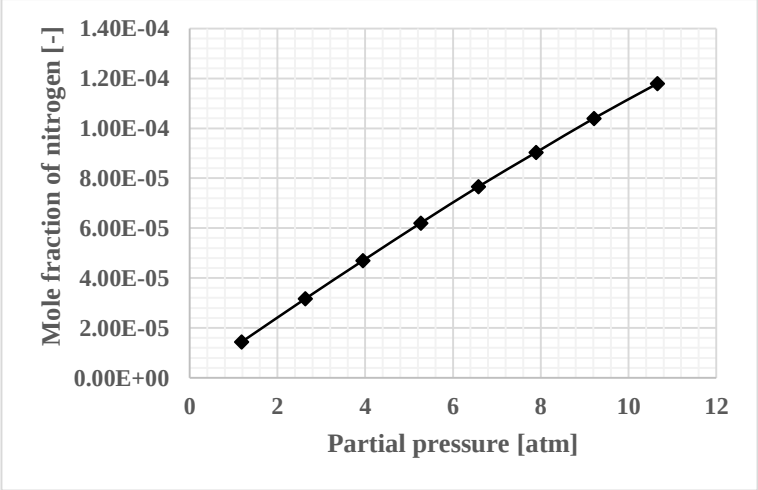

Figure 2-3. Solubility of nitrogen in water at 19.4 °C.

**Source: Perry et al. (1997)*

Frolich et al. (1931) investigated solubility of gases in liquids, particularly at high pressures and concluded that Henry's law can be used to predict solubilities over a wide pressure range (up to 100 atm) with errors in limits that are allowed in the field

of engineering. They provided a practical rule which points out that, at a given temperature, the solubility of gases in liquids is a linear function of pressure until the pressure reaches to one-half to two-thirds of saturation pressure of the gas.

Wiebe et al. (1933) studied solubility of nitrogen for even higher pressures (up to 1000 atm) at three different temperatures (50, 75 and 100°C) and they showed that Henry's law cannot predict solubility of nitrogen in water for really high pressures. Later, Krichevsky and Kasarnovsky (1935) proposed an equation which can calculate solubilities of slightly soluble gases in solvent with low vapour pressure, at a wide range of temperatures (0 to 100°C) and pressures up to 1000 atm. They validated their correlation for nitrogen and hydrogen in water. Prausnitz et al. (1999) have illustrated the limit of Krichevsky-Kasarnovsky equation on a graph (see **Appendix 2**) by comparing the predicted solubilities with the experimental results of Wiebe et al. (1934) for nitrogen in liquid ammonia. They observed that the experimental results deviate from the predicted values at 70°C and over 600 bars.

After a decade, Krichevsky-Ilinskaya introduced extra parameters to the original Krichevsky-Kasarnovsky equation and they managed to widen the application range of the equation particularly for high soluble light gases (Prausnitz et al. 1999). Orentlicher and Prausnitz (as cited in Clever & Battino (1975)) conducted a research on the Krichevsky-Ilinskaya equation in 1964 and provided thermodynamic parameters for correlating hydrogen solubilities in eight different liquids. Battino et al. (1984) also investigated the solubility of nitrogen and air in different liquids and mixed solvents for a wide range of temperatures and pressures. Their extensive work which was published provides empirical equations and includes detailed chemical data.

2.2.3 Summary

To sum up, this section provides an introduction to the solubility of gases and points out the importance and applicability of Henry's Law related to the present work. It includes a discussion of the effect of temperature and pressure on the solubility of gases in the liquids,as well as several useful references on the topic of predicting solubilities at high temperatures and pressures.

Temperatures and pressures that exist in the usual wet central heating systems are far less than the limitations mentioned for the validity of Henry's law. Therefore, Henry's law is found to be applicable for the purpose of the present study. Henry's law provides accurate predictions of solubilities of ordinary gases in water within the range of uncertainty allowed in engineering calculations at moderate temperatures and pressures. The law gives a simple relationship between the partial pressure of gases over a liquid and the dissolved gas amount in the liquid. Moreover, working with Henry's law in this study ensures consistence and comparablility of results with the experiments conducted as part of preceding research using the same equipment.

2.3 Bubble Formation in Central Heating Systems

As narrated earlier in the introduction section of this chapter (**Section 2.1**), dissolved gases are responsible from bubble formation in wet central heating systems. They penetrate into the system either during injection of water to the pipework from the main taps or inevitably leak in through various parts of the closed-loop (Fsadni et al. 2011b). In the UK, water from the mains usually comes with pressures between 2 to 5 bars (depending on the time of the day) at temperatures ranging from 4 to 20°C (depending on the month of the year). The amount of dissolved gases in liquids varies with temperature and pressure. And in winter, water reaches its coldest temperature causing it to absorb a higher amount of gases as mentioned in **Section 2.2**. These gases in the flowing liquid are released as bubbles when they experience high temperatures and/or low pressures inside the heat exchanger. Bubble formation is induced by local supersaturated conditions which occur on the primary heat exchanger wall of the boiler. Similar bubble formation phenomenon, caused by local supersaturation on spherical and plate heaters that are submerged, were reported and investigated intensively by several researchers (Divinis et al. 2005; Divinis et al. 2006; Karapantsios et al. 2008).

The boiler term, used earlier, can raise some questions in mind regarding the origins of bubble formation, but there is no possibility that suitable conditions for nucleate boiling in such systems can exist (Fsadni et al. 2011). Theoretical calculations for the boiler heat exchanger wall temperature proposed by Fsadni et al. (2012) suggest that

boiler wall temperature is less than boiling point (100°C) of water at atmospheric pressure for a wide range of system conditions. In general, when heating system is working, the system pressure is higher than the atmospheric pressure, thus boiling point of the water in the system should be higher than its boiling point under atmospheric pressure. Therefore, the nucleate boiling phenomenon is not expected to take place and it can be said that supersaturation is the only phenomenon causing bubble nucleation in wet central heating systems. In order to understand bubble formation process in wet central heating systems, it is necessary to introduce the supersaturation phenomenon before proceeding further.

2.3.1 Supersaturated gas-liquid solutions

Danckwerts (1970) has mentioned that desorption of gases from liquids occurs when the concentration of dissolved gas in the liquid is higher than concentration at the interface. In other words, partial pressure of the gas, which needs to be in equilibrium with the bulk liquid, is greater than the partial pressure at the surface. In some cases, it can be greater than the total pressure at the surface. For example, a liquid can be saturated with CO_2 at a partial pressure of 10 bars and if one reduces total pressure at the surface to 1 bar at once, equilibrium at the surface of the bulk liquid will vanish, thus the solution will form bubbles in order to readjust the concentration balance at the interface. This phenomenon is called supersaturation and is much the same as the daily experience we observe when a bottle of carbonated drink is opened.

Supersaturation term is expressed by Jones et al. (1999) as system's propensity to produce bubble. They have provided the saturation ratio and the supersaturation concepts defined by Lubetkin and Blackwell (1988) as follows:

- Saturation ratio: is the ratio of actual dissolved gas amount (x_{act}) in the solution and maximum amount of dissolved gas (saturated) that can be hold up by the liquid (x_{sat}) at specific temperature and pressure.

$$\alpha = \frac{x_{act}}{x_{sat}} \qquad \textbf{(2-4)}$$

- Supersaturation level: is tendency to produce bubbles.

$$\sigma = \alpha - 1 \tag{2-5}$$

Supersaturation in gas-liquid systems can be reached by a sudden reduction in the pressure and/or increase in temperature. Jones et al. (1999) use a figure showing dissolved carbon dioxide concentration in water at 1 atm as an example for defining supersaturation concept. We will adapt the same idea and will introduce the concept with the figure plotted for nitrogen (**Figure 2-2**) as it is more relevant to the current study. The reason for this is that air is the gas that penetrates into the system and nitrogen constitutes a significant amount of its composition (78 %).

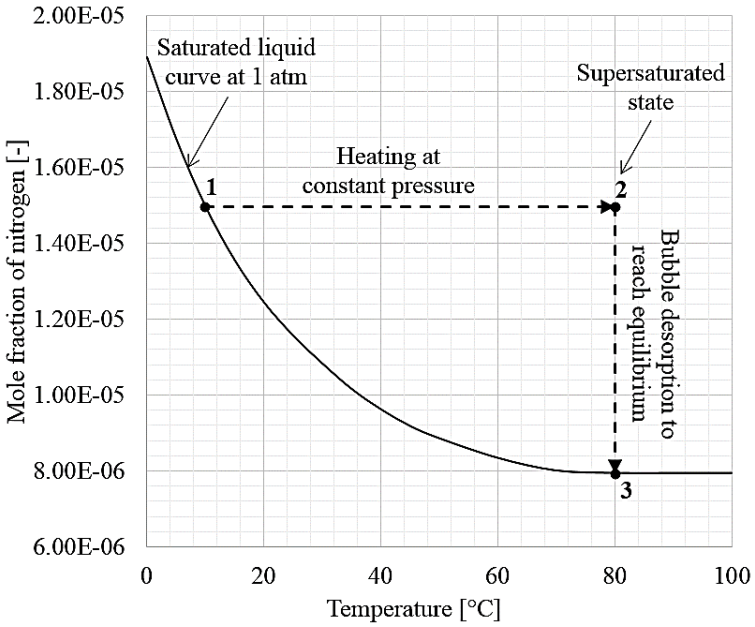

Figure 2-4. Solubility of nitrogen against temperature at partial pressure of 1 atm.

**Source: Table 2-1.*

Figure 2-4 visualizes the change of dissolved nitrogen concentration in water with respect to temperature at 1 atm. If one has a saturated nitrogen-water solution at 10°C with 1 atm partial pressure (Position 1), actual dissolved gas amount ($x_{act} = x_1$) in the solution can be easily calculated by Henry's law. Later, imagine that the gas-liquid solution heats up to 80°C at constant pressure, the solution will eventually come to point 2 which is supersaturated. In other words, solution has more dissolved

gas than it can hold-up at that specific temperature and pressure. At this point, solution has a tendency to produce bubbles and reduce the amount of dissolved nitrogen in the liquid to the amount of saturated solution can hold ($x_{sat} = x_3$) in order to reach equilibrium state called 'saturated state' (Position 3).

Jones et al. (1999) have suggested that it would be functional to integrate Henry's law (**Equation (2-2)**) with **Equations (2-4)** and **(2-5)** which gives the opportunity to investigate supersaturation concept from the view of pressure. This approach identifies critical bubble radius defined in the classical theory of nucleation. The pressure difference between two states (refers to point 2 and 3 in **Figure 2-4**) of the bubble desorption processes may be explained using the relationship of Henry's law when the vapour pressure of liquid is neglected. Neglecting vapour pressure of the liquid means that partial pressure of the gas in the liquid will be equal to the total pressure ($p \cong P$). Combination of equations mentioned earlier leads to **Equation (2-6)**.

$$\Delta P = P_{act} - P_{sat} = K_H(x_{act} - x_{sat}) = P_{sat}\left(\frac{x_{act}}{x_{sat}} - 1\right) = P_{sat}\sigma \qquad \textbf{(2-6)}$$

During bubble formation, pressure difference originating from the spherical shape of the bubble can be described by the Laplace equation (**Equation (2-7)**):

$$\Delta P = \frac{2\gamma}{r_b} \qquad \textbf{(2-7)}$$

Where; r_b is bubble radius and γ represents interfacial surface tension between the liquid and gas. When thermodynamic equilibrium between the solution and the bubble is established, it can be said that bubble has reached its critical radius (Jones et al. 1999).

2.3.2 Bubble nucleation in supersaturated solutions

Talanquer & Oxtoby (1995) state that a solution which is metastable with respect to its vapour phase is necessary to observe a bubble nucleation. This unstable condition

can be achieved in three different ways; (i) superheating the liquid that leads to boiling phenomenon, (ii) “stretching” which basically is the process of forcing the solution to produce bubbles by experiencing negative pressure known as cavitation, and (iii) forcing the solution to absorb more than its saturation limit leading to supersaturated solution. The latter is the main concern of the current study.

In general, bubble nucleation can be divided into two main types as homogeneous and heterogeneous nucleation. If the bubble nucleation process takes place entirely in the liquid, it is called homogenous nucleation, whereas heterogeneous nucleation term is used if the bubble nucleation exists at the boundary between the liquid and other phase / phases (Blander & Katz 1975). **Figure 2-5** illustrates a schematic representation of classical homogenous and heterogonous nucleation.

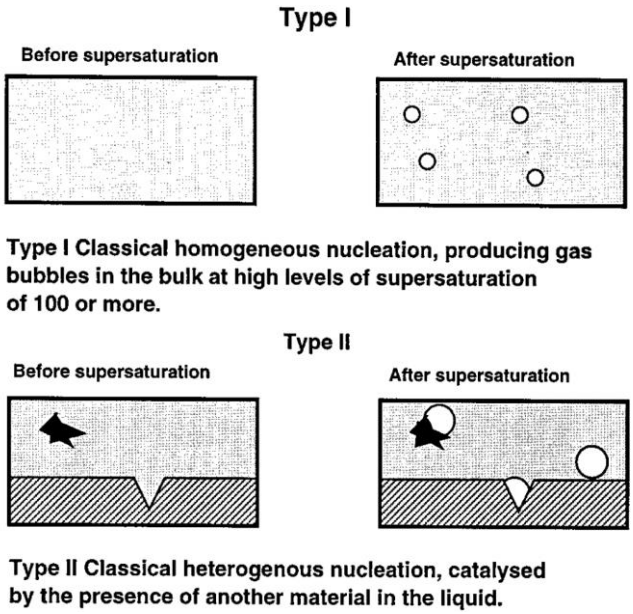

Figure 2-5. Schematic representations of type I classical homogenous (top) nucleation and type II classical heterogeneous nucleation (bottom) (Jones et al. 1999).

Classical nucleation theory is commonly used to define and predict bubble nucleation rates during type I and II nucleation. Several researchers have reviewed the classical nucleation theory throughout the years (for further understanding see the works of Bowers et al. (1995), Jones et al. (1999) and Sear (2007)). Jones et al. (1999) point out that these classical types of nucleation do not fulfil or satisfy experimentally observed higher bubble nucleation rates than predicted by classical nucleation theory in supersaturated solutions. Therefore, in an effort to characterize nucleation types

particularly for supersaturated solutions, they introduced two extra types in addition to the classical nucleation types: type III pseudo-classical nucleation and type IV non-classical nucleation. Schematic illustration of type III and IV nucleation are shown in the **Figure 2-6** below:

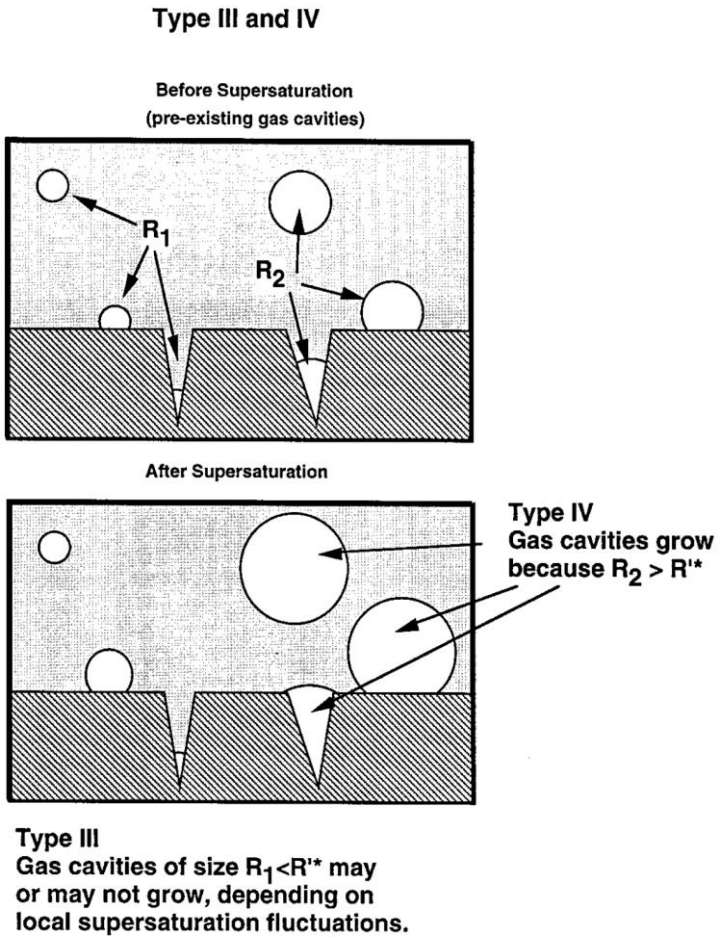

Figure 2-6. Schematic representations of type III pseudo classical nucleation and type IV non-classical nucleation (Jones et al. 1999).

Type I classical homogenous nucleation in supersaturated liquids requires high levels of supersaturation because of the high nucleation energy barrier needed to start nucleation. Rubin & Noyes (1987) have studied the critical supersaturation levels of several gases before homogeneous nucleation of bubbles occur. They used chemical reaction to reach supersaturated solutions at ordinary conditions (pressure and temperature) and noted that amount of dissolved diatomic gases in liquids can reach up top 80 times higher than their saturation points before homogenous nucleation starts. Furthermore, Jones et al. (1999) discussed and provided evidence that type-II

classical heterogeneous nucleation in supersaturated liquids shows similar energy barrier requirements with the type-I classical homogeneous nucleation. Main reason being that if the system does not contain any gas cavities before supersaturation, homogenous nucleation is required initially to fill the cavities with gas pockets and then maintain nucleation from that point on.

On the other hand, type III and IV offer bubble formation with less nucleation energy barriers thus lower supersaturation levels. Type III involves both homogenous and heterogeneous nucleation from the filled gas cavities or gas pockets traveling in the bulk fluid. The nucleation energy barrier is lower than the levels expected from type I and II nucleation because of already existing bubble cavities that hold critical radiuses smaller than the critical radius predicted by classical nucleation theory. Furthermore, type IV non-classical nucleation does not require nucleation energy barrier since the curvature of each gas cavity or pockets are larger than the critical radius predicted by classical nucleation theory. Detailed summary of previous observations that lead to the development of type III and IV nucleation have been provided by Jones et al. (1999).

Bubble nucleation at relatively low supersaturation levels is common experience for carbonated soft drinks where supersaturation levels were around 5 (Enríquez et al. 2013). Devereux & Lee (2011) have conducted a research on bubble nucleation in stout beers and reported that type IV nucleation can be the only type which can lead to bubble nucleation caused by supersaturation at low saturation levels. Moreover, Enríquez et al. (2013) conducted a research concerning nucleation at even lower supersaturation levels and reported that particles flowing in the liquid, cavities on the solid boundary or free gas pockets (small bubbles) are the cause of bubble nucleation sites which lead to bubble nucleation at low supersaturation levels.

It is beyond the scope of the current study to examine models that can be used to predict bubble nucleation rates and their detachment diameters since extensive literature review and discussion on the models developed to estimate bubble nucleation rates and their detachment diameters from nucleation sites are provided in the PhD thesis of Fsadni (2012). Moreover, Fsadni (2012) compared and modified

suitable models through experimental work particular for wet central heating systems and is recommended for interested readers to go through for more information.

2.3.3 Summary

To summarize the section, the importance of supersaturation and nucleation in supersaturated solutions related to the bubbles observed in wet central heating systems have been discussed and reviewed. After reviewing the literature for bubble nucleation phenomenon in supersaturated solutions, it is argued that the origins of bubble formation in wet central heating systems is more likely caused by type III or IV nucleation characterized by Jones et al. (1999). The main reason for this is that the saturation ratios commonly observed at the primary heat exchanger wall of the boiler in ordinary wet central heating systems are lower than 1.5 (Fsadni et al. 2011b) which requires low or zero nucleation energy barriers. Therefore, type III or IV nucleation is responsible from the two-phase flow structures seen in pipelines of wet central heating systems.

2.4 Two-phase Flow in Pipelines

Multiphase flow is defined by Angeli (2014) as a flow of two or more phases travelling together through any kind of flow system .She further points out that, within multiphase flows, investigating two-phase flow is very important. Because, it offers easier analysis compared to three or four phase flows, hence, provides a better understanding for more complicated systems. Two-phase flow can include different pairs such as; gas-liquid, liquid-liquid, gas-solid and liquid-solid. Gas-liquid flow is the main concern of the current study since the phase pair observed in wet central heating pipelines are air bubbles and water.

Two-phase flow phenomenon has been investigated intensively throughout the years because of its popularity in variety of industries. Detailed knowledge starting from the basic concepts to complicated analysis can be found in the works of Govier & Aziz (1972); Chisholm (1983); Levy (1999); Brennen (2005) and more recently Angeli (2014). Chisholm (1983) summarizes the usage of gas-liquid flow in pipelines in industries with 11 examples of plants and situations where two-phase

flow occurs, such as; tubular boilers, boiling water reactors, refrigeration etc. A more convenient classification is made by Angeli (2014) with 5 main types:

- Pipeline transport systems; e.g. oil and gas transport pipelines.
- Evaporation systems; e.g. boiling/pressurized water reactors, refrigeration.
- Vapour condensation systems; e.g. process condensers, refrigeration.
- Gas-liquid mas transfer; e.g. absorption, stripping, distillation.
- Liquid-liquid extraction; e.g. pharmaceutical, energy, mining.

All of the references mentioned previously have introduced the flow patterns that is observed in two-phase flow after providing the description of two-phase flow and pointed out that recognizing the patterns is necessary for a better understanding two-phase flows. Therefore, two-phase flow patterns seen in circular pipes are given in the following section in order to determine the flow pattern observed in wet central heating system pipework.

2.4.1 Flow patterns in two-phase flow

Levy (1999) states that if two-phases travel together through constricted space, they tend to organize themselves in a different formation. Angeli (2014) argues that the existence of deformable interfaces between each phase is responsible for this different arrangement and it is the most significant difference between single phase and two-phase flows. Moreover, surface area for the mass, momentum or energy transfer between phases are significantly affected by the geometric distribution of the phases (Brennen 2005). These different arrangements of phases while travelling through the flow path are called flow patterns or flow regimes. Flow patterns can vary according to many parameters, like flowrates of each phase, properties of phases, channel size and inclination etc.

A lot of effort has been put on summarising the effects of different parameters (phase volume fluxes, volume fraction or properties of phases) on flow patterns throughout the years and these are generally presented as flow regime maps (see Govier & Aziz 1972, Chisholm 1983 or Brennen 2005). However, Brennen (2005) argues that these maps are generally dimensional and can be applied specifically for the particular pipe diameters and phases used by the researcher. Even though intense

investigations were conducted to develop generalized flow regime maps that can predict flow patterns for different pipe sizes and fluids, there is no universal, dimensionless flow regime map developed yet.

The pipeline in wet central heating system is composed of vertically and horizontally positioned circular pipes if there is no extra ordinary design requirement. Therefore, flow patterns occurring in vertical and horizontal flow is the interest of the current study. The flow pattern identification is generally conducted by direct observation of two-phase flow patterns through experiments (Brennen 2005). The main difference between vertical and horizontal two-phase flow is the effect of gravity on the phases. This is presented in the next two sections.

2.4.1.1 Vertical flow

In general, vertical two-phase flow in circular pipes can be defined by six different types according to the phase distributions along the pipe (Levy 1999; Angeli 2014). The gravitational force and the flow directions are parallel to each other; therefore, there is no significant effect of gravity on the phase alignment and the patterns tend to portray a symmetric appearance. These six different types are illustrated in **Figure 2-7**.

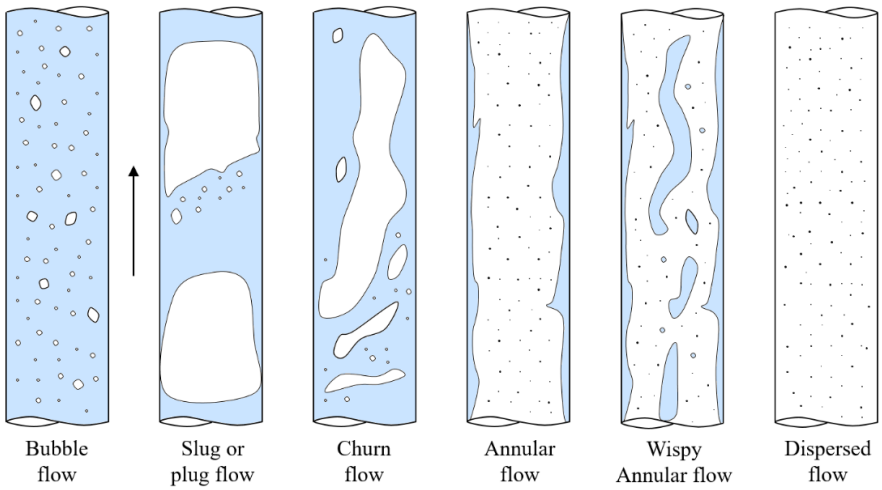

Figure 2-7. Flow patterns in the vertical two-phase flow. Adapted from Levy (1999) and Angeli (2014).

- Bubble flow: The bubbles (gas) are dispersed in the continuous phase (Liquid) with different shapes and sizes (Levy 1999). Angeli (2014) mentions that increase in gas flow rate, results in the dominance of the coalescence

phenomenon which leads to increase in bubbles sizes and formation of elongated bubbles.

- Slug or plug flow: This type of flow is differentiated from other patterns by the big bubbles nearly occupying the channel with slugs of liquid between them (Levy 1999). Elongated big bubbles tend to be bullet shaped with a circular cap and typically occur because of bubble coalescences at elevated gas volume fractions (Angeli 2014).
- Churn flow: Similar to slug flow but occurs at high gas and liquid velocities. Phases are highly distorted, unstable and they collapse because of turbulences. Churn flow is the pattern in between slug and annular flow (Angeli 2014).
- Annular flow: A film of liquid forms at the edge of the walls and gas, with or without drops of liquid, travels in the middle (Levy 1999). Observed when the gas velocities are increased higher than churn flow and if the liquid droplets exist in the centre section of the flow, the pattern is called annular-mist (Angeli 2014).
- Wispy annular flow: Occurs if both gas and liquid velocities are increased beyond the conditions observed at annular flow. Liquid droplets coalesce and create large wisps of liquid (Angeli 2014).
- Dispersed flow: Most of the pipe volume is occupied by gas molecules and there are small droplets of liquid in the core section (Levy 1999).

2.4.1.2 Horizontal flow

Flow patterns observed in horizontal pipelines are characterized similar to the patterns occurring in vertical pipelines but show significant difference because of the gravitational force. The flow direction is normal to the gravitational force direction, hence, the patterns illustrate asymmetric arrangement when compared to vertical two-phase flow (Angeli 2014). The patterns experienced during horizontal two-phase flow can be divided into four main types which are presented in **Figure 2-8** with some extra patterns in between two flow regimes.

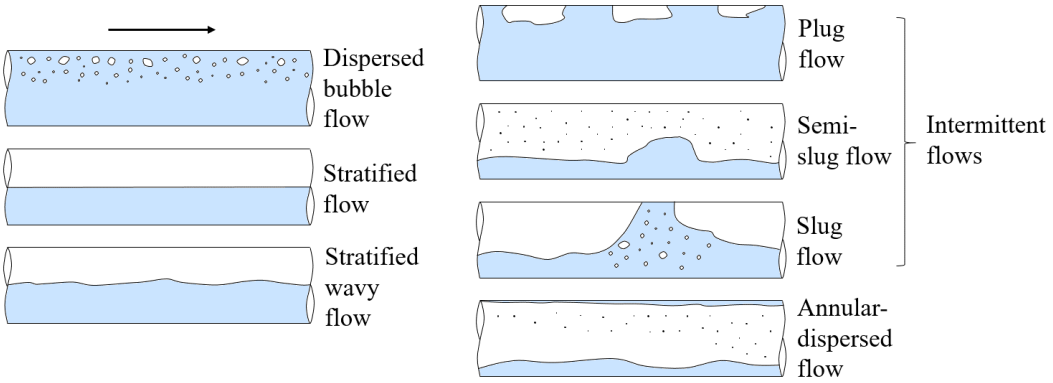

Figure 2-8. Flow patterns in horizontal two-phase flow. Adapted from Levy (1999).

- Bubble flow: Bubbles are dispersed in the liquid with different sizes and shapes and they tend to accumulate at the upper part of the pipe. The bubble distribution across the pipe section can become more uniform as the flow velocities are increased (Angeli 2014).
- Slug or plug flow: Large elongated bubbles are travelling at the upper part of the pipe and slug flow can turn into plug flow if the bubbles are dispersed freely in the liquid (Angeli 2014).
- Annular flow: In horizontal flows, annular flow is asymmetric, unlike in vertical flow, and the liquid film on the bottom part of the pipe is thicker than the film on the upper wall. Drops of liquid can also travel in the middle section of the pipe, along with the gas phase (Angeli 2014).
- Stratified flow: Each component of the two-phase flow travels separately, where liquid occupies the bottom of the pipe and gas flow the upper. If the flow of the phases are relatively low, smooth stratified flow shown in **Figure 2-8** takes place. However, the stratified wavy flow can develop at higher gas velocities (Angeli 2014).

2.4.1.3 Flow pattern in wet central heating systems' pipework

Before proceeding to the review of bubble distributions observed in pipelines, it is necessary to determine which type of flow pattern can be expected from two-phase flow through wet central heating systems. Initial estimate would be the bubble flow pattern shown in the **Figures 2-7** and **2-8** based on the visual observations carried out by the researcher during the experiments. Furthermore, bubble diameters and their

void fractions that occur in such systems are relatively low when compared to pipe diameter, which is 20 mm. **Table 2-3** summarizes the bubble diameter and volumetric void fraction ranges (see **Section 3.5** for the definitions of bubble diameter and volumetric void fraction) obtained at observation points given in **Figures 3-23** and **3-24** throughout the experiments.

Table 2-3. Bubble diameters and volumetric void fractions observed in wet central heating systems

Parameter	**Range**
Bubble diameter (mm)	0.05 – 3.56
Volumetric void fraction (-)	6.6768e-6 – 0.0005

In addition, flow pattern maps proposed by Wiesman for vertical and Mandhane et al. for horizontal two-phase flows cited in Brennen (2005) were utilized in the present study to validate the initial flow pattern estimate. These particular flow pattern maps are considered to be suitable on account of the phase pairs and pipe diameters used during their time of development. Air-water mixture through 25mm circular pipe was used during their experiments, which is very similar to the flow conditions occurring in central heating systems.

Figures 2-9 and **2-10** illustrate the aforementioned flow pattern maps. It can be seen from both figures that volumetric flux (superficial velocity) of phases are required to use them. Therefore, calculation of volumetric fluxes were performed and presented in **Tables 2-4** and **2-5** for vertical and horizontal setups from the experiments conducted in the test rig built for the current work. Data ranges summarized in the tables are from the bubble distribution measurement discussed in **Section 4.3**. First, total sample volume captured for each observation point which have 8 focal planes (2000 frames per focal plane) across the pipe section was calculated (see **Section 3.5.4** for each sample volume and **Section 3.7** for optimum frame number per focal plane). Secondly, total bubble volume captured at each position is calculated as explained in **Sections 3.4.2** and **3.5.5**. Then, volume flow rate of water measured from the flow meter is converted from LPH to m^3/s. Next, volume flow rate of bubbles is calculated by assuming that total bubble volume measured in total sample volume is directly proportional with the volume flow rate of water. Finally,

volumetric fluxes of each phase are calculated by dividing the volume flow rates to the cross section area of the pipe. It is important to mention here that maximum bubble volume captured occurred at the lowest water flow rate and vice versa.

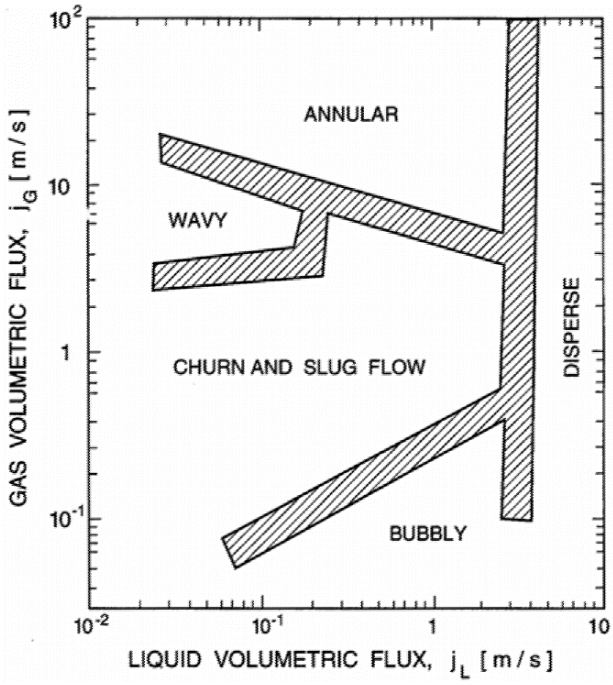

Figure 2-9. Flow regime map for air-water mixture during vertical two-phase flow through 25 mm diameter pipe and hatched regions show experimentally observed transition regions (Brennen 2005).

Table 2-4. Volumetric flux of phases in vertical downward flow.

Parameter	**Range**
Total sample volume analysed for each position (m^3)	1.56721e-4
Bubble volume captured (m^3)	3.31e-10 – 2.72e-8
Volume flow rate of water (m^3/s)	1.67e-4 – 3.472e-4
Volume flow rate of air (m^3/s)	7.33e-10 – 2.9e-8
Cross section area of pipe (m^3)	3.142e-4
Volumetric flux of water (m/s)	**0.531 – 1.105**
Volumetric flux of air (m/s)	**2.33e-6 – 9.23e-5**

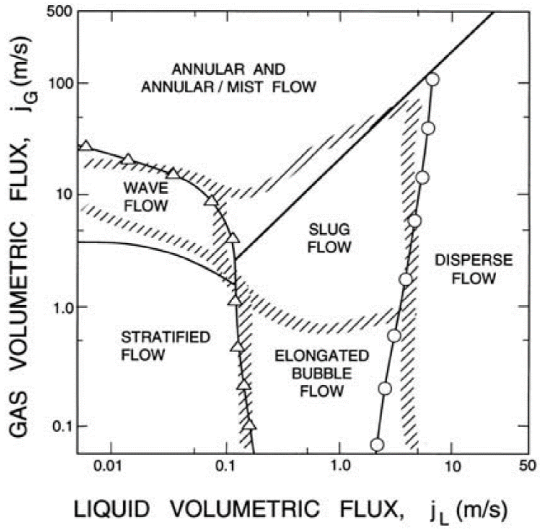

Figure 2-10. Flow regime map for air-water mixture during horizontal two-phase flow through 25 mm diameter pipe, solid lines and points show experimentally observed transition regions and hatched areas illustrates theoretical predictions (Brennen 2005).

Table 2-5. Volumetric flux of phases in horizontal flow.

Parameter	**Range**
Total sample volume analysed for each position (m^3)	1.56721e-4
Bubble volume captured (m^3)	2.12e-10 – 52.8e-8
Volume flow rate of water (m^3/s)	1.67e-4 – 3.472e-4
Volume flow rate of air (m^3/s)	4.7e-10 – 5.6e-7
Area of cross section of pipe (m^3)	3.142e-4
Volumetric flux of water (m/s)	**0.531 – 1.105**
Volumetric flux of air (m/s)	**1.5e-6 – 1.78e-3**

After considering the volumetric fluxes calculated for each phase for vertical and horizontal flows (**Tables 2-4** and **2-5**) and substituting the values into the flow pattern maps (**Figures 2-9** and **2-10**), it is clear that two-phase flow occurring in wet central heating systems falls in the region of bubble flow for vertical downward flow and elongated bubble flow for horizontal flow. Furthermore, it is validated that initial flow pattern estimate was right.

2.4.2 Two-phase bubbly flow behaviours

Following the validation of the two-phase flow pattern occurring in central heating system's pipeline as bubble flow, literature review regarding air-water bubble flow in pipes was carried out as well and is to be presented in this section. Two-phase bubbly flow is defined in Iskandrani & Kojasoy (2001) as a two-phase flow with bubbles dispersed in the continuous phase, where the maximum bubble size is much smaller than the diameter of the pipe. It is a common phenomenon that can be observed in many industries, therefore, various studies have been carried out on the subject throughout the years. Investigation of interfacial structures of two phase's flows is very important because it significantly affects the mass, momentum and energy transfer between the phases (Yadav et al. 2010). In connection with the above-mentioned statement, literature review is presented through the aspects of bubble distributions, bubble sizes and bubble velocities.

2.4.2.1 Bubble distributions across the pipe section in bubbly flows

In general, bubble distributions are discussed in terms of local void fraction measurements across the pipe section and presented with distribution profiles. Bubble distributions can vary according to the pipe orientation and superficial velocities of phases as stated previously in **Section 2.4.1** while reviewing flow patterns that occur in two-phase flow. Both factors are effective during air-water bubbly flow. Since the pipe orientation is the most significant factor affecting bubble distribution this section is divided into two parts: vertical downward and horizontal bubbly flow. Studies on vertical upward bubbly flow is not included in the following review because experiments of the current research were conducted on downward vertical and horizontal pipelines. Moreover, effects of superficial phase velocities on bubble distribution profiles is discussed.

2.4.2.1.1 Vertical downward bubbly flow

Early work on downward bubble flow in pipes carried out by Oshinowo & Charles (1974) and their visual observetions indicated that bubbles travel in the middle section of the pipe, causing coring phenomenon, in contrast to upward bubble flow, where bubbles tend to move towards the pipe wall, causing wall peaking

distributions. Later, wall and core peaking phenomenons were qualitatively predicted by Drew & Lahey (1982), Wang et al. (1987) and more recently by Yang & Thomas (1998).

Usui & Sato (1989) gave an explanation for the coring phenomenon during downward bubble flow, stating that velocity profile of the liquid across the pipe section creates a lift force on the bubbles towards the channel centre. This force causes a tendency on bubbles to travel in the middle of the pipe during downward bubbly flow and leads to coring phenomenon as pointed out by the early researchers. However, their experiment results for bubbly flow distributions across the pipe section did not correspond to their expectations. Experiments were conducted through 16 and 24 mm tube diameters at 1 m/s water superficial velocity and two different (0.117 and 0.0324 m/s) air superficial velocities, resulting in bubble flow with void fractions in the range of 0.2 to 0.5. The results show peak void fraction values not in the middle section but at r/R = 0.4 to 0.6.Hence, Usui & Sato (1989) argued that deformation of the bubbles can lead to variations in turbulence and velocity profile of the liquid, and thus changes the pressure field. These changes cause bubbles to move closer to the pipe wall. This can otherwise be simply expressed as the intention of the bubbles to escape from the water in the centre which is traveling at a higher velocity. They concluded that the challenge between these two forces results in peak void fractions at r/R = 0.4 to 0.6.

More detailed investigation of solely downward bubble flow was carried out by Kashinsky & Randin (1999). Their visual observations of bubbly downward flow also showed that the bubbles are pushed away from the pipe wall, leading to coring phenomenon, and pure liquid layer is formed near wall region. They also pointed out that “gas hanging” phenomenon can be observed if the volumetric flux of the liquid was lower than 0.5 m/s. The pipe inner diameter was 42.3 mm and three different liquid super facial velocities (0.5, 0.75 and 1 m/s) with air superficial velocities in the range of 0.019 to 0.09 m/s leading to void fractions between 0.01 and 0.2 were utilized during their experiments. In addition, mean bubble diameter was controlled and kept at 0.8 or 1.5 mm by the special mixer design, without changing other flow conditions. Throughout their investigation, a sharp decrease in the void fraction of bubbles closer to the pipe wall and levelled void fraction distribution in the inner

sections were obtained. Bubble distributions across the pipe became more levelled as the average void fraction decreased and peak void fractions occurred in the centre section of the pipe in general. However, off-centre peaking phenomena was observed at highest void fractions of 0.2 during 0.5 and 0.092 m/s superficial velocities of liquid and air respectively. Moreover, they mentioned that decrease in the superficial liquid velocities led bubbles to move closer to the wall and the effect of bubble diameter on the bubble distributions close to the pipe wall showed no significant changes during 0.5 m/s liquid volumetric fluxes. However at high liquid superficial velocity (1 m/s), small bubbles were inclined to move closer to the wall when compared with test at 0.5 m/s liquid velocities.

Further investigation of downward bubble flow at higher liquid velocities (0.6-5 m/s) compared to the previous researchers were conducted by Ishii et al. (2004), Hibiki et al. (2004) and Hibiki et al. (2005) on the same test rig. Similar centre peaked void fractions in addition to some off-centre peaked profiles were observed by Ishii et al. (2004) and they highlighted the need for further investigation. They also stated that core peaking becomes more significant at higher liquid volumetric fluxes, coinciding with the experiments of Kashinsky & Randin (1999). Furthermore, Ishii et al. tested two different pipe diameters (25.4 and 50.8 mm) and concluded that bubble distribution in the bigger pipe was flatter when compared to the smaller pipe. Later, Hibiki et al. (2004) proposed a classification of the void fraction distributions using only three types ; off-centre peaked, bell-typed and core-peaked. Off- centre peak signifies profiles where peak void fraction occurs not in the centre but closer to the wall, however, it is not similar to the wall-peaked phenomenon observed in upward flow, where there is a sharp increase in void fraction close to the wall. Bell-typed represents profiles that have peak in the core with an inflection point and a decrease near the wall. Core-peak denotes profiles where there is a linear increase in void fraction when moved away from the wall to the middle of the channel without any inflection point. Hibiki et al (2004) suggested a phase distribution map shown in **Figure 2-11** for downward bubble flow via combining their data with previous researchers'.

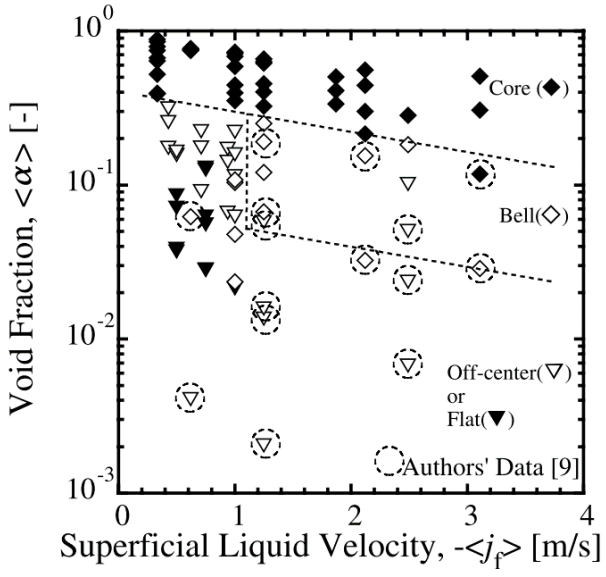

Figure 2-11. Phase distribution map for downward bubble flow (Hibiki et al. 2004).

From **Figure 2-11**, the researchers stated that at fairly high void fractions, bubble distributions are more likely to show core-peak profiles and there is a shift from core-peak type to bell-type or off-centre peak types as the void fraction reduces. Transition from core-peaked type to bell-type seems to be affected from the liquid velocity, where void fraction limit for the pattern transition line lowers as the liquid velocity increases. Bell type distributions are favoured in the moderate void fractions and liquid volume fluxes higher than 1 m/s, whereas off-centre or flat distributions are observed at low void fractions. They consider the flat distribution as the transition between off-centred and bell-types.

Axial development of downward bubble flow at three different positions along the vertical pipe was analysed by Hibiki et al. (2005). They concluded that there is no significant difference occurring in distribution profiles along the vertical pipe, as long as there are no outstanding big bubbles (see the article for the definition of specific bubble diameter limit). Moreover, they mention that overall void fraction across the pipe section reduces along the flow direction due to the increase in pressure.

Recently, Bhagwat & Ghajar (2012) visually captured the effect of liquid and gas superficial velocities on downward bubble flow through 12.7 mm circular pipe (see **Appendix 3** for their visual observations). They varied the superficial liquid velocity

while maintaining the gas volume flux constant in order to observe the effect of liquid velocity and vice-versa for the effect of gas volume flux. There was significant increase in bubble numbers and decrease in bubble sizes when superficial velocity of the liquid was increased. Moreover, bubble shapes became noticeably spherical as the liquid velocity increased, compared to low liquid velocities obtained when high number of deformed bubbles were observed. In addition, there was a bubble-free region close the pipe wall at low liquid flow rates. However, bubble-free region got smaller and bubbles moved closer to the wall as the liquid velocity was increased. On the other hand, bubble sizes got bigger when the superficial velocity of gases was increased and led the bubbles to elongate in a lateral direction, which can cause transition from bubble to slug flow.

2.4.2.1.2 Horizontal bubbly flow

Experimental investigation of horizontal bubble flow through pipes is well a studied phenomenon by various researchers. Kocamustafaogullari & Wang (1991), Kocamustafaogullari et al. (1994) and Kocamustafaogullari & Huang (1994) are leading researches on the subject where all of the studies were carried out at the same test rig. Measurements were taken with air-water bubble flow through 50.3 mm diameter pipe at superficial liquid and gas velocities that varied from 3.75 to 6.59 and from 0.21 to 1.37 m/s, respectively. Superficial velocity ranges of phases employed in their experiments resulted in average void fractions from 0.063 to 0.2.

Kocamustafaogullari & Wang (1991) showed that bubbles tend to travel at the upper part of the pipe because of the buoyancy forces. Accordingly, distribution profiles across the pipe section peaked close to the top wall at approximately r/R = 0.8 – 0.9 in all of their experiment results, regardless of the phase superficial velocities. There was a sharp decrease in void fraction close to the upper wall after the peak point, consequently, they argued that probe interference or high hydraulic resistance of water between droplet and wall can cause sudden decrease in void fraction near the pipe wall. Increasing gas flow rate at constant liquid velocity indicated that local peak in the distribution profile and average void fraction across the pipe gets bigger. In addition, measured bubble volumes at the bottom of the pipe got higher as the gas velocities enlarged. On the other hand, local peak void fraction in the distribution

profile and average void fraction across the pipe lessened as the superficial liquid velocity increased at constant gas flow rates. Moreover, increasing liquid velocity led bubble distribution profiles to flatten compared to lower liquid velocities with a distinctive peak close to the top wall.

Subsequently, axial development of horizontal bubble flow was examined and introduced in Kocamustafaogullari & Huang (1994). They measured three axial positions after the inlet at L/D = 25, 148 and 253 and the structure of two-phase flow was presented in 3D perspective plots for each axial position. In general, they stated that bubble distributions at first positions showed nearly constant void fractions across the pipe section with a slight peak value close to the upper wall. However, distribution profile was developed along the horizontal pipe and was shifted from levelled distribution to the profiles they obtained earlier in Kocamustafaogullari & Wang (1991). The peak void fractions at upper part of the pipe increased as they traveled from L/D = 25 to 253. This phenomenon is specifically pronounced at low gas flow rates. As a result, they conculuded that "full-developed" bubbly two-phase flow cannot be established because flow pattern development is a continuous process in horizontal pipes.

Similar bubble distribution profiles during horizontal bubble flow were also observed experimentally by Andreussi et al. (1999), Iskandrani & Kojasoy (2001) and more recently by Bottin et al. (2014). However, bubble distribution profiles obtained by Bottin et al. (2014) did not show a sharp decrease after the peak point, and peak void fractions always occurred at the top position of their local measurements. Morover, axial development measurements were also conducted by Bottin et al. (2014) and their results correlated well with Kocamustafaogullari & Huang (1994). Furthermore, extensive research on numerical study of bubble flow in horizontal pipes became popular in the last two decades with improvements in computer sciences. Such useful numerical studies can be found in Yoshida et al. (1998), Ekambara et al. (2008), Haoues et al. (2008), Haoues et al. (2009), Ekambara et al. (2012) and Yeoh et al. (2012).

2.4.2.2 Bubble velocities in turbulent bubbly flows

Liquid velocity profile or bubble velocity profiles are other important parameters in the concept of two-phase bubbly flow and they have been studied by various researchers. Effect of bubbles in liquid velocity profile was investigated by Wang et al. (1987) for downward and upward bubbly flow. They stated that velocity profiles flatten when compared to single-phase flows because of the presence of secondary phase in the flowing liquid. Similar velocity profiles were obtained for both upward and vertical two-phase flows, where a slight increase was observed when approached to the wall during vertical downward flow. According to Wang et al. (1987), coring phenomenon during the vertical downward flow leads more liquid to travel in the part closer to the wall and this results in an increase in velocity. Similar wall peaking liquid velocity profiles were observed by Kashinsky & Randin (1999), where they showed that bubble effect on the liquid velocity profile becomes insignificant; since the void fraction reduces, liquid flow rate increases, and bubble sizes gets smaller. Hibiki et al. (2005) also observed small wall peaking velocity profiles but concluded that velocity profiles in bubble downward flow can be simply predicted with power-law profiles.

During vertical downward flow, buoyancy forces and liquid inertia are directly opposite to each other and gas phase tends to refuse flowing with the liquid. This results in a reduction on gas phase velocities, where in upward flow, average bubble velocities are higher than average liquid velocity (Bhagwat & Ghajar 2012). Ishii et al. (2004) also mention that bubbles travel slower than the liquid around them, owing to buoyancy and drag forces occurring during downward bubble flow. Additionally, reduction in turbulence intensity in liquid phase due to bubbles are mentioned in the literature. However, Ishii et al. (2004) argue that they did not observe significant turbulence intensity reduction. They asserted that the bubble diameters utilized during their experiments were significantly bigger than previous studies conducted on vertical downward flow, which can lead to this different observation.

Bubble velocities measured during horizontal bubble flow was investigated by Kocamustafaogullari & Wang (1991) . They argued that peak velocities closer to the pipe wall in vertical downward flow were not observed in horizontal flow. Peak

velocities occur in the centre region of the pipe and bubble velocities reduce as they approach to the wall. Later, Kocamustafaogullari & Huang (1994) measured bubble velocities at three axial locations on horizontal bubbly flow, and mentioned that bubble velocity profiles tend to develop and reach the velocity profile that can be predicted by $1/7^{th}$ power law. This is similar to Hibiki et al. (2005)'s suggestions to use power law to predict bubble velocities across the vertical pipe. Iskandrani & Kojasoy (2001) also compared the $1/7^{th}$ power law profile with their experimental results for bubble velocities and concluded that power law offers a simple and reliable way of predicting bubble and liquid velocities across the horizontal pipe at relatively low void fractions and small bubble diameters.

Controversial to vertical flow, bubble presence effects the liquid velocity oppositely in horizontal flow, where, as the bubble numbers increases velocity in the centre and bottom of the pipe increases (Bottin et al. 2014). Bubble accumulation at the upper part of the pipe reduces the flow velocity at the upper section and in order to balance the continuum equation, velocities at the centre and bottom regions increase significantly (Kocamustafaogullari & Huang 1994).

2.4.2.3 Bubble sizes in turbulent bubbly flows

Bubble formation in central heating systems is the result of type-III or IV nucleation as discussed in **Section 2.3**. Velocity of the liquid is the main factor determining the size of the detached bubble from its nucleation site (Fsadni et al. 2011). Fsadni (2012) extensively contributed to literature on bubble detachment models that are used to predict bubble detachment diameters. He compared these models with the experimental results obtained from the same test rig used in the current study. Therefore, factors affecting bubble sizes after they are detached are the main focus of the current research. In this regard, first, studies on break-up and coalescences of the bubbles in turbulent bubbly flow mechanism is discussed. Secondly, review on the dissolution of air bubbles in a turbulent pipe flow during undersaturated flow conditions is presented.

2.4.2.3.1 Break-up and coalescences

The main process that determines bubble sizes in turbulent bubbly flows is the break-up and coalescences of bubbles. Break-up and coalescences of the bubble in the turbulent flow is a continuous process and a dynamic equilibrium can be obtained after a sufficient amount of time (Liu & Li 1999). When the dynamic balance is reached, two distinctive diameters can be noted. Generally, the concept is discussed around those two pre-defined bubble diameters: 1- the largest bubble diameter that can resist break-up (d_{max}) and 2- the smallest bubble diameter that remains stable against coalescences (d_{min}). In other words, bubbles smaller than d_{min} will coalescence to form bigger bubbles, while bubbles bigger than d_{max} will break-up into smaller bubbles (Rahman et al. 2009).

. According to Thomas (1981), Kolmogoroff and Hinze suggest that d_{max} can be derived from a dimensional analysis, based on the assumption that rate of energy dissipation is responsible for the parameters defining the structure of turbulence fluctuations. Basically, their theory suggests that if the critical weber number is exceeded, bubble will break up. Accordingly, they derived the following **Equation (2-8)**;

$$d_{max} \sim \left(\frac{\gamma}{\rho_c}\right)^{3/5} \epsilon^{-2/5} \qquad \textbf{(2-8)}$$

Where γ is the surface tension, ρ is the density of the liquid and ϵ is the turbulence dissipation rate. Turbulence dissipation rate can be estimated by the following **Equation (2-9)**.

$$\epsilon = {u^3}/{l} \qquad \textbf{(2-9)}$$

Later, Liu & Li (1999) summarized the constants that can be utilized for **Equation (2-8)** in specific cases.

More recently, Razzaque et al. (2003) provided **Equation (2-10)** for d_{max}, derived by Hesketh, particularly for the bubbly pipe flow.

$$d_{max} = 1.38(We_c)^{0.6}\left[\frac{\gamma^{0.6}}{{\rho_c}^{0.5}{\mu_c}^{0.1}}\right]\left(\frac{\rho_c}{\rho_d}\right)^{0.2}\left(\frac{D^{0.5}}{U^{1.1}}\right) \quad \textbf{(2-10)}$$

We_c is the critical Weber number and D is the pipe diameter. Critical Weber number is determined as 1.1 by Hesketh, and later 1.05 for low void fraction two-phase bubbly flow. Razzaque et al. (2003) reorganized **Equation (2-10)** to generalize it for other two-phase flow pairs, as **Equation (2-11)** illustrates.

$$\frac{d_{max}}{D} = 1.38(We_c)^{0.6}\left(\frac{\rho_c}{\rho_d}\right)^{0.2}\left(\frac{\mu_c}{\rho_c UD}\right)^{0.5}\left[\frac{\gamma}{\mu_c U}\right]^{0.6} \quad \textbf{(2-11)}$$

On the other hand, Thomas (1981) states that, coalescence of bubbles go through two stages: 1- draining film between two colliding bubbles reaches critical thickness and 2- the rest of the film ruptures between two bubbles. d_{min} was derived by Thomas (1981) by utilizing a similar dimensional analysis previously used by Kolmogoroff and Hinze to derive d_{max}. **Equation (2-12)** demonstrates their main result, which can be used to predict minimum bubble diameter at immobile interface (with flow surfactants):

$$d_{min} = 2.4\left(\frac{\gamma^2 h^2}{\mu_c \rho_c \epsilon}\right)^{1/4} \quad \textbf{(2-12)}$$

where, h is the critical rupture thickness which can be assumed as 10^{-7} m. Later Liu & Li (1999) considered both cases with or without surfactants. **Equation (2-13)** was derived for immobile interfaces where the liquid contained surfactants.

$${d_{min}}^{3.11} = \frac{\gamma^{1.38}B^{0.46}}{0.0272\mu_c{\rho_c}^{0.84}\epsilon^{0.89}} \quad \textbf{(2-13)}$$

For the two-phase flow without any surfactants (mobile bubble surfaces), **Equation (2-14)** was derived to be used for predicting smallest bubble stable against coalescence. This equation can be numerically solved by the Newton Method.

$$1363.3\frac{\gamma^{1.29}{\mu_c}^{0.02}B^{0.26}}{E^{1.7}{\mu_d}^{1.02}{\rho_c}^{0.55}\varepsilon^{0.7}{d_{min}}^{2.03}}+217.3\frac{\gamma^{1.38}B^{0.46}}{E^{0.7}\mu_c{\rho_c}^{0.84}\varepsilon^{0.89}{d_{min}}^{3.11}}=1 \quad \textbf{(2-14)}$$

Here, B is London-van der Waals constant assumed to be 1e-28 Jm, and E is the dimensionless curvature radius of the liquid film between two colliding bubbles, defined by **Equation (2-15)**.

$$E=12.61+2.166\tan^{-1}(2M^{0.8}) \quad \textbf{(2-15)}$$

where M is the interface mobility coefficient that can be determined by **Equation (2-16)**.

$$M=1.12\frac{\mu_c}{\mu_d}\left(\frac{\pi\gamma}{\rho_c\varepsilon^{2/3}{d_{min}}^{5/3}}\right)^{1/2} \quad \textbf{(2-16)}$$

Experimental investigation and comparison of d_{max} and d_{min} provided in the **Equations (2-10)** and **(2-14)** were conducted by Razzaque et al. (2003) for air-water flows through horizontal pipes. Here, they used a pipe with an inner diameter of 25.4 mm and three measurement positions along the horizontal pipe. The liquid velocity was varied from 1 to 3 m/s, and three different two phase flow void fractions – 0.0007, 0.0015 and 0.003—were utilized in their experiment. They concluded that, bubbles at the downstream of the horizontal pipe gets bigger because of coalescences. Furthermore, they stated that **Equation (2-10)** provides accurate predictions for maximum bubble sizes which can occur in horizontal pipe flow at low void fractions.

2.4.2.3.2 Dissolution

Dissolution of secondary phase during two-phase flow at undersaturated conditions is another factor that can effect bubble size throughout pipelines. Reduction in average bubble diameter and void fractions along the horizontal flow due to the dissolution phenomenon is reported by Fsadni & Ge (2012), Fsadni (2012) and Ge et al. (2013) . Saturation ratio at typical central heating system's pipework normally starts with oversaturated conditions, but drops below 1 very quickly, hence, they run at undersaturated conditions most of the time. Therefore, it is expected to observe a dissolution phenomenon as the air-water flows through the pipework.

In general, it is accepted that concentration gradient between the liquid and air bubble is responsible for the dissolution process. Bubbles shrink and disappear after sufficient amount of time, due to the mass transfer from bubble into ambient liquid. Shedd (2005) provided previously derived equations to predict dissolution time of small bubbles in quiescent liquid. He reports that velocity gradient between the liquid and bubble can lead to convective mass transfer, therefore, decrease in dissolution times due to increase in mass transfer coefficient. Lezhnin et al. (2003) particularly investigated bubble dissolutions in turbulent air-water flow in pipelines, and developed a model to predict size variations as the bubble travels with liquid. First, they noted that mass transfer from the bubble to its ambient liquid can be expressed with the convective mass transfer equation given in **Equation (2-17)**.

$$q = k(C_b - C_\infty) \tag{2-17}$$

where q is the mass flux, k is the mass transfer coefficient, C_b is the mass concentration on bubble boundary and C_∞ represents mass concentration in the ambient liquid. Mass concentration on the bubble boundary (C_b) is assumed to be equal to the gas concentration at saturated water for a particular system temperature and pressure. Both mass concentrations used in **Equation (2-17)** were monitored throughout the test rig in this study as well, where C_∞ is equal to x_{act} and C_b is equal to x_{sat} (see **Sections 3.2.2.2** and **3.2.4** for more details on mass concentration calculations). Later, Lezhnin et al. (2003) point out that **Equation (2-18)** can be

written using the mass conservation law, utilized on a single bubble, and used in conjunction with **Equation (2-17)** to model bubble size change due to dissolution.

$$\rho_g \frac{dR}{dt} + \frac{R}{3}\frac{d\rho}{dt} = q \qquad \textbf{(2-18)}$$

Lezhnin et al. (2003) argued that the most difficult term to estimate in the **Equations (2-17)** and **(2-18)** is the mass transfer coefficient (k). They cited that Sherwood number ($Sh = kd_b/D$) can be used to determine the coefficient and obtained **Equation (2-19)** for Sherwood number estimation from the detailed work of Levich on convective mass transfer from bubble to surrounding liquid.

$$Sh \propto \frac{d_b}{L} Re^{3/4} Sc^{1/2} \qquad \textbf{(2-19)}$$

where Sh is the Sherwood number, d_b is the bubble diameter, L is the characteristic length—which is pipe diameter (D) in the current research—Re is the Reynold number and Sc is Schmidt number. Moreover, they also pointed out that a similar Sherwood number estimation can be derived from Higbie's penetration theory. This approach was used by several researchers to develop different empirical formulas for the Sherwood number. Shedd (2005) also proposed a similar bubble dissolution model which can be used for both stagnant and moving bubbles.

Later, the approach proposed by Lezhnin et al. (2003) was adopted to model dissolution of bubbles in turbulent flow travelling through central heating systems' pipework by Ge et al. (2013) at undersaturated system conditions. Liquid velocity was varied from 0.25 to 0.52 m/s, boiler exit temperature was around 80 °C and system pressure was maintained at 2.7 bars. Saturation ratio of the system was varied from 0.89 to 0.97. They assumed that coalescences of bubble trough the test rig is negligible due to the low void fractions observed in such systems. There were five focal planes used across the pipe section at two different positions on the horizontal pipeline of the test rig. Average bubble diameter ratio at each focal plane was utilized to revise the empirical formula of Sherwood number as in **Equation (2-20)**.

They showed that the equation provides an accurate prediction of the system conditions used in their experiments, within the range of 10% uncertainty.

$$Sh = 0.34 \frac{d_b}{L} Re^{0.86} Sc^{0.5} \quad \textbf{(2-20)}$$

In addition, Ge et al. (2013) conducted a parametric study to investigate the effect of different parameters on bubble dissolution predictions like, saturation ratio, pipe inner diameter, bulk fluid pressure, and velocity showed in **Equation (2-20)**.

2.4.3 Summary

This section started with a literature review on two-phase flow patterns in vertical and horizontal pipe flows. Main difference between the two orientations turned out to be the arrangement of phase-pairs, where buoyancy forces dominate. During air-water flow, symmetrical arrangement was expected from vertical flow. On the other hand, bubbles tend to flow at the upper parts of the pipe during horizontal flow, leading to an asymmetrical distribution. Afterwards, the two-phase flow pattern which may appear in a typical central heating systems' pipework was determined to be as bubble flow. This conclusion was reached by using flow pattern maps of Wiesman and Mandhane et al. cited in Brennen (2005). Later, two-phase bubbly flow behaviours in pipes were reviewed and discussed in three sections. Firstly, bubble distributions across the pipe section were presented. Effects of liquid and gas superficial velocities on bubble distribution and bubble distribution development along the flow direction was discussed. Secondly, previous investigations on bubble velocity measurements at horizontal and vertical bubbly flow were reviewed. Finally, bubble sizes in turbulent bubbly flows were demonstrated by means of dissolution, break-up, and coalescences phenomena.

2.5 Summary

This chapter was divided into three main sections. In the first one, literature review on solubility of gases in the liquids was explained and then effects of temperature and pressure on solubility were discussed. In addition, the importance of solubility of gases in liquids and the use of Henry's law with regards to the current study was revealed. Secondly, bubble formation specific to central heating systems was reviewed. In this context, useful definitions for supersaturated gas-liquid solutions and bubble nucleation types responsible for bubble formation in central heating systems were evaluated. Finally, the main aspects of two-phase flow in pipelines were investigated. Expected flow pattern was determined through the use of flow pattern maps provided by prominent scholars in the field, and two-phase flow behaviours—such as bubble distributions, velocities, and sizes—during turbulent bubbly flow were discussed. At the end of each section, detailed summaries highlighting critical points are provided for a better understanding.

CHAPTER 3 EXPERIMENTAL DESIGN AND METHODOLOGY

3.1 Introduction

This chapter presents the details related to the experiments conducted to investigate the two-phase phenomenon that occurs in wet central heating systems. In this regard, **Section 3.2** starts with introduction to the test rig and provides detailed information related to the equipment that is installed on the pipeline. Next, modifications applied to the test rig are explained in **Section 3.3**. Bubble measurement technique and image analysis used to retrieve information regarding the two-phase flow properties are described and discussed in **Section 3.4**. Later, experimental data processing and the uncertainties involved are given in **Sections 3.5** and **3.6**. In **Section 3.7**, the frame independent test applied to the experiment technique to achieve reliable results is explained and its results are given. Following that, **Section 3.8** provides necessary information regarding the experimental procedure and experimental condition control with two typical examples. Finally, the chapter is concluded with a brief summary in **Section 3.9**.

3.2 Experimental Facility

The main aim of the project is to perceive a better understanding of the two-phase flow phenomenon that is observed in domestic wet central heating systems. Towards this aim, the experimental facility was designed and constructed with the assistance of Brunel University and Spirotech b.v. (Netherlands) as part of the research project carried out by Fsadni (2012) at TOWC006a, Brunel University. The schematic diagram of the test rig in **Figure 3-1** depicts all the equipment used in the research project.

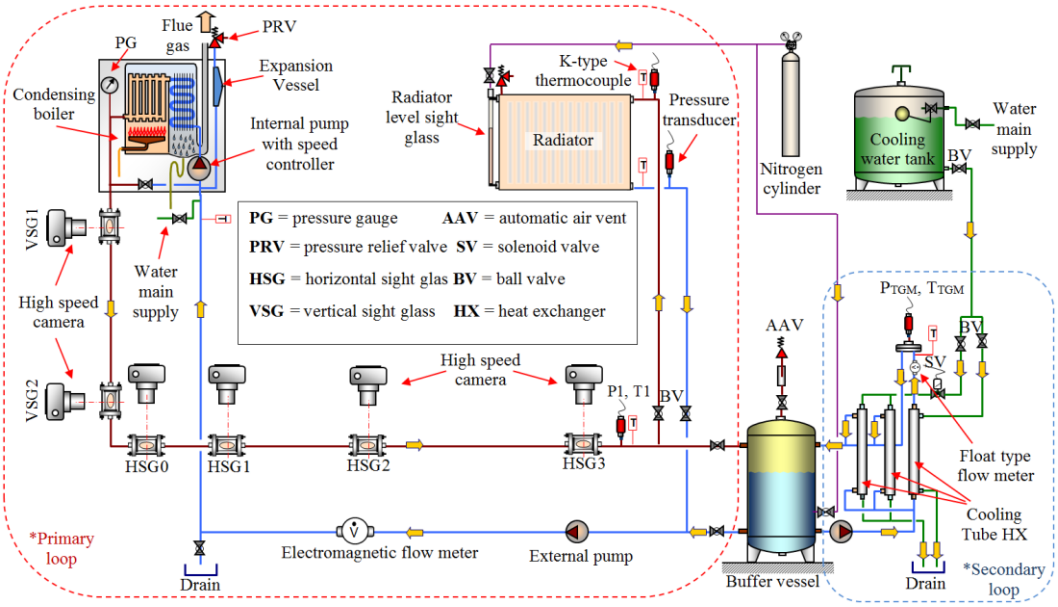

Figure 3-1. Schematic diagram of the test rig.

The test rig mainly consists of two closed loops which are connected at the buffer vessel. The primary loop includes ordinary equipment that can be found in every wet central heating system such as boiler, pipework, radiator, etc. It also contains the sight glasses which allow observation of the flow inside the pipework. Filming of the flowing liquid is done by a high speed camera through these sight glasses. A microscopic lens is mounted to the camera for desired magnification and metal-halide light source is used for illumination. The secondary loop is mainly used to remove the heating load that is supplied by the boiler, thus simulating the heat load required in domestic houses and, in addition, it enables the partial pressure measurements of dissolved gases in the liquid by the device called the TGM device. A nitrogen cylinder is used to inject nitrogen into the system to increase the amount of dissolved gas in the liquid flowing through the radiator or buffer vessel. The flow rate of the system is adjusted by the voltage controller connected to the pump inside the boiler.

During the experiments, all conditions of the system were monitored by five K-type thermocouples, four pressure transducers and an electromagnetic flow meter. All of the sensors were calibrated before the experiments with appropriate devices to make sure that acquired data were reliable. The signals from the measurement equipment were collected at the National Instrument data acquisition device and were monitored

in real-time by the LabVIEW software on a PC monitor. All of the measured conditions were recorded and saved for further investigation if needed. Further details of each separate equipment mentioned above will be explained in the following sections.

3.2.1 Primary loop

The primary loop is the main part of the test rig, where filming of the fluid flow takes place through sight glasses by a high speed camera. Standard 22 mm copper pipe is installed throughout the test rig because of the fact that it is commonly used in the UK and also in Europe. The copper pipe is highly durable, easy to work with and has biostatic properties which prevent the growth of bacteria. Copper pipes used in the test rig have 1 mm wall thickness, thus resulting in a 22 mm outlet diameter and 20 mm inlet diameter. There are two types of compression fittings used throughout the system pipework which are brass and plastic.

3.2.1.1 Boiler, radiator, internal pump controller and external pump

Vaillaint ecoTEC pro 24 combination boiler (Vaillant 2008) provides necessary energy to heat up the flowing liquid. The selection of the boiler was done by the sponsor company (Spirotech b.v., Netherlands). In doing this, they considered new building regulations (Building regulations UK 2010) and the fact that the helical rectangular tube structure of the heat exchanger inside the selected boiler type is commonly used by different boiler manufactures because of its high efficiency (Fsadni 2012).

Figure 3-2 illustrates the images related to the combination boiler that was used in the present study. The schematic diagram on the left gives a detailed view of the main parts inside the boiler and on the right is the original image from the actual boiler. Combination boilers can be used for both central heating and hot water requirements of houses. In the current study, however, the hot water side of the system was cancelled and not used because of the fact that the main interest in the research project is to understand the behaviour of microbubbles in closed-loop of central heating systems. The control panel on the front of the boiler is used to change its settings such as heating load, hot water temperature, etc. Factory maximum

temperature setting at the hot water outlet is 75°C but here it was increased to 85°C with the code provided in the installation manual (Vaillant 2008).

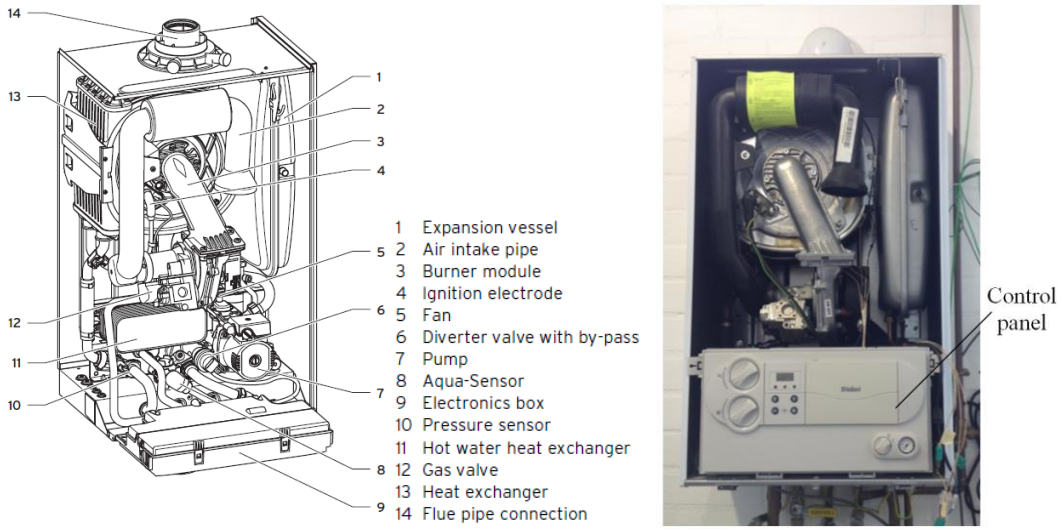

Figure 3-2. Function elements of the combination boiler (Vaillant 2008) on the left and original picture of the boiler from the test rig on the right.

Pump supplied with ecoTEC pro 24 combination boiler is a single-stage pump which does not allow changing the pump speed. However, the adjustable bypass valve in the boiler enables one to control the pump discharge height. The discharge pressure can be changed between 170 mbar and 350 mbar by turning the valve. Approximate pressure associated with each by-pass valve position is provided by the boiler manual as follows (Vaillant 2008): 350 mbar at right-hand stop (turned all the way down to the right), 250 mbar at middle-position (five full turns to the left from right-hand stop) and 170 mbar at left-hand stop (turned all the way down to the left).

Radiator installed in the test rig is shown in **Figure 3-3**. It is a single panel type-10 radiator with a maximum power output of 900 W. The radiator is 600 mm wide and 800 mm high and it is installed at 3400 mm from the floor level. Two thermocouples measure the temperature difference between the inlet flow and outlet flow. Heat loss caused by the radiator surface may be calculated by combining the flow rate measured by the electromagnetic flow meter and the temperature difference between the entrance and the return line of the radiator. The function of the pressure relief valve placed on the top left part of the radiator is to remove excess gases that can accumulate on the top part of the radiator. The nitrogen injection valve introduces

nitrogen gas into the system through the radiator when needed, and the level sight glass on the right side of the radiator is used to observe the liquid level inside the radiator.

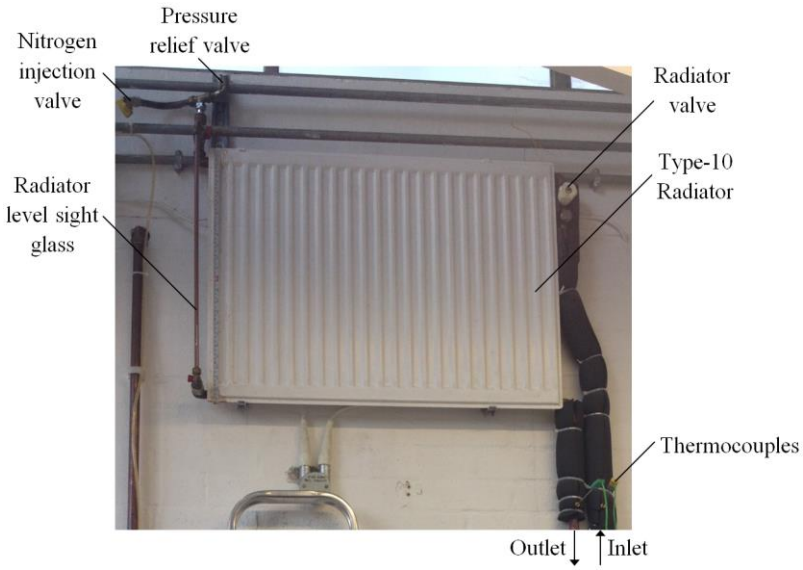

Figure 3-3. Single panel type-10 radiator

Figure 3-4 illustrates the voltage controller installed on the internal pump (left) and the external pump (right). Voltage controller adjusts the voltage level of the internal pump thus enabling the control of system flow rate. External pump is added to the test rig in order to reach higher flow rates that are desired for the current study. A Groundfos type UBS15-60 pump is installed in the return line of the pipework right before the electromagnetic flow meter (see **Figure 3-1**). The pump has a three-stage speed control facility. Operating conditions of the external pump are defined by the manufacturer as temperatures from 15°C to 110°C and pressures up to 10 bars (Groundfos 2012).

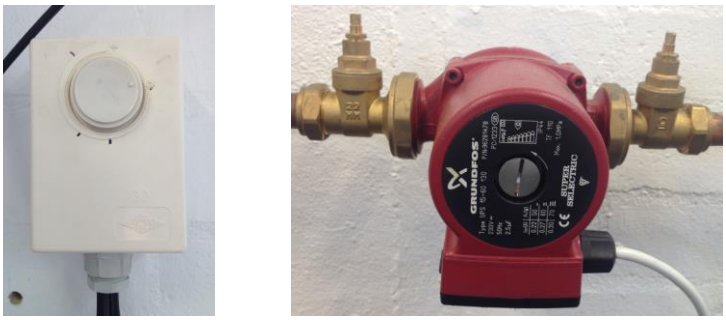

Figure 3-4. Voltage controller (left) and external pump (right).

3.2.1.2 Thermocouples, pressure transducers and flow meter

System conditions are observed with the use of thermocouples, pressure transducers and electromagnetic flow meter at the positions shown in the schematic diagram of the test rig (**Figure 3-1**). Altogether there are seven thermocouples in the test rig, five of them installed during the current study. Pressure measurement is done by four thermocouples three of which are in the primary loop and one on the TGM device in the secondary loop. Additionally, flow rate of the system is measured with an electromagnetic flow meter. Calibration of all the equipment used to monitor system conditions is described in **Section 3.3.2**.

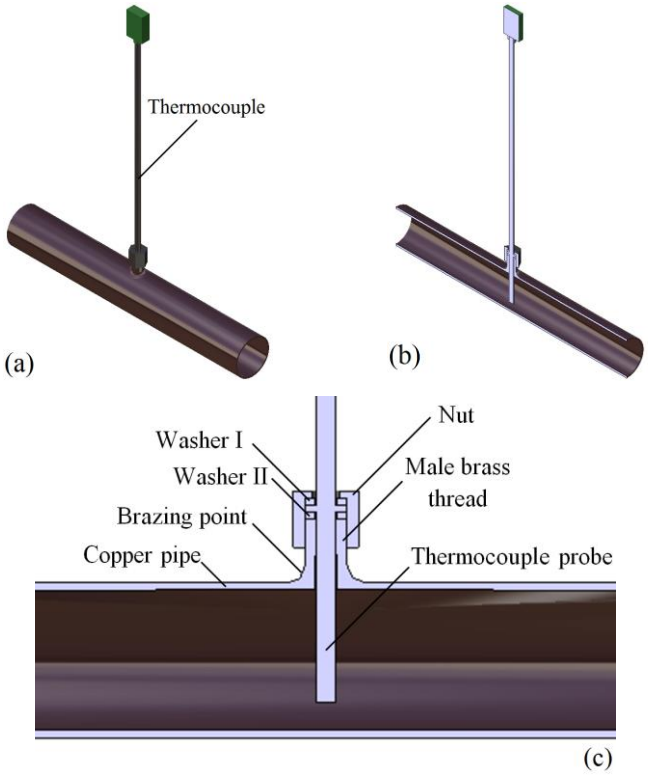

Figure 3-5. (a) 3D CAD model; (b) Cross-section of 3D CAD model; and (c) detailed 2D cross-section view of thermocouple assembly.

K-type thermocouples (**Figure 3-5**) used in the system were chosen according to their temperature measurement range, which is approximately from -40°C to 1100°C (Fsadni 2012) and the thermocouple probe is insulated with 150 mm long stainless steel 310 mineral (RS 2010). The copper pipe was drilled and then male brass thread was brazed inside the hole. Later, thermocouple probe with 3 mm diameter was inserted into the hole and assembled using two sealing washers and a nut as shown in

Figure 3-5. The tip of the probe was inserted to approximately 16 mm from the top of the pipe wall.

Three pressure transducers used in the primary loop were PTX 7517 series industrial pressure transmitters. The transmitter's pressure measurement range is from 0 bars to 10 bars at temperatures from -40°C to 100°C (Druck 2010). First, the copper pipe was drilled and then steel pipe with 6 mm outlet and 4 mm inlet diameter tube was brazed to the pipe hole. Steel pipe with 150 mm length was inserted to around 6 mm from the top of the pipe wall. Later, the female brass housing was brazed to the other end of the steel pipe and finally, pressure transducer was screwed to the female brass housing with the help of thread seal tape. 150 mm length steel pipe ensures that the temperature of the fluid that is in contact with the sensor is minimized hence reducing the errors that can be caused by high temperatures. The 3D CAD model and detailed cross-section of the pressure transducer setup is shown in **Figure 3-6**.

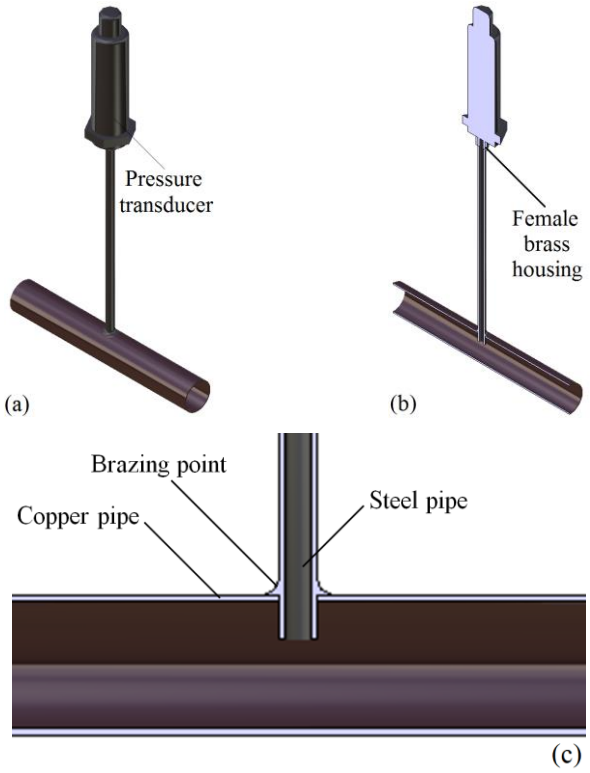

Figure 3-6. (a) 3D CAD model; (b) cross-section of 3D CAD model; and (c) detailed 2D cross-section view of pressure transducer assembly.

The flow rate of the system is monitored by a 500 series low flow electromagnetic flow meter which is supplied by Litremeter Company. Working conditions of the

flow meter are given by the manufacturer as temperatures from -20°C to 160°C and pressures up to 16 bars (Litremeter 2010). A picture of the flow meter utilised in the test rig is given in **Figure 3-7**. The flow meter is installed on the return line of the test rig between the boiler and the external pump (see **Figure 3-1**).

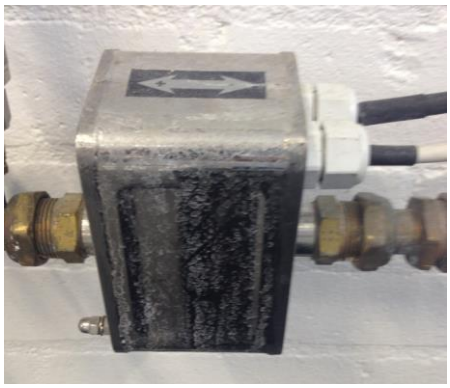

Figure 3-7. The electromagnetic flow meter.

3.2.1.3 Sight glass design

As mentioned before, during the experiments the two-phase flow was filmed by a high-speed camera and a special transparent section was needed for viewing the flow. To this end, a sight glass design with square cross-section has been developed by Fsadni (2012) during previous research. However, sight glasses which Fsadni used then had been damaged when the current study began. The glasses inside the aluminium case were cracked and scratched, affecting light entrance as well as camera images. Moreover, brass compression fittings on each side of the sight glass's copper pipe and the connection between the copper pipes and the flanges were leaking. Therefore, renewal of the sight glass design was required.

First, the connections between the copper pipes and the flanges were separated from each other and replaced with new copper pipes. The new copper pipes were brazed to the steel flanges instead of being attached by epoxy resin to ensure that the system is water tight. Secondly, a 90 mm long aluminium case was designed as a rectangular section (30.6 mm x 24 mm) with 2 mm thickness and manufactured by the university technicians in the workshop. Later, the two observation holes across each other (top and bottom) were drilled with the dimensions given in **Figure 3-8**. The size of the holes was determined after considering the frame size used by Fsadni (2012). The

original design had four observation holes on each side of the aluminium case, however two of them were removed since they were not used (Fsadni 2012).

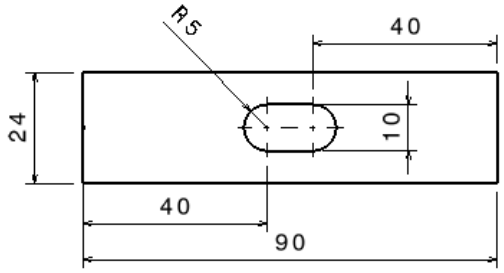

Figure 3-8. Top view of the aluminium case.

Next, two Schott borofloat 33 type borosilicate flat glasses (Schott 2012) were glued to the inner side of the aluminium case with epoxy resin. The aluminium case and glued glasses were heated up to 85°C in a heating oven to confirm that the difference in thermal expansion coefficients of glass and aluminium does not break up the adhesion properties of epoxy resin during the experiments. The flat glasses are of rectangular section (90 mm x 20 mm) with 3.3 mm standard thickness, resulting in a square (20 mm x 20 mm) inner section for the fluid to flow through. Flat surface, which was preferred by Fsadni (2012) was also used in the present study because of the fact that circular glass section increases the effect of light refraction (Prodanovic et al. 2002). Then, OTTO Primer 1216 (Ottochemie 2013) silicone metal primer was applied to the inner surface of the aluminium case and the flat glasses to increase the adhesion of the sealant. After the metal primer, the gaps between the glass and the aluminium case were sealed with OTTO Seal S28 (Ottochemie 2014) type aquarium and glass block silicone. The silicone strips along the four corners of the square inner section ensure that no liquid will leak out from the system and they also reduce the effect of transition from the circular pipe to the square cross-section sight glass. Finally, aluminium case was reassembled as shown in **Figure 3-9**.

The steel flanges and the aluminium case were mounted with the help of bolts, washers and nuts. OTTO primer and the sealant mentioned above were applied again to the contact surface of aluminium case and the two flanges to prevent any leakage. Special care was given to clearing any excess silicone that can result from tightening the sight glass structure. Excess silicone at the inner section may affect the flow

structure inside the pipe. Therefore, it was cleared before the sealant dried out to ensure that there is no obstacle in the path of flowing liquid. In the present study two identical sight glasses were restored and used for the observation of the flow.

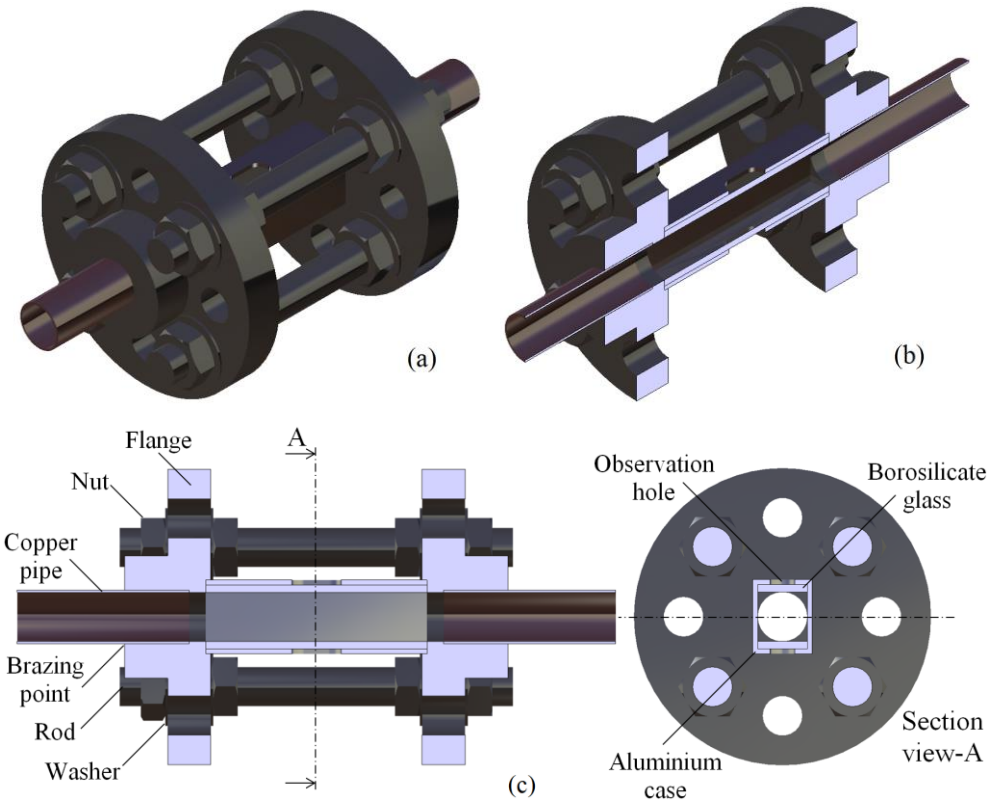

Figure 3-9. (a) 3D CAD model; (b) cross-section of 3D CAD model; and (c) detailed 2D cross-section view of sight glass assembly.

3.2.2 Secondary loop

The primary and secondary loops join together at the buffer vessel with a capacity of 40 litres, as shown in the **Figure 3-10**. The secondary loop is mainly used for removing the heat load and measuring gas partial pressures of the flowing liquid. Major parts of the secondary loop of the test rig are the three-tube heat exchangers, gas partial pressure measurement device (TGM), circulation pump and a solenoid valve. The Groundfos type UBS25-60 (Groundfos 2009) pump circulates the water through the closed-loop. The standard automatic air vent (AAV) installed at the top of the buffer vessel removes any accumulated air content from the system without losing pressure (Spirotech 2013). The nitrogen injection valve at the bottom of the buffer vessel was used to inject nitrogen if needed.

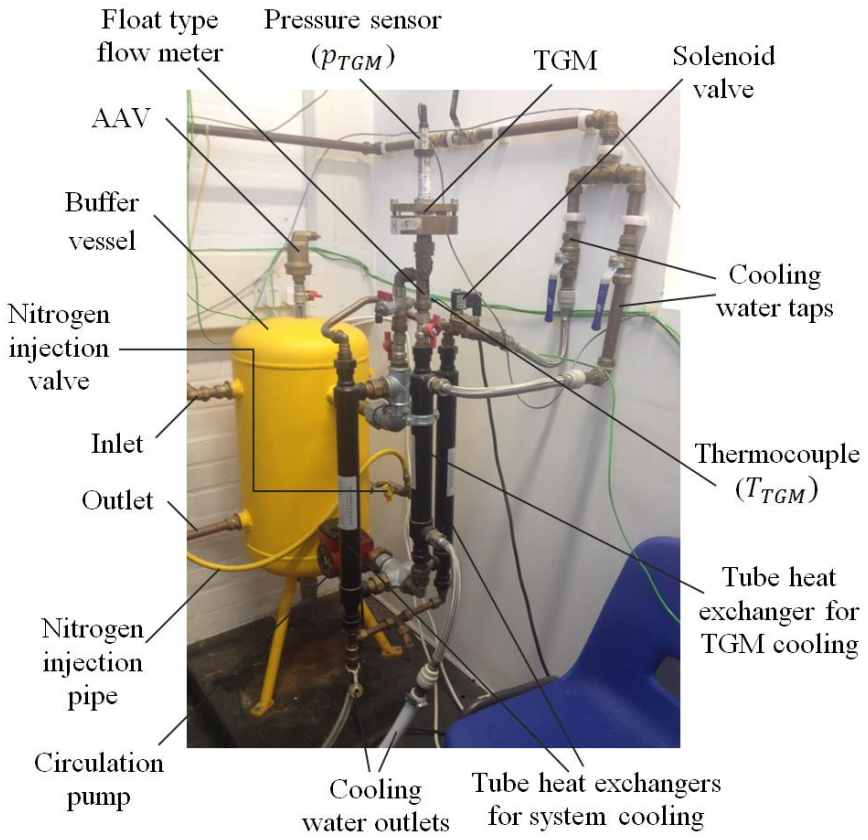

Figure 3-10. Secondary loop.

3.2.2.1 Cooling heat exchangers and boiler exit temperature control

There are three tube-in-tube heat exchangers in the secondary loop. Cooling water for the tube heat exchangers is supplied by the tap water from the mains which comes at temperatures ranging from 4°C to 20°C (depending on the time of the year). Two of the heat exchangers are used for removing the system heat load and the third is used to cool down the flowing liquid which passes through the TGM device. Cooling water from the tap separates into two branches one of which directly goes into the TGM heat exchanger and the other one passes through the solenoid valve before going into the system cooling heat exchangers.

Cooling water for the TGM heat exchanger is supplied continuously in order to obtain a stable temperature inside the device. The system fluid travelling through the TGM device is measured by the float type flow meter shown in **Figure 3-11** and the valve on the flow meter is for adjusting the flow rate of the fluid that passes through the TGM device. During the experiments conducted in the present study, the flow

rate was set approximately to 1.5 litres per minute to achieve a TGM temperature in the desired range (see **Section 3.2.2.2**).

Figure 3-11. Float type flow meter that controls the TGM heat exchanger.

Removal of the heat load and control of the boiler exit temperature is achieved through the use of the solenoid valve shown in **Figure 3-12**, which controls the cooling water supply to two of the cooling heat exchangers. The valve is turned on or off based on the temperature measurement (T_1) gathered from the hot water pipework at the boiler exit (see **Figure 3-1**). It is controlled by the logic set through the LabVIEW software (see **Section 3.2.4**). The desired threshold level is set through the LabVIEW front panel and the logic in the software compares the temperature measurement from thermocouple (T_1) with the set threshold level. If the measured temperature is higher than the value set in the interface, the solenoid valve opens and cooling starts until the threshold level is equal to or higher than the measured temperature (T_1).

Figure 3-12. Solenoid valve used to control system cooling.

3.2.2.2 Continues total gas measurement device (TGM)

Gas partial pressure measurements are done via the so-called TGM (Total gas measurement) device designed and supplied by Spirotech b.v. The device has been regularly used by Spirotech b.v.'s research and development team as well as Fsadni (2012) during his three years research at Brunel University. It combines the head-space gas pressure method proposed by Watten & Smith (1997) with direct sensing membrane diffusion method used by APHA (1992) as cited in Watten & Smith (1997).

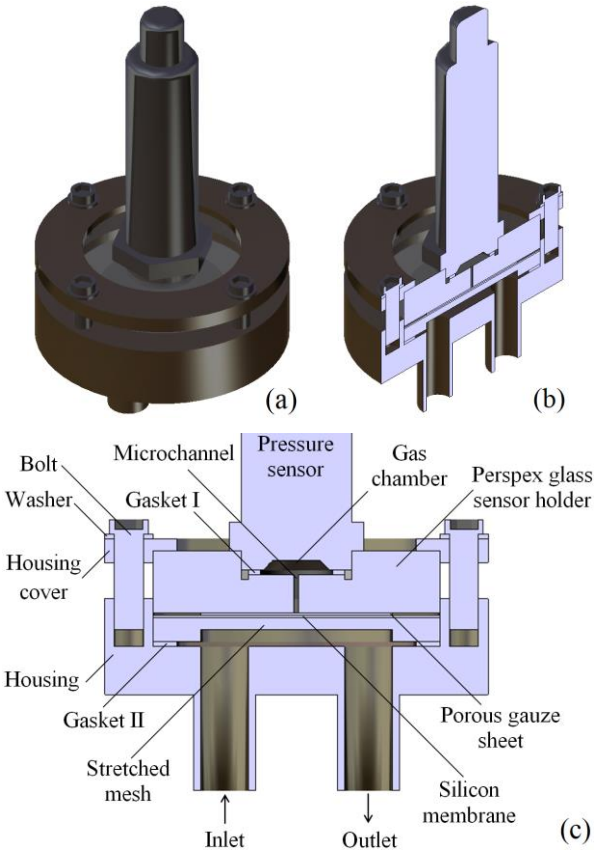

Figure 3-13. (a) 3D CAD model; (b) cross-section of 3D CAD model; and (c) detailed 2D cross-section view of total gas measurement device.

Figure 3-13 illustrates a 3D CAD model and detailed cross-section view of the TGM device. TGM requires fluid temperatures to be between 20°C and 45°C (Fsadni 2012) in order to avoid any damage that can be caused by high temperatures on materials like perspex glass, silicone membrane and nylon sheet. Therefore, as mentioned in the previous section (**Section 3.2.2.1**), water passes through the tube-

in-tube heat exchanger before reaching the TGM device. Fluid flow rate is set around 1.5 litres per minute using the valve on the float type flow meter; this results in TGM temperatures ranging from 30°C to 35°C depending on the season.

First, flowing liquid encounters a porous stretched steel mesh, but a small amount of liquid can pass through the porous medium. This is stopped by the semi-permeable silicone membrane which allows gas particles to pass through while it blocks the liquid. A porous nylon sheet placed on the semi permeable membrane makes sure that no liquid particles can pass through. Later, gas particles travel through the micro channel and fill up the gas chamber between the sensor and the perspex glass. Keller PAA-35S type (Keller 2009) highly precise pressure transmitter measures total gas pressure (p_T) inside the chamber. The gas chamber between the perspex and the sensor contains water vapour and dissolved gas molecules; therefore water vapour pressure (p_v) at TGM temperature is subtracted from the total gas pressure (p_T) measured by the transmitter to obtain the partial pressure of dissolved gases (p_g) in the gas chamber. The amount of dissolved gas in the liquid (x_g) is then calculated by **Equation (3-1)** using Henry's law as mentioned previously in **Section 2.2**.

$$x_g = \frac{p_T - p_v}{K_H} \tag{3-1}$$

It is assumed that nitrogen is the only gas present in the gas chamber of the TGM device because of the facts mentioned in the **Section 3.2.3** and the procedure followed during the experiments (see **Section 3.8.1**). The temperature dependent proportionality constant (K_H) in **Equation (3-1)** is selected from the data provided for nitrogen in **Table 2-2** according to the measured TGM temperature.

During the assembly of the TGM device, special care was given to mount the pressure sensor at the last stage in order to avoid the possibility of compressed air in the gas chamber which may lead to errors in pressure measurements. First, silicon membrane and porous gauze sheet were positioned on the stretched mesh and the perspex glass was placed on them. Then, the housing cover was placed on top of the device and assembled with four washers and four bolts as shown in **Figure 3-13**. Valves that control the system water entrance to the device were opened so that air in

the device could leave the system through the micro channel. Lastly, pressure transmitter was mounted on the glass perspex with the silicone gasket to prevent any leakage. The device was checked and cleaned regularly on every experiment day, in the early morning, to prevent any errors that could be caused by fouling of the semi-permeable membrane.

3.2.3 Nitrogen cylinder

Tap water that is used to fill the domestic central heating systems contains dissolved gases that are found in the air (Fsadni 2012) which consists of 78% nitrogen, 21% oxygen and 1% other gases. The dissolved gas compositions found in central heating systems have been measured by Fsadni (2012) with Orbisphere dissolved gas sensors 3654 and 3655. He concluded that nitrogen is the dominant gas that is found in the closed loop with some oxygen and hydrogen. It was observed that the amount of oxygen in the system liquid tends to drop after filling up the system with tap water because of the oxidation between untreated metal surfaces in system parts such as radiators, buffer vessels etc. Meanwhile the amount of hydrogen increases because it is one of the end products of oxidation. However it was found that the amount of both oxygen and hydrogen dissolved in system fluid is negligible when compared to the amount of nitrogen found throughout the system (Fsadni 2012). Therefore, in the test rig of the present study the oxygen-free nitrogen cylinder in **Figure 3-14** was used to increase, when needed, the amount of dissolved gas in the system. There are two different injection positions in the experimental rig; one on the top left corner of the radiator and other at the bottom of the buffer vessel. As a matter of routine, at the end of each experiment day nitrogen injection is applied to increase the amount of dissolved nitrogen in the system liquid in order to attain the desired mix of dissolved gases the next morning. Detailed experimental procedure regarding the nitrogen injection process will be given in the **Section 3.8**.

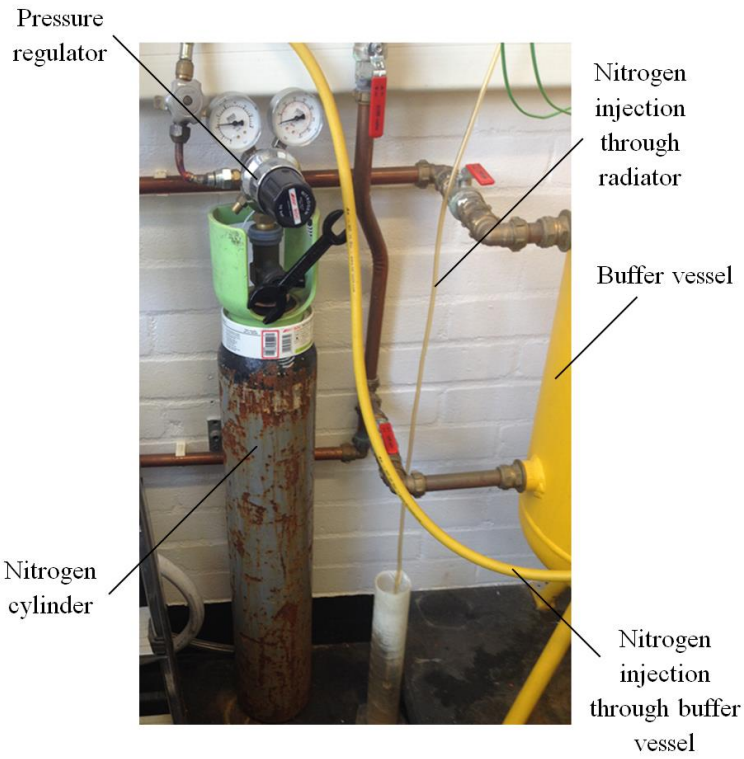

Figure 3-14. Nitrogen cylinder.

3.2.4 Data acquisition and monitoring with LabVIEW

All of the signals from the measurement equipment are collected at the National Instruments cDAQ-9172 chassis as shown in **Figure 3-15**.

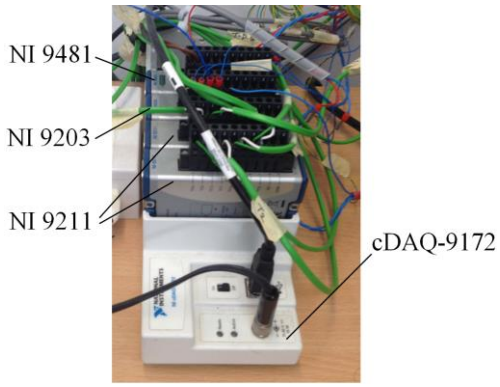

Figure 3-15. NI-cDAQ-9172 chassis with four modules used in experimental facility.

The chassis has eight-slots which can be used with C Series I/O modules. It can measure a broad range of analogue and digital I/O signals and sensors using a USB 2.0 interface (NI 2008). The chassis is mounted with two NI-9211 4-channel

thermocouple input modules, one NI 9203 type 8-channel ±20 mA 16-Bit analogue input module and a NI 9481 4-channel SPST electromechanical relay module. Signals from thermocouples are transmitted to the NI-9211 module while NI-9203 module is used to send signals from the pressure sensors and electromagnetic flow meter. The solenoid valve which controls the cooling system of the test rig is connected to NI-9481 module.

The block diagram of signals from the measurement equipment that was developed by Fsadni (2012) with the LabVIEW software during his studies has been modified and improved for use in the present study. Details regarding the relevant modifications of the LabVIEW block diagram are given in **Section 3.3.1**. **Figure 3-16** illustrates the final front panel setup of the software which enables control of the solenoid valve, on-line monitoring of temperatures, pressures, flow rate, dissolved gas concentration in the liquid (x_{act}), saturation concentration (x_{sat}) of the liquid at pipeline conditions T_1 and P_1, and the saturation ratio (α) defined in **Equation (2-4)**. The block diagram also includes features to save measured data for further investigations after the experiments if needed.

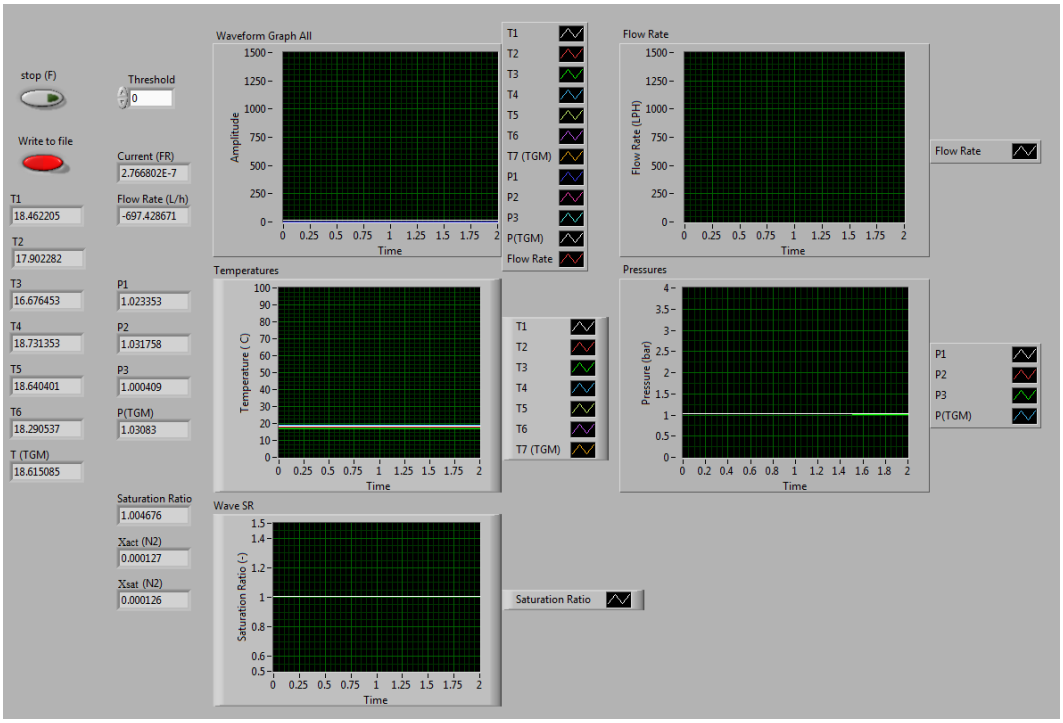

Figure 3-16. Front panel of the LabVIEW software.

3.3 Modification of the Experimental Facility

Modification of the experimental facility was required to improve and adapt it in order to carry out the aims of the current study. This section starts with a description of the alteration of the data acquisition system in a way that the saturation ratio and the dissolved gas amounts could be monitored online. Second, description of sensor calibrations and their use in the LabVIEW software are given. Later, plastic compression use, external pump selection and installation of voltage control to internal pump are explained. Lastly, the detailed pipework setup for vertical and horizontal flow measurements are presented.

3.3.1 LabVIEW software

Fsadni's block diagram for the LabVIEW software (Fsadni, 2012) has been modified to improve its effectiveness and adapt it to the purposes of the current study. **Figure 3-17** illustrates the modified block diagram of the LabVIEW software.

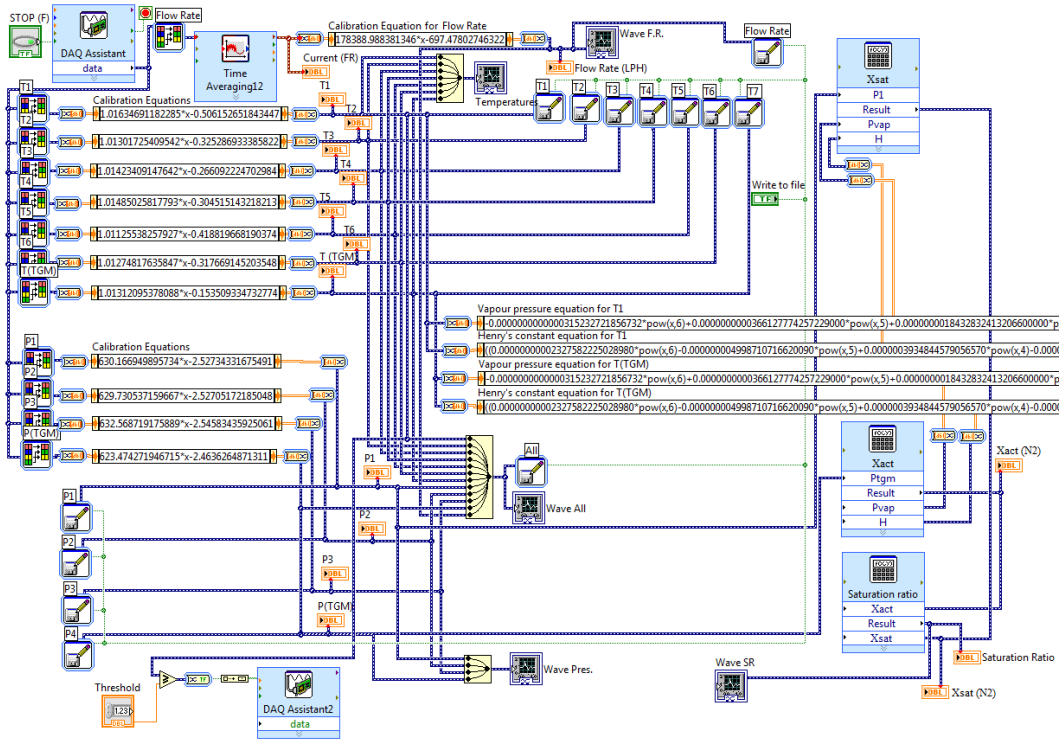

Figure 3-17. Block diagram of the LabVIEW software.

First, the old calibration equations for seven thermocouples, four pressure transducers and an electromagnetic flow meter were replaced with the new equations obtained from the recent calibration procedure mentioned in **Section 3.3.2**. Second, in order to achieve boiler exit temperature control (see **Section 3.2.2.1**) during the experiments, the logic which controls the solenoid valve for system cooling was changed from comparing the threshold level with temperature at the boiler inlet (T_7) to comparing it with boiler outlet temperature (T_1). Third, several calculation features were placed in the block diagram to enable online monitoring of the saturation ratio (α) of the liquid at boiler exit pipeline of the test rig.

The monitoring of the saturation ratio (α) was done as follows. The temperature measurements from the boiler exit pipeline (T_1) and the TGM device (T_{TGM}) were directed into the correlations given in **Appendices 16** and **17** to obtain Henry's proportionality constant (K_H) and the vapour pressure (p_v) of water at particular temperatures. Correlations used to find Henry's proportionality constant and vapour pressure of water were acquired from the graphs plotted with the data provided in Perry et al. (1997). Afterwards, these values were used to calculate actual dissolved gas amount (x_{act}) and saturation concentration (x_{sat}) of the liquid for particular temperatures and pressures. Actual dissolved gas amount in the liquid was calculated with the temperature and pressure measurements obtained from the TGM device (T_{TGM} and P_{TGM}) using **Equation (3-1)**, as explained in **Section 3.2.2.2.** The amount of dissolved gas at saturated conditions was calculated from the temperature and pressure measurements of the liquid at the boiler exit pipeline (T_1 and P_1). This corresponds to the maximum amount of dissolved gas (in saturated solution) that can be found at the boiler exit conditions. **Equation (3-1)** was also used to calculate the saturation concentration but instead of gas pressure measurements obtained from the TGM device, static pressure experienced by the liquid at boiler exit pipeline was used. Finally, the saturation ratio (α) was obtained using **Equation (2-4)**.

3.3.2 Sensor calibrations

The sensors mentioned in the previous sections were calibrated with the appropriate devices in order to make sure that the measured data is reliable. The thermocouples and pressure sensors used in the test rig were calibrated at Brunel University with the

water bath and the dead weight tester shown in **Figure 3-18**. The electromagnetic flow meter was sent to the manufacturer (Litremeter 2010) for calibration. The relevant calibration procedure was conducted and certificated calibration data was provided by the manufacturer.

Figure 3-18. Water bath (left) and dead weight tester (right).

In general, the calibration procedure employed in the current study can be described by the graph given in **Figure 3-19**.

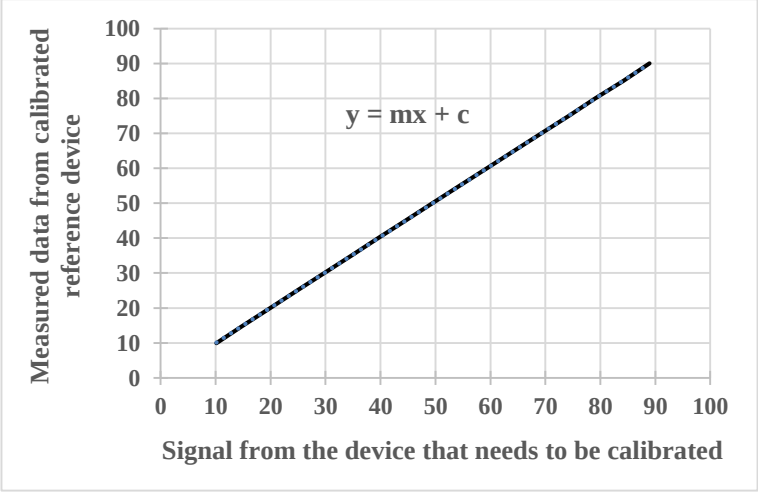

Figure 3-19. Calibration procedure for the sensors.

Basically, sensors were placed in an environment where the applied conditions were known and their responses from the sensors to gradually increasing conditions were gathered. For instance, the thermocouples were placed in the water bath of **Figure 3-18** where the temperature of the water was measured with a reference thermometer. The temperature of the water was increased gradually and the reading from the thermocouples and the reference device were noted. A similar trend, as shown in **Figure 3-19**, was obtained when the noted data was plotted on x-y plot. Here, the x-

axis represents the signals from the device which is going to be calibrated and y-axis is the measurement from the reference device. The linear relationship between these two measurements was used to calibrate the sensors in the test rig. All of the calibration equations obtained from the procedure mentioned above are given in appendix section (from **Appendices 4** to **15**) and used in the block diagram of LabVIEW software to calibrate the measured data (see **Figure 3-17**).

3.3.3 Brass and plastic compressions

The only compression fittings the test rig had when the current study began were brass ones. During the familiarization period with the test rig, it was observed that the brass compression fittings at the points which were used more showed signs of serious wear, such as pipe deformation and leakage. Particularly, the copper pipe and brass fittings used at both ends of the sight glasses were damaged because of their frequently changing position. Therefore, it was decided that the type of fitting would be chosen according to the position of the connection. The connection points that remained relatively fixed during the experiment were left with brass compressions but plastic push-fit (Speedfit 2015) compressions were installed at the connection points that were frequently opened and closed. **Figure 3-20** shows example images of straight coupling brass and plastic compression fittings used in the test rig. Plastic push-fit compressions provide greater flexibility throughout the test rig enabling quick and secure solutions for the heating and plumbing systems.

Figure 3-20. Brass (left) and plastic (right) compression fittings.

3.3.4 External pump selection

Previously, water circulation throughout the primary test rig was sustained only by the pump inside the boiler. Maximum water flow rate that could be reached in the

test rig with a single pump was 1,050 litres per hour (LPH) which corresponds to a flow velocity of approximately 0.93 m/s in 22 mm diameter copper pipes. Curry (2001) suggests that water velocity throughout the system pipe work should be between 0.5 m/s to 1.5 m/s in order to avoid both sludge settling because of low velocity and noise disruption because of high velocity. Flow velocities investigated by the previous researcher (Fsadni 2012) were lower than 0.5 m/s inside the pipeline of the test rig. For the current study, the sponsor company requested that the flow velocity be increased into the flow velocity range suggested by Curry (2001). Therefore, an extra pump was inserted into the primary loop of the test rig thus increasing the flow rates through the pipeline where sight glasses were installed.

The system-head curve is defined as the curve that illustrates the relationship between the system flow rate and head-loss for a specific system and it can be used to predict the system operation point (Melvin 2005). Head loss through the test rig follows **Equation (3-2)** (Walski et al. 2010):

$$h = K \times Q^2 \tag{3-2}$$

where Q is the volumetric flow rate of the system, K is the resistance coefficient of the system and h is the head loss through the system. Pump discharge height was changed by tightening the by-pass valve as discussed in **Section 3.2.1.1** and system flow rates were observed in the test rig against each pump discharge height. Test results were used to calculate the system resistance coefficient K needed in **Equation (3-2).** Data from the test and calculated system resistance coefficients were tabulated as presented in **Table 3-1.**

Table 3-1. System-head curve test.

Pump discharge height (mbar)	System flow rate (L/h)	System resistance coefficient (mbar.h^2/L^2)
170	745	0.000306
250	895	0.000312
350	1050	0.000317

Arithmetic average of the three system resistance coefficients in **Table 3-1** were utilized as the overall system resistance coefficient defined in **Equation (3-2)**. The system-head curve for the current test rig shown in **Figure 3-1** was then given by **Equation (3-3)** below, which was used to plot system curve in **Figure 3-21**.

$$h = 0.000312 \times Q^2 \tag{3-3}$$

Performance curves of two different Groundfos pumps were obtained from the data provided by the manufacturer (Groundfos 2012) and combined with the performance data of the single-stage pump inside the boiler (Vaillant 2008) according to the procedure given for serially connected pumps in Groundfos (2004). The curve in **Figure 3-21** was plotted in order to decide which pump would be suitable for the current experiments. The point where the pump performance curve and the system-head curve intersect is the predicted operation point of the system. After considering the cost and needs of the research, it was decided that Groundfos type UPS15-60 would satisfy the requirements of the current study. It was estimated that the system flow rate would be approximately 1300 LPH (point 1 in **Figure 3-21**) with maximum power. 1300 LPH volumetric flow rate results from 1.15 m/s flow velocity in 22 mm diameter copper pipe which offers the possibility to investigate several different flow rates in the suggested flow velocity range given in Curry (2001).

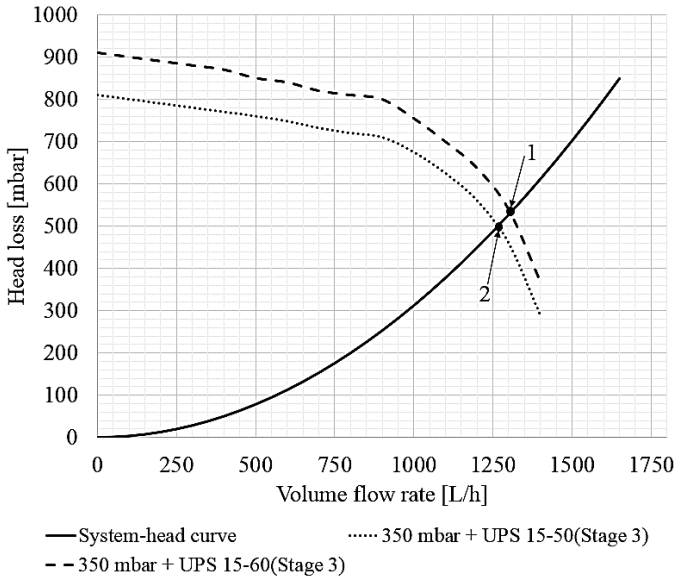

Figure 3-21. Operation point with serially connected pumps.

3.3.5 Internal pump controller

In the test rig of (Fsadni 2012) the system flow rate was controlled through two ball-valves installed at the buffer vessel inlet and outlet (location of the ball-valves can be seen from **Figures 3-1** and **3-14**). However, it has been reported by Loeffler (2011) that using the ball-valve as a throttling device can damage the seals and that it is more common and effective to use them as either fully open or closed. During the preliminary tests, it was discovered that controlling and stabilizing the flow rate with ball-valves was very difficult. Moreover, significant amount of signal fluctuations from electromagnetic flow meter were monitored during these tests. Consequently, for regulating the flow rate it was decided to switch to pump speed control instead, which indeed turned out to be much more effective and practical.

The voltage controller shown in **Figure 3-4** was connected to the pump inside the boiler and the pump's speed adjusted by altering the voltage applied to it. Basically, the device transforms the fixed voltage supplied by the grid to a variable voltage output. Originally, the internal pump would be turned on and off through the control panel of the boiler. In the new setting, the three-phase wire connection was removed from the control panel and wired to the voltage controller as shown in **Figure 3-22**.

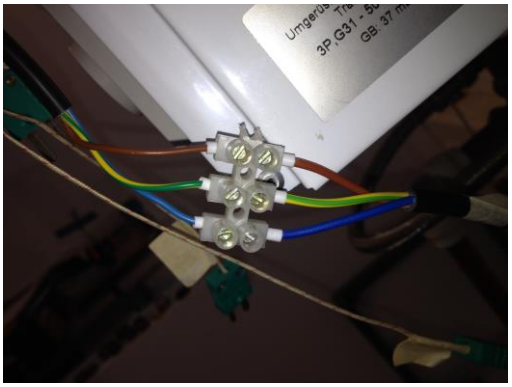

Figure 3-22. Three-phase wiring of the internal pump and voltage controller.

It is worth mentioning here that the by-pass valve inside the boiler, which was mentioned in **Section 3.2.1.1,** was kept fully open during the experiments and flow rate control carried out solely via the voltage controller.

3.3.6 Vertical setup

The pipe work just after the boiler exit was modified as indicated in **Figure 3-23** so that the two-phase bubbly flow characteristics right after the boiler (VSG1) and their development during vertical downward flow (VSG2) could be investigated. There was need for more room behind the sight glass because of the nature of the bubble measurement method used. Therefore, a double 90-degree bend structure was employed to create the space needed for positioning the fibre optic light guide to provide necessary illumination. Detailed camera and lighting positions will be discussed later in **Section 3.4.1.2**.

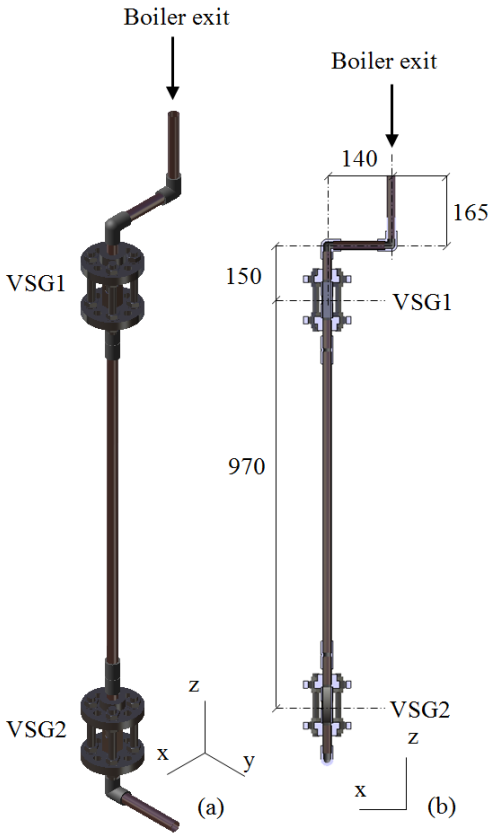

Figure 3-23. (a) A 3D CAD model of the vertical setup; and (b) cross-section view with dimensions.

Hot water enters the vertical pipe after the boiler and travels along for 165 mm. Then changes its direction at the first 90-degree bend and travels horizontally for 140 mm before it reaches the second 90-degree bend. The second 90-degree bend turns the flow back to vertical direction where sight glasses are installed. The middle point of the first sight glass (VSG1) is approximately 150 mm away from the second 90-

degree bend. And there is a distance of 970 mm between the middle points of the two sight glasses which is the maximum distance that can be achieved in the current test rig without altering the boiler position. A picture of the actual modified test rig for the vertical flow measurements can be found in **Appendix 18**.

3.3.7 Horizontal setup

Four measurement positions were used to investigate horizontal bubbly flow along the horizontal pipeline of the test rig after the boiler exit. 3D CAD model and detailed cross section view of the sight glass positions are shown in **Figure 3-24**. It is important to note that there were two sight glasses available during the present study and **Figure 3-24** represents only the measurement positions used for horizontal inspection not the actual test rig. Pictures of the actual test rig during the measurements at HSG1 and HSG2 can be found in **Appendix 19**.

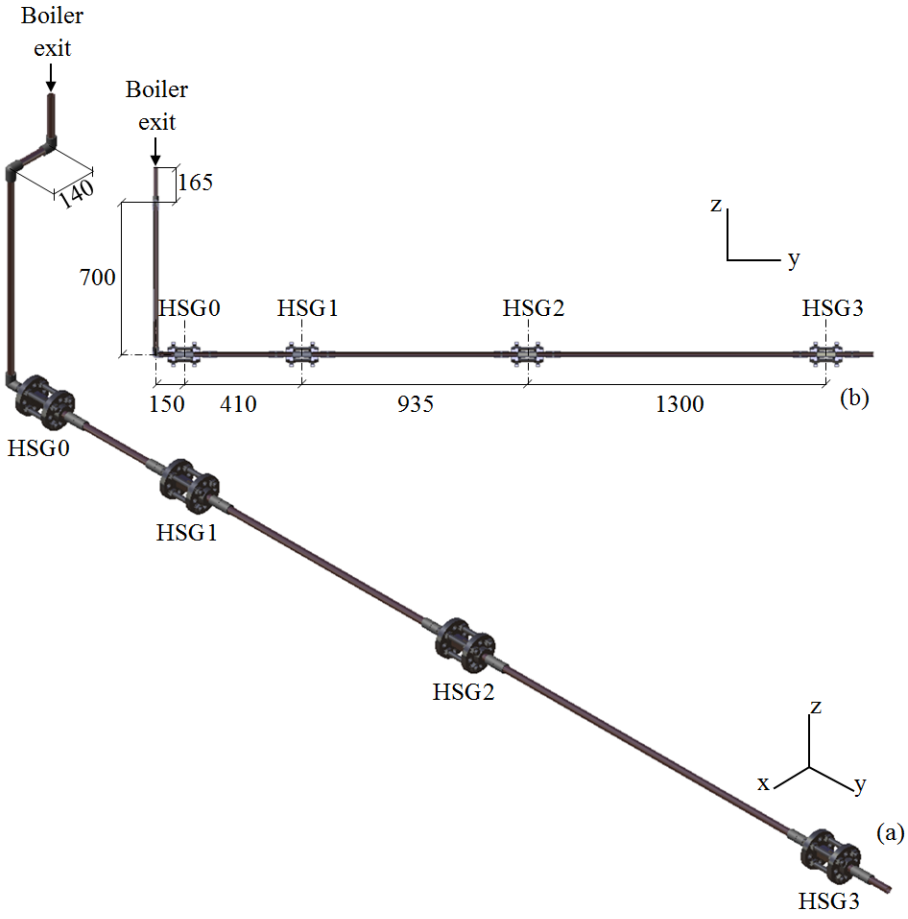

Figure 3-24. (a) A 3D CAD model of the horizontal setup; and (b) cross-section view with dimensions.

Pipework just after the boiler is identical to the vertical setup given in **Figure 3-23** except for the part after the double 90-degree bend structure. A vertical pipe is used between the second bend and the third one and the distance between the two bends is around 700 mm. The first sight glass (HSG0) is placed right after the third bend with the purpose of observing the effect of the 90-degree bend on two-phase bubbly flow. The distance between the middle point of the HSG0 and the bend is about 150 mm, the shortest distance that can be achieved with the current sight glass design. The remaining sight glass positions were chosen such that the distance between consecutive sight glass pairs would gradually increase (410 mm, 935 mm and 1300mm).

3.4 Bubble Measurement Technique

Investigation of two-phase flow has been of great interest to researchers in a variety of industrial and academic engineering areas. Consequently, different experimental techniques to analyse the flow structure have been developed over the past decade. Extensive description of different types of experimental measurement techniques applied to investigate the phenomenon can be found in Crowe (2006) and Crowe et al. (2012). There are advantages and disadvantages of each technique. For instance, some of them can be used only for void fraction measurements whereas others provide information related to the bubble shapes and sizes as well as void fractions. It is beyond the scope of the current study to discuss the pros and cons of each measurement technique.

The experimental technique employed in the current study has been originally chosen by the researcher who carried out the study preceding the current one and this is because of the fact that a similar technique had been employed by the research and development team of the sponsor company, Spirotech b.v., for several years (Fsadni 2012). The experimental instruments were kept identical, except for the microscopic lens used for magnification, in order to have the consistency necessary for meaningful comparison of results with previous findings obtained by using the same test rig. The equipment for investigation of the two-phase flow process was provided by the EPSRC and was borrowed several times, each for a three-month period,

during the present study (three years). The magnification lens used by Fsadni (2012) was unavailable the first time the equipment was delivered and so the measurements had to start with a different lens with which the initial data were obtained. Later, based on the experience of these preliminary measurements, it was decided that there was actually no need to change the lens used the first time. The two-phase flow process was filmed by the high-speed camera and the images were analysed using an image processing software called Image-Pro Analyzer 7.0. Details of the measurement technique used in the current study are given in the following.

3.4.1 Camera measurements

The high-speed video camera used to film the bubbles in the pipeline of the central heating test rig is shown in **Figure 3-1**. Bubbles found in central heating systems are of microscopic size (Fsadni & Ge 2012). Therefore, magnification was a necessity and it was acquired by the Leica Monozoom 7. Basic features of the camera and the lens system is shown in **Figure 3-25**.

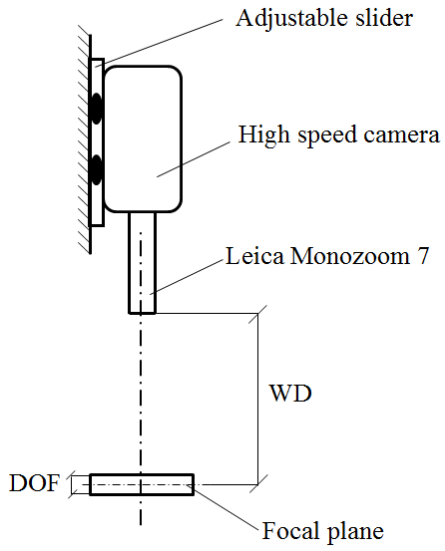

Figure 3-25. High-speed camera, magnification lens and focal plane.

Leica Monozoom 7 was attached to the high-speed camera and together they were mounted to an adjustable slider which provides the back and front movement of the system. The focal plane shown in **Figure 3-25** represents the plane passing through the focal point of the particular camera and lens setup. Focal length, which is the

distance from the lens to the focal point, is defined as a working distance (WD) and it can only be varied by changing the objective lens used on the magnification knob. The main significance of the focal plane is that the objects which are in the focal plane appear clearer and sharper in the image than the objects which are out. Depth of field (DOF) is the depth of the focal plane where the objects appear acceptably sharp and clear as illustrated in **Figure 3-26** for better understanding. The words shown in the figure appear sharp and clear in the middle which is the section in the focal plane but get blurry towards the top and the bottom parts which are out.

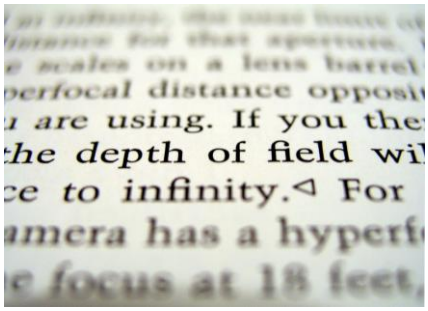

Figure 3-26. Concept of depth of field (DOF) (Anon n.d.).

3.4.1.1 Camera and lens settings

The camera and lens system employed in the current study provide a variety of settings for magnification, resolution, sample rate, and exposure time. **Table 3-2** shows the camera and lens settings used during the experiments. These particular settings have been selected after a lot of testing on the measurement equipment in conjunction with image processing technique used to analyse the filmed images.

Table 3-2. Camera and lens settings.

Camera	Phantom v5.1
Zoom	Leica Monozoom 7
Amplifier	3.0x
Objective	2.0x
Zoom level	1
Resolution	768 × 768 pixels
Sample rate	50/2100 fps
Exposure time	20 μs

First of all, resolution of the images obviously needed to be the highest possible with the equipment used as the image quality increases with higher resolution. Higher image quality means more details in the image, and hence enhanced image processing performance in the further stages of the measurements. Phantom v5.1 video camera offers a maximum resolution of 1024 x 1024 (Phantom 2007). However, during the experiments it proved impossible to get the available maximum resolution because of restrictions caused by the magnification knob. The image obtained with the highest resolution has wider viewpoint but it was intercepted by the magnification knob which restricts the viewed part of the focal plane. Therefore, the second highest resolution available (768 x 768) had to be chosen.

Secondly, magnification settings (amplifier, objective and zoom level) of the Leica Monozoom 7 have been determined through the consideration of the bubble sizes found in the system. Bubble diameters found in central heating pipeline vary from 0.05 mm to 2 mm the average diameter being around 0.1 mm for each set of sample data (Fsadni 2012). Therefore, 4 mm x 4 mm frame size was decided to be sufficiently big for the present study. The amplifier, objective and zoom level given in the **Table 3-2** provide a size of frame at approximately 4 mm x 4 mm.

Thirdly, two different sample rates (shutter speed) have been used throughout the experiments. 2100 frames per second (fps) was used to obtain the data related to the bubble velocities whereas 50 fps was used for the rest of the measurements. 2100 fps is the fastest sample rate that can be reached by the specific camera and it ensures the capturing of the movement of a bubble within a frame at the flow rates used for the current study. Void fraction, average bubble diameter and distribution measurements were conducted with 50 fps sample rate so that a new bubble would pass through the frame between each sample and counting the same bubble twice is avoided. 50 fps was decided after examining the bubble velocity measurements across the pipe section. Lowest bubble velocity measured throughout the measurement positions given in **Figures 3-23** and **3-24** was 0.2196 m/s. The slowest bubble requires 0.018 seconds to travel along a 4 mm frame so 50 fps (0.02 seconds between each frame) ensures that a bubble would have sufficient time to travel more than frame size (4 mm) between each sample.

Finally, the exposure time, which is the time that shutter stays open for each frame, was selected after experimenting with different values. Simply, more light enters the camera as the exposure time increases. However, it must be chosen carefully because, while there is a need for sufficient light, in order to prevent blurriness an object should not move significantly during the exposure time. After trying different values of exposure time and with the help of some image processing, it was decided that choosing 20 μs provided a good trade off: at the fastest velocity, which was measured at around 1.4 m/s, the bubble travels 0.028 mm in the chosen exposure time, and a movement of 0.028 mm between each sample is sufficiently practically negligible.

3.4.1.2 Camera and light positions

The camera and lens system shown in **Figure 3-25** were mounted onto a 3-way pan-tilt head on the tripod which offers tilting and panning with separate axes and controls. Separate axes control provides the capability for changing an axis of the camera without affecting other axes. Special care was given to the spirit levels on the tripod to make sure that the system is exactly horizontal and/or vertical depending on the measurement. The tripod mechanism could not be used for the measurements conducted at the VSG2 because its position was very close to the floor. Therefore, the camera was demounted from the adjustable slider and attached to a separate 2-way slider on the floor (see **Appendix 20**). Moreover, separate level ruler was used to verify the axes of the camera system as well as the sight glasses (see **Appendix 21**) for both vertical and horizontal measurements.

A detailed representation of the camera and light setup for vertical and horizontal measurements are given in **Figures 3-27** and **3-28**, respectively. Both measurements had nearly the same arrangement; the only difference being that all of the equipment was rotated by 90 degrees in one compared to the other. The camera system was placed in front of the observation hole with at a distance of 29 or 30 mm from the sight glass and moved towards the sight glass with the use of the adjustable slider to film the flow across the sight glass in eight different positions. The eight sample volumes (with about 2 mm intervals) used across the sight glass section are shown in the figures. The fibre optic light guide was positioned approximately 15 mm behind

the hole on the other side. The distances mentioned above were measured carefully with stainless steel ruler and rulers on the adjustable sliders (see **Appendices 20** to **23**). The 60-Watt metal-halide light source, which produces high intensity white light without producing the excessive heat associated with other similar products in the market, provided the necessary illumination for the camera measurements (GE 2007).

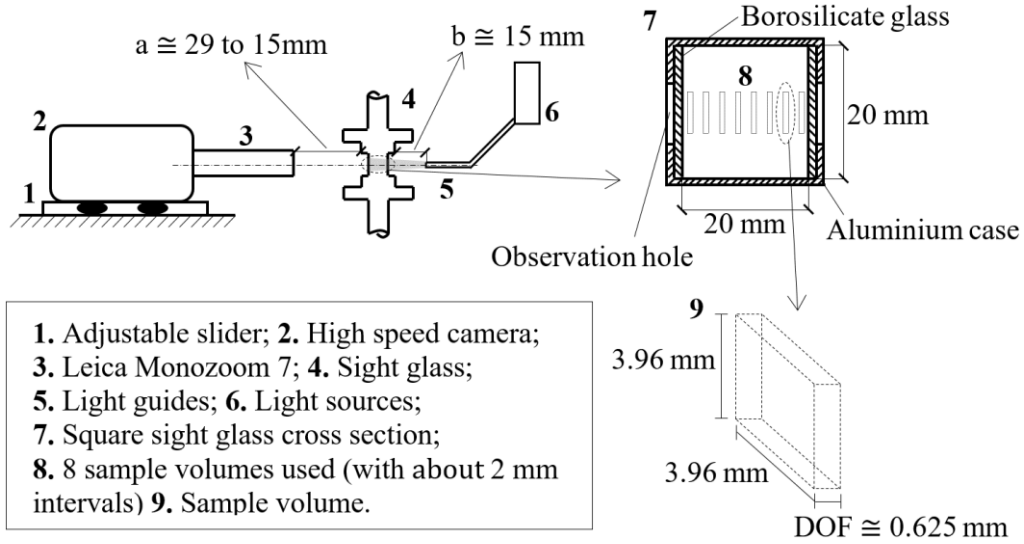

Figure 3-27. Detailed camera and light positions for vertical flow measurements at the positions given in **Figure 3-23**

Furthermore, the effect of the light source intensity was used to validate that the camera and the light guide are on the same axis. Light intensity was first maximized to obtain a bright light image and then reduced gradually (see **Figure 3-29**). The first image (top left corner) was captured at maximum intensity where the image viewed is bright white, and as the intensity of the light reduces the centre of the light guide becomes visible. After ensuring that the centre of the light guide was in the middle of the image, the light intensity was reduced until the bright light disappeared (bottom right corner). This process was applied twice with the help of the adjustable slider at the first and the last sample volume given in **Figures 3-27** and **3-28** to make sure that the axes of the camera and the light guide are on the same line.

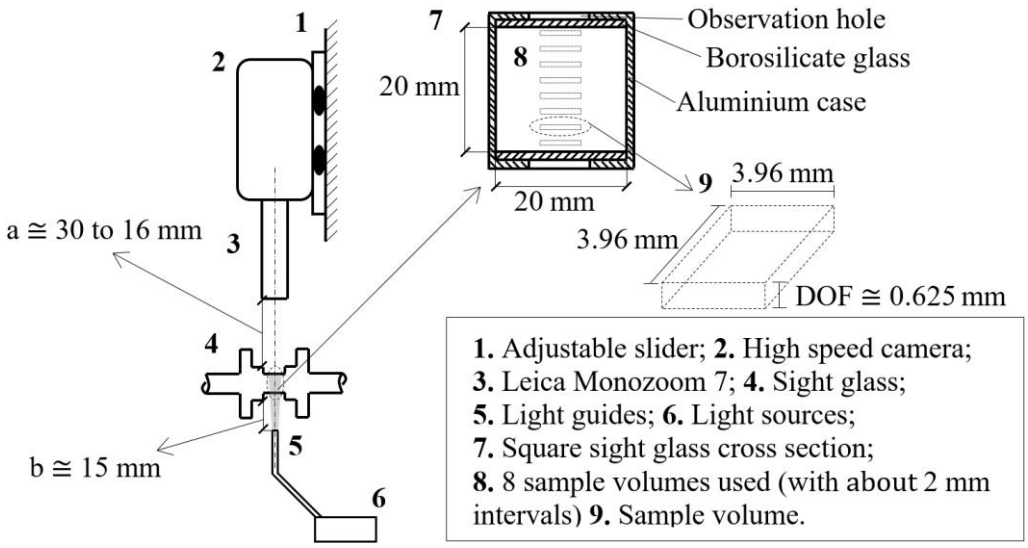

Figure 3-28. Detailed camera and light positions for horizontal flow measurements at the positing given in **Figure 3-24**

Background intensity of the last image (bottom right corner) shown in **Figure 3-29** was monitored with the software used to control the camera (Phantom Camera Controller) and arranged to be between 90 to 105 (see **Appendix 24**) greyscale during the experiments to enable distinguishing of the bubbles from the background at the stage of image analysis. The consistency of the background intensity is crucial for the current study's aim to achieve meaningful and comparable results from image analysis.

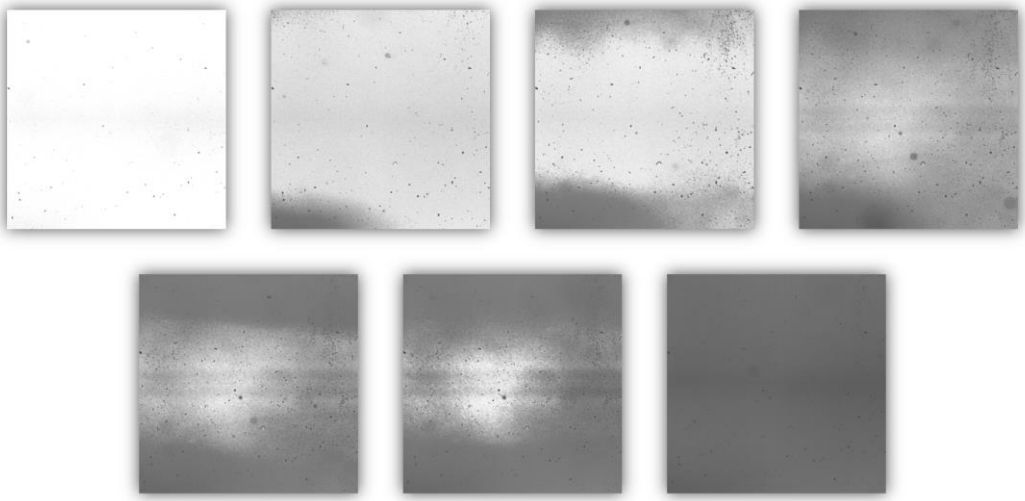

Figure 3-29. Verifying that the light and the camera are on the same axis.

3.4.2 Image analysis

Image processing software called Image-Pro Analyzer 7.0 was used to process the images captured by the high speed camera. The film recorded for each sample volume was saved as a ".cine" file by the Phantom Camera Controller software. Phantom high speed video cameras from Vision Research Inc. stores and retrieves the recordings in .cine file format (Research 2007). Image processing software cannot be used directly to analyse .cine files and requires conversion of video file to multiple images. Therefore, Phantom Cine Viewer software was used to convert the .cine file to .tif images enabling the application of the image processing routine (see **Section 3.4.2.2**) to a single image each time (MediaCybernetics 2010). The following two sections will provide detailed information regarding the image processing method used in the present study.

3.4.2.1 Software calibration

First of all, the image processing software requires information regarding the equivalent size of each pixel in real life. The software uses this information to calculate the real size of objects or images of interest. In order to get this information, series of images of metal bearing balls of two different sizes (1 and 2 mm diameters) were captured with the specific camera and lens setup mentioned in **Section 3.4.1.1**. The camera and light setup given for horizontal measurements (see **Figure 3-28**) was established and metal bearing balls were placed on the upper glass of the sight glass design. Metal balls were grade 10 type and their diameter tolerance was given as ± 0.00254 mm by their manufacturer (Bearings 2010). Diameter tolerance provided for the bearing balls was considerably smaller than the minimum bubble diameter (0.05 mm) identified by the previous researcher (Fsadni 2012) and therefore, accepted to be suitable to use as a calibration tool in the current study. **Figure 3-30** shows original and captured images of bearing balls.

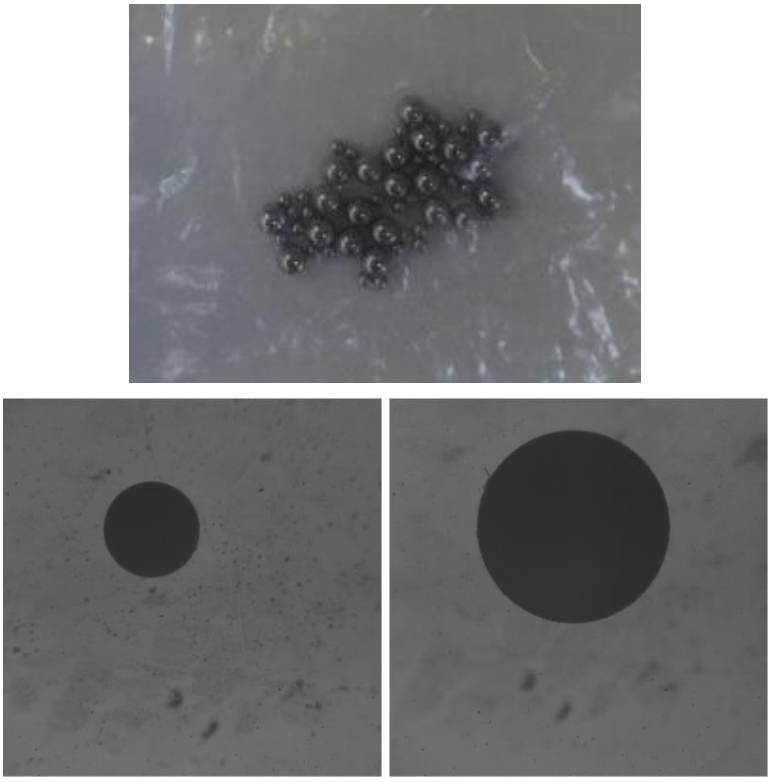

Figure 3-30. Real images of bearing balls (top), captured image of small metal ball with 1 mm diameter (bottom left) and captured image of big metal ball with 2mm diameter (bottom right).

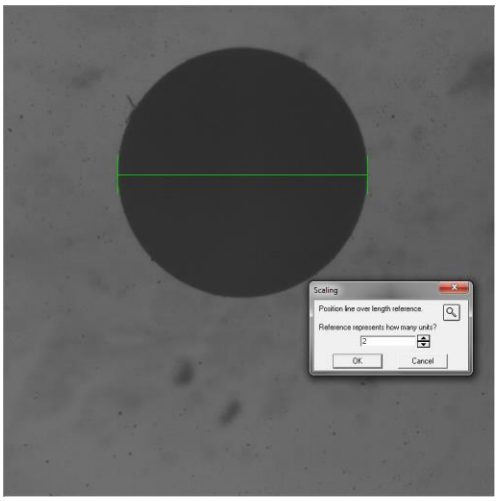

Figure 3-31. Calibration stage of the image processing software.

Captured image of the big ball was imported to the Image-Pro Analyzer and used to calibrate the software as shown in **Figure 3-31**. The green line shown in the image below represents the length that is to be defined. The reference line was placed carefully to the middle of the black shadow so that it would be positioned at its

diameter and defined as 2 mm. The software than calculated the size of each pixel as 0.0051546 mm which led to the frame size of 3.9588 x 3.9588 mm^2. This information was saved with a specific name which could later be called and applied to other images captured with the same camera and lens setup.

3.4.2.2 Image processing routine

The next step was to determine a procedure which would enhance the images for bubble identification and measure bubbles that are in the focal plane. Image-Pro Analyzer offers lots of different options that can be applied to an image to enhance its quality in a way relevant to the purpose. The following steps will describe the image processing procedure implement in the current research;

- Background Correction: First, unwanted spots which can cause difficulties during image analysis need to be removed. The spots originate from the small dirt particles on the glass of the sight glass design and camera lens. They become more noticeable because of the magnification used, especially on the first and last focal planes shown in **Figures 3-27** and **3-28** which are positioned close to the upper and lower glasses of the sight glass design. Background correction was used to remove these unwanted spots from the images and it was done by subtracting a background image (without any bubbles) from each picture.

  One background image was determined within each set of images (for each focal plane) by going through images one by one. In some cases finding a background image was very difficult because of the high number of bubbles. Photoshop CS6 software was used in these cases to manipulate different image parts and combine different layers in one picture.

  Figure 3-32 illustrates the result of background correction on a typical image obtained from the experiments. The original image containing the undesirable spots is the top left one and the background image (without any bubbles) is shown on the top right. If one examines these two images carefully, one notices that the unwanted spots are located in exactly the same locations in both of the images. The resulting image after the background subtraction is the bottom one in the figure where it can be clearly seen that background

correction removes unwanted spots and enhances the image for further processing.

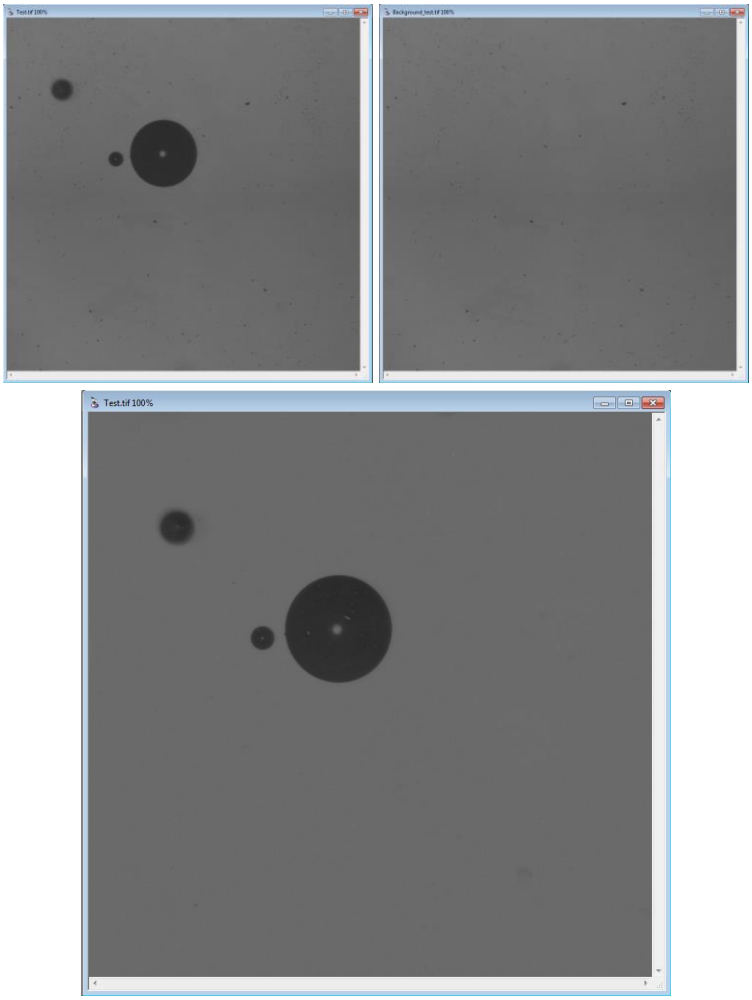

Figure 3-32. Original image (top left), background image (top right) and image after background subtraction (bottom).

- Filter application: Three types of filters were applied to enhance the processing image. First a flatten filter was used to even out intensity variations in the background pixels. Then, a sharpen filter was applied to point out the edges by significantly enhancing all intensity transitions in the image. Lastly, a sobel filter was used to extract and enhance the edges of the bubble images by the means of intensity gradient between neighbouring pixels (MediaCybernetics 2010). The sobel filter is a crucial part of the image processing because it enhances the image so that the bubbles that are in focus can be differentiated from the ones that are not. For example, the typical image that appears in **Figure 3-32** contains three bubbles; but one of them

appears blurry whereas other two are sharp and clean which means that the blurry one is outside the focal plane used. What is needed is to count and measure the bubbles that are in the focal plane while neglecting the others. **Figure 3-33** displays the stages of development in image processing with successive application to the image prepared previously (after background correction) of the three filters. The significance of the sobel filter can be observed from the third image where the edges of two clean and sharp bubbles were enhanced in contrast with the edges of the blurry bubble.

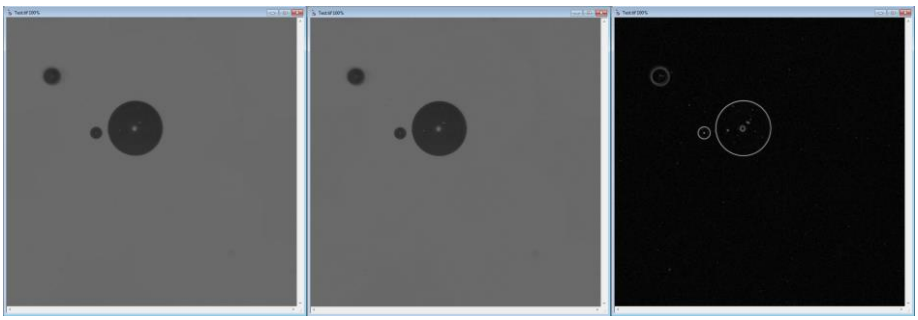

Figure 3-33. Effect of the flatten (left), sharpen (middle) and sobel (right) filters.

- Software calibration: Calibration information saved for the specific camera and lens setup was chosen from the special calibration list (see **Section 3.4.2.1**).
- Count and size menu: Count/size feature was used to count and measure the bubbles within the focal plane. First, count/size options were selected so that the holes in the objects would be filled to avoid counting the small circle that appears in the middle of the objects. Then measurement types and filter ranges were defined to neglect very small (less than 10 pixel diameter) and non-spherical (more than 1.1 aspect ratio and roundness) objects. Later on, object selection by means of picking the right intensity range was made so that two of the clean and sharp bubbles were measured. The intensity range was selected to be between 60 to 255 grey levels which led to the picture given on the left in **Figure 3-34**. The intensity range was decided after spending considerable amount of time on different set of images. Pixels that have grey intensity value higher than 60 were filled with red colour. This creates connected circles at the edge of the sharp and clean bubbles whereas a

full circle did not form around the blurry bubble. Subsequently, count and measure features were applied to capture and measure concerned quantities of the objects marked during intensity selection. The picture on the right in **Figure 3-34** represents the image after count and measure where bubbles in the focal plane were marked with red circles around them.

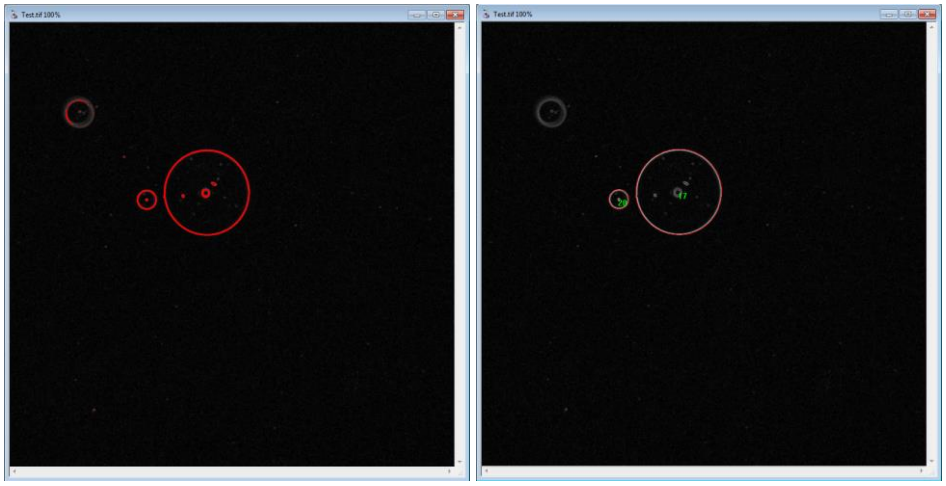

Figure 3-34. Manual intensity selection (left) and image after count and measure (right).

- Saving and loading object outlines: Outlines of counted and measured bubbles were saved and loaded to an image resulting after undoing the sobel filter. **Figure 3-35** illustrates the image after the sobel filter was undone (left) and a preview of the processed image after the object outlines were loaded (right).

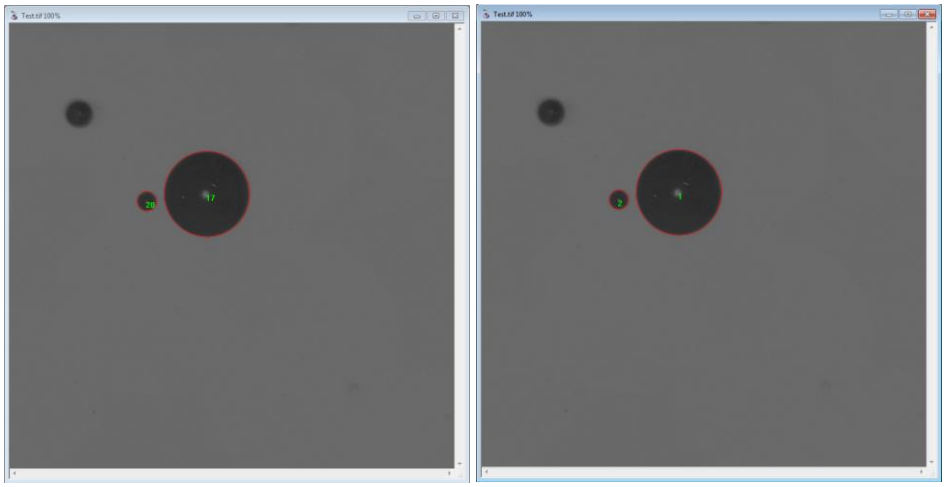

Figure 3-35. Image after sobel filter was undone (left) and image after bubble outline was loaded (right).

- Data collection: Data collector feature was implemented to gather the data of interest from the processed image.
- Snapping the processed image: A tool called the snap was used to capture the recent image with bubble outlines in order to be able to save the processed image with a new name ending with "_processed" right after it has been analysed.

All of the settings used in each step were given with screenshots from the Image-Pro Analyzer in **Appendices 25** to **32**. The procedure explained above was recorded as a macro within the software and implemented into a pre-written macro used to process all images in a directory. The codes from the macro that have been used in the current study can be found in **Appendix 33**. After the code completes processing the images in the directory, all of the data are exported to an excel sheet (see **Appendix 34**) for further data processing.

3.4.3 Apparent depth of the sight glass

In the beginning of our research the intention was to use 10 focal planes across the pipe section to obtain the data related to bubble distributions. In this plan there would be 10 focal planes with 2 mm intervals across the 20 mm depth of the sight glass. However, the observations during the familiarisation period did not agree with what was expected and the number of focal planes were reduced to 8 (see **Figures 3-27** and **3-28**). It was noticed that the depth of the sight glass appeared smaller than it was designed. The reason was thought to be the refraction of light while travelling through different mediums (water, glass and air). Therefore, two different experiments were conducted to test whether light refraction was the cause of this unexpected observation. Galbraith (1955) provides a method that can be used to measure optical depth by reading the travel distance of the microscope between focusing the microscope to the upper and lower surface of the object. In our case the object is the depth of the sight glass.

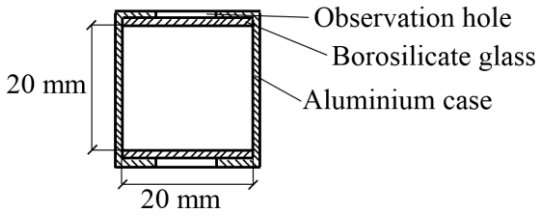

Figure 3-36. Cross-section view of sight glass design.

In order to apply Galbraith's method, the camera and light setup for horizontal measurements (**Figure 3-28**) was put in place and the system was drained so that there would be no water between the two borosilicate glasses on the top and bottom of the design (see **Figure 3-36**). The camera was placed where the distance between the lens and the aluminium case was 32 mm (the length is shown with "a" in **Figure 3-28**) and moved downward gradually (1 mm intervals) with the help of adjustable slider. This procedure allows one to move the focal plane of the camera lens setup (see **Figure 3-25**) from outside of the sight glass design and pass through the cross-section all the way to outside again at the opposite side.

Small water droplets just underneath the top glass started to appear clean and sharp when the distance between the aluminium case and lens was 30 mm. With lowering of the camera continued the water droplets on the inner surface of bottom glass started to appear sharply when the distance between the lens and aluminium case was 10 mm. **Figure 3-37** illustrates the water droplets observed on the top and bottom glasses of the design.

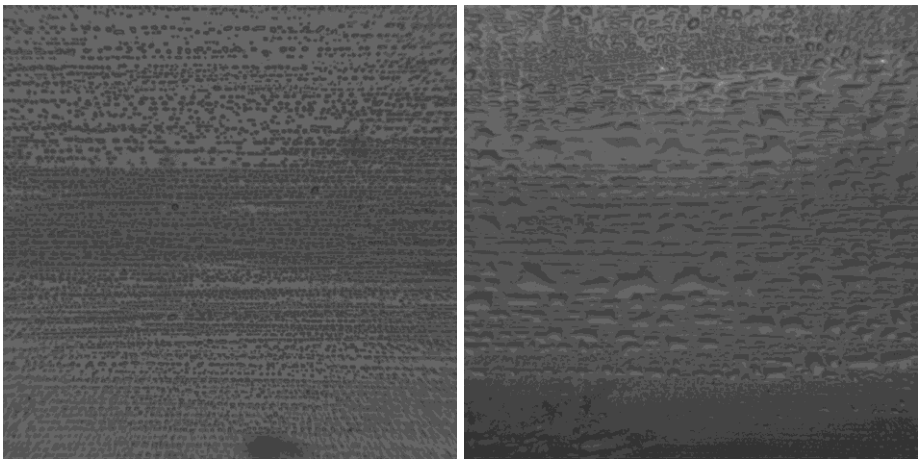

Figure 3-37. Water droplets just underneath the top glass (left) and inner side of the bottom glass (right) when the system was drained.

To test the effect of water between the glasses, the system was filled with water and boiler was used to heat up the liquid to temperatures around 80°C which would be used in the experiments. Later, the same procedure applied previously was repeated to measure the depth of the sight glass design when filled with hot water. It was noted that scratches and dirt just underneath the upper glass appeared when the distance between the lens and the aluminium case was 30 mm. The camera continued to move downwards until scratches and dirt on the inner side of the bottom glass appeared. The distance between the aluminium case and the lens was 14 mm when the scratches and dirt on the bottom glass appeared clean and sharp (see **Figure 3-38**).

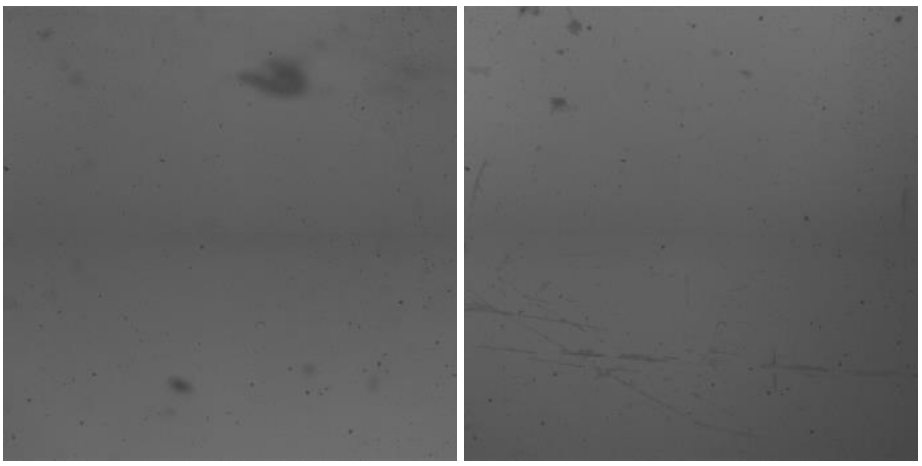

Figure 3-38. Scratches and dirt particles seen underneath the top glass (left) and inner side of the bottom glass (right) when the system was filled with water.

The tests show that the depth of the sight glass when there is no water in the system appears to be 20 mm (30 mm – 10 mm) which is the original design depth of the sight glass. However, the depth seems to be 16 mm ($30 - 14$ mm) when filled with water which confirms that water between the glasses affects the apparent depth. Nassar (1994) has studied this phenomenon and provided useful references which concern a similar problem. There the challenge was to find a solution of the problem of apparent depth of an object underwater where there was not a glass medium between water and air like in our case. The theoretical analysis explained in the following paragraphs has been adapted to our case from the concepts mentioned in Nassar's article.

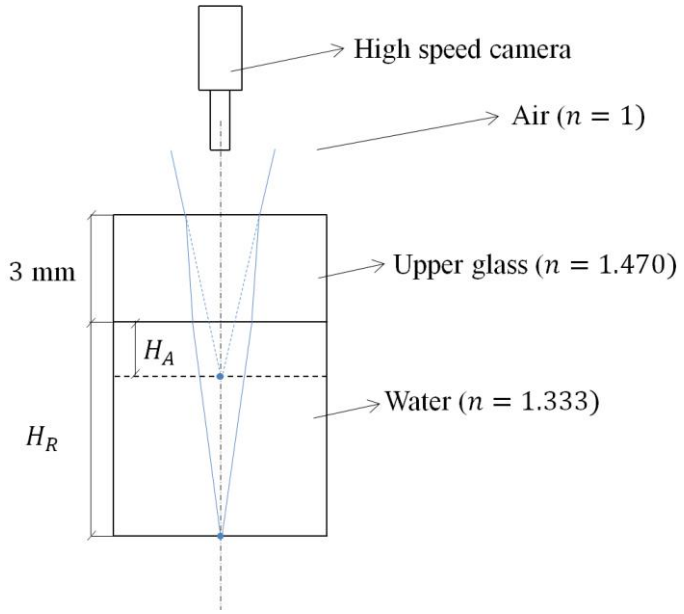

Figure 3-39. Schematic diagram of light refraction analysis.

The theoretical light refraction analysis was conducted to compare the test results and provide further validation that light refraction leads to the smaller depth observation. The diagram in **Figure 3-39** is based on the assumption that the glass on the upper surface is completely horizontal and the camera is placed directly above or at very small angles. It displays the light rays coming from the depth (H_R) in question where they get refracted while passing through different mediums according to Snell's Law (Nassar 1994). Snell's Law defines the relation between the angle of incidence and refraction. Light rays travel through water until they reach the glass surface. At the water-glass interface, they bend towards the normal line while entering into the glass medium whose refraction index (n) is higher than that of water. Then they travel along the glass medium (approximately 3 mm) and reach the glass-air interface. As they cross from the glass to the air medium, light rays bend away from the normal because the refractive index of water is smaller than the glass's. By extending the refracted lights at the glass-air interface backwards until they intersect one obtains the apparent depth (H_A) which is less than real depth (H_R).

Figure 3-40 illustrates the close-up diagram showing the angles of incidence and refraction and the right triangles used for further trigonometric analysis. The angle of incidence in water is θ_w and the angles of refraction in glass and air are θ_g and θ_a, respectively ($\theta_a > \theta_w > \theta_g$).

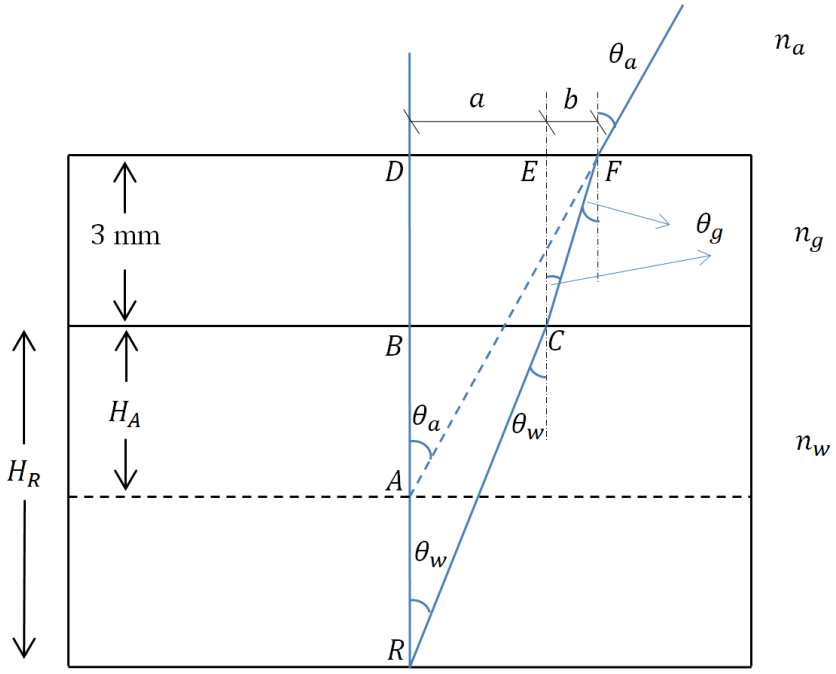

Figure 3-40. Close-up diagram to show refraction angles and right angle triangles used.

The following equations are obtained by applying Snell's Law and trigonometric functions on right angle triangles (ΔRBC, ΔADF and ΔCEF in **Figure 3-40**).

From Snell's Law:

$$n_w \sin\theta_w = n_g \sin\theta_g = n_a \sin\theta_a \tag{3-4}$$

From trigonometric functions using the right angle triangles:

$$\tan\theta_w = \frac{a}{H_R} \tag{3-5}$$

$$\tan\theta_a = \frac{a+b}{3+H_A} \tag{3-6}$$

$$\tan\theta_g = \frac{b}{3} \tag{3-7}$$

Rearranging **Equation (3-4)**) and combining with the trigonometric functions (**Equations (3-5)**, **(3-6)** and **(3-7)**) with the assumption that the incident and refraction angles are very small ($\sin\theta \cong \tan\theta$), one gets:

$$\frac{n_w}{n_g} = \frac{\sin\theta_g}{\sin\theta_w} = \frac{\tan\theta_g}{\tan\theta_w} = \frac{H_R\ b}{3\ a} \tag{3-8}$$

$$\frac{n_w}{n_a} = \frac{\sin\theta_a}{\sin\theta_w} = \frac{\tan\theta_a}{\tan\theta_w} = \frac{H_R\ (a+b)}{a\ (3+H_A)} \tag{3-9}$$

Rearranging **Equation (3-8)** so as to leave length a alone gives:

$$a = \frac{n_g H_R b}{n_w 3} \tag{3-10}$$

And using **Equation (3-10)** to replace a in **Equation (3-9)** leads to**:**

$$\frac{n_w}{n_a} = \frac{\frac{n_g H_R}{n_w 3} + 1}{\frac{n_g}{n_w 3}(3+H_A)} \tag{3-11}$$

Equation (3-11) can be used to estimate the apparent depth if we know the refractive indices of the mediums and real depth. The theoretical apparent depth is found to be approximately 14 mm using the refractive indices given in **Figure 3-39** and the real depth of the sight glass which is 20 mm. This is different from the experimentally determined apparent depth of 16 mm a 2-mm difference between the theoretically and experimentally determined apparent depths is thought to be reasonable and therefore one can safely conclude that light refraction is responsible for the apparent depth difference. The difference can be because of the fact that camera, lights, distance measurements, camera movements and sight glass design were measured, moved and assembled manually which can lead to human errors. Moreover, the

effect of temperature and wavelength of lighting on refraction indices was not taken to account which may introduce extra inaccuracy.

Ross & Nawaz (2003) mentioned that divers can perceive objects as magnified under water but it was considered to be irrelevant for the current study since there is a big difference between the situations. Moreover, Nassar (1994) carried out a study to calculate the apparent horizontal position (which can lead to bigger images) in addition to apparent depth position. It can be clearly seen from their analysis that at very small observation angles the horizontal shift in the apparent position is negligible. Therefore, the magnification effect is not considered in the later stages of the current work.

3.4.4 Determination of depth of field

The concept of depth of field was described previously in **Section 3.4.1** and its determination is important in calculating the accurate value for the sample volume captured (see **Figures 3-27** and **3-28**) and thus the volumetric void fraction of two-phase flow. DOF was determined by the previous researcher as 1.5 mm (Fsadni 2012). However, there the procedure used for this is not explained in sufficient detail, which is problematic since the determination procedure should be conducted in conformity with the image processing technique. Because, the procedure and the settings used for image processing can lead to different results, as this is the step where the differentiation of in and out of focus bubbles occur.

The method used to measure apparent depth (see **Section 3.4.3**) was adapted for use in determining the DOF of the camera and lens setup. Previously, the object was assumed to be the depth of the sight glass, whereas here three different objects were used; the metal ball (with 1 mm diameter) mentioned previously in the software calibration part (**Section 3.4.2.1**), a sand particle (see **Appendix 35** for the actual picture) and an air bubble. The camera and light setup for the horizontal measurements (**Figure 3-28**) was put in place and the objects were placed on and under the upper glass of the sight glass as shown in **Figure 3-41**. The metal ball and sand particle were simply placed on the top of the glass whereas the stagnant bubble just underneath the glass was achieved by shutting down the boiler and the pumps suddenly while there was high number of bubble production.

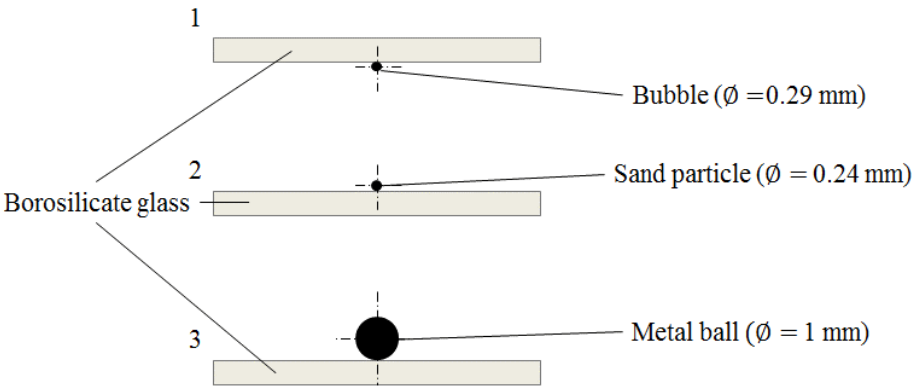

Figure 3-41. Position of the objects used in the determination DOF.

The camera was again placed above the aluminium case (see **Section 3.4.3**) and was moved downwards gradually with the help of the adjustable slider. This time, it was moved 0.3125 mm each time by rotating the Allen key by 90° (see **Appendix 36** for the actual picture) which was attached to the screw that moves the adjustable slider. The distance moved with a full rotation (360°) was decided by measuring the distance moved after 10 full rotations. First, it was estimated that a single rotation (360°) led to 1 mm shift but after some tests, it was observed that the camera actually moves a little bit more than the estimated distance. In order to determine the distance accurately, the screw was fully rotated 10 times and it was observed that the camera moved by 12.5 mm. Thus, it was concluded that a single full rotation (360°) shifted the camera setup 1.25 mm. Therefore, a 90° rotation of the Allen key would shift the camera by 0.3125mm

In the beginning, the object was out of focus but it started to become sharp and clear as the camera changed its position. Later, the image of the object started to get blurry again as the movement of the camera continued and lastly, the image of the object disappeared. An image of each position was captured and put through the image processing procedure determined earlier (see **Section 3.4.2.2**). **Figure 3-42** depicts the original image of the object and the processed image for the three different objects used. In the figure "a" denotes the distance between the objective and aluminium case (as in **Figure 3-28**). The objects with a red circle around them are those that were identified as being in focus.

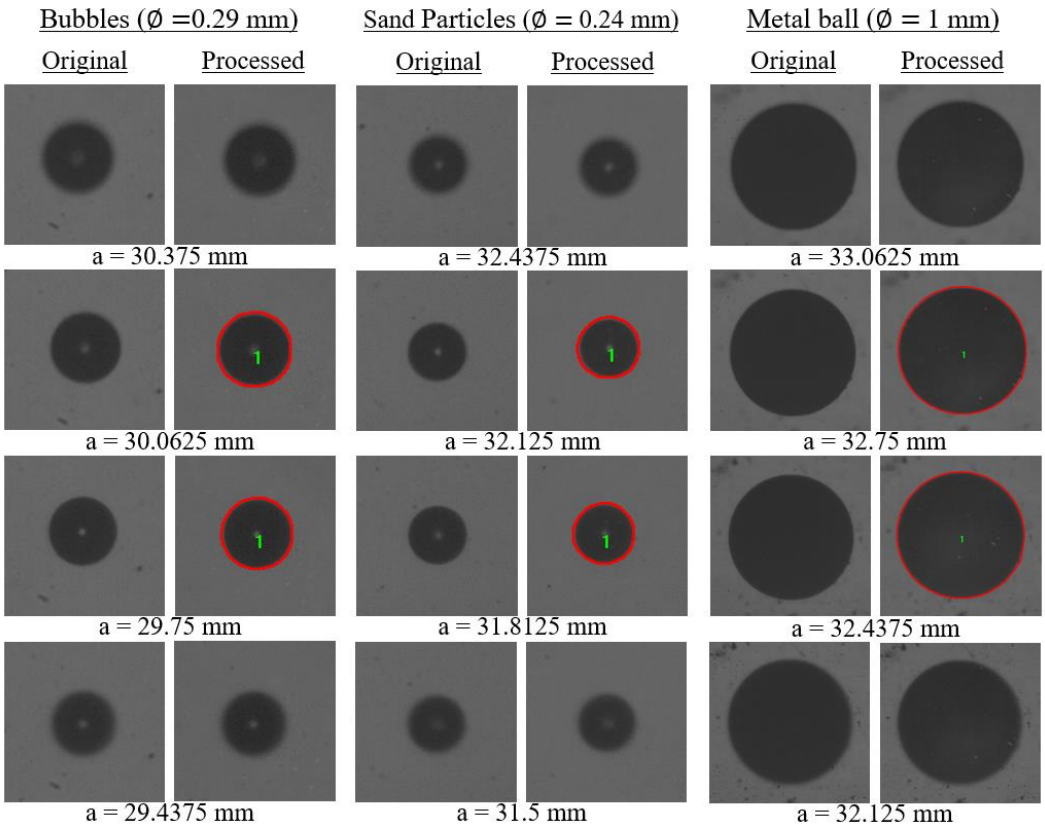

Figure 3-42. Original and processed images of three objects used in DOF determination.

The tests conducted using the three different objects show that the image processing software identifies the object as in focus two times. The schematic diagram showing the possible positions of the focal plane and the object corresponding to the findings obtained from **Figure 3-42** is presented in **Figure 3-43**.

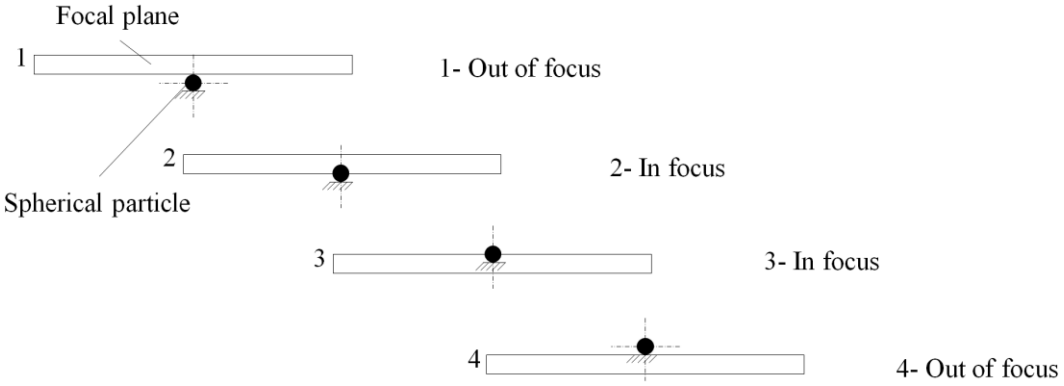

Figure 3-43. Schematic diagram of the focal plane movement through an object.

First, the object is out of focus (position number 1) and next, half the object should be in the focal plane allowing it to be captured as a sharp and clear (positions number 2 and number 3). Lastly, the object is out of the focal plane (position number 4). The detailed diagram representing length analysis achieved by basic geometry is given in **Figure 3-44**.

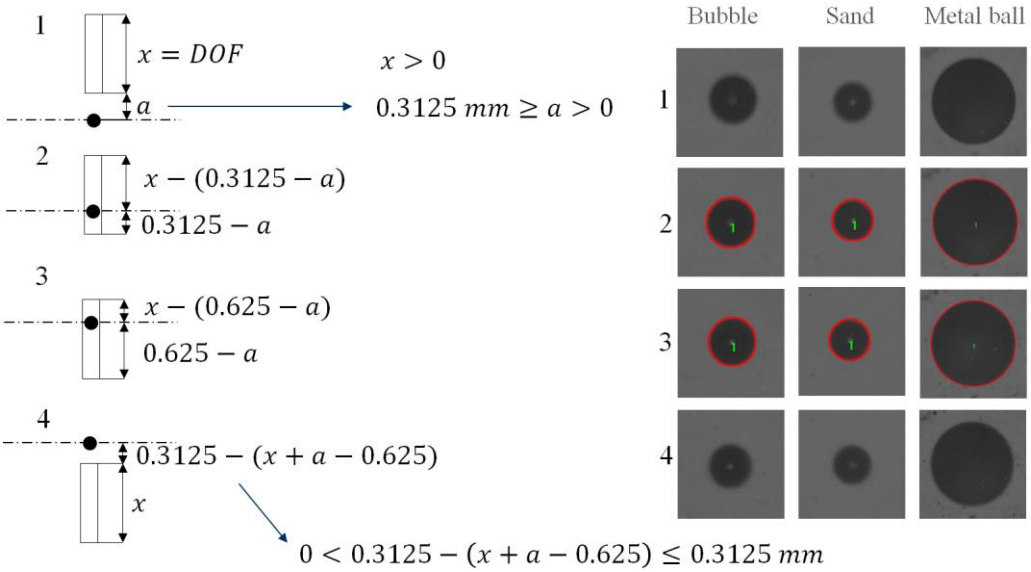

Figure 3-44. Detailed diagram used to determine the DOF.

In **Figure 3-44**, x represents the DOF distance which would be determined at the conclusion of the analysis and a is the unknown vertical distance between the central line of the spherical particle and the bottom line of the focal plane. It is necessary to warn reader here that the distance "a" shown in **Figure 3-44** should not be confused with the distance denoted by "a" in the earlier sections (check **Figures 3-27**, **3-28** and **3-42**). At point 1, the object is out of focus and there must be a distance (a), which is unknown, between the middle point of the object and bottom line of the focal plane. This distance needs to be less than or equal to 0.3125 mm and greater than zero; otherwise the object cannot be in focus at point 2 after the 0.3125 mm shift. Points shown with 2, 3 and 4 symbolize the lengths after each 0.3125 mm step. At point 4, where the object is out of focus again, the length between the upper line of the focal plane and middle of the object should be equal or smaller than 0.3125 mm and bigger than 0 for the same reasons mentioned at point 1.

The following constraints can be summarized from the length analysis explained above:

$$x > 0$$

(3-12)

$$0.3125\ mm \geq a > 0$$

(3-13)

$$0 < 0.3125 - (x + a - 0.625) \leq 0.3125\ mm$$

(3-14)

There is no way to determine the exact value of a in the **Equations (3-13)** and **(3-14)**, hence the possible maximum (0.3125 mm) and minimum (0 mm) values from **Equation (3-13)** are substituted into **Equation (3-14)** leading to the two equations given below:

When $a = 0.3125\ mm$

$$0.625\ mm > x \geq 0.3125\ mm$$

(3-15)

and in the limit as $a \to 0$

$$0.9375\ mm > x \geq 0.625\ mm$$

(3-16)

After combining the **Equations (3-15)** and **(3-16)** by adding them up and dividing by 2, the range for x (DOF) value was defined by the following equation;

$$0.78125\ mm > x \geq 0.46875\ mm$$

(3-17)

Depth of the sample volume (DOF) was chosen as *0.625 mm* which is the point that lies in the middle of the range given in **Equation (3-17)** with an uncertainty of ± 0.15625 mm and used for calculating the volumetric void fraction during the analysis

of experimental data. The uncertainty for the determined DOF is moderately high (% 25) but this does not affect comparative studies within the current study. Because, factors (camera and lens settings, background intensity and image processing routine) that can influence the depth of the sample volume were fixed and never changed throughout the experiments. Uncertainty can be reduced by implementing further improvements to the measurements technique to decrease the minimum distance that the camera can be moved in each step; this can be done through, for example sensitive camera control and more accurate distance measurements.

3.5 Data Processing

The current research investigates the two-phase flow structures observed in the pipework of wet central heating systems. In this respect several parameters were calculated to analyse this phenomenon using the measured data from the experiments, such as temperature, pressure, bubble diameter, etc. This section describes how these calculations were quantified and processed for further analysis.

3.5.1 Saturation ratio

Saturation ratio of the system at the boiler exit was estimated through the use of **Equation (2-4)** which was given earlier in **Section 2.3.1** and details about how to monitor saturation ratio with LabVIEW during the experiments were described in **Section 3.3.1**. The abovementioned two sections contain all of the necessary information relating to the calculation of saturation ratio used in the current study. For convenience, **Equation (3-18)** is provided below. This equation was derived in the abovementioned sections and can be used directly to calculate the saturation ratio.

$$SR = \frac{x_{act}}{x_{sat}} = \frac{\frac{p_{TGM} - p_{v_{TGM}}}{K_{H_{TGM}}}}{\frac{P_1 - p_{v_1}}{K_{H_1}}} \qquad \textbf{(3-18)}$$

Here p_{TGM} is the total gas pressure measurement obtained from the pressure sensor placed on the TGM device, $p_{v_{TGM}}$ is the vapour pressure of water at TGM temperatures, $K_{H_{TGM}}$ is Henry's constant at TGM temperature, P_1 is static pressure measurement gathered from the pressure transducer placed after the forth sight glass on the horizontal pipeline (HSG3), p_{v_1} is the vapour pressure of water at boiler exit temperature and K_{H_1} is Henry's constant at boiler exit temperature. It is worth mentioning here that when using the derived saturation ratio equation one should ensure that convenient units are implemented.

3.5.2 Bubble diameter

Bubble diameters were determined using an image processing software as explained in the **Section 3.4.2**. Image-Pro calculates the average length of the diameters measured at two-degree intervals connecting two outline points and passing through the centroid (MediaCybernetics 2010). **Figure 3-45** was captured to illustrate how the software calculates the mean diameter of the detected objects.

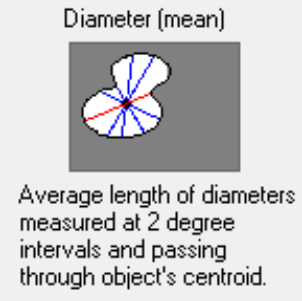

Figure 3-45. Description of mean diameter provided in the software.

Each diameter that is involved in the mean diameter calculation is calculated by the **Equation (3-19)** below:

$$d_b = l_{pix} N_{pix} \tag{3-19}$$

where d_b is the bubble diameter, l_{pix} is the real size of the pixel which is defined during calibration of the software explained in **Section 3.4.2.1** and N_{pix} is the number of pixels.

3.5.3 Average bubble diameter

Bubble diameters gathered from the image processing software for a specific set of data were arithmetically averaged so that the average bubble diameter for each set of images was obtained. **Equation (3-20)** shows the mathematical representation of arithmetic average used in the study;

$$d_{avg} = \frac{1}{n}\sum_{i=1}^{n} d_i \tag{3-20}$$

where n is total number of bubbles identified as in focus within the image set and d_i represents the diameter of the i^{th} bubble.

3.5.4 Sample volume of each frame

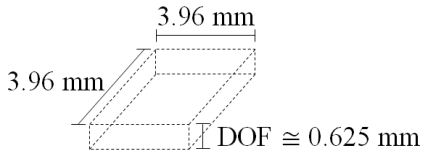

Figure 3-46. Schematic drawing of sample volume.

Figure 3-46 illustrates the schematic drawing of the sample volume for each frame. Its volume was calculated as 9.801 mm^2 by multiplying the image area with the determined DOF (see **Equation (3-21)**). The real size of the image was determined after applying the spatial calibration recorded for the specific camera and lens setup as explained in **Section 3.4.2.1** and DOF determination introduced in **Section 3.4.4**.

$$V_S = w_f l_f DOF \tag{3-21}$$

where w_f is the width of the frame, l_f is the length of the frame and DOF is the depth of field.

3.5.5 Bubble volume inside the focal plane

Calculation of the bubble volume inside the focal plane needs a further assumption because of the possible positions at which the bubble can be located inside the focal plane. **Figure 3-47** depicts some of the different possible bubble locations: failure to take this into account can lead to errors during the calculation of bubble volume in the focal plane.

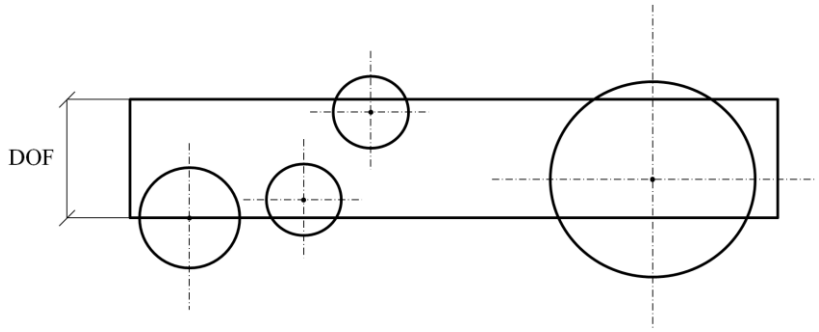

Figure 3-47. Possible bubble positions inside the focal plane.

Four different possible positions of a bubble for four different sizes are shown in the figure above. All of them can be captured and identified as an in focus bubble because in each case at least half of the bubble is in the focal plane and this is enough for it to be captured by the software as an in focus bubble (see **Sections 3.4**). However, it can be clearly seen that none of the four examples are totally inside the focal plane. Moreover, there is no way of estimating the exact vertical position of a bubble captured as in focus with the equipment used in the current study. Therefore, the bubbles are treated as if in the middle of the DOF as presented in **Figure 3-48**.

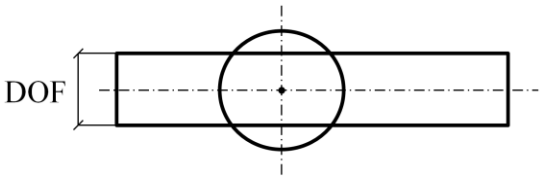

Figure 3-48. Assuming that centre of bubbles in focus is located in the middle DOF.

If the bubble diameter is equal or smaller than the DOF, the volume of the bubble inside the focal plane can simply be calculated by **Equation (3-22)** and assuming that the bubble is spherical.

$$V_b = \frac{\pi {d_b}^3}{6}$$

(3-22)

where d_b is the bubble diameter. So the bubble volume calculation is straightforward when its diameter is smaller than the DOF. However, if the bubble diameter is bigger than determined DOF, then **Equation (3-22)** needs to be corrected in order to subtract the sections that lie outside the focal plane. Kern & Bland (1938) provided a way of calculating the portion of a sphere cut off by two parallel planes. **Figure 3-49** shows a simplified diagram of a section of a sphere.

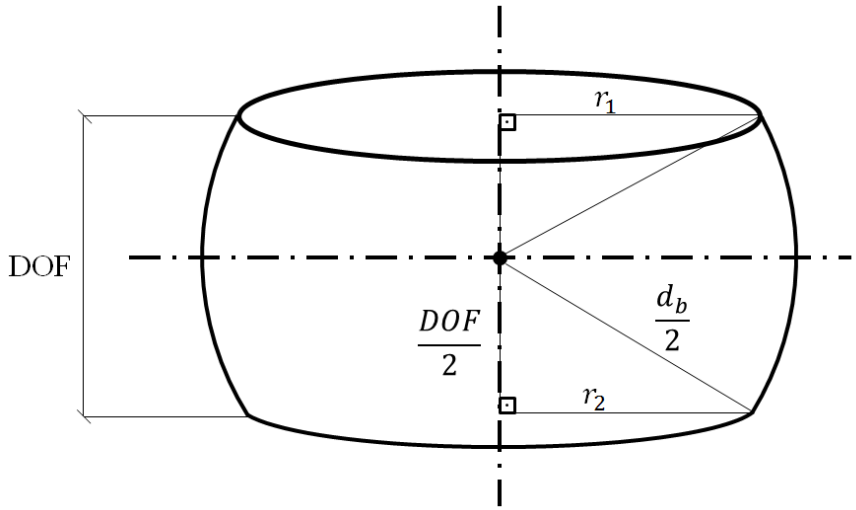

Figure 3-49. Schematic drawing for the bubble volume correction.

In this diagram DOF is the distance between the top and the bottom line of the sphere section that is inside the focal plane, and r_1 and r_2 represent the radii of the circles at the top and bottom of the sphere section, respectively. **Equation (3-23)** can be used to calculate the volume of the sphere part in **Figure 3-49** (Kern & Bland 1938);

$$V_b = \frac{\pi DOF}{6}(3{r_1}^2 + 3{r_2}^2 + DOF^2)$$

(3-23)

In order to calculate the correct bubble volume inside the focal plane r_1 and r_2 have to be calculated using the values known. **Equation (3-24)** gives the radius of the

bottom circle in terms of the known dimensions (d_b and DOF). It is obtained by applying Pythagoras' theorem to the right angled triangle in the lower half of the sphere part given in **Figure 3-49**.

$$r_2 = \sqrt{\left(\frac{d_b}{2}\right)^2 - \left(\frac{DOF}{2}\right)^2}$$

(3-24)

In our case r_1 is equal to r_2 because of the assumption that the bubble in the focal plane is in the middle point of DOF. Therefore, by substituting **Equation (3-24)** into **Equation (3-23), Equation (3-25)** below can be obtained for calculating the volume of a bubble lying inside the focal plane when its diameter is larger than the determined DOF.

$$V_b = \left(\frac{\pi}{6}\right) \times \left(6\left(\frac{{d_b}^2}{4} - \frac{DOF^2}{4}\right) + DOF^2\right) \times DOF$$

(3-25)

3.5.6 Volumetric void fraction

The volumetric void fraction is a common parameter used in two-phase flow studies. It is defined as the ratio of volume of secondary phase (V_b), which is the bubble in our case, to volume of sample analysed (V_s) as given in **Equation (3-26)**:

$$\varepsilon_v = \frac{V_b}{V_s}$$

(3-26)

The cumulative void fraction for the set of images obtained from a particular position can be calculated by the ratio of the sum of the bubble volumes determined to the total sample volume analysed as in **Equation (3-27)**):

$$\varepsilon_{v_{cum}} = \frac{\sum_{i=1}^{n} V_{b_i}}{\sum_{i=1}^{m} V_{s_i}}$$

(3-27)

where n is the total number of bubbles and m is the total number of images used in each set of images.

3.5.7 Bubble count per frame

The average bubble number counted per frame is calculated by **Equation (3-28)**:

$$N_{bpf} = \frac{n}{m}$$

(3-28)

where n is the total number of bubbles and m is the total number images used in each set of images.

3.5.8 Bubble velocity

The velocity of a bubble travelling along the frame was obtained using a high shutter speed during filming of the flow. The shutter speed was increased to 2100 fps so that movement of the bubble between each frame can be observed. **Figure 3-50** illustrates a typical sequence of images showing a single bubble moving across the frame.

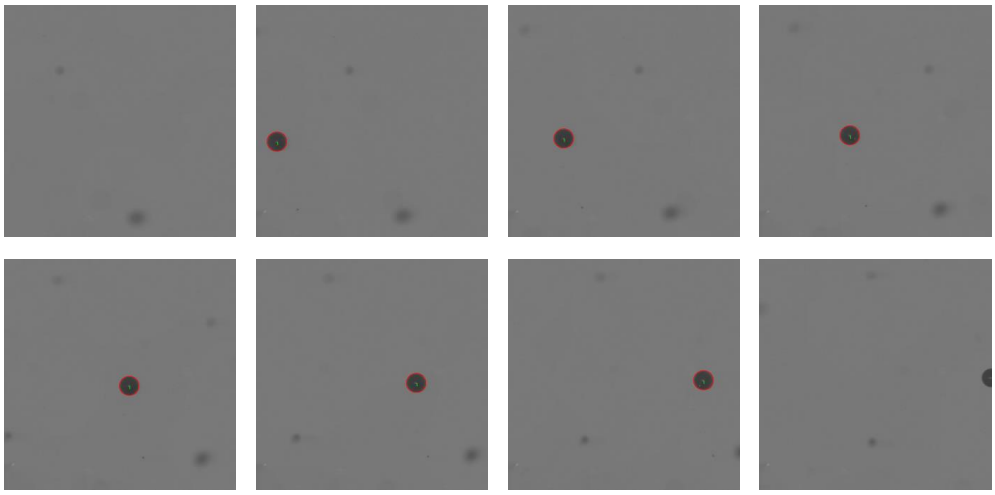

Figure 3-50. Typical sequence of images captured at 2100 fps and used to calculate bubble velocity.

Coordinates of the centroid of the bubble can be gathered from the image processing software; hence the distance travelled between each frame by the bubble can be calculated. Furthermore, the time difference between each frame is known ($\frac{1}{2100}$ seconds) and if we divide the distance travelled by the bubble in each step to the time difference between each frame, it gives the velocity of the bubble. **Equation (3-29)** defines the mathematical form of the bubble velocity calculated for the i^{th} step:

$$u_{b_i} = \frac{l_{b_i}}{t_s} \tag{3-29}$$

where l_{b_i} is the distance travelled by the bubble between each frame at the i^{th} step and t_s is the time between each frame. Bubble velocities across the pipe section at each frame interval were calculated with **Equation (3-29)** and then arithmetically averaged to get an average bubble velocity representing across the focal plane position as in **Equation (3-30):**

$$u_{b_{avg}} = \frac{\sum_{i=1}^{p-1} v_{b_i}}{(p-1)} \tag{3-30}$$

where p is the number frames in which the bubble is identified as in focus.

3.6 Uncertainty Analysis

Experimental results presented without an uncertainty analysis are not acceptable nowadays. Such an analysis supplies one with a reliable way of assessing the importance and repeatability of the data (Moffat 1988). The aim of the current study is to investigate the two-phase flow phenomenon in the pipeline of wet central heating systems and therefore different parameters were calculated from the experimental measurements presented. It is impossible to obtain the real value of any measurement thus any measured value would involve some uncertainty. These uncertainties lead to further errors in calculated parameters. This section will discuss

the uncertainty analysis conducted in this study to find uncertainties involved in those experimental parameters.

Imagine a calculated parameter (y) which depends on n different measurements ($X_1, X_2, X_3 \ldots . X_n$). This relationship can be expressed with the following **Equation (3-31)**:

$$y = f(X_1, X_2, \ldots X_n) \tag{3-31}$$

Total experimental uncertainty consists of two types of errors which are systematic and random errors and it can be calculated by adding these up. Systematic errors are fixed, repeatable and mostly arise from the instrumentation. These errors can be decreased by calibration. On the other hand, random errors are unknown entities which can be caused by anything, including for instance environmental conditions, and can be reduced by increasing the amount of data gathered. Coleman & Steele (1999) proposed the following **Equation (3-33)** for finding the absolute uncertainty of a calculated parameter shown in **Equation (3-31)**.

$$U_{abs} = \sqrt{\left(\frac{\partial y}{\partial X_1}\right)^2 \left(U_{X_1}\right)^2 + \left(\frac{\partial y}{\partial X_2}\right)^2 \left(U_{X_2}\right)^2 + \cdots + \left(\frac{\partial y}{\partial X_n}\right)^2 \left(U_{X_n}\right)^2} \tag{3-32}$$

In **Equation (3-32)**, U_{abs} is the absolute uncertainty of y value, $\frac{\partial y}{\partial X_1}$ is the derivative of y with respect to X_1 and U_{X_i} is the absolute uncertainty of measurement X_i. By dividing both sides of **Equation (3-32)** with y, relative uncertainty (U_{rel}) of calculated parameter in terms of % can be expressed with the following **Equation (3-33)**:

$$U_{rel} = \sqrt{\left(\frac{X_1}{y}\frac{\partial y}{\partial X_1}\right)^2 \left(\frac{U_{X_1}}{X_1}\right)^2 + \left(\frac{X_2}{y}\frac{\partial y}{\partial X_2}\right)^2 \left(\frac{U_{X_2}}{X_2}\right)^2 + \cdots + \left(\frac{X_n}{y}\frac{\partial y}{\partial X_n}\right)^2 \left(\frac{U_{X_n}}{X_n}\right)^2} \tag{3-33}$$

Experimentally measured relative uncertainties which come from the instruments used are listed in **Table 3-3**. Relative uncertainty of measurements were determined through the calibration conducted in the laboratory as explained in **Section 3.3.2** and they represent the percentage error that occurs at the largest difference between the line of best fit and measured condition with a pre-calibrated measurement device.

Relative uncertainty of calculated parameters are discussed in detail and calculated by applying **Equations (3-32)** and **(3-33)** as proposed by Coleman & Steele (1999) in conjunction with the information listed in **Table 3-3**. Additional information that needs to be used in the calculation will be provided within the relevant section.

Table 3-3. Uncertainty values of measured experimental conditions.

Measured parameter	Instrument	Uncertainty (%)
Flow rate	Euromag Electromagnetic Flowmeters 500 series	± 0.81
P_1- Static pressure	DRUCK PTX-7517	± 0.44
P_2- Static pressure		± 0.53
P_3- Static pressure		± 0.51
P_{TGM}- Gas partial pressure	Keller PAA-35S	± 0.27
T_1- Fluid temperature	K-type thermocouples	± 0.37
T_2- Fluid temperature		± 0.31
T_3- Fluid temperature		± 0.34
T_4- Fluid temperature		± 0.34
T_5- Fluid temperature		± 0.25
T_6- Fluid temperature		± 0.19
T_{TGM}- Fluid temperature		± 0.20

3.6.1 Saturation ratio

Saturation ratio was calculated using **Equation (3-34)** below:

$$SR = \frac{x_{act}}{x_{sat}} = \frac{\frac{p_{TGM} - p_{v_{TGM}}}{K_{H_{TGM}}}}{\frac{P_1 - p_{v_1}}{K_{H_1}}} \quad \textbf{(3-34)}$$

To find the relative uncertainty that occurs in the saturation ratio calculation, it would be simpler to investigate (x_{act}) and x_{sat} separately. The first step would be to find the relative uncertainty of actual dissolved gas amount (x_{act}) in the liquid which can be express as **Equation (3-35)** below:

$$x_{act} = \frac{p_{TGM} - p_{v_{TGM}}}{K_{H_{TGM}}} = {K_{H_{TGM}}}^{-1}\left(p_{TGM} - P_{v_{TGM}}\right) = {K_{H_{TGM}}}^{-1}p_{TGM} - {K_{H_{TGM}}}^{-1}P_{v_{TGM}} \quad \textbf{(3-35)}$$

Using **Equation (3-32)**, absolute uncertainty for x_{act} can be written as:

$$U_{abs_{x_{act}}} = \sqrt{\left(\frac{\partial x_{act}}{\partial p_{TGM}}\right)^2 \left(U_{p_{TGM}}\right)^2 + \left(\frac{\partial x_{act}}{\partial P_{v_{TGM}}}\right)^2 \left(U_{P_{v_{TGM}}}\right)^2 + \left(\frac{\partial x_{act}}{\partial K_{H_{TGM}}}\right)^2 \left(U_{K_{H_{TGM}}}\right)^2} \quad \textbf{(3-36)}$$

Inserting the related derivatives of x_{act} into **Equation (3-36)** we obtain the formula given below:

$$U_{abs_{x_{act}}} = \sqrt{\left({K_{H_{TGM}}}^{-1}\right)^2\left(U_{p_{TGM}}\right)^2 + \left(-{K_{H_{TGM}}}^{-1}\right)^2 \left(U_{P_{v_{TGM}}}\right)^2 + \left(P_{v_{TGM}} - p_{TGM}\right)^2 \left(U_{K_{H_{TGM}}}\right)^2} \quad \textbf{(3-37)}$$

Dividing both sides of **Equation (3-37)** by x_{act} gives **Equation (3-38)** which enables one to calculate the relative uncertainty of calculated x_{act}.

$$U_{rel_{x_{act}}} = \sqrt{\left(\frac{U_{p_{TGM}}}{P_{v_{TGM}} - p_{TGM}}\right)^2 + \left(\frac{U_{P_{v_{TGM}}}}{P_{v_{TGM}} - p_{TGM}}\right)^2 + \left(\frac{U_{K_{H_{TGM}}}}{K_{H_{TGM}}}\right)^2} \quad \textbf{(3-38)}$$

In order to be able to use **Equation (3-38)**, it is necessary to determine the absolute uncertainties of gas partial pressures at TGM (p_{TGM}) and vapour pressure ($P_{v_{TGM}}$)

estimated by the temperature measurement at TGM (T_{TGM}). In addition, determination of relative uncertainty of Henry's constant estimated by measured temperature at TGM is also needed. The relative uncertainty of p_{TGM} is given in the **Table 3-3**; however, the absolute uncertainty of p_{TGM} is needed in the **Equation (3-38)**. Maximum deviation of p_{TGM} and T_{TGM} from the calibration best fit lines occur at 1.75 bar with ± 0.004725 bar and at 44.88°C with ± 0.088 °C absolute uncertainty, respectively.

Determination of uncertainties in vapour pressure and Henry's constant estimation was calculated in a similar way because both parameters were estimated through the correlations that depend on the temperature measurement. There are two uncertainties that need to be considered here. One is the error influenced by the temperature measurement at TGM and the other is the uncertainty that comes from each correlation used. For simplicity, uncertainties that arise from temperature measurement is calculated by the propagation rule mentioned in work of Bevington & Robinson (2003) for the cases where the calculated parameter depends on the sum of the measured variable that is raised to the power. The correlations used to estimate Henry's constant and vapour pressure are given in the **Appendices 16** and **17**. Both correlations are 6th order polynomials hence there are six temperature values raised to the power.

Relative uncertainty of Henry's constant caused by the temperature measurement was calculated as ± 2.06 % by **Equation (3-39)** after inserting temperature and absolute uncertainty given previously for the maximum deviating point (44.88°C ± 0.088 °C).

$$\frac{U_{K_H}}{K_H} = \frac{6U_{T_{TGM}} + 5U_{T_{TGM}} + 4U_{T_{TGM}} + 3U_{T_{TGM}} + 2U_{T_{TGM}} + U_{T_{TGM}}}{2T_{TGM}} \quad \textbf{(3-39)}$$

Similarly, relative uncertainty of vapour pressure estimation caused by the temperature measurement was calculated as ± 1.03 % by **Equation (3-40)**:

$$\frac{U_{P_v}}{P_v} = \frac{6U_{T_{TGM}} + 5U_{T_{TGM}} + 4U_{T_{TGM}} + 3U_{T_{TGM}} + 2U_{T_{TGM}} + U_{T_{TGM}}}{4T_{TGM}} \quad \textbf{(3-40)}$$

The difference between the denominators of **Equations (3-39)** and **(3-40)** originates from the positive or negative signs in front of each of the temperature values that is raised to the power (see **Appendices 16** and **17**).

The next step is to add on the uncertainties caused by the correlation itself. **Table 3-4** illustrates the absolute and relative uncertainties of the largest difference between the fitted curve (correlations used) and data.

Table 3-4. Absolute and relative uncertainties of Henry's constant and vapour pressure correlations.

Used correlation	Absolute uncertainty	Relative uncertainty
Henry's constant	9.24e-4 atm ± 0.0308e-4 atm	± 0.33%
Vapour pressure	0.009909 bar ± 4.39788e-5 bar	± 0.44 %

When we combine both uncertainties (from temperature measurement and correlation itself) that have been derived for Henry's constant and vapour pressure parameters, absolute and relative uncertainties that can be used directly in **Equation (3-38)** can be calculated. **Table 3-5** shows the combined absolute and relative uncertainties of Henry's constant and vapour pressure values that can be used in **Equation (3-38)**.

Table 3-5. Combined absolute and relative uncertainties of Henry's constant and vapour pressure.

Calculated parameter	Absolute uncertainty	Relative uncertainty
Henry's constant ($K_{H_{TGM}}$)	9.24e-4 atm ± 0.221762e-4 atm	± 2.39 %
Vapour pressure ($P_{v_{TGM}}$)	0.009909 bar ± 0.146e-3 bar	± 1.47 %

After substituting the values discussed above into the **Equation (3-38)**, relative uncertainty of actual dissolved gas amount in the liquid is calculated as ± 2.41 % as shown in the calculation below:

$$U_{rel_{x_{act}}} = \sqrt{\left(\frac{0.004725}{0.009909 - 1.75}\right)^2 + \left(\frac{0.146e-3}{0.009909 - 1.75}\right)^2 + (0.0239)^2}$$

$$U_{rel_{x_{act}}} = 2.41\ \%$$

Similarly relative uncertainty of dissolved gas amount at saturated solution can be calculated with **Equation (3-41)** below that is obtained after applying **Equation (3-33)**.

$$U_{rel_{x_{sat}}} = \sqrt{\left(\frac{U_{p_1}}{P_{v_1} - p_1}\right)^2 + \left(\frac{U_{P_{v_1}}}{P_{v_1} - p_1}\right)^2 + \left(\frac{U_{K_1}}{K_{H_1}}\right)^2} \quad \textbf{(3-41)}$$

Regarding the uncertainty calculations, the only difference between **Equations (3-38)** and **(3-41)** is that the measured gas partial pressure (p_{TGM}) is replaced by the static pressure measurement of the liquid at pressure sensor 1 (p_1). The static pressure measurements show its maximum deviation from the best fit calibration line at 1.93 bars with ± 0.008492. Rest of the values in the **Equation (3-41)** are exactly same as the ones calculated previously. Hence the following calculation of the relative uncertainty of dissolved gas amount at saturated condition gives ± 2.43 %:

$$U_{rel_{x_{sat}}} = \sqrt{\left(\frac{0.008492}{0.009909 - 1.93}\right)^2 + \left(\frac{0.146e-3}{0.009909 - 1.93}\right)^2 + (0.0239)^2}$$

$$U_{rel_{x_{act}}} = 2.43\ \%$$

Finally, the formula given in **Equation (3-32)** is applied to the saturation ratio calculation given in **Equation (3-34)** and leading to **Equation (3-42)** below:

$$U_{abs_{SR}} = \sqrt{\left(\frac{\partial SR}{\partial x_{act}}\right)^2 \left(U_{x_{act}}\right)^2 + \left(\frac{\partial SR}{\partial x_{sat}}\right)^2 \left(U_{x_{sat}}\right)^2} \quad \textbf{(3-42)}$$

After substituting relevant derivatives into the above, **Equation (3-43)** is obtained:

$$U_{abs_{SR}} = \sqrt{(x_{sat}{}^{-1})^2 \left(U_{x_{act}}\right)^2 + (-x_{act}x_{sat}{}^{-2})^2 \left(U_{x_{sat}}\right)^2} \quad \textbf{(3-43)}$$

Dividing both sides with SR gives the relative uncertainty of saturation ratio as in **Equation (3-44)**:

$$U_{rel_{SR}} = \sqrt{\left(\frac{U_{x_{act}}}{x_{act}}\right)^2 + \left(\frac{U_{x_{sat}}}{x_{act}}\right)^2} \quad \textbf{(3-44)}$$

Inserting into **Equation (3-44)** the relative uncertainties calculated for the dissolved gas amount for the actual and saturated levels, the relative uncertainty of saturation ratio is calculated as ± 3.42 % as shown below.

$$U_{rel_{SR}} = \sqrt{(2.41)^2 + (2.43)^2} = 3.42\%$$

Table 3-6 displays the range and relative uncertainty of saturation ratio calculation used in the current study.

Table 3-6. Range and relative uncertainty of saturation ratio.

Calculated parameter	Parameter range	Relative uncertainty
Saturation ratio	0.37-1.2	± 3.42 %

3.6.2 Bubble diameter

Bubble diameter measurements were carried out through image processing as explained in **Section 3.4.2** and the uncertainty of the bubble diameter measurement originates from the calibration stage of the image processing software. The procedure applied to calibrate the software which was conducted with a metal bearing ball is explained in **Section 3.4.2.1**. **Figure 3-51** is the schematic diagram of the diameter spherical particle captured by the image processing soft software.

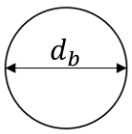

Figure 3-51. Schematic diagram of bubble diameter.

The image processing software calculates the diameter values using the following equation:

$$d_b = l_{pix} N_{pix} \tag{3-45}$$

where l_{pix} is the real length of each pixel after calibration and N_{pix} is the number of pixels along the diameter of the particle in **Figure 3-51**.

Error probation rule given in **Equation (3-32)** is applied to **Equation (3-45)** and **Equation (3-46)** is obtained for the absolute uncertainty of bubble diameter:

$$U_{abs_{d_b}} = \sqrt{\left(\frac{\partial d_b}{\partial l_{pix}}\right)^2 \left(U_{l_{pix}}\right)^2 + \left(\frac{\partial d_b}{\partial N_{pix}}\right)^2 \left(U_{N_{pix}}\right)^2} \tag{3-46}$$

After inserting respective derivatives of d_b into **Equation (3-46)**, the following equation is obtained:

$$U_{abs_{d_b}} = \sqrt{\left(N_{pix}\right)^2 \left(U_{l_{pix}}\right)^2 + \left(l_{pix}\right)^2 \left(U_{N_{pix}}\right)^2} \tag{3-47}$$

Dividing both sides of **Equation (3-47)** with d_b gives **Equation (3-48)** which can be used to calculate the relative uncertainty of bubble diameter.

$$U_{rel_{d_b}} = \sqrt{\left(\frac{U_{l_{pix}}}{l_{pix}}\right)^2 + \left(\frac{U_{N_{pix}}}{N_{pix}}\right)^2} \quad \textbf{(3-48)}$$

It can be noted from the **Equation (3-48)** that there are two types of uncertainties in the total uncertainty of bubble diameter. One of these is the uncertainty of the real length of each pixel after calibration which simply corresponds to uncertainty in the size of the metal bearing ball. Its manufacturer provides its diameter as 1 mm with ± 0.00254 mm absolute uncertainty. This in turn leads to ± 0.254% relative uncertainty. The latter is the uncertainty that arises during the definition of calibration information for the image processing software. The diameter of the bearing ball is defined manually during software calibration and involves human error. In order to reduce this error, the calibration procedure was repeated 10 times and pixel number along diameter of the bearing ball noted. Relative uncertainty in the number of pixels along the diameter of bearing ball used during calibration is calculated as ± 0.53 %.

After substituting the relative uncertainty in the real size of each pixel and number of pixels counted along the bearing ball in to **Equation (3-48)**, the relative uncertainty in bubble diameter is calculated as ± 0.59 % as shown below:

$$U_{rel_{d_b}} = \sqrt{(0.254)^2 + (0.53)^2} = 0.59\ \%$$

Table 3-7 illustrates the range and relative uncertainty of bubble diameter calculated in the present work.

Table 3-7. Range and relative uncertainty of bubble diameter.

Calculated parameter	Parameter range	Relative uncertainty
Bubble diameter	0.05 – 3.9 mm	± 0.59 %

3.6.3 Sample volume of each frame

Sample volume of each frame was calculated by the equation given below:

$$V_S = w_f l_f DOF \tag{3-49}$$

where w_f is the width of the frame, l_f is the length of the frame and DOF is the depth of field. After applying the same error propagation as implemented in the previous sections, **Equation (3-50)** is arrived at, representing the relative uncertainty of sample volume calculation.

$$U_{rel_{V_S}} = \sqrt{\left(\frac{U_{w_f}}{w_f}\right)^2 + \left(\frac{U_{l_f}}{l_f}\right)^2 + \left(\frac{U_{DOF}}{DOF}\right)^2} \tag{3-50}$$

The relative uncertainty of width and length of the sample are the same and arise from the calibration procedure as is the case with the uncertainties derived for bubble diameter calculation. Therefore, ± 0.59 % relative uncertainty calculated for bubble diameter can be used for the relative uncertainties of frame width (w_f) and length (l_f) in the **Equation (3-50)**. Furthermore, relative uncertainty in DOF determination was found as ± 25% in **Section 3.4.4**. After replacing the determined relative uncertainties in **Equation (3-50)**, the relative uncertainty in sample volume is found to be ± 25.01 % from the calculation presented below.

$$U_{rel_{V_S}} = \sqrt{(0.59)^2 + (0.59)^2 + (25)^2} = 25.01\ \%$$

Calculated sample volume and its relative uncertainty are presented in **Table 3-8**.

Table 3-8. Volume and relative uncertainty of sample volume.

Calculated parameter	Volume	Relative uncertainty
Sample volume	9.7950609 mm^3	± 25.01 %

3.6.4 Bubble volume inside the focal plane

As discussed in **Section 3.5.5**, there are two ways of calculating the bubble volume inside the focal plane which depends on bubble diameter. However, the bubble volume inside focal plane calculated for the bubbles which have bigger diameter than DOF is neglected in uncertainty analysis to simplify the process. Furthermore, according to the researcher's experience, it is acceptable to neglect the effect of big bubble volume calculation in uncertainty analysis since a significant majority of the bubbles that were captured had smaller diameter than the determined DOF.

Bubble volume is calculated by **Equation (3-51)** given below:

$$V_b = \frac{\pi {d_b}^3}{6} \tag{3-51}$$

Applying the error propagation given in **Equations (3-31)** to **(3-51)** leads to the following formula for the absolute uncertainty of bubble volume:

$$U_{abs_{V_b}} = \sqrt{\left(\frac{\partial V_b}{\partial d_b}\right)^2 \left(U_{x_{d_b}}\right)^2} \tag{3-52}$$

After this **Equation (3-53)** is obtained by substituting the necessary derivatives of V_b into **Equation (3-52)**:

$$U_{abs_{V_b}} = \sqrt{\left(\frac{\pi {d_b}^2}{2}\right)^2 \left(U_{x_{d_b}}\right)^2} \tag{3-53}$$

The relative uncertainty of bubble volume calculation can then be calculated as in **Equation (3-54)** after dividing both sides of **Equation (3-53)** by V_b.

$$U_{rel_{V_b}} = 3\left(\frac{U_{x_{d_b}}}{d_b}\right) \tag{3-54}$$

Calculation of the relative uncertainty of bubble volume gives ± 1.77 % as shown below:

$$U_{rel_{V_b}} = 3(0.59) = 1.77\ \%$$

The parameter range and relative uncertainty in bubble volume calculation is presented in **Table 3-9**.

Table 3-9. Range and relative uncertainty of bubble volume.

Calculated parameter	Parameter range	Relative uncertainty
Bubble volume	6.54e-5 – 0.1278 mm^3	± 1.77 %

3.6.5 Volumetric void fraction

Volumetric void fraction is simply the ratio of bubble volume to a sample volume given in **Equation (3-26)** and after applying the error propagation procedure explained previously, the following equation (**Equation (3-55))** is obtained for calculating the relative uncertainty in volumetric void fraction:

$$U_{rel_{\varepsilon_v}} = \sqrt{\left(\frac{U_{V_b}}{V_b}\right)^2 + \left(\frac{U_{V_s}}{V_s}\right)^2} \quad \textbf{(3-55)}$$

Relative uncertainty in volumetric void fraction is calculated to be ± 25.07 % after inserting the relative uncertainty values for bubble and sample volume given in **Table 3-8** and **Table 3-9** into **Equation (3-55)** as shown in the calculation below.

$$U_{rel_{\varepsilon_v}} = \sqrt{(1.77)^2 + (25.01)^2} = 25.07\ \%$$

Table 3-10 illustrates the range and relative uncertainty of volumetric void fraction calculations used in the research.

Table 3-10. Range and relative uncertainty of volumetric void fraction.

Calculated parameter	Parameter range	Relative uncertainty
Volumetric void fraction	6.6768e-6 – 0.013 mm^3	± 25.07 %

3.6.6 Bubble velocity

Bubble velocity is calculated through **Equation (3-29)** which is the ratio of distance between each frame to time between subsequent frames (see **Section 3.5.8**). Thus, two factors can affect the uncertainty of calculated bubble velocity. The first is the uncertainty of distance measurement and the second the time measurement. Uncertainty in time measurement is assumed to be negligible since it is controlled by the camera and there is no detailed information provided by its manufacturer. The only factor that is considered in bubble velocity uncertainty is the error in distance measurement. Distance measurements were conducted by the image processing software thus here image processing software is the source of the error. Furthermore, an uncertainty in the bubble velocity calculation arises from software calibration as explained for error in bubble diameter (see **Section 3.6.2**). Therefore, relative uncertainty for bubble velocity is assumed to be equal to the uncertainty calculated for the bubble diameter. **Table 3-11** shows the range and relative uncertainty of calculated bubble velocities in the present work.

Table 3-11. Range and relative uncertainty of bubble velocity.

Calculated parameter	Parameter range	Relative uncertainty
Bubble velocity	0.1 – 1.5 m/s	± 0.59 %

3.7 Frame Independence Test

The number of frames to be captured for each focal plane position was decided through the frame independence test because the parameters of interest fluctuate as the number of processed image increases. The idea of frame independence test arises

from the continuum concept explained by Crowe et al. (2012) with a deductive example for density of gas molecules in a sample. There they considered the sample of molecules and discussed the variation of density of the molecules as the volume of the sample increases from being infinitesimal to a volume at which the fluctuations become negligible, as shown in **Figure 3-52**.

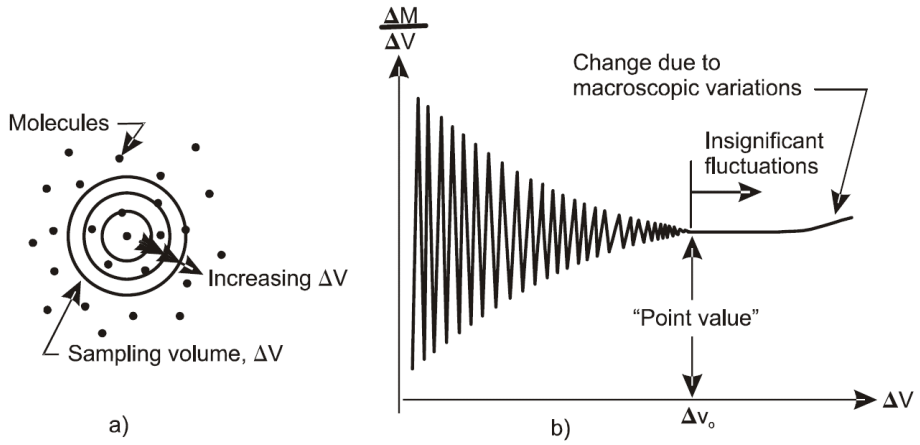

Figure 3-52. Fluctuation of density of mixture with the size of sample volume (Crowe et al. 2012).

In this figure ΔV is the sample volume and ΔM is the mass of the molecules. The diagram on the left represents the number of molecules in an increasing volume and the plot on the right shows how the mass of the molecules per volume changes as the sample volume increases. The main aim was to find the smallest volume of sample at which the fluctuation of the quantity of interest when the sample volume increased is within acceptable levels. Moreover, accuracy of the results obtained from particle size analysis increases as the number of data grow (Rawle 2014). On the other hand, the time it takes to conduct the experiments, image analysis and post processing of the data also grow as the number of data increases. Therefore, the frame independence test was adapted to the current study in order to optimise the time and accuracy of experiments by investigating the change in the parameters as the analysed image number increases.

In order to conduct necessary test, the system conditions were regulated to a certain point where bubble number captured in the focal plane would be moderately low. In order to conduct the necessary test, system conditions were regulated to a certain point where the number of bubbles captured in the focal plane would be moderately

low. This was achieved by increasing the flow rate to 1300 LPH and keeping the saturation ratio at 0.75 (see **Section 3.8** for the details of how to control system conditions). The captured bubble count per frame decreases as the flow rate increases and bubble production decreases as the saturation ratio of the liquid goes down (Fsadni 2012). Boiler exit temperature and pressure were kept at 80 °C and 2.7 bars, respectively. Moreover, boiler heating load was set as 10kW from the control panel (see **Figure 3-2**). After stabilisation of system conditions, bubble measurement equipment was set up as shown in **Figure 3-27** for vertical measurements at first sight glass (see VSG1 in **Figure 3-23**), and first focal plane (1 mm distance to the glass surface) was used throughout the test. The camera and lens setup determined for the present study (see **Table 3-2**) was used and 3000 frames were recorded within 60 seconds. The images were then analysed by the procedure explained in **Section 3.4.2** and data was processed as discussed in **Section 3.5**.

Figures 3-53 to **3-57** represent the results obtained from the test. The first two figures show how the calculated values of average diameter and void fraction change as the number of analysed frames increases. Both figures point to a similar pattern in which the diameter and void fraction values fluctuate in the beginning and fairly flatten later. This pattern gives us the confidence that the values would stabilise after a certain point and the change would be acceptable. The next three figures were plotted to investigate further and decide on the optimum number of frames. They display the percentage change of the average diameter and volumetric void fraction values as the number of analysed images grows. The percentage change in average diameter remains under 5% after 700 frames (see **Figure 3-55**). However, the percentage change in volumetric void fraction drops to lower than 5% after 2000 frames (see **Figures 3-56** and **3-57**).

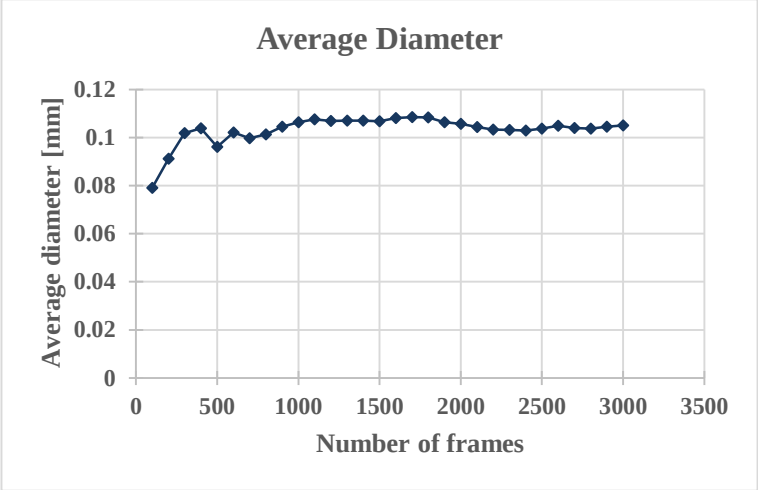

Figure 3-53. Average diameter value change as the number of frames increases.

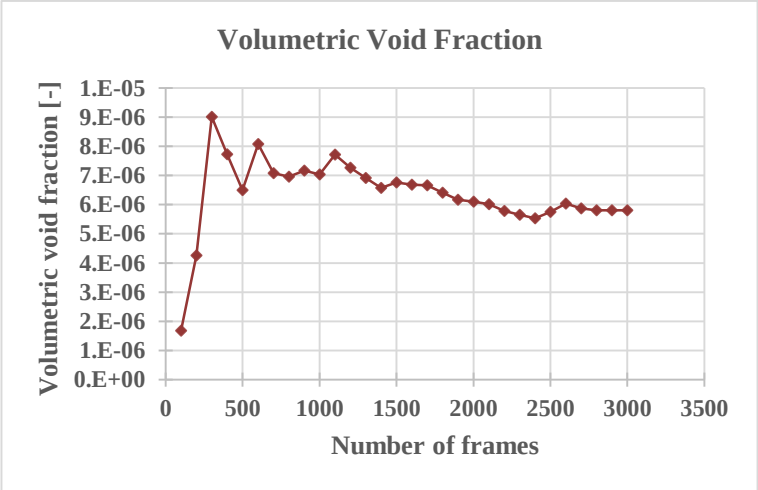

Figure 3-54. Volumetric void fraction change as the number of frames increases.

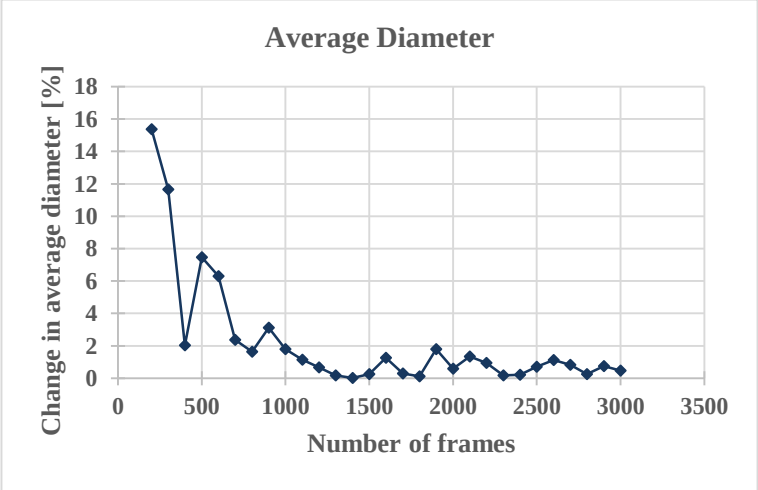

Figure 3-55. Percentage change in average diameter as the number of frames increases.

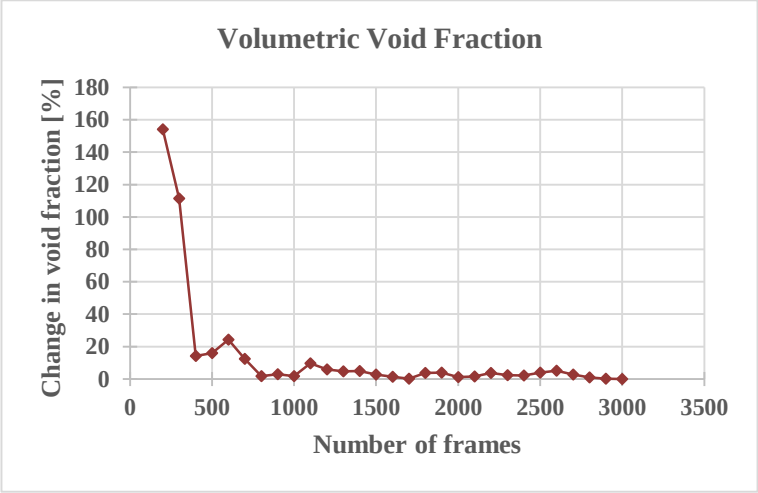

Figure 3-56. Percentage change in volumetric void fraction as the number of frames increases.

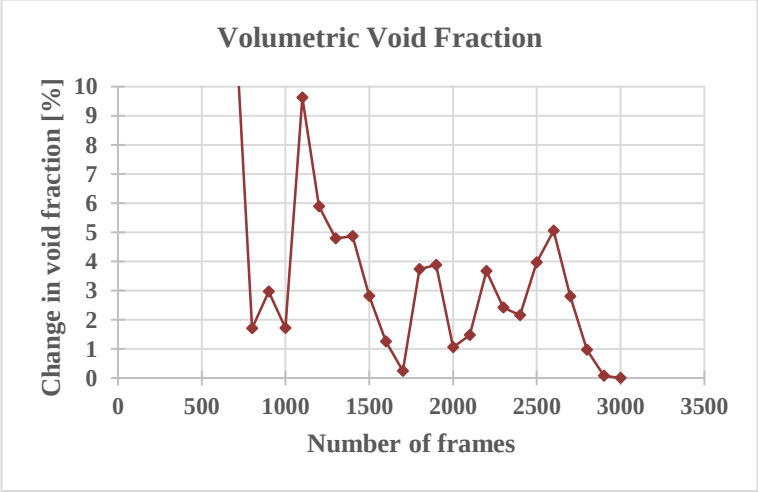

Figure 3-57. Close-up look for the percentage change in volumetric void fraction as the number of frames increases.

2000 frames for each focal point produced a .cine file requiring approximately 1.8 gigabyte of memory and it took 2 minutes to save the recorded films on an external hard drive. 40 seconds recording time and 2 minutes saving time for each focal plane allows one to capture 8 focal planes (see **Figures 3-27** and **3-28**) in approximately 30 minutes. Furthermore, image processing time for each set of 2000 images was around 30 minutes. Therefore, 2000 frames for each focal point was determined to be acceptable and used for the current study after considering the accuracy and the time requirements for filming and analysing.

3.8 Experimental Procedure and Control of the System Conditions

As mentioned before, the bubble measurement equipment was borrowed from the EPSRC each time for a three-month period after which it had to be sent back and so the experiments needed to be conducted during this period of three months. Modification of the test rig (see **Section 3.3**) was done while the camera was away. The system was drained and stood ready for the camera arrival. Draining the system minimizes the oxidation that can arise between the water and system parts especially at buffer vessel (Fsadni 2012). Before the experiment period, the system was filled with tap water and run for 4 hours at 80°C boiler exit temperature and 2.7 bar system pressure. After 4 hours of hot water circulation, the system was drained and filled with fresh water. This process was repeated every day for a week (4 or 5 times) before the camera arrival to make sure there were no dust or rust particles travelling through the system pipework. **Sections 3.8.1** and **3.8.2** in the following describe the detailed experimental procedure applied on each experiment day and the control of system conditions is explained in detail using two examples.

3.8.1 Experimental procedure

A fixed experimental procedure was developed and applied throughout the tests in order to be able to obtain the same conditions each experiment day. The following section summarizes the experimental procedure applied.

Before the experiment day:

- System pressure is arranged to be around 2.2 bars by injecting or removing cold water.
- AVV is closed to prevent any gas molecules to escape from the system,
- Nitrogen is injected through the buffer vessel and radiator until 2.7 bars to allow the system liquid to absorb nitrogen during the night in order to obtain certain saturation ratios the next morning.
- The external pump is turned on to circulate the system water through the pipework.

On the experiment day:

- AVV was opened so that excess nitrogen not absorbed by the liquid can escape.
- TGM is checked and cleaned before turning on the boiler.
- Boiler is turned on followed by a wait until the system temperature reaches desired levels.
- System flow rate is adjusted to desire values by the voltage controller installed to the internal pump of the boiler.
- After the desired temperature and flow rates are reached the system pressure is adjusted to desired values by adding (to increase) or removing (to reduce) fresh water.
- The system temperature, pressure, flow rate and saturation ratio are monitored through LabVIEW and camera measurements are conducted at desired conditions.
- Boiler is shut down followed by a wait until the system cools down.
- The procedure mentioned earlier for the things to be done before the experiment day applied before leaving the laboratory.

This procedure was employed each day for the experiment period and after the bubble measurement equipment was returned, system was drained and left empty during the times that no experiments were conducted.

3.8.2 Control of the system conditions

System conditions were collected and saved at the end of each experiment day in case there would be a need for further analysis. Two figures given in this section represent the system condition graphs plotted using those collected data after experiments. **Figure 3-58** illustrates a typical variation of system conditions during an ordinary experiment day. The example is from the bubble distribution measurements where bubble measurements were taken at two different saturation ratios (0.9 and 0.75) at 80°C, 2.7 bars and 1250 LPH flow rate.

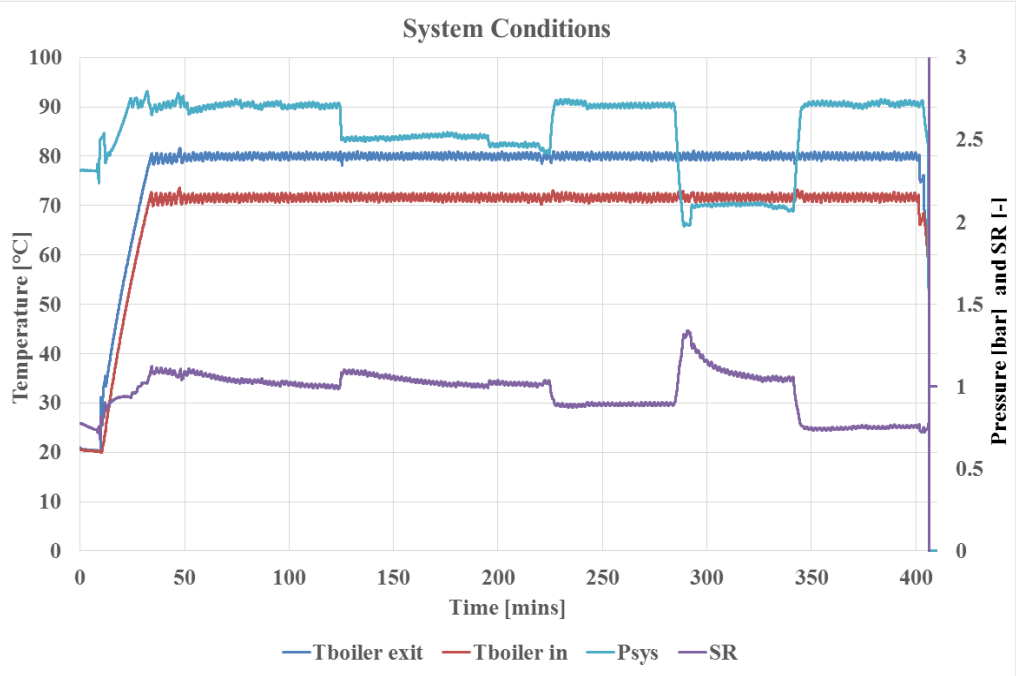

Figure 3-58. Typical system conditions plot for bubble distribution measurements.

First, the boiler was started and temperature setting was adjusted to be 85 °C from the control panel of the boiler. There was a sharp increase of the system temperature during the first 40 minutes and there was also growth in system pressure while system temperature was increasing. To lower it to desired values (2.7 bars) some amount of water was removed from the system. When the system temperature reached 80°C, the algorithm which controls the solenoid valve (see **Section 3.2.2.1**) was activated and system temperature was stabilized at 80°C. Saturation ratio of the system shows reduction after the temperature and pressure were stabilized at 80°C and 2.7 bars respectively. This is because bubbles generated at the primary heat exchanger of the boiler travel through the system pipework and escape from the AVV placed at the top of the buffer vessel.

After 125 minutes, system pressure was reduced to 2.5 bars to increase bubble generation thus faster escape of dissolved gases. This processes was necessary because at high flow rates saturation ratio decreases very slowly and manipulation of the system pressure helps us to achieve desired saturation ratios quicker. Reducing system pressure increases saturation ratio of the system which results in more bubble generation. The amount of actual dissolved gas in the system needed for reaching the

desired saturation ratios at 80°C and 2.7 bars was calculated using **Equation (3-18)** and noted in advance. The actual dissolved gas was monitored online and the pressure was increased back again to 2.7 bar when the actual dissolved gas amount reached calculated values.

The camera measurements were conducted around the times shown between 225 to 275 minutes for a saturation ratio value of 0.9. After that, system pressure was reduced again to 2.2 bars and there was a wait until the actual dissolved gas amount would decrease to the values which would result in a saturation ratio value of 0.75 when the pressure was increased back to 2.7 bars. Measurements for 0.75 saturation ratio were made between 340 to 400 minutes shown in the figure above. Later, the boiler was closed and system was left for cooling. After the system cooled down, the procedure given in the previous section was implemented to increase the dissolved gas amount in the system liquid by injecting nitrogen to reach similar conditions next morning for different flow rates.

The next example shows how the system temperature and pressure can be controlled on an experiment day. **Figure 3-59** shows the system conditions from the test conducted to investigate the effect of temperature and pressure on bubble production. The system flow rate was constant at 950 LPH and the boiler exit temperature was increased gradually from 60°C to 80°C at 2.7 bars. After that the system pressure was gradually decreased from 2.7 to 2.2 bars at 80°C constant boiler exit temperature. Saturation ratio was kept at around 1 all the time during the measurements.

Similarly, the system boiler was started again at the time shown with 90 minutes and again there was a sharp increase in temperature and pressure. At the time shown around 110 minutes the temperature and pressure were at the desired (60°C at boiler exit and 2.7 bars system pressures) levels but saturation ratio was higher. Therefore, the system was run for approximately 60 minutes at constant temperate and pressure until the saturation ratio went down to values around 1. When the desired conditions were achieved, the bubble measurements were conducted and then the threshold setting for the boiler exit temperature (see **Section 3.2.2.1**) amended at the front panel of the LabVIEW from 60°C to 65°C and the same procedure was repeated until

the measurements at 80°C were conducted. Afterward, temperate was kept constant and pressure was reduced gradually by removing water from the system.

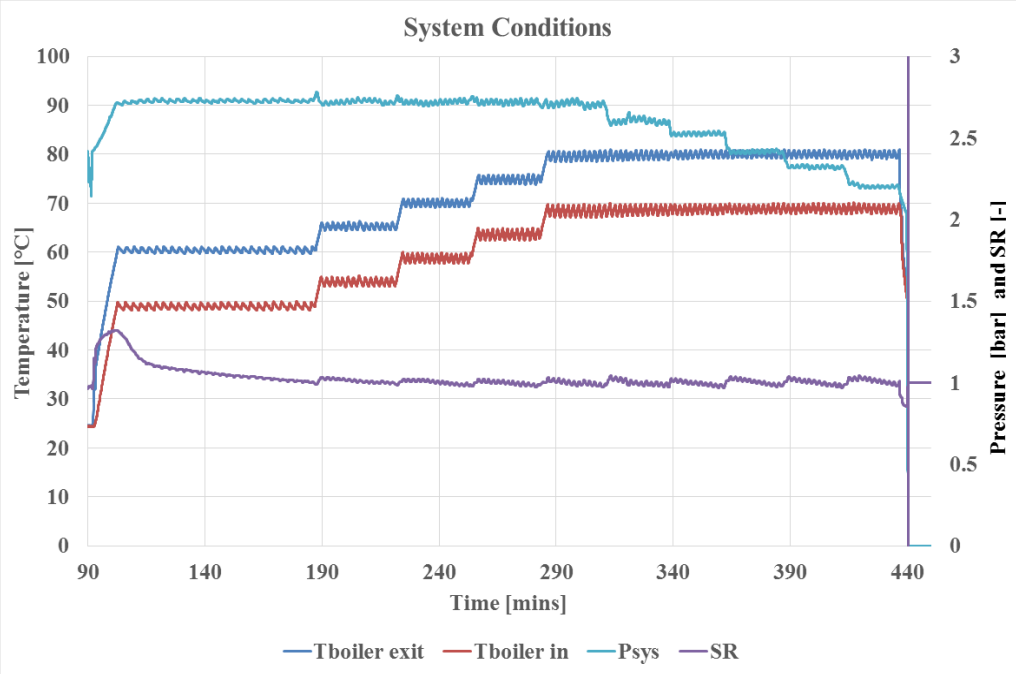

Figure 3-59. System condition plots for effect of pressure and temperature measurements.

3.9 Summary

This chapter included a comprehensive description of the experiments conducted during the current research. The main intention was to provide the information and knowledge necessary to replicate exactly the same experiments with similar equipment. Components of the test rig were explained in detail and alterations to the test rig were described. Later, the bubble measurement technique was discussed in conjunction with image analysis. The image analysis procedure was explained step by step with further analysis on apparent depth of sight glass and DOF determination. Apparent depth shift was explained using Snell's law and compared with experimental observations. The importance of DOF determination was pointed out with detailed analysis and procedure for an accurate determination of DOF was developed. Next, data processing and uncertainty analysis were presented and with a view to showing that they were at a level comparable with that of previous work.

Implementation of the frame independent test was explained and its result was presented. In the last section of the chapter, experimental procedure and control of system conditions were presented. The next chapter will focus on the results of the experiments conducted using the methodology explained in this chapter.

CHAPTER 4 EXPERIMENTAL RESULTS AND DISCUSSIONS

4.1 Introduction

While the previous chapter explained the design and methodology of the experiments, this chapter presents the results of the experimental measurements. The results include the parameters that are important in two-phase studies such as; bubble void fractions, average bubble diameters, and bubble velocities. Firstly, effects of several different parameters on bubble production rates, void fractions, and average diameters in central heating systems are presented in **Section 4.2**. Secondly, bubble volume and size distributions across the vertical and horizontal pipes of the test rig are illustrated and discussed under **Sections 4.3** and **4.4**. Next, bubble velocity profiles and their development along the vertical and horizontal pipes are presented in **Section 4.5**. Later, bubble sizes observed in central heating systems are submitted in **Section 4.6**. Finally, the chapter concludes with a brief summary under **Section 3.7**.

4.2 Effect of System Parameters on Two-Phase Flow at Boiler Exit

This section demonstrates the test results conducted to investigate the effect of each system parameter on two-phase flow behaviours in central heating systems. In this regard, several system parameters were varied one at a time (temperature, pressure, heating load, saturation ratio, and flow rate) while keeping other parameters constant throughout the experiments. The experimental conditions utilized for each parameter are provided in its own section. System conditions were controlled as explained in

Section 3.8.2. Bubble measurements were conducted at the first sight glass in the vertical line right after the boiler (VSG1) in order to avoid the effect of two-phase flow development at vertical and horizontal pipes which could lead to possible coalescences or dissolutions. Detailed position of VSG1 is provided in **Figure 3-23**. Single focal plane was used throughout the experiments. Measurements were gathered from the first focal plane, closest to the camera, and detailed schematic diagram of focal planes, camera, and light positions is given in **Figure 3-27**.

4.2.1 Effect of temperature

Effect of temperature on bubble production was measured and presented in the following **Figures 4-1** to **4-3**. X-axes in the figures represent boiler exit temperature and y-axes are the related data (bubbles per frame, void fraction, and average bubble diameter). System temperature was increased 5 °C at a time, from 60 to 80 °C at constant 2.7 bars pressure and 950 LPH flow rate. Saturation ratio of the system was kept around 1 and boiler heating load setting was set to 10 kW from the control panel of the boiler. When the boiler exit temperature is increased, saturation ratio of the system also increases (see **Section 2.2.1**). Therefore, filming of the flow was delayed for sufficient amount of time to let the saturation ratio drop back to 1 (see **Section 3.8.2** and **Figure 3-59** for more details).

Figure 4-1 shows the variation of bubbles per frame against each boiler exit temperature. As the boiler exit temperature increases, a clear pattern appears which indicates a steady increase in bubbles measured per frame. Similarly, measured volumetric void fraction gets higher as the temperature escalates as observed in **Figure 4-2**. Both figures suggest that bubble production on the heat exchanger surface of the boiler increases as the boiler exit temperature gets higher. The reason is thought to be the effect of temperature on the number of active cavities, which are the main source responsible for bubble production in supersaturated solutions (see **Section 2.3**). According to Bernardin & Mudawar (2002), the number of surface cavities which act as bubble nucleation sites increases exponentially with increasing liquid-solid interface temperature. Moreover, higher boiler exit temperatures lead to higher heat exchanger wall temperatures which in turn can increase the gas diffusivity at the wall and lead to higher bubble productions (Fsadni et al. 2012).

Because of the possible reasons mentioned, it is plausible to conclude that as the boiler exit temperature gets higher, bubble per frames and volumetric void fractions increase, causing higher bubble production rates.

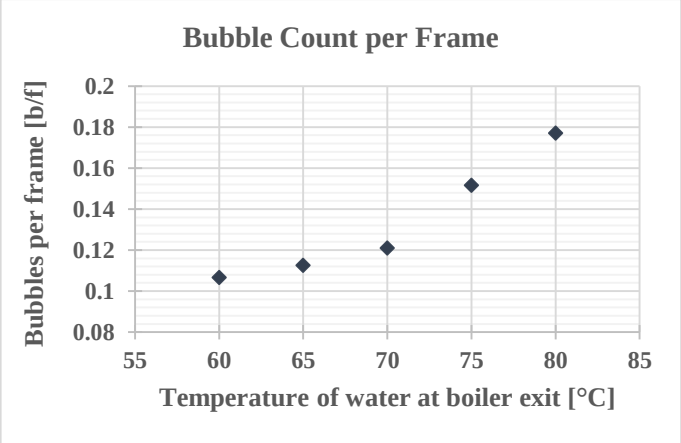

Figure 4-1. Effect of temperature on bubble count per frame at boiler exit.

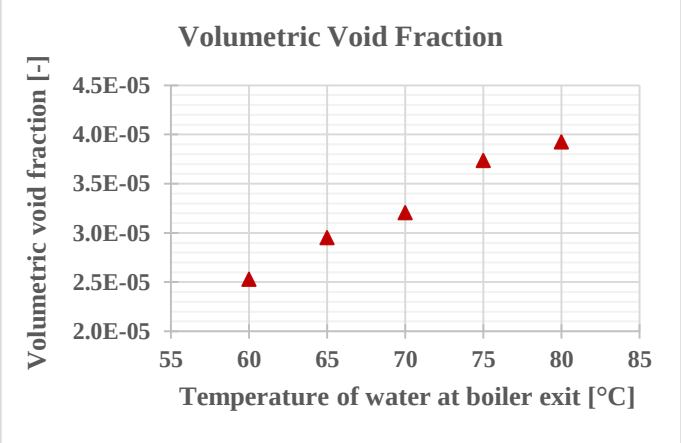

Figure 4-2. Effect of temperature on volumetric void fraction at boiler exit.

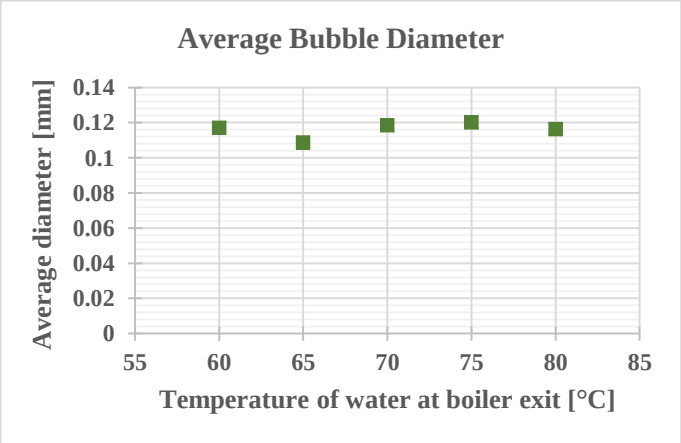

Figure 4-3. Effect of temperature on average bubble diameter at boiler exit.

Figure 4-3 illustrates average bubble diameters measured at each system temperature, however, no particular pattern has been observed. Average diameters are fluctuated around 0.12 mm for all used the temperatures. Unfortunately, the writer could not find any previous studies relating average bubble diameters with supersaturated solution temperatures for direct comparison. Nonetheless, after reviewing bubble detachment diameter predictions summarized in Fsadni (2012) for two-phase solutions, it is concluded that none of the models developed by previous researchers correlate bubble diameters with system temperature. Hence, it is acceptable to disregard the relation of boiler exit temperature with average bubble diameter in the current study.

4.2.2 Effect of pressure

Experiments to test the effect of pressure on two-phase flow were carried out right after the measurements conducted to test the effects of temperature. Reduction of the system pressure had begun after the last measurement at 80 °C was reached during the preceding test. Similar increase in saturation ratio at each temperature increase also occurred during pressure reduction. When the boiler exit pressure gets lower, saturation ratio of the system increases (see **Section 2.2.2**). Therefore, filming of the flow was delayed for sufficient amount of time to let the saturation ratio drop back to 1 (see **Section 3.8.2** and **Figure 3-59** for more details). Results of the pressure measurements are presented in the following **Figures 4-4** to **4-6**. Axes are similar to the figures in the previous section, except the x-axes where boiler exit pressure is represented instead of temperature. System pressure was decreased 0.1 bars each time, starting from 2.7 to 2.2 bars at constant 80 °C boiler exit temperature, and the rest of the conditions were identical to the conditions given in **Section 4.2.1**.

Figure 4-4 shows the change in measured bubbles per frame against boiler exit temperature. It can be seen that the bubble count per frame decreases as the boiler exit pressure increases. Consequently, volumetric void fraction measurements obtained for each boiler exit pressure also shows a decrease with increasing pressures in **Figure 4-5**. This indicates that bubble production is promoted at low system pressure. A matching conclusion was reached by Fsadni et al. (2012) during their studies on the same test rig. However, they argued that this trend does not coincide

with the predictions of classical nucleation models and they confidently demonstrated that non-classical model predicts a decrease in bubble nucleation rate as the system pressure increases.

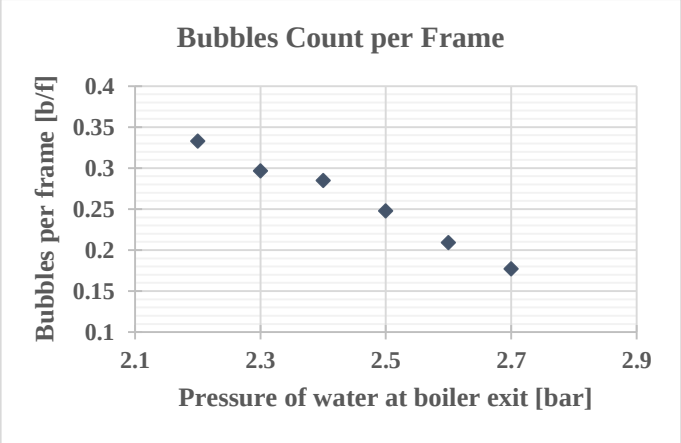

Figure 4-4. Effect of pressure on bubble count per frame at boiler exit.

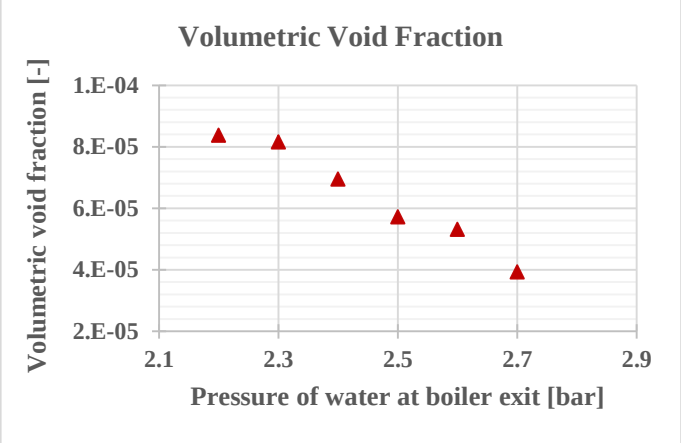

Figure 4-5. Effect of pressure on volumetric void fraction at boiler exit.

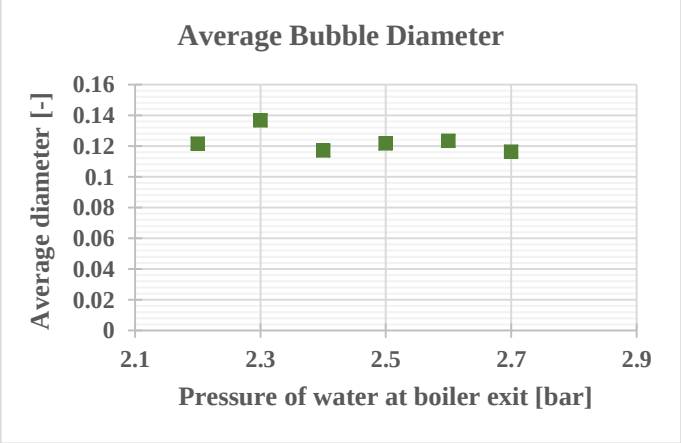

Figure 4-6. Effect of pressure on average bubble diameter at boiler exit.

Moreover, average bubble diameters measured at each system pressure are given in the **Figure 4-6**. Similar to the effect of temperature measurement, there is no particular pattern that can be related to system pressure and average bubble diameters measured in central heating systems. Average bubble diameters were more or less levelled around 0.12 mm for pressures. Comparable tests were conducted in Fsadni et al. (2011) on the same test rig where measurements were carried out at system pressures 2, 2.5, 3, 3.5 and 3.75 bars. Biggest average bubble diameter was observed at the lowest pressure, however, in the rest of the system pressures, average bubble diameters did not show a clear reduction. Even though, our pressure range is smaller than the previous research, a similar trend can be noted: at 2.3 bars, average bubble diameter is larger than the diameters observed at higher pressures. And average bubble diameter at higher system pressures tends to exhibit a levelled profile which does not indicate an obvious pattern.

Furthermore, Fsadni et al. (2011) stated that bubble diameter detachment model proposed by Winterton, does not predict any variation with the system pressure. They discussed that previous studies on bubble detachment diameters in supersaturated solutions are focused on models that integrate the balance of the drag and surface tension forces on nucleating bubble. For this reason, it is difficult to find comparable studies. However, Fsadni et al. (2011) mention that Prodanovic et al. (2002)'s study on subcooled boiling concluded that bubble detachment diameters are significantly affected by system pressure. They observed that bubble detachment time from the nucleation site significantly decreases as the system pressure increases, thus allowing a lesser amount of gas diffusion into the gas bubble, resulting in smaller bubbles. This may also explain the reduction in bubble production as pressure increases.

In general, bubble count per frame and volumetric void fraction measurements show similar trends; where there is reduction with increasing system pressure, and vice-versa, for the tests conducted for the effect of temperature. Moreover, there is no clear relationship between the system temperature and pressure with average bubble diameters. Comparable measurements to show effects of pressure on two-phase flows in central heating systems were conducted by the previous researcher (Fsadni 2012) and current results are in line with previous observations.

4.2.3 Effect of heating load

A test was conducted to show the effects of heating load on bubble production, presented in **Figures 4-7** to **4-9**. Axes in the figures are almost identical to the figures used previously, except for the x-axes which represents heating load in this section. Heating load of the boiler was varied at the control panel, originally installed on the boiler by the factory (see **Figure 3-2**). Six different heating load settings were used, obtained by increasing 2 kW each time from 8 to 18 kW. Rest of the system conditions were kept constant throughout the experiments. Boiler exit temperature was 80 °C, system pressure was 2.7 bars, system flow rate was 950 LPH, and saturation ratio was around 1.

Figure 4-7 illustrates captured bubbles per frame against heating load. It can be clearly observed that bubble numbers per frame increases as the heating load of the boiler gets higher. Consequently, volumetric void fraction measured at each heating load also increases as the heating load escalates (**Figure 4-8**). Both figures indicate that bubble production increases as the heating load gets larger. The reason for that is identical to the reasons mentioned in previous section, addressing the effects of temperature (**Section 4.2.1**). Higher heating loads lead to higher heat exchanger wall temperatures, in turn increasing diffusivity at the wall to cause higher bubble productions (Fsadni 2012). Furthermore, active nucleation sites increase at higher liquid-solid temperatures (Bernardin & Mudawar 2002). A similar conclusion was reached by Fsadni (2012) from their experiments regarding the effect of heating load on bubble production using the same test rig.

Effects of heating load on average bubble diameters are presented in **Figure 4-9**.Average bubble diameters were more or less levelled around 0.12 mm for all heating loads. Accordingly, there was no particular pattern observed between average bubble diameter and heating loads. The reasons mentioned in **Section 4.2.1** for not finding any relation between temperature and average diameter also holds for this case and there is no need to repeat them.

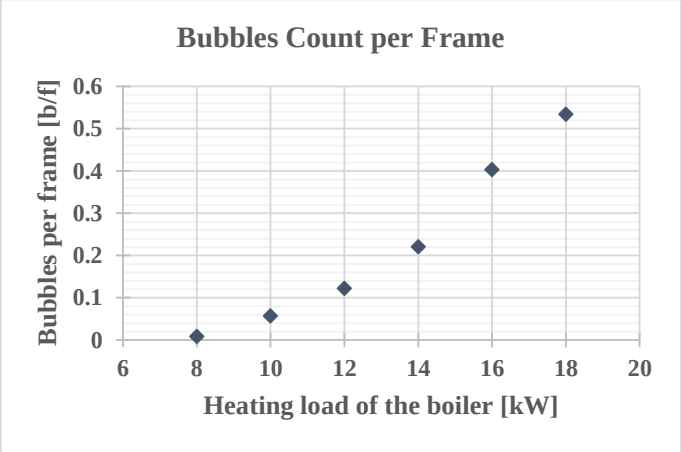

Figure 4-7. Effect of heating load on bubble count per frame at boiler exit.

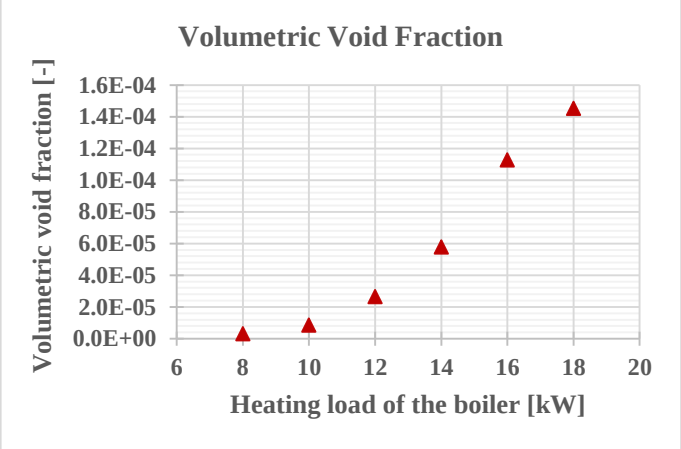

Figure 4-8. Effect of heating load on volumetric void fraction at boiler exit.

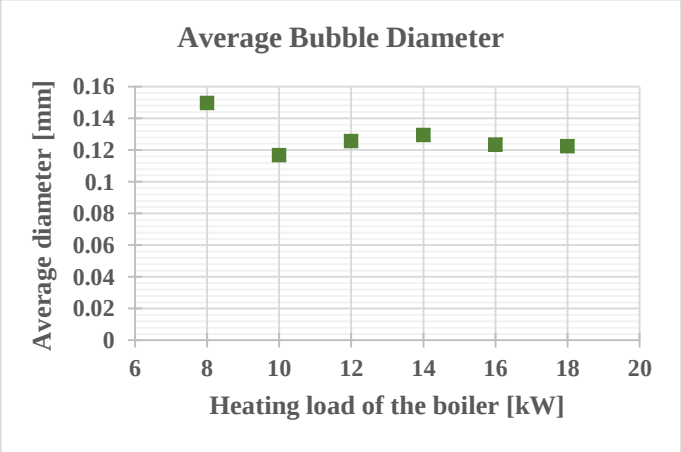

Figure 4-9. Effect of heating load on average bubble diameter at boiler exit.

4.2.4 Effect of saturation ratio

Saturation ratio of the test rig was varied from 1.2 to 0.37 and the results are presented in **Figures 4-10** and **4-12**. Axes are similar to the figures presented earlier, except for the x-axis which represents the saturation ratio of the system in this section. System was started as explained in **Section 3.8.1** and saturation ratio was reduced as time passed because of the automatic air vent (AAV) installed on the buffer vessel. Bubbles travel through the test rig and escape from the AAV, thus decreasing dissolved gas amounts in the system liquid (see **Section 3.8** for more details). The time needed to reach such low saturation ratios is very long, therefore, this particular test was conducted in three days. Saturation ratios from 1.2 to 0.83 was conducted on the first day, and from 0.73 to 0.55 on the second day. Finally, rest of the saturation ratios were completed on the third experiment day. System conditions were identical for each day: system pressure was 2.7 bar, temperature was 80 °C, flow rate was 950 LPH, and boiler heating load was set to 10 kW.

Bubbles captured per frame against each saturation ratio is shown in **Figure 4-10**. There is a clear decrease in bubble numbers per frame as the saturation ratio gets lower. Similarly, volumetric void fractions shows the same behaviour, as can be seen in **Figure 4-11**. Here, bubble production from the boiler heat exchanger reduces as the saturation ratio of the system decreases. There is a sharp decrease in bubble productions at oversaturated conditions whereas reduction becomes moderate at undersaturated conditions. Bubble productions and volumetric void fraction becomes negligible at saturation levels lower than 0.6. The relationship between bubbles per frame and volumetric fractions are reliable since saturation ratio is the most significant factor effecting bubble nucleation in supersaturated solutions (see **Section 2.2**). Higher saturation ratio at constant system conditions leads to more dissolved gases in liquid, therefore, increases bubble production rates (Fsadni et al. 2012). Moreover, same conclusions for the effects of saturation ratio on bubble production was drawn by Fsadni et al. (2012) where they also measured bubble production rates at different saturation ratios using the same test rig.

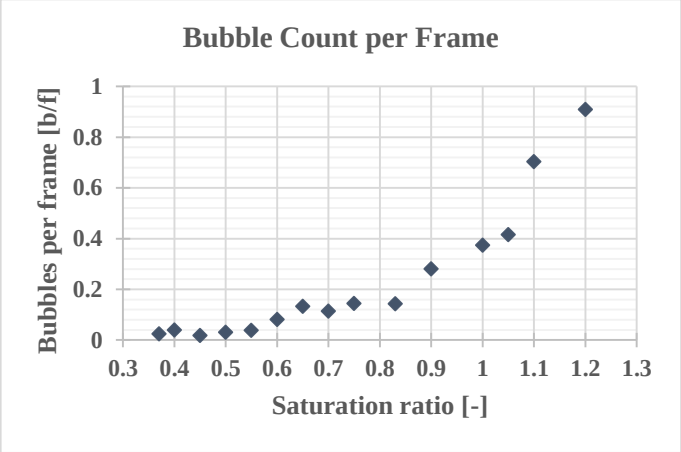

Figure 4-10. Effect of saturation ratio on bubble count per frame at boiler exit.

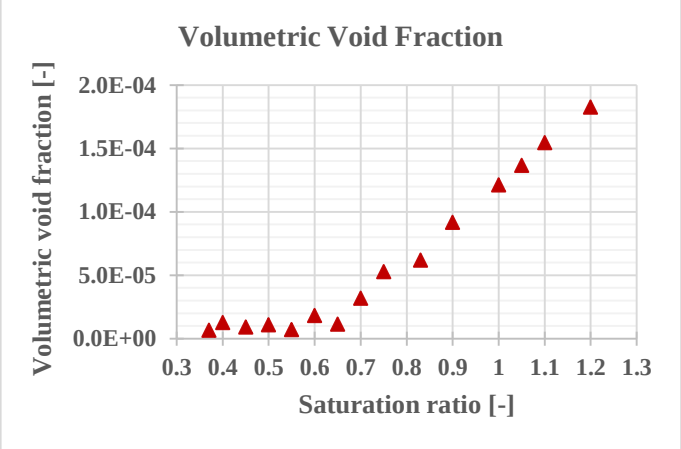

Figure 4-11. Effect of saturation ratio on volumetric void fraction at boiler exit.

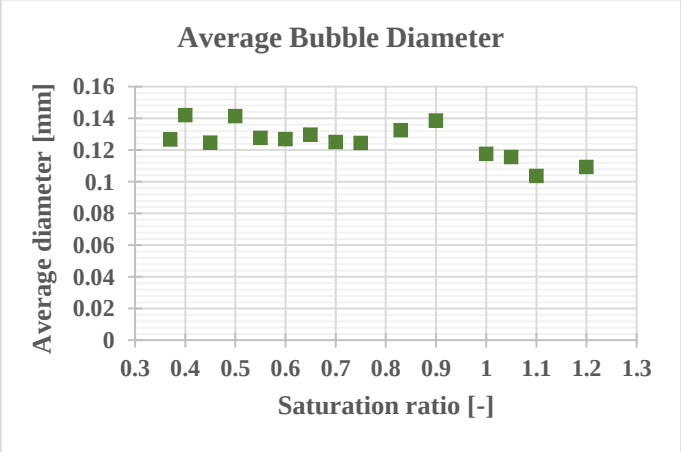

Figure 4-12. Effect of saturation ratio on average bubble diameter at boiler exit.

Average bubble diameters measured at each saturation ratio (**Figure 4-12**) exhibit lower values at oversaturated conditions, on the other hand, average diameters at undersaturated conditions show a slightly higher values than oversaturated levels and follow quasi-constant behaviours later on. Lower average diameters at oversaturated conditions were attributed to the high number of bubble production, where smaller bubbles dominate size distributions, leading to a decrease in average diameter. This again indicates that there is no particular relationship between average bubble diameter and saturation ratio observed in the current study. Quasi-constant behaviour of the average bubble diameters at different saturation ratios was also observed by Fsadni et al. (2011).

4.2.5 Effect of flow rate

Investigation of the effect of flow rate on two-phase flow structure right after the boiler is conducted and presented in the following **Figures 4-13** to **4-15**. Axes are similar to the figures in previous sections, however, x-axes represent flow rate in this section. Flow rate was changed from 600 to 1250 LPH as explained in **Section 3.3.5** by the voltage controller installed to the internal pump. Utilized flow rates lead to bulk fluid velocities in the range of 0.531 to 1.105 m/s in the pipeline. System conditions were constant throughout the experiments, where boiler exit temperature was 80 °C, 2.7 bars pressure, 10kW heating load, and saturation ratio was kept around 4 different saturation ratios: 0.75, 0.9, 1 and 1.1.

Both **Figures 4-13** and **4-14** show that bubbles per frame and volumetric void fraction measurements decreases as the flow rate increases for all of the saturation ratios. However, unlike other parameters discussed previously, these results cannot be used to relate bubble production rates with flow rate. Because, analysed sample of volume measured per liquid flow rate varies as the flow rate changes. Moreover, liquid velocity profiles, void fraction, and average size distributions measured at VSG1, is not quasi-constant across the pipe section and can significantly vary according to the flow rate (see **Sections 4.3**, **4.4** and **4.5**).

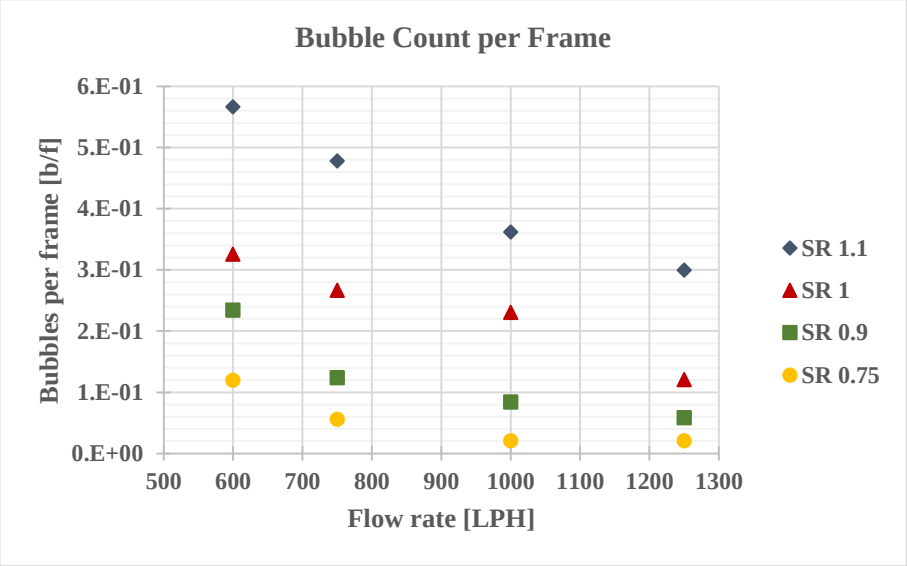

Figure 4-13. Effect of flow rate on bubble count per frame at boiler exit.

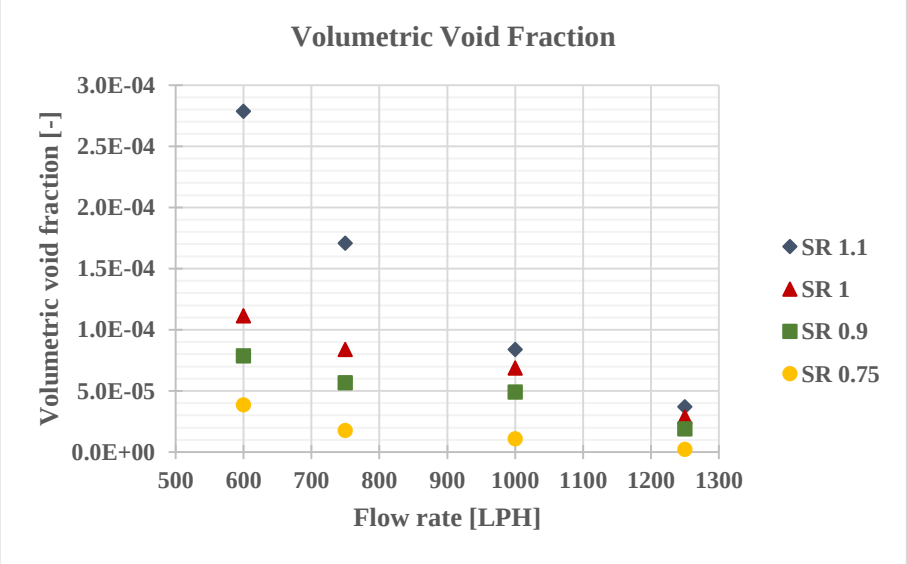

Figure 4-14. Effect of flow rate on volumetric void fraction at boiler exit.

Even though, results in this section cannot be used to relate bubble productions with flow rate, two-phase flow void fractions that can be expected from different flow rates can be pronounced. It can be clearly concluded that, for all of saturation ratios, volumetric void fractions decreases as the flow rate of the liquid increases. Moreover, experiment results presented in the following sections of this study also show that there is reduction in void fraction as the superficial velocity of the liquid increases (see **Sections 4.3** and **4.4**). Similar results were mentioned in two-phase

flow literature, rendering current experiment results reliable (see **Section 2.4** for previous studies on the effects of liquid flow rate on two-phase flow).

Figure 4-15 illustrates average bubble diameters measured at each flow rate for four different saturation ratios. Even though there seems to be a reduction in average bubble diameter as the flow rate increases, a clear pattern does not appear. The reason is believed to be the effect of 90 degree bend on the bubble size distributions at VSG1, which is clearly shown in the **Section 4.4.1**.

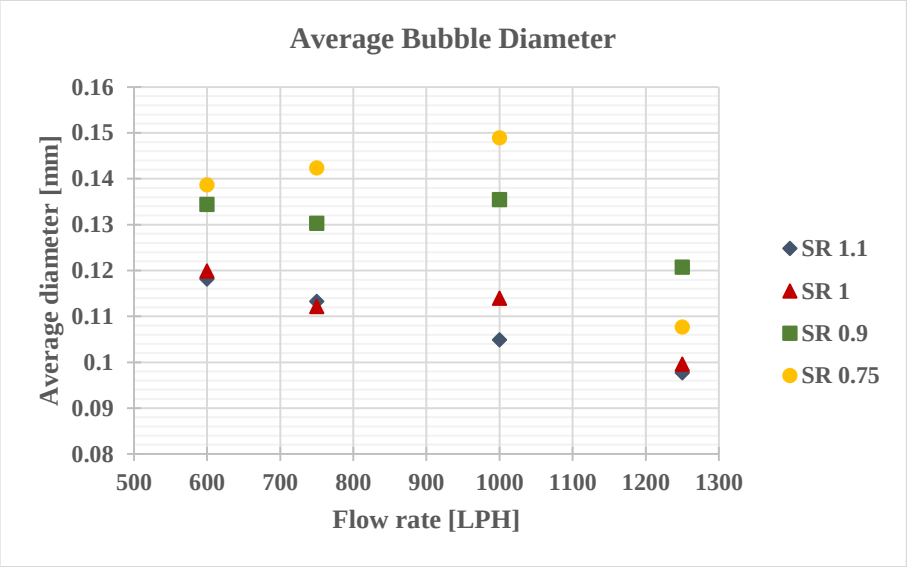

Figure 4-15. Effect of flow rate on average bubble diameter at boiler exit.

4.3 Bubble Volume Distributions across the Pipe Section

Bubble volume distributions across the pipe section was investigated in terms of local void fractions measured at each focal plane shown in **Figures 3-27** and **3-28** for vertical and horizontal setups respectively. There were 8 focal planes across the sight glass section and camera was moved towards the sight glass approximately 2 mm at each step (starting from the closest plane to the camera) by the help of the adjustable slider (see **Sections 3.4, 3.5** and **3.7** for more details). Test conditions during the measurements were controlled as explained in **Section 3.8.2**. Variation of system

conditions shown in **Figure 3-58** illustrates a typical system condition during an experiment day for one particular flow.

Table 4-1. summarizes the system conditions utilized for bubble distribution measurements. There were four different flow rates for two different saturation ratios at constant system pressure and temperature, which were 2.7 bars and 80 °C respectively. Heating load setting at the control panel of the boiler was 10 kW. Saturation ratios are determined to be undersaturated during the measurements because system tends to stay at oversaturated conditions for a short time and drops below 1 fairly quick, hence, does not provide enough time to capture both sight glasses at constant saturation ratio. Whereas, saturation ratio reduces acceptably slow at undersaturated conditions which offers sufficient time for filming both positions. Therefore, two saturation ratios, 0.9 and 0.75, were determined to be used during the distribution measurements.

Table 4-1. System conditions during bubble distribution measurements.

Flow rate (LPH)	**Superficial liquid velocity at pipeline (m/s)**	**Pressure at boiler exit (bar)**	**Temperature at boiler exit (°C)**	**Saturation ratio (-)**
600	0.531	2.7	80	0.9 and 0.75
750	0.663	2.7	80	0.9 and 0.75
1000	0.884	2.7	80	0.9 and 0.75
1250	1.105	2.7	80	0.9 and 0.75

4.3.1 Effect of pressure sensor and thermocouple

This section presents the results of the experiments conducted to test the effect of pressure sensor and thermocouple on bubble distributions during horizontal bubble flow. Pressure sensors and thermocouples are used frequently in pipelines and they had been used before or between the sight glasses by the previous researcher (Fsadni 2012) during his studies on the same test rig. After the preliminary tests at the time of current research, it was suspected that instruments in front of the sight glass may have significant effects on bubble distributions, sizes, and velocities across the pipe section. . Therefore, tests were decided to be carried out at HSG1 shown in **Figure 3-24**, with and without instruments installed before the measurement position. The

schematic diagram (**Figure 4-16**) illustrates the distance of the instruments to the sight glass and two-phase flow is filmed at the system conditions listed at **Table 4-1**. More details regarding the positions and diameters of the pressure sensor and thermocouple can be found in **Section 3.2.1.2**.

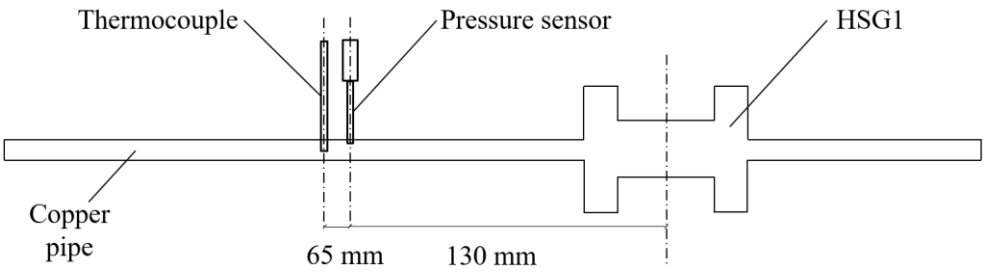

Figure 4-16. Distance of the pressure sensor and thermocouple to the HSG1.

The results are presented in **Figures 4-17** to **4-24**, where x-axis is the volumetric void fraction of bubbles and y-axis represents the normalized distance to the pipe wall (r/R) in the graphs where 1 and -1 represents top and bottom of the pipe respectively. It is worth noting that x-axis is presented on logarithmic scale in order to evaluate distributions in further detail. Because, average void factions found in central heating systems' pipework is very low and the difference between bubble volumes at top part is significantly higher than the bubble volumes at the bottom part which can supress the details of the profile when plotted on normal scale.

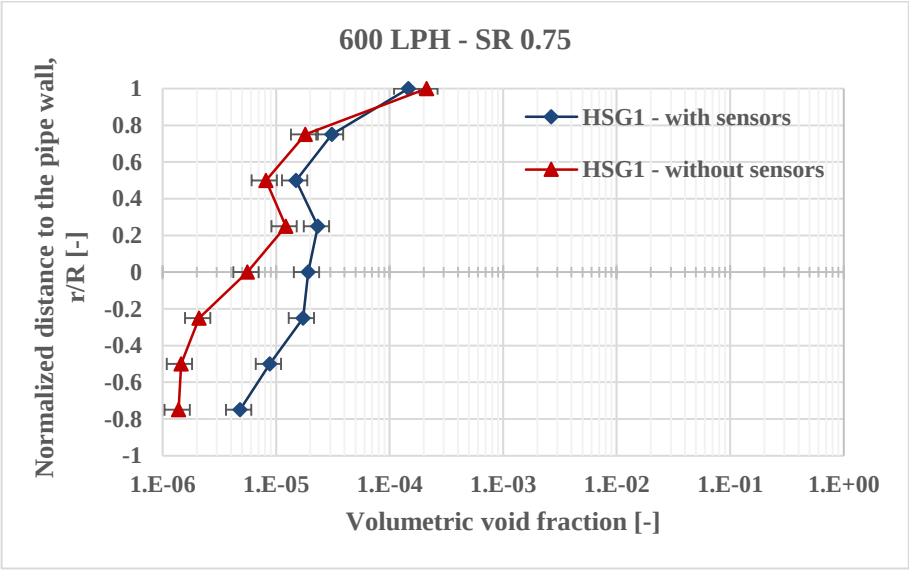

Figure 4-17. Effect of pressure sensor and thermocouple on bubble distribution at saturation ratio 0.75 and flow rate 600 LPH.

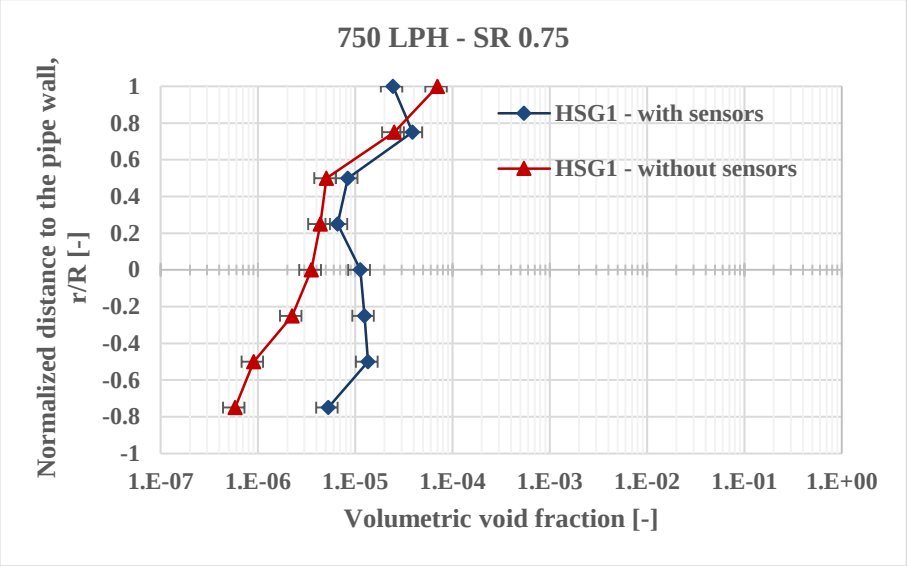

Figure 4-18. Effect of pressure sensor and thermocouple on bubble distribution at saturation ratio 0.75 and flow rate 750 LPH.

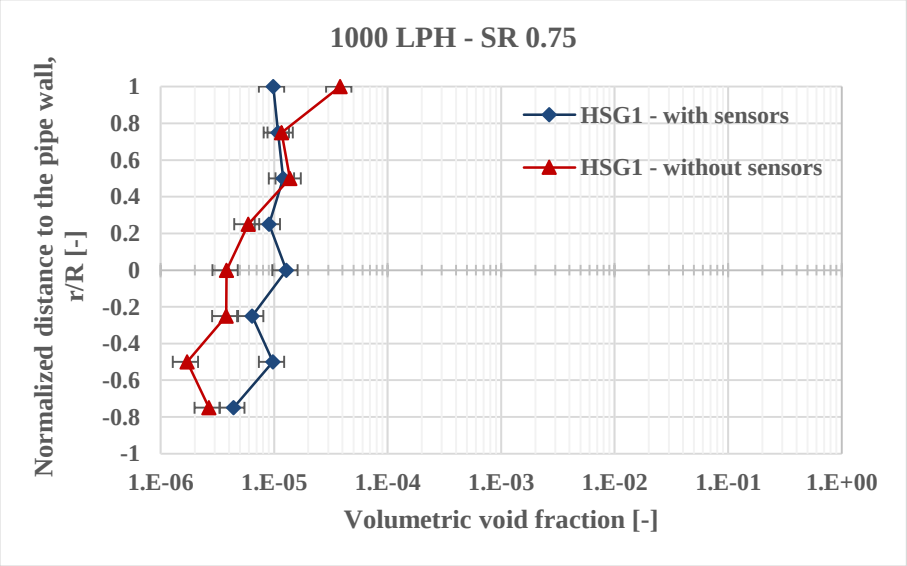

Figure 4-19. Effect of pressure sensor and thermocouple on bubble distribution at saturation ratio 0.75 and flow rate 1000 LPH.

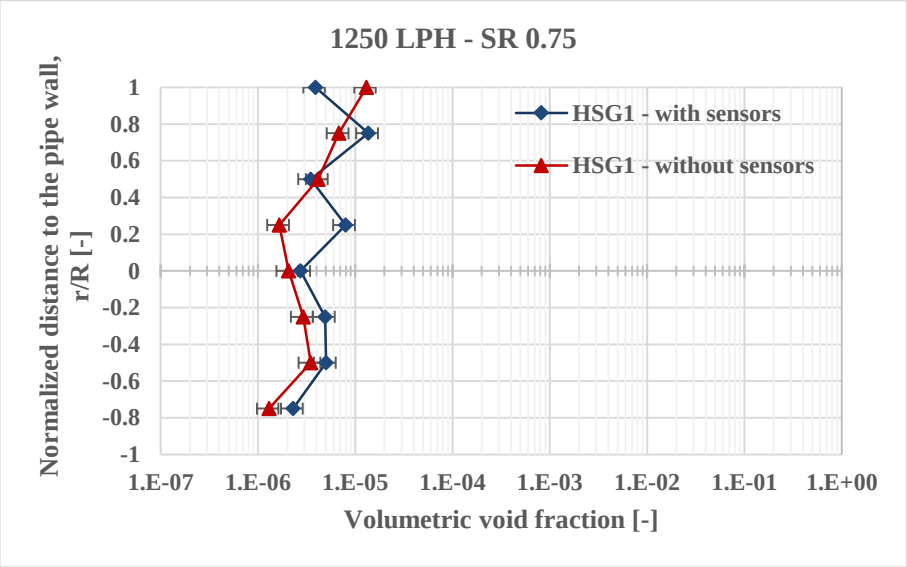

Figure 4-20. Effect of pressure sensor and thermocouple on bubble distribution at saturation ratio 0.75 and flow rate 1250 LPH.

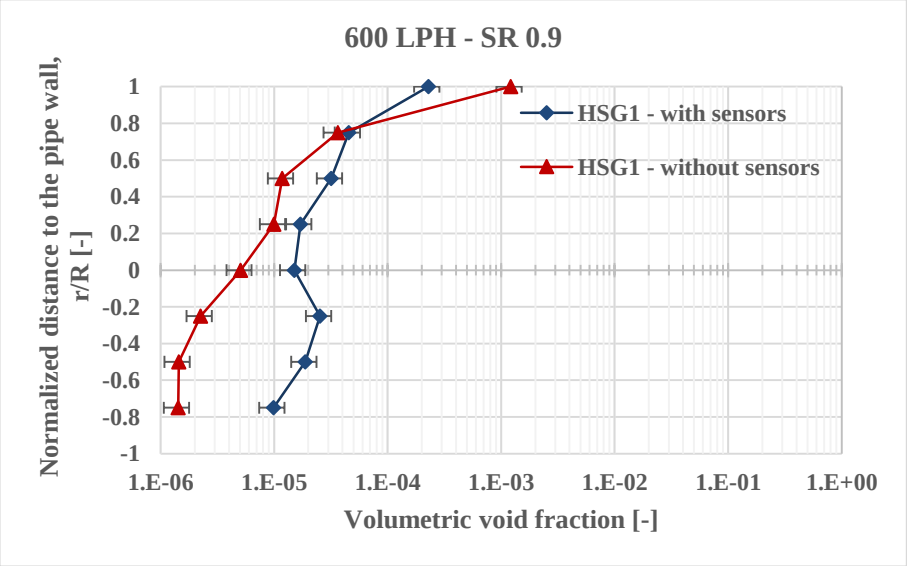

Figure 4-21. Effect of pressure sensor and thermocouple on bubble distribution at saturation ratio 0.9 and flow rate 600 LPH.

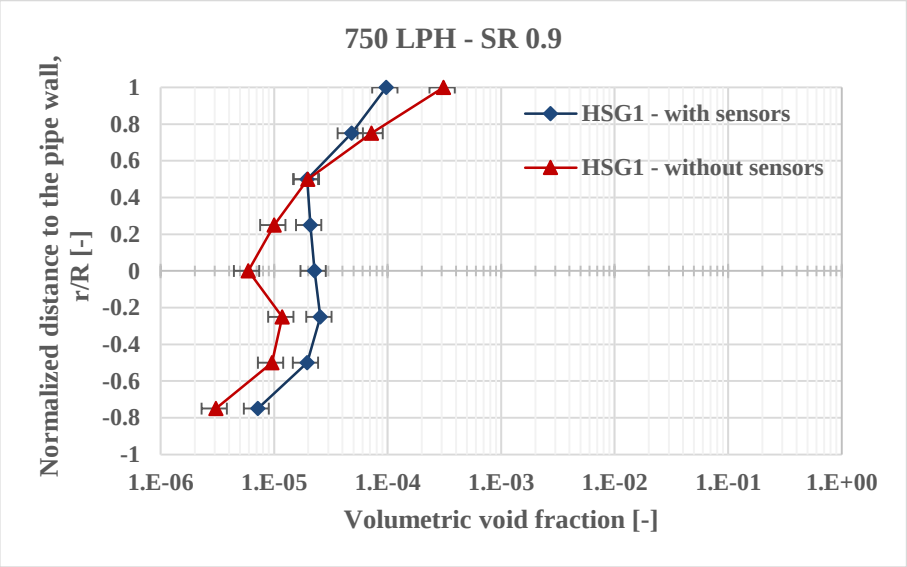

Figure 4-22. Effect of pressure sensor and thermocouple on bubble distribution at saturation ratio 0.9 and flow rate 750 LPH.

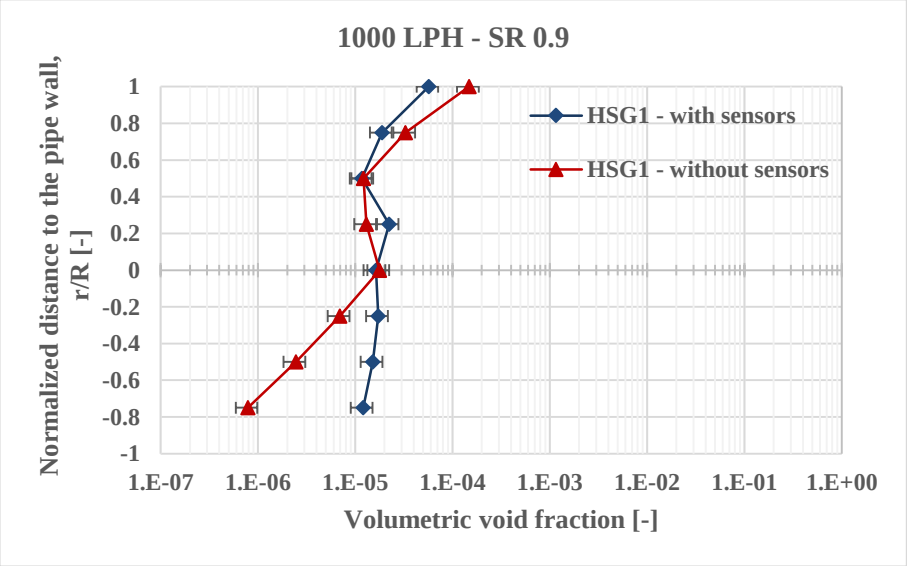

Figure 4-23. Effect of pressure sensor and thermocouple on bubble distribution at saturation ratio 0.9 and flow rate 1000 LPH.

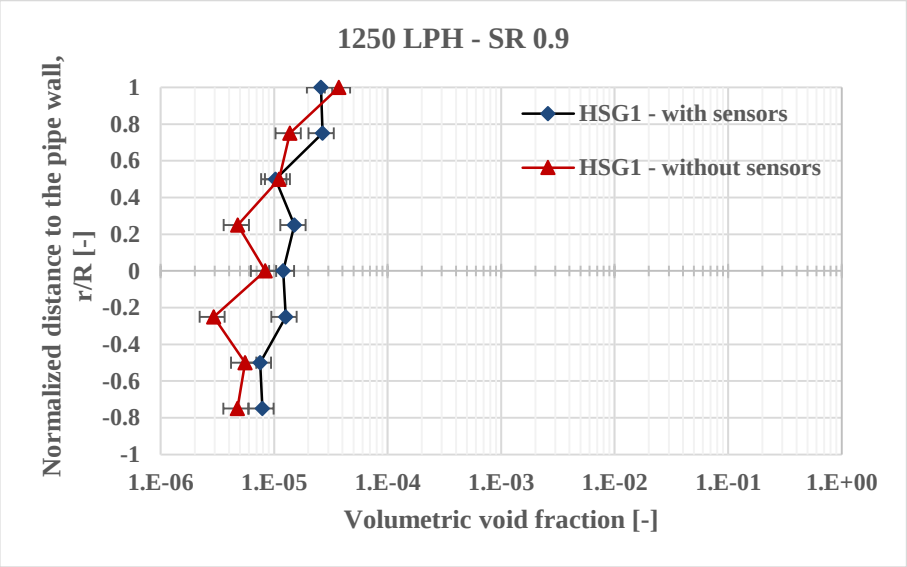

Figure 4-24. Effect of pressure sensor and thermocouple on bubble distribution at saturation ratio 0.9 and flow rate 1250 LPH.

In general, all of the figures indicate that pressure sensor and thermocouple have remarkable effects on bubble distribution and the effects are more pronounced as the bulk fluid velocity escalates, thus decreasing average void fractions (average void fractions at saturation ratio 0.75 is lower than at 0.9). First four figures represent the results at saturation ratio 0.75 for four different flow rates, and later four figures are for saturation 0.9.

It can be noted from **Figure 4-17** that at 600LPH, more bubbles travel at the upper part of the pipe than at the bottom for both measurements (with and without sensors). However, void fractions measured at the top part of the pipe is higher when there were no sensors, and vice-versa for the bottom part. This points out that the sensors interfere with the two-phase flow distribution and tend to push bubbles towards the bottom of the pipe. When the liquid flow rate was increased to 750 LPH (**Figure 4-18**), the difference in distribution profile was more significant, where peak void fraction during the measurement with sensor did not occur at the first plane but at the second. Later, the peak void fraction shifted back to top positions when the sensors were removed and higher values of local void fractions can be noted at the bottom when the instruments were installed similar to the measurements at 600 LPH. Further increasing the liquid velocity (**Figures 4-19** and **4-20**) causes distribution profiles to flatten as stated previously by Kocamustafaogullari & Wang (1991) and Bottin et al.

(2014). Peak void fractions still appeared at the top plane when the sensors were not on the pipeline, however, profiles plotted for the cases with sensors did not peak at the top of the pipe and showed fluctuations across the pipe section.

Same conclusions can be reached from the results shown in **Figures 4-21** to **4-24** for saturation ratio 0.9, where average void fractions grew when compared to the results for saturation ratio 0.75. After evaluating the results presented in this section for both saturation ratios, it was decided not to install the pressure sensor and the thermocouple before the measurement positions, in order to avoid the effects on bubble distribution profiles, sizes, and velocities that may rise from their presence. Instruments were installed right after the last horizontal position (HSG3) shown in **Figure 3-1**.

4.3.2 Vertical downward flow

Bubble distributions on the vertical pipeline of the test rig were measured and local void fractions across the two sight glasses are presented from **Figures 4-25** to **Figure 4-28**. Y-axes in the figures represent local volumetric void fraction of bubbles and x-axes are the normalized distances to the pipe wall (r/R); where 1 and -1 represent the pipe wall closest to the camera and the pipe wall farthest to the camera, respectively. Two sight glasses were positioned as shown in **Figure 3-23** with 970 mm distance between each sight glass. There were double 90 degree bends right after the boiler exit before the vertical pipeline where measurements were conducted. When each particular condition given in **Table 4-1** was obtained, 8 focal planes at VSG1 were measured and then camera was moved to the second position to film the focal planes at VSG2.

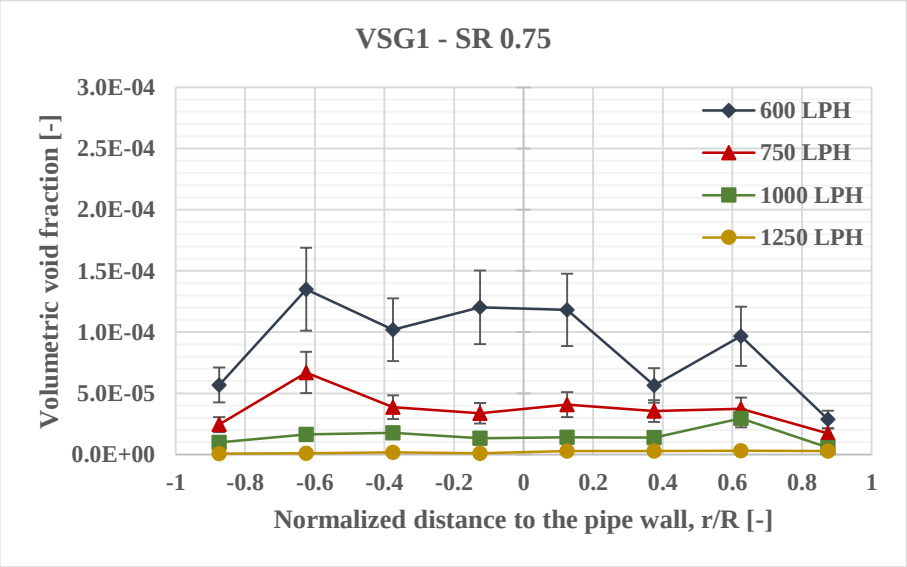

Figure 4-25. Bubble distributions across the pipe section during vertical downward flow at VSG1 and saturation ratio 0.75.

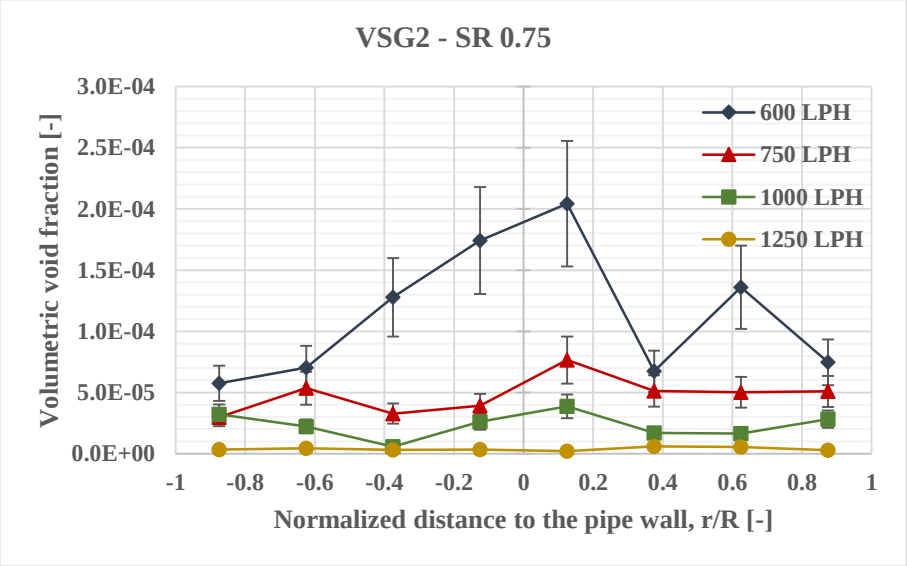

Figure 4-26. Bubble distributions across the pipe section during vertical downward flow at VSG2 and saturation ratio 0.75.

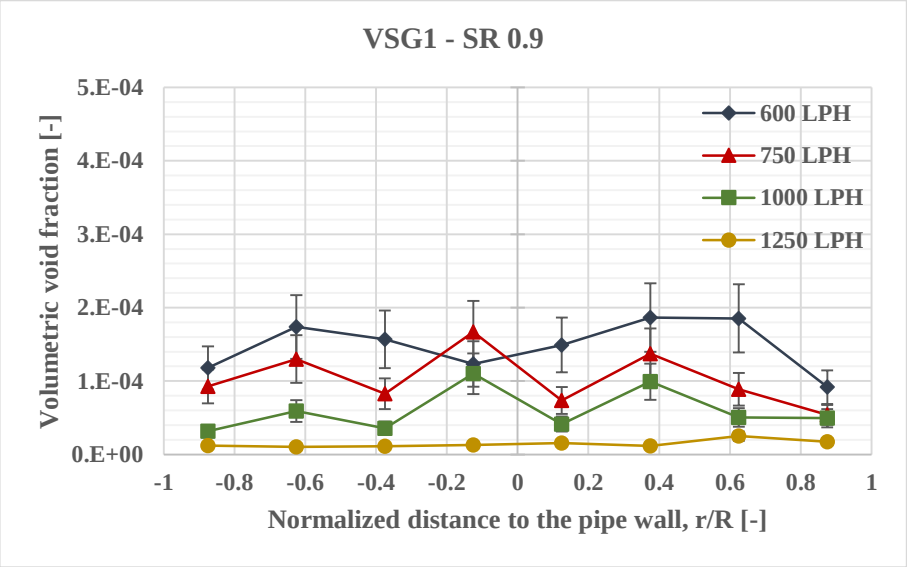

Figure 4-27. Bubble distributions across the pipe section during vertical downward flow at VSG1 and saturation ratio 0.9.

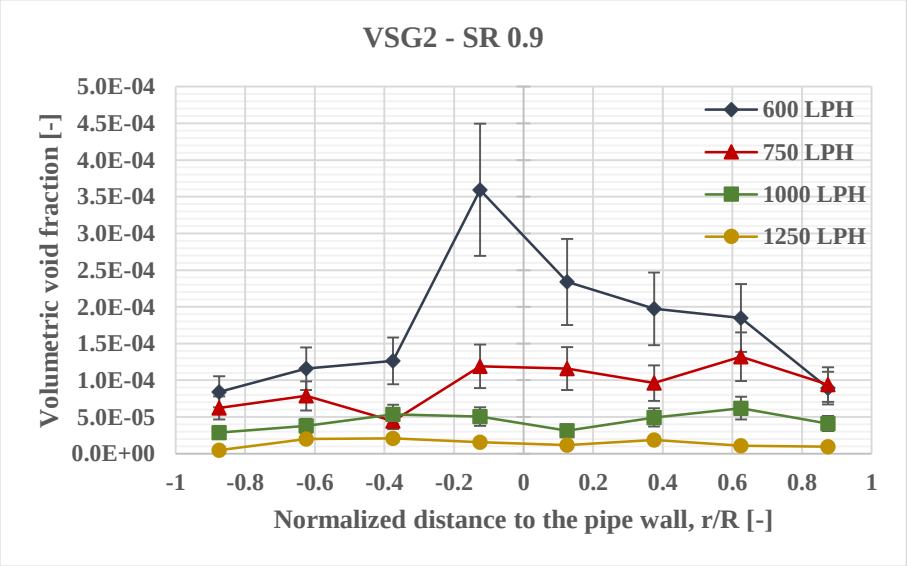

Figure 4-28. Bubble distributions across the pipe section during vertical downward flow at VSG2 and saturation ratio 0.9

In general, bubble distributions show flatter profiles as the liquid volume flow rate increases. This disagrees with the experimental data of Kashinsky & Randin (1999) and Ishii et al. (2004) where they noted that core peaking phenomenon becomes noticeable as the liquid velocity increases. However, void fractions and bubble diameters obtained in both researchers' experiments are significantly higher than bubble diameters and void fractions occurring in the pipeline of central heating

systems. Moreover, liquid and gas flow rates were controlled carefully in those experiments, whereas, bubble production cannot be controlled in the present study since it is highly dependent on liquid flow rate (see Fsadni et al. (2012)). Therefore, disagreements are thought to be reasonable because Kashinsky & Randin (1999) also mention that void fraction profiles flatten when the average void fraction across the pipe section decreases, which coincides with the current data.

Furthermore, Kashinsky & Randin (1999) pointed out that decrease in the superficial liquid velocities leads bubbles to move closer to the wall. This opposes with the observations carried out by Bhagwat & Ghajar (2012). They observed that bubbles distribute more evenly as the liquid velocity increases at the same time with significant reduction in diameters of bubbles. This corresponds with the results obtained in current work. Even though, observations of Kashinsky & Randin (1999) and Bhagwat & Ghajar (2012) do not confirm each other entirely, the difference in the nature of their experiments needs to be conceived. Whereas, Kashinsky & Randin (1999) utilized bubble size control so bubble diameters were approximately constant throughout their experiments, Bhagwat & Ghajar (2012) did not utilize any kind of bubble control. On the other hand, Kashinsky & Randin (1999) noted that bubbles tend to move closer to the pipe wall as their diameters decrease, which is consistent with the overall observations of Bhagwat & Ghajar (2012). Subsequently, it is worth mentioning that Bhagwat & Ghajar (2012)'s observations appear to be more similar to the current study than Kashinsky & Randin (1999)'s, since the former experiment did not involve any bubble size control mechanism.

Void fraction profiles obtained during present research can be associated with two of the downward bubble flow distribution types characterized by Hibiki et al. (2004). There is no void fraction profile obtained in the current work that can be related to the bell-type distribution. Even though, most of the bubble distributions are levelled across the pipe section and indicate off-centre peaked type, there was core-peaked profiles observed at VSG2 during 600LPH flow rates for both saturation ratios. It can be concluded that, bubble distribution profiles in wet central heating systems tend to show core peaked distributions as the fluid velocity decreases. This can be correlated with increase in average void fraction as pointed out by Kashinsky & Randin (1999). Centre-peaked profiles were seen only at VSG2. The reason for this is thought to be

the double 90 degree bend placed just before the entrance of the vertical pipe, which can significantly affect bubble distributions at VSG1.

Axial development of void fraction distributions along the vertical line do not show significant differences between each position, except at 600LPH for two saturation rations. Investigations of Hibiki et al. (2005) indicate that, as long as there are no big bubbles, bubble distribution profile is not affected while it travels along the vertical pipe. Maximum void fractions and bubble diameters (see **Figures 4-74**, **4-75** and **4-86**) found in the vertical flow during the current study is at 600LPH. Therefore, the shift in the bubble distribution profile is thought to be reasonable. At VSG1, void fraction profile indicates off-centre peaked type profiles, whereas at VSG2, void fraction distribution type shifts to centre-peaked. This demonstrates that distribution profile is more likely to be effected by the flow path history, especially at two-phase flows with higher average void fractions and bigger bubbles. As a conclusion, it can be said that double 90 degree bend before the vertical line can significantly affect the distribution profile and this effect is pronounced at the lowest flow rate condition.

4.3.3 Horizontal flow

Local void fraction measurements at four different axial positions on horizontal pipeline of the test rig is presented in **Figures 4-29** to **4-36**. There was 90 degree bend before the first sight glass (HSG0) and distance between each sight glass position is increased gradually (L/D = 7.5, 28, 74.75 and 139.75) in order to measure bubble distributions at each position during the conditions provided in **Table 4-1**. Schematic diagram of the internal structure of the 90 degree bend before the first sight glass is provided in **Appendix 37** and details of each sight glass position can be found in **Figure 3-24**. At this point, it is important to remind the reader that there were two sight glasses available to use in the test rig, therefore, measurements were repeated twice for each experiment condition. First, sight glasses at second and third positions (HSG1 and HSG2) were assembled and experiments were conducted similar to procedures mentioned for vertical flow experiments in **Section 4.3.2**. When desired system conditions were reached, 8 focal planes at HSG1 were filmed and then camera was moved to the next positon (HSG2) to continue the measurements. Later, HSG1 and HSG2 were removed from the pipeline and the sight

glasses were installed to the positions decided for HSG0 and HSG3. Same procedure followed for HSG1 and HSG2 was repeated for HSG0 and HSG3. Following figures demonstrate the effect of liquid flow rate on each axial position and the axes used in the figures are identical to the ones that are plotted to evaluate the effects of pressure sensor and thermocouples on bubble distribution (see **Section 4.3.1**).

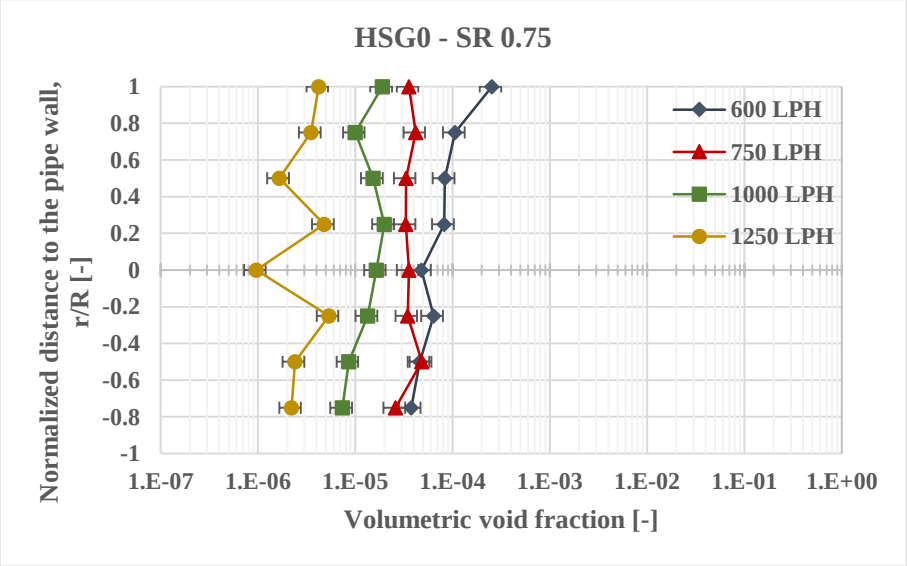

Figure 4-29. Bubble distribution at HSG0 and saturation ratio 0.75.

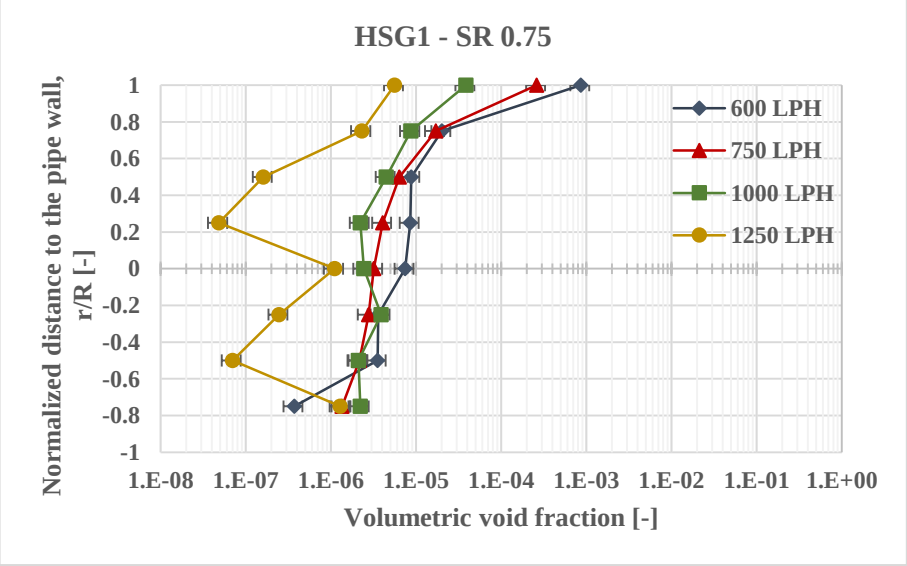

Figure 4-30. Bubble distribution at HSG1 and saturation ratio 0.75.

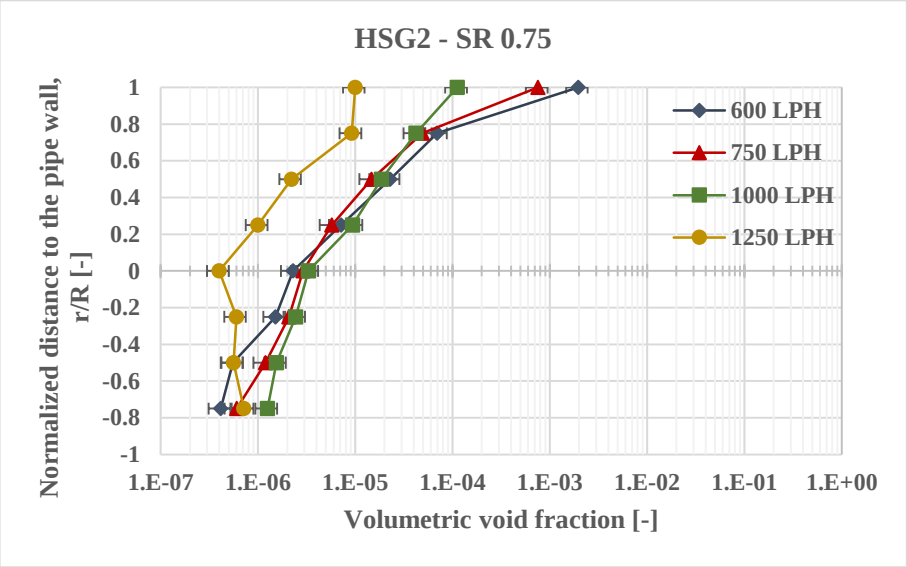

Figure 4-31. Bubble distribution at HSG2 and saturation ratio 0.75.

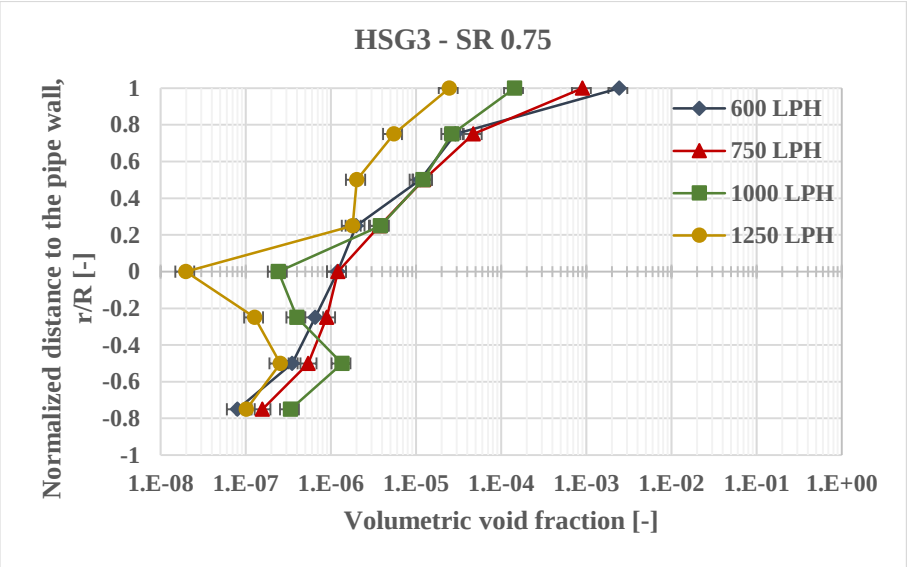

Figure 4-32. Bubble distribution at HSG3 and saturation ratio 0.75.

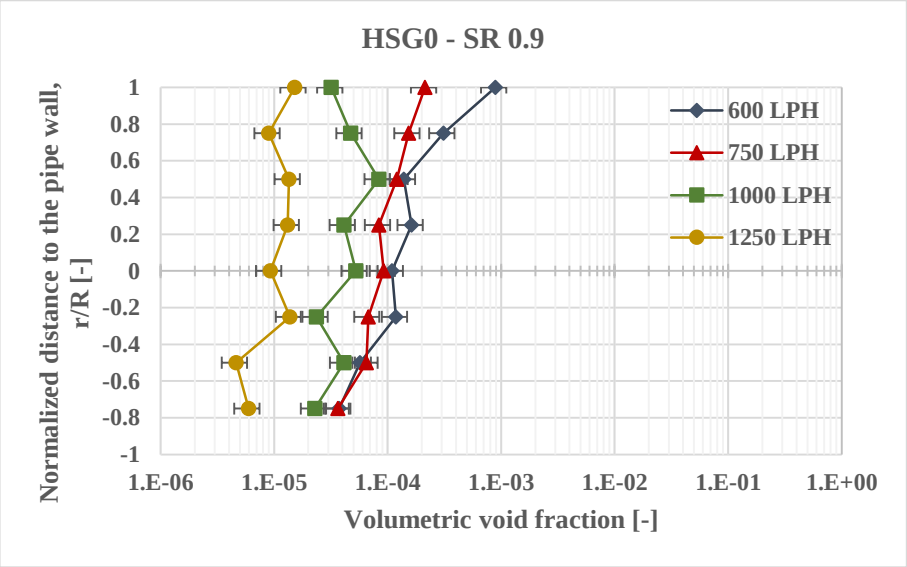

Figure 4-33. Bubble distribution at HSG0 and saturation ratio 0.9.

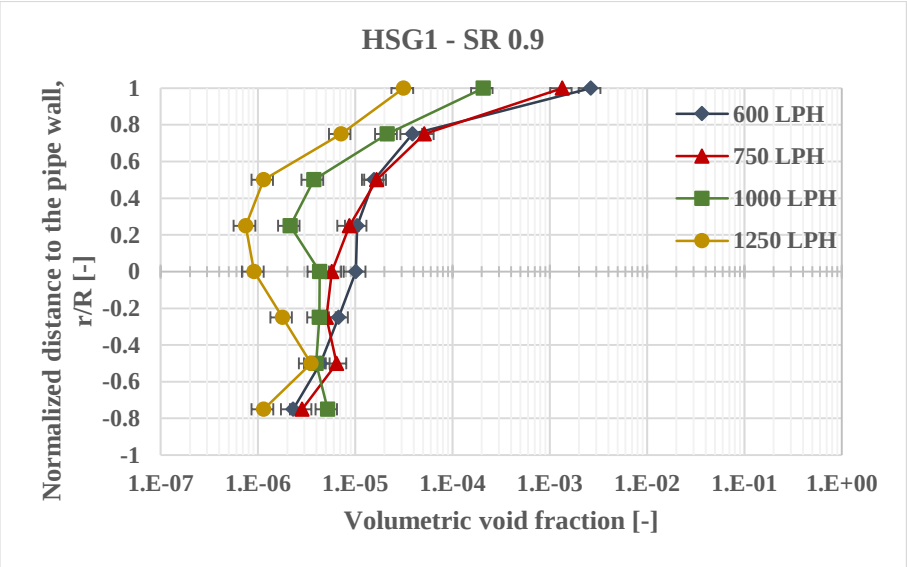

Figure 4-34. Bubble distribution at HSG1 and saturation ratio 0.9.

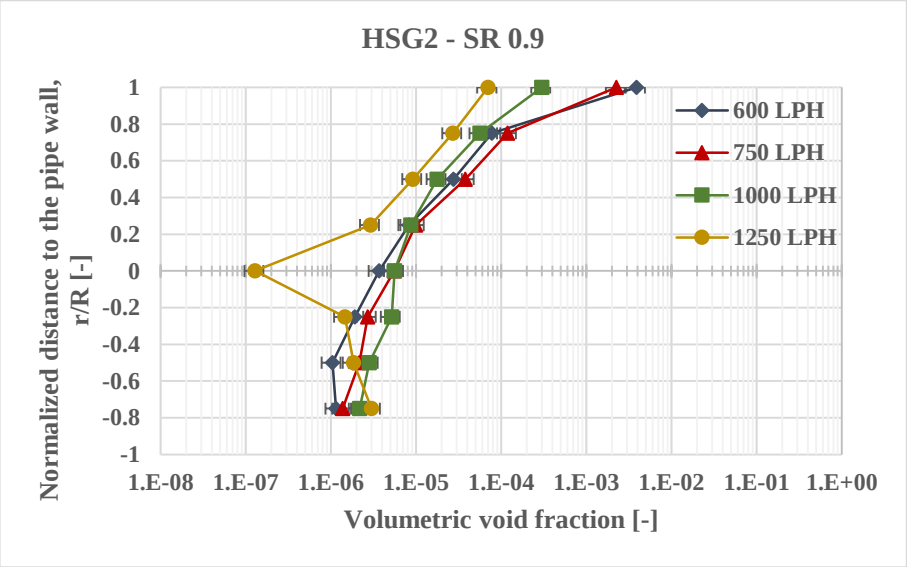

Figure 4-35. Bubble distribution at HSG2 and saturation ratio 0.9.

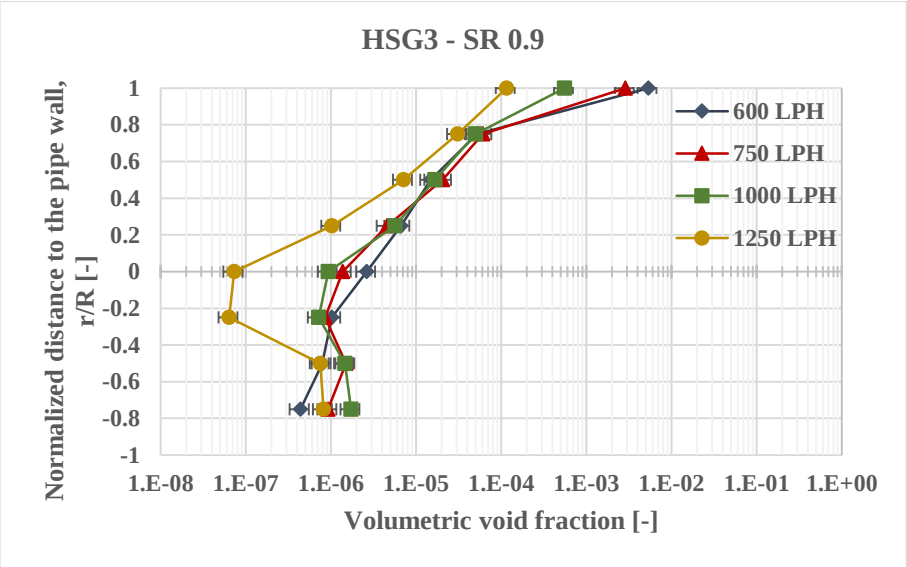

Figure 4-36. Bubble distribution at HSG3 and saturation ratio 0.9.

In general, it is clear that average void fraction of bubbles reduces and bubble distribution profiles level across the pipe section as the liquid velocity increases. These are typical observations that were obtained by other researchers previously (see **Section 2.4.2.1.2**). However, flattening phenomenon of the distribution profiles as the liquid velocity increases is pronounced at first sight glass (HSG0) for both saturation ratios (**Figures 4-29** and **4-33**). Results for both saturation ratios at HSG0, at 600 LPH showed typical distribution profiles which can be expected from

horizontal bubble flow where peak void fraction occurs at the top and lessens across the pipe section. After increasing the flow rate to 750 LPH, distribution profile is levelled across the pipe section. Further increasing the flow rate causes distribution profiles to become even more flat with slight fluctuations. Furthermore, the distribution profiles at HSG1, HSG2 and HSG3 (**Figures 4-30** to **4-32** and **Figures 4-34** to **4-36**) did not show this flattening phenomenon as significant as at HSG0, where there is clear evidence that 90 degree bend before first sight glass affects the two-phase flow arrangement across the pipe section.

Investigation of 90 degree elbow effect on two-phase flow structures were carried out experimentally in the last decade by several researchers. Kim et al. (2007), Yadav et al. (2010) and Talley & Kim (2010) focused on the effect of 90 degree bend, assembled between horizontal and vertical upward flow. On the other hand, 90 degree bend, installed between upward to horizontal pipeline was studied by Yadav, Worosz, et al. (2014) and Yadav, Kim, et al. (2014). Unfortunately, the writer could not find any investigation similar to the present case study where 90 degree bend is used to direct downward flow to horizontal line. However, following two conclusions can be drawn from the above-mentioned researches. First, 90 degree bend induces spatial oscillations in void fraction profiles after the bend and this promotes coalescences (Kim et al. 2007; Yadav et al. 2010; Talley & Kim 2010). Secondly, effect of 90 degree bend in single phase flow and two-phase flow is similar, where 90 degree bend leads to secondary flow in the flow, influencing bubble distribution at downstream of bends (Yadav, Worosz, et al. 2014; Yadav, Kim, et al. 2014).

After considering the previous studies related to 90 degree bend effect on two-phase flow structure, it can be confidently stated that, the bend results in a remarkably levelled bubble distribution phenomenon at HSG0. The secondary flow caused by the bend affects the distribution after bend and can lead to the observation obtained in the present study. Furthermore, all of the results indicate that, observed local void fractions at the top plane in each position decreases as the fluid velocity increases. This is due to the levelling of distributions across the pipe section as the flow rate escalates as discussed previously. Moreover, slope of distribution profiles at each position lowers as the flow travels on horizontal pipe after the bend, regardless of

liquid velocity. This indicates that bubble distributions across the pipe tend to develop along the horizontal line, which is discussed in the next section.

4.3.4 Bubble volume distribution development along the horizontal pipeline

The data presented in the previous section (**Section 4.3.3**) was reorganized and replotted to illustrate the development of void fraction profiles along the horizontal pipe for each flow rate in **Figures 4-37** to **4-44**. Instead of bubble distribution at each position for four different flow rates, distributions at four different positions at one flow rate and saturation ratio were plotted. The axes are identical to the previous figures which illustrate bubble distribution on horizontal pipeline of the test rig.

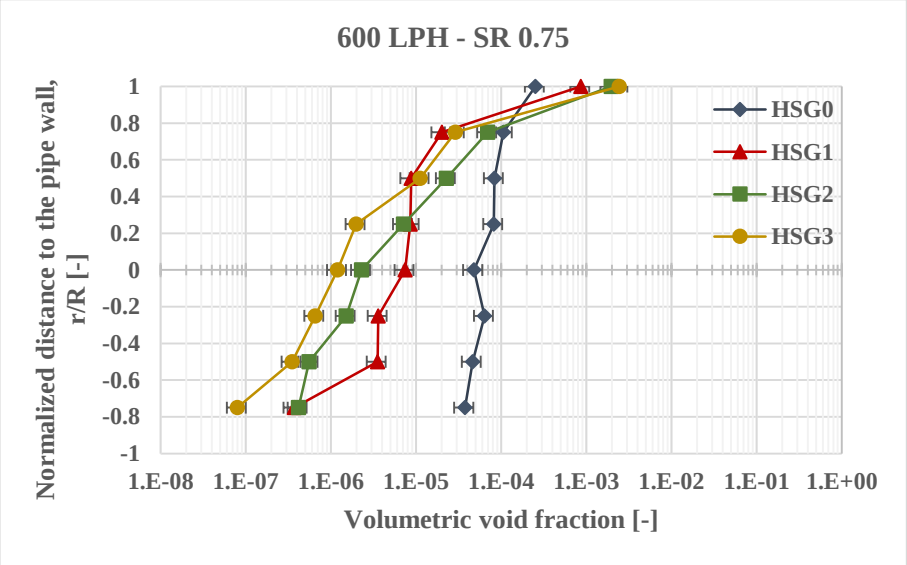

Figure 4-37. Bubble distribution development along the horizontal pipeline at 600 LPH and saturation ratio 0.75.

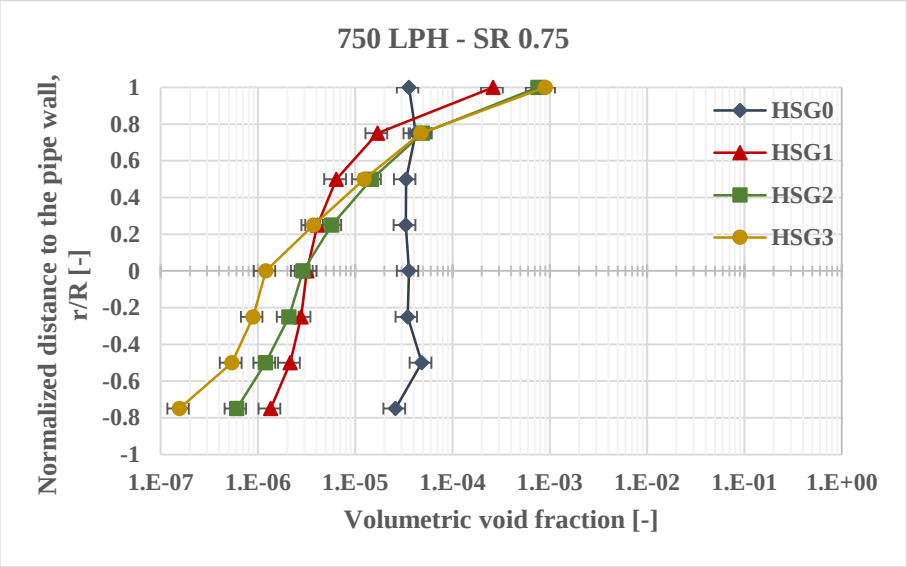

Figure 4-38. Bubble distribution development along the horizontal pipeline at 750 LPH and saturation ratio 0.75.

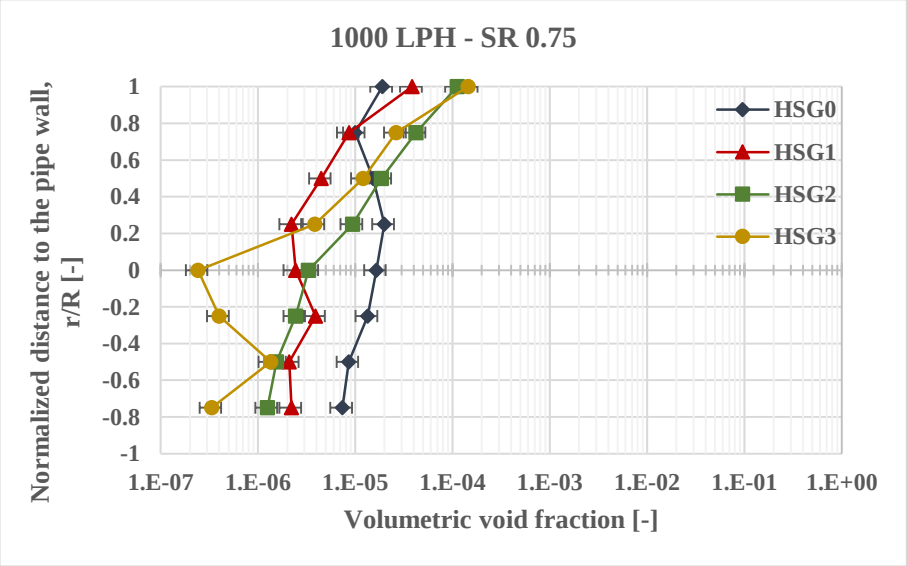

Figure 4-39. Bubble distribution development along the horizontal pipeline at 1000 LPH and saturation ratio 0.75.

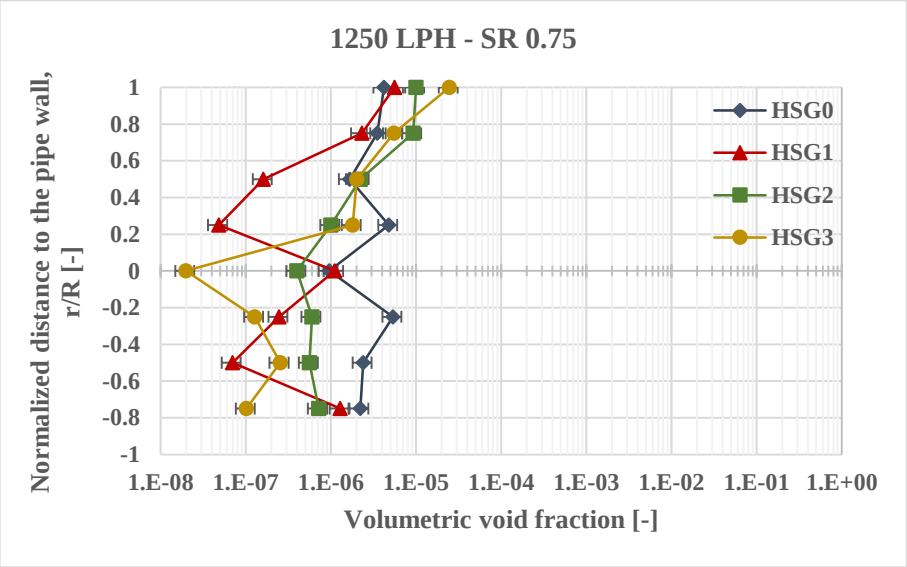

Figure 4-40. Bubble distribution development along the horizontal pipeline at 1250 LPH and saturation ratio 0.75.

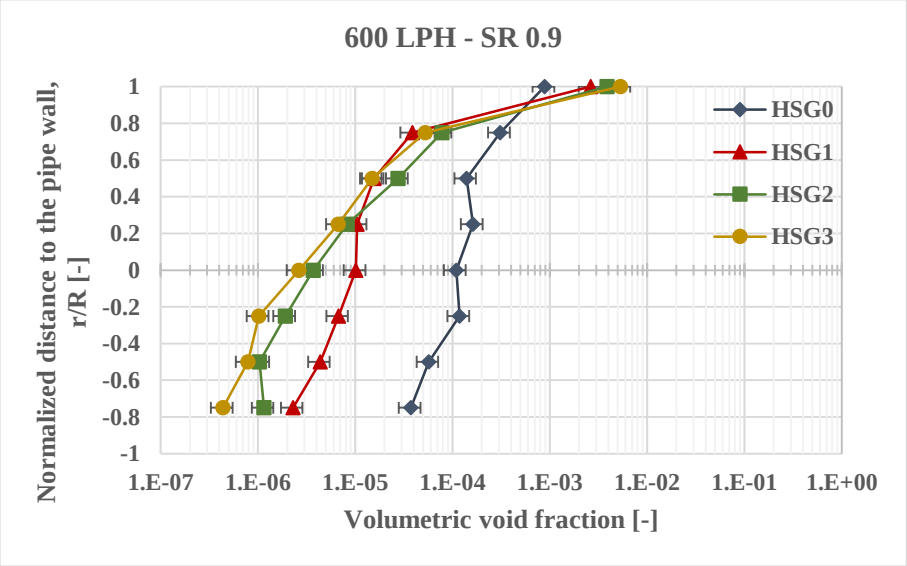

Figure 4-41. Bubble distribution development along the horizontal pipeline at 600 LPH and saturation ratio 0.9.

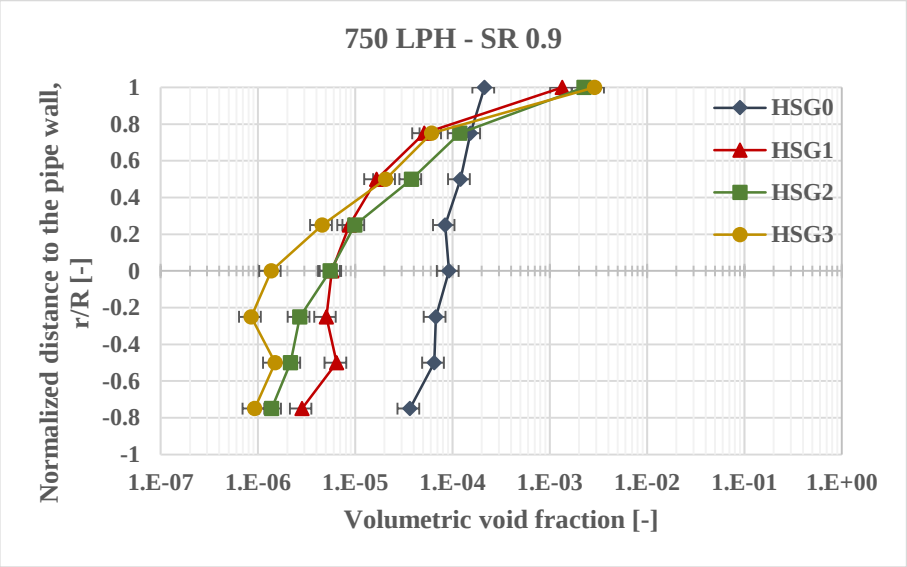

Figure 4-42. Bubble distribution development along the horizontal pipeline at 750 LPH and saturation ratio 0.9.

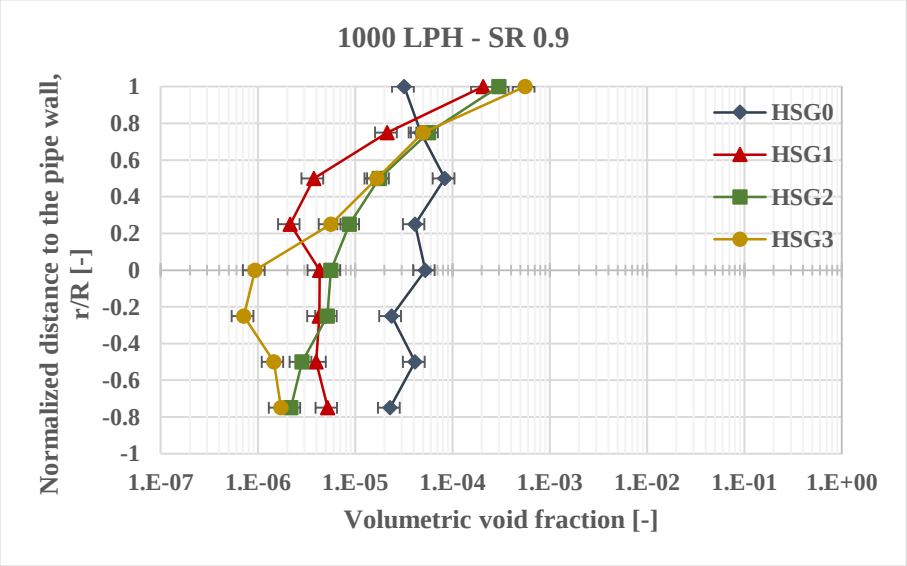

Figure 4-43. Bubble distribution development along the horizontal pipeline at 1000 LPH and saturation ratio 0.9.

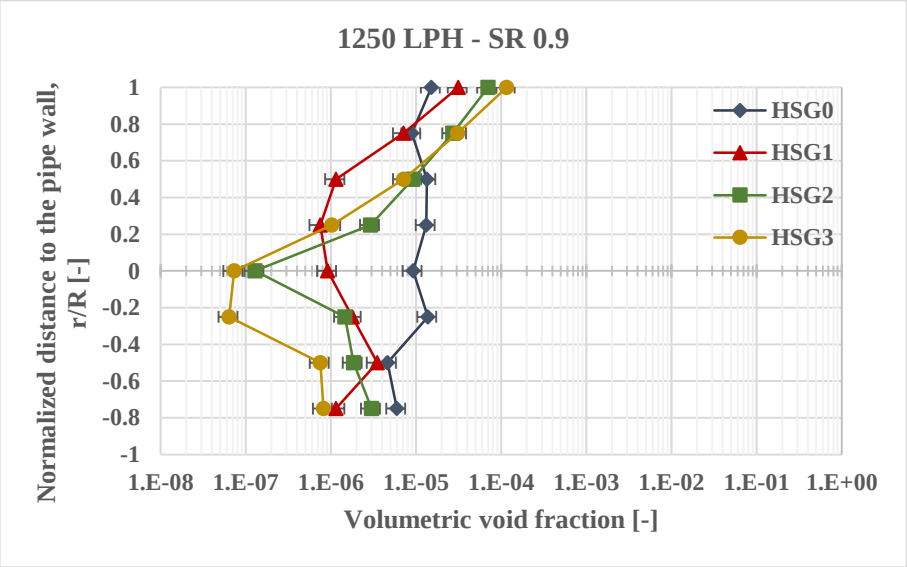

Figure 4-44. Bubble distribution development along the horizontal pipeline at 1250 LPH and saturation ratio 0.9.

Figure 4-37 illustrates bubble distribution developments at 600LPH during saturation ratio 0.75, where at first sight glass after the bend (HSG0), flow distribution is levelled compared to rest of the profiles along the axis. When the two-phase flow arrive at HSG1, void fraction at the top of the plane gets higher, and vice-versa at the bottom. Development of distribution profile continues along the horizontal pipeline to the next two positions (HSG2 and 3). Similar trends can be observed for higher flow rates and for saturation ratio 0.9 (**Figures 4-38** to **4-44**). However, fluctuations and flattening behaviours discussed previously in **Section 4.3.3**. are pronounced as velocity increases and average void fraction decreases. Nevertheless, void fractions at the upper part of the pipe continue to rise along the horizontal pipe for all of the measurements.

Two-phase flow development on horizontal pipes was investigated by Kocamustafaogullari & Huang (1994) as discussed in **Section 2.4.2.1.2**. Their observations were similar: levelled void fraction distributions at the inlet section of their test rig and continued development of flow structure with rising void fractions at the upper part of the pipe along the horizontal flow. They concluded that two-phase flow development is a continuous process and do not reach the so-called "fully-developed flow". In addition, Yadav, Kim, et al. (2014) point out the continuous build-up of gas phase on the top part of the pipe during bubble flow

development after 90 elbow . They also observed transition from bubbly flow to plug flow pattern further downstream of the bend and argued that migration of bubble to the top part of the pipe is due to the buoyancy effects and this accumulation leads to the coalescences phenomenon.

After assessing the studies conducted regarding the bubbly flow development in horizontal pipes, it is concluded that the experiment results in the current study agrees well with the observations in the literature. Moreover, it is generally agreed that the development of two-phase flow is a continuous process along the horizontal pipe line and accumulation of bubbles at the upper part of the pipe increases along the horizontal pipe.

4.4 Bubble Size Distributions across the Pipe Section

Size distribution across the pipe section is an important parameter in the study of bubbly two-phase flow in pipes. Similar to bubble volume distributions, it can significantly vary according to pipe orientation and superficial velocities of phases. Average diameters measured (see **Section 3.5.3** for definition) at each focal plane (**Figures 3-27** and **3-28**) for vertical and horizontal pipes, are plotted against normalized distance to the pipe wall and presented in **Figures 4-45** to **4-56** of this section. The conditions utilized during the bubble size distribution measurements were identical to the conditions provided in **Table 4-1**. In other words, data obtained during bubble distribution measurements (see **Section 4.3** for more detail) were processed to create figures in this section.

4.4.1 Vertical downward flow

Average bubble diameter distributions across the positions on the vertical pipeline of the test rig are illustrated (VSG1 and VSG2) in the following **Figures 4-45** to **4-48**. Similar to the void fraction distribution graphs (see **Section 4.3.2**), x-axis represents normalized distance to the pipe wall (r/R), but y-axis is the average diameter in this case. Experimental data in this section was gathered during the bubble distribution measurements discussed in the previous section, and detailed positions of the vertical sight glasses were provided in **Figure 3-23**. First two figures (**Figures 4-45** and

4-46) are results for saturation ratio 0.75 for each vertical position, at four different velocities. Results at saturation ratio 0.9 are demonstrated in **Figures 4-47** and **4-48**.

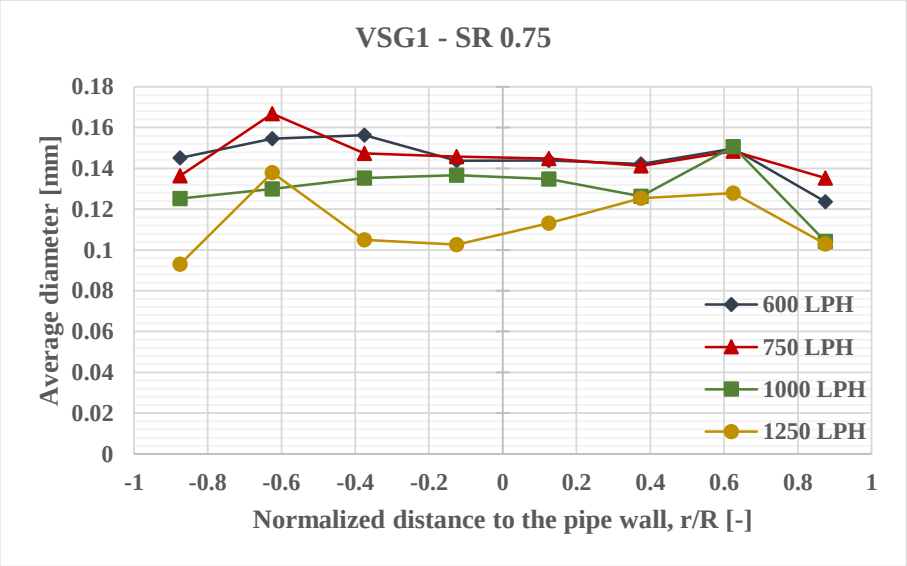

Figure 4-45. Average bubble diameter distribution across the pipe section at VSG1 and saturation ratio 0.75.

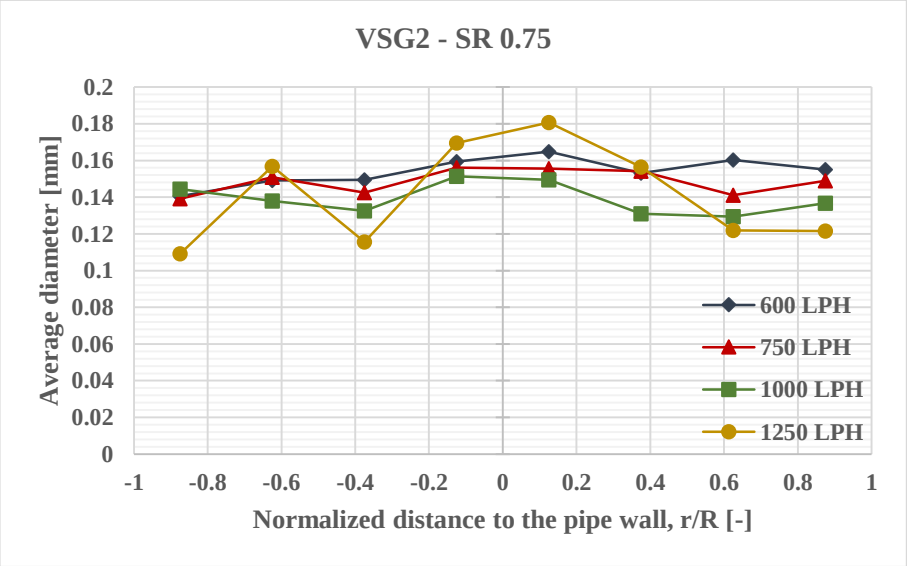

Figure 4-46. Average bubble diameter distribution across the pipe section at VSG2 and saturation ratio 0.75.

Bubble distributions in **Figure 4-45** show fluctuated profiles because of double 90 degree bend before its position (VSG1) and oscillations of the size distribution profile pronounces as the fluid velocity increases. Effect of liquid velocity on size distribution profiles at VSG1 are reasonable, since turbulence and the effect of the

bend significantly increases as the fluid velocity increases, especially right after the two bends. It can also be noted that average bubble diameters across the pipe section reduces as liquid velocity increases. This agrees well with the visual observation in Bhagwat & Ghajar (2012). Their experiments were conducted to show the effect of liquid velocity on bubbly flow at constant gas flow rates (see **Appendix 3** for their observation).

On the other hand, bubble size distribution profiles (**Figure 4-46**) develop until the flow reaches second position at the downstream of the pipe (VSG2), where profiles are more likely to peak at central positions rather than closer to the pipe wall. The effect of liquid velocity on average bubble size is similar to the first position as well. Comparable core-peak size distribution profiles were mentioned by Hibiki et al. (2004) and Hibiki et al. (2005). Their measurements also show that during bubbly flow through a circular pipe with a 25.4 mm diameter, larger bubbles tend to travel at inner sections and average bubble diameter gets lower when proceeded towards the pipe wall. Moreover, Kashinsky & Randin (1999)'s experiments with two different average bubble sizes revealed that smaller bubbles tend to approach closer to the pipe wall at higher velocities (1 m/s). Whereas, at low liquid velocities (0.5 m/s) there is no significant effect of bubble sizes on void fraction distribution. This can explain the pronounced centre-peaked average bubble size at higher flow rate in **Figure 4-46**.

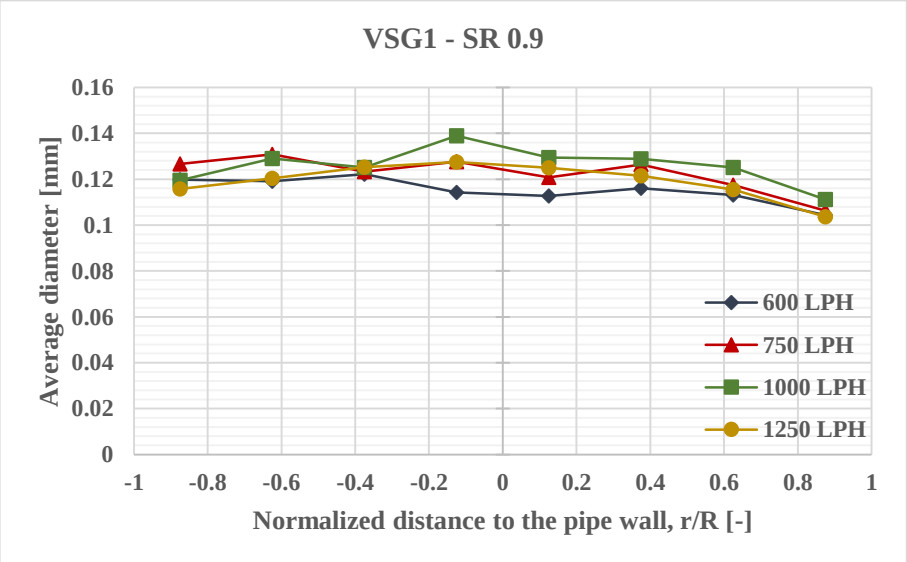

Figure 4-47. Average bubble diameter distribution across the pipe section at VSG1 and saturation ratio 0.9.

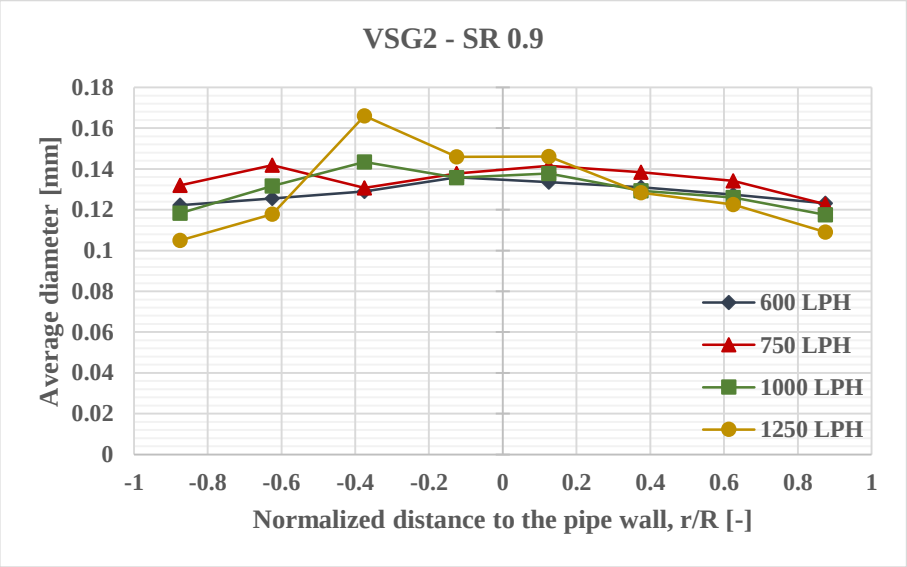

Figure 4-48. Average bubble diameter distribution across the pipe section at VSG2 and saturation ratio 0.9.

At saturation ratio 0.9 (**Figure 4-47**), even though less than the ones observed for saturation ratio 0.75, bubble size distribution fluctuations are still visible at VSG1, and centre-peaked average bubble sizes were obtained at VSG2 (**Figure 4-48**). This indicates that fluctuations are more likely to be suppressed as saturation ratio increases, thus, higher average void fractions and size distributions develop from VSG1 to VSG2 – similar to the results obtained for saturation ratio 0.75. Difference in average bubble sizes at each flowrate cannot be distinguished when compared to the results at saturation ratio 0.75. In general, for both saturation ratios, bubble size distributions developed along the vertical line, and at VSG2, bigger bubbles travelled in the middle of the pipe, whereas, at VSG1, size distribution profiles illustrated fluctuations because of double 90 degree bend. Moreover, noticeable centre-peak size distribution profile at VSG2 for both saturation ratios became evident.

4.4.2 Horizontal flow

Average bubble diameter distributions for each position on the horizontal pipe (see **Figure 3-24**) of the test rig are presented in **Figures 4-49** to **4-56**. Similar to the figures given for vertical downward flow results in the previous heading (**Section 4.4.1**), local average diameter distributions for each horizontal position are plotted against normalized distance to the pipe wall. However, the axes are switched and y-

axis became normalized distance to the pipe wall and x-axis, the average bubble diameter. Each figure is plotted for a particular horizontal position and includes results for 4 different flow rates in order to visualize the effect of flow rate on size distribution across the pipe section. The data for the following figures were also obtained during bubble distribution measurement discussed in **Section 4.3** and were processed to present size distributions.

First four **Figures 4-49** to **4-52**, are the results for saturation ratio 0.75. The significant difference between the vertical and horizontal flow can be noted instantly, where diameters average bubble tend to decrease across the depth, from top to bottom. On the other hand, in vertical downward bubbly flow, there is a more levelled size distribution in the middle section and bubble sizes get lower as the measurement point approaches the wall. During horizontal flow, a similar size reduction trend across the pipe section was observed by Andreussi et al. (1999) and Bottin et al. (2014): Andreussi et al. (1999) plotted maximum bubble size measured across the pipe section and demonstrated that it is decreasing from top to bottom; Bottin et al. (2014) plotted sauter-mean diameters measured across the pipe section during horizontal bubbly flow and their results showed the same trend.

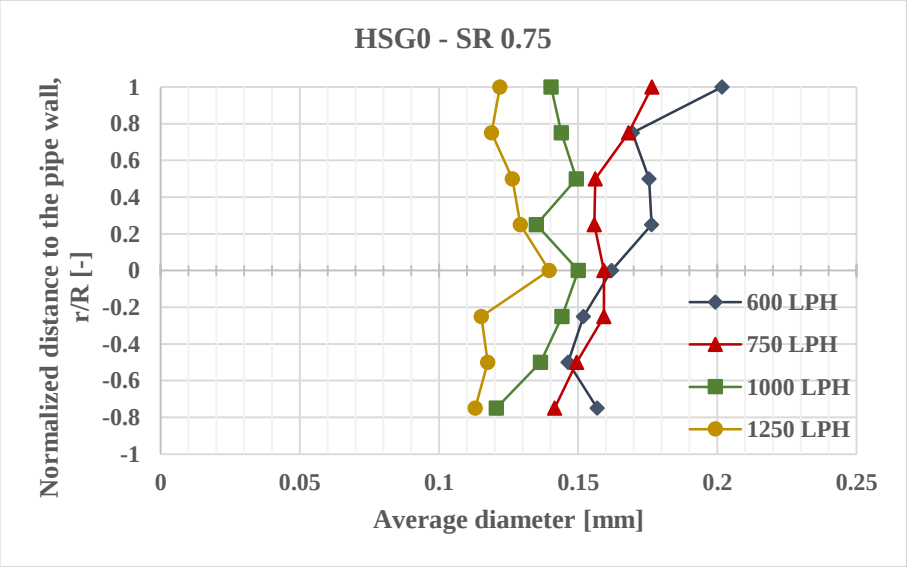

Figure 4-49. Average bubble diameter distribution across the pipe section at HSG0 and saturation ratio 0.75.

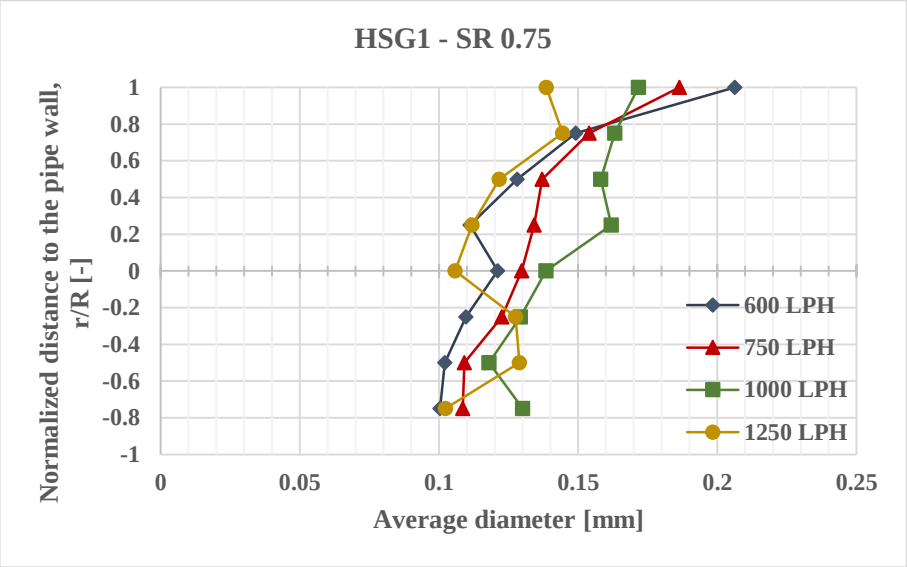

Figure 4-50. Average bubble diameter distribution across the pipe section at HSG1 and saturation ratio 0.75.

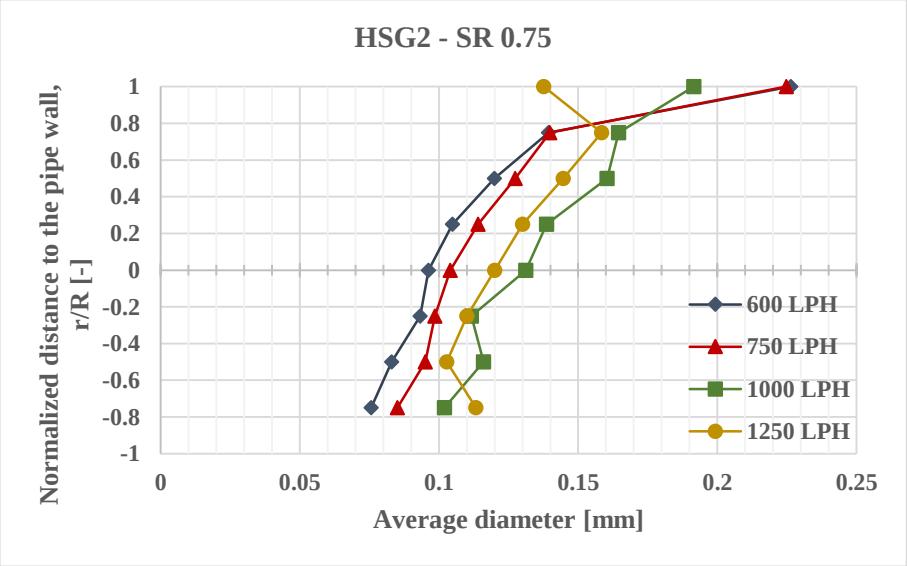

Figure 4-51. Average bubble diameter distribution across the pipe section at HSG2 and saturation ratio 0.75.

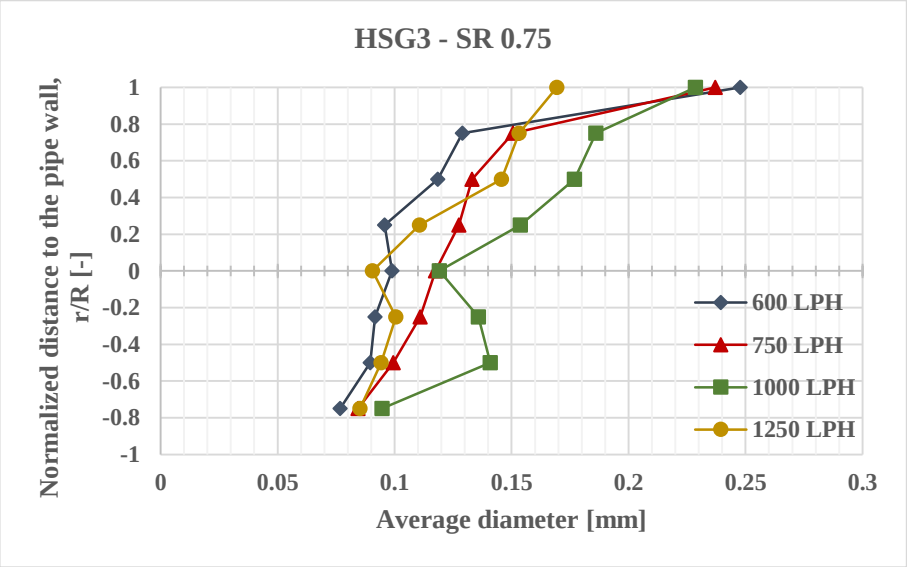

Figure 4-52. Average bubble diameter distribution across the pipe section at HSG3 and saturation ratio 0.75.

Bubble distributions at horizontal pipeline for both saturation ratios revealed a decrease in average bubble diameters from top to bottom. However, the profiles varied according to the flow rate at HSG0 (**Figures 4-49** and **4-53**). Effect of liquid right after the 90 degree bend was observed for void fraction distributions as well, which coincides with average bubble distribution. Average size distributions across the pipe section shows a flattening profile as the liquid velocity increases. At 1250 LPH, size profiles are nearly levelled across the pipe section. This is similar to the size distribution profiles observed at vertical downward flow. 90 degree bend effects the flow structure and increases turbulence, therefore, bubble diameters are levelled across the pipe section. Furthermore, from the rest of the positions, it can be noted that diameter distribution develops after HSG1 and exhibits a similar trends afterwards. All of the patterns observed at saturation ratio 0.75 is valid for saturation 0.9.

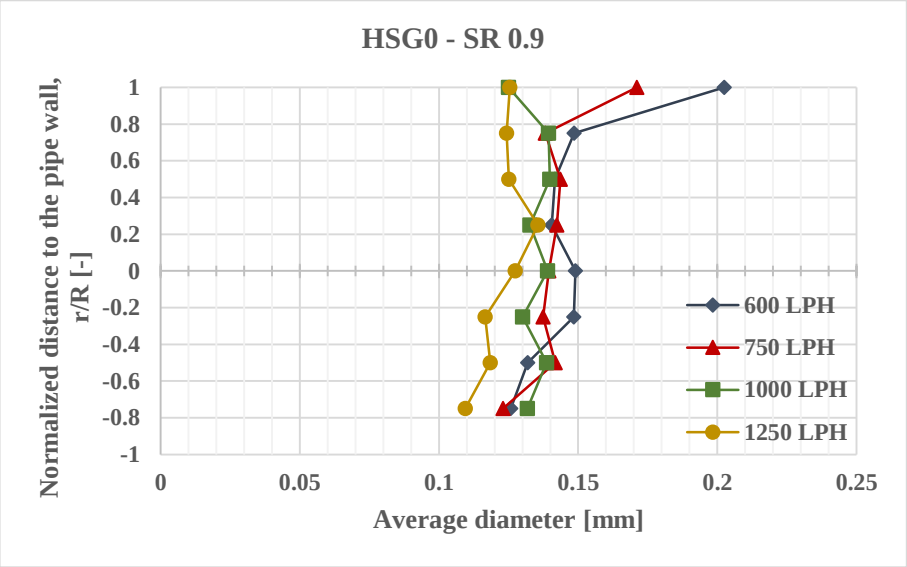

Figure 4-53. Average bubble diameter distribution across the pipe section at HSG0 and saturation ratio 0.9.

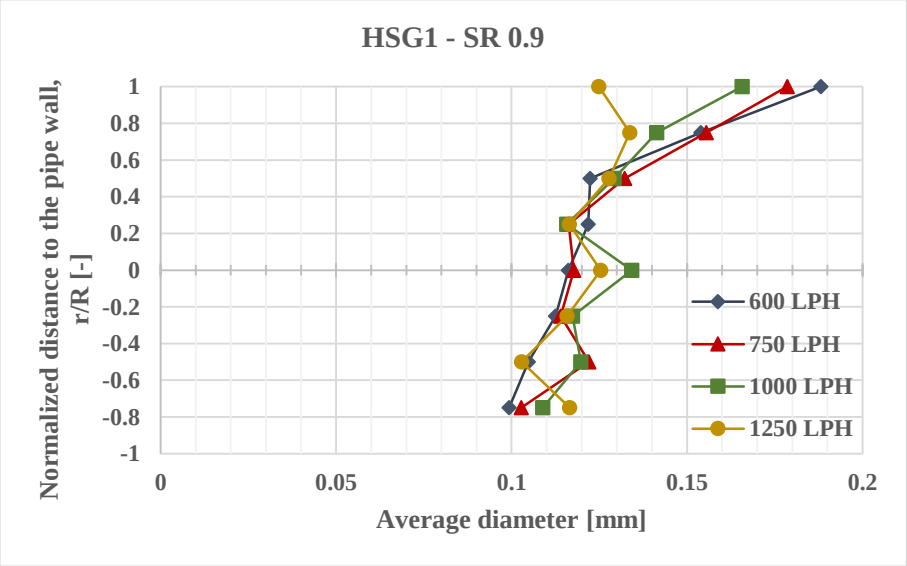

Figure 4-54. Average bubble diameter distribution across the pipe section at HSG1 and saturation ratio 0.9.

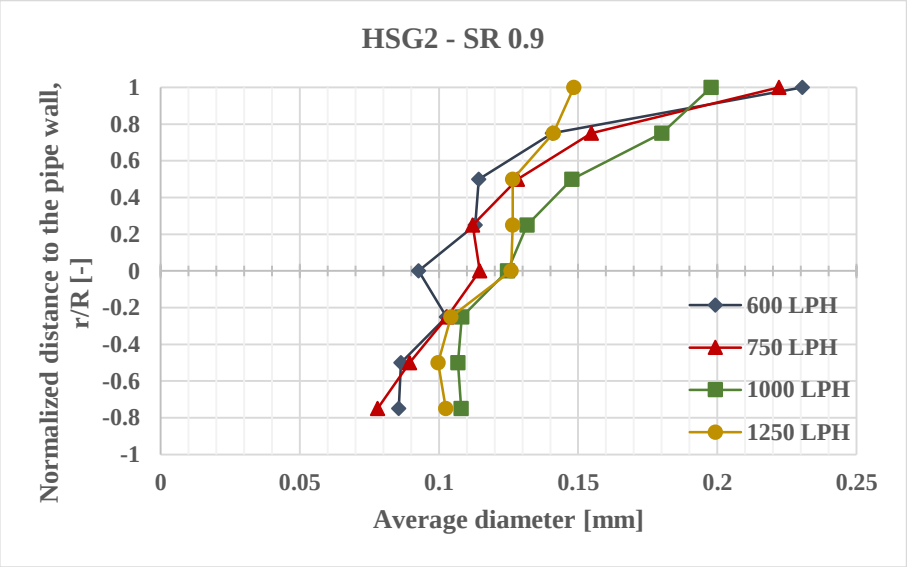

Figure 4-55. Average bubble diameter distribution across the pipe section at HSG2 and saturation ratio 0.9.

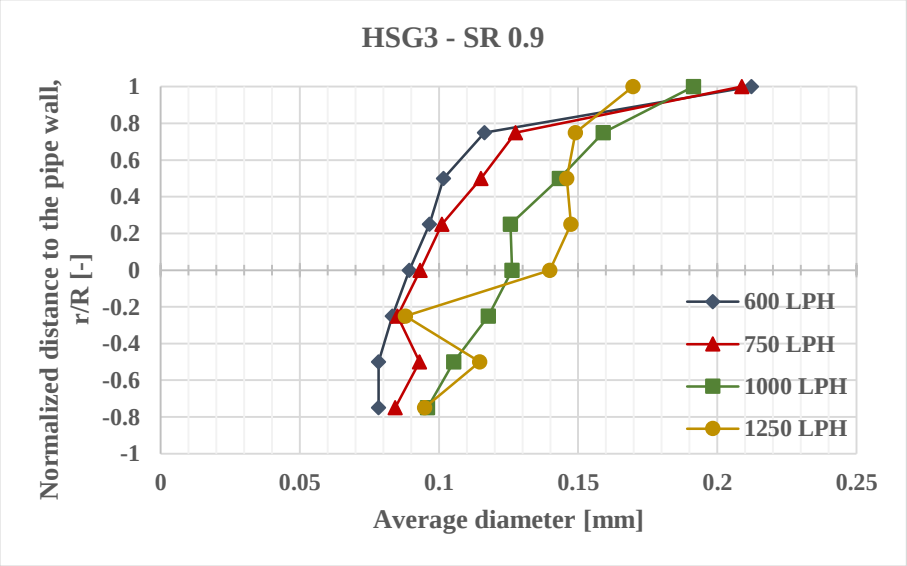

Figure 4-56. Average bubble diameter distribution across the pipe section at HSG3 and saturation ratio 0.9.

4.5 Bubble Velocity Profiles

In this heading, bubble velocity measurements across the pipe section for vertical and horizontal pipeline of the test rig will be presented. Details regarding the bubble velocity calculations are described in **Section 3.5.8**. There were four different flow

rates utilized in the current experiments, for each positions on the vertical and horizontal pipes. Moreover, focal plane number used for bubble velocity measurements was increased to 16 in order to assess velocity profiles in more detail. Focal planes shown in **Figures 3-27** and **3-28** were placed at 2 mm intervals with each other during bubble distribution measurements. However, distance between each focal plane was reduced to 1 mm for bubble velocity measurements. System conditions were kept undersaturated as summarized in **Table 4-1**. Bubble velocity distributions measured at each position is compared with the universal power-law given by De Chant (2005) to evaluate whether the power law (**Equation (4-1)**) can be used to predict bubble velocities across the pipe section in turbulent bubbly flow, as suggested by previous researchers (see **Section 2.4.2.2**).

$$\frac{u_l}{u_{max}} = \left(\frac{y}{R}\right)^{\frac{1}{n}} \tag{4-1}$$

Here, u_l is the local bubble velocity measured in each plane, u_{max} is the maximum bubble velocity measured across the pipe section for one particular flow rate, y is the distance to the centre of the pipe, R is the radius of the pipe, and n is the exponential constant that can be predicted according to each case.

4.5.1 Vertical downward flow

Bubble velocities right after the double 90 degree bend on vertical pipeline of the test rig are presented in the **Figures 4-57** and **4-58**. Figures in this section are plotted on graphs, where x-axis is the normalized distance to the pipe wall, and y-axis is the normalized local velocity. Details regarding the positions of sight glasses can be found in **Figure 3-23**.

At first position (**Figure 4-57**) bubble velocity profiles show high levels of fluctuations and the profiles do not agree well with the power-law profile plotted when n=4. However, as the flow develops and reaches VSG2 (**Figure 4-58**), bubble velocity profiles exhibit less fluctuations and agrees acceptably well with the universal power law profile. High level of fluctuations at VSG1 is attributed to the double 90 degree bend before its positions, where its effects on the flow structure are

thoroughly demonstrated in previous sections (**Sections 4.3** and **4.4**). Development of bubble velocity profile is clearly seen and shows that simple power-law can be used to predict bubbly flow measurement as predicted by previous researchers (see **Section 2.4.2.2**). Exponential constant n was determined to give best predictions for VSG2 at 4, therefore, n=4 was used for comparison in the rest of the experiments.

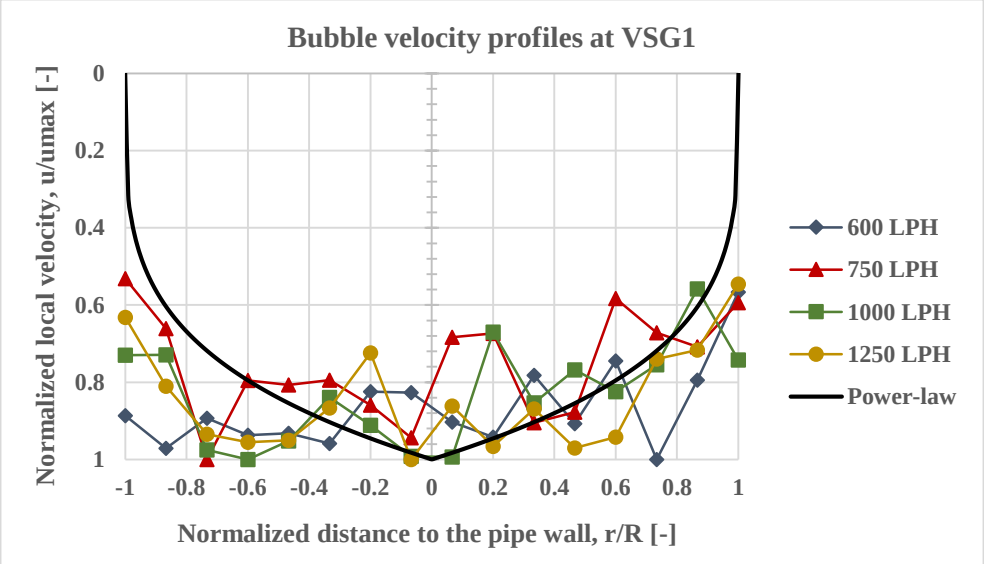

Figure 4-57. Bubble velocity profiles across the pipe section at VSG1.

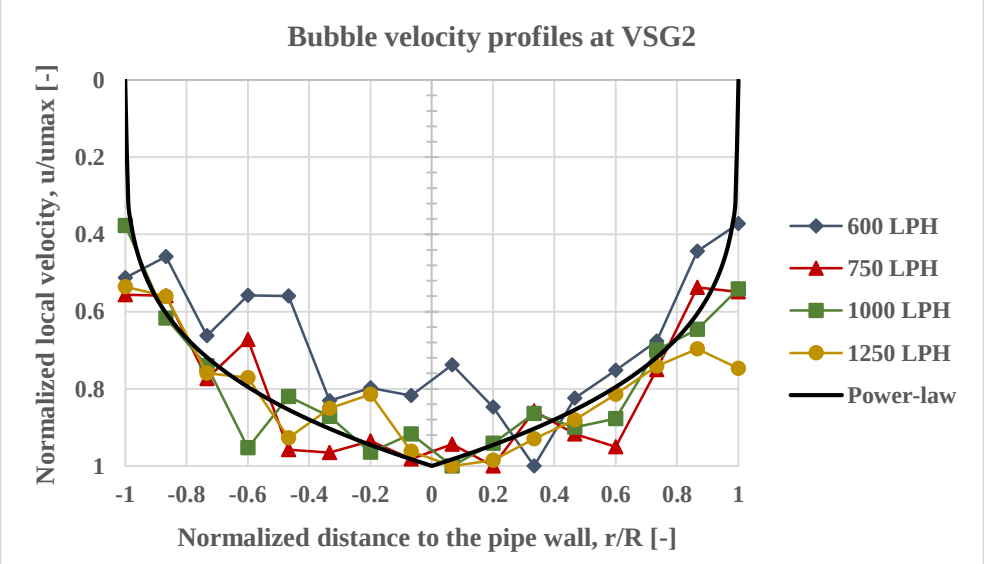

Figure 4-58. Bubble velocity profiles across the pipe section at VSG2.

Furthermore, **Table 4-2** summarizes the average bubble diameters across the pipe section at each vertical position for four different liquid flow rates. Average bubble

velocity measurements at each position are always lower than average bulk fluid velocity. This indicates that bubbles travel slower than the surrounding liquid. Similar observations were mentioned in the literature hitherto (see **Section 2.4.2.2**) and it is the result of buoyancy and drag forces.

Table 4-2. Average bubble velocity measurements at each vertical position.

Liquid flow rate (LPH)	Average bulk fluid velocity at pipe (m/s)	Average bubble diameter at VSG1 (m/s)	Average bubble diameter at VSG2 (m/s)
600	0.531	0.4977	0.5232
750	0.663	0.5911	0.6479
1000	0.884	0.8622	0.8356
1250	1.105	1.0166	1.0914

4.5.2 Horizontal flow

Bubble velocity measurements at horizontal pipeline of the test rig are presented in the **Figures 4-59** to **4-62**. Axes in the figures are shifted when compared to the results for vertical flow; x-axis is normalized velocity and y-axis is the normalized distance to the pipe wall. Detailed sight glass positions on horizontal pipeline of the test rig are provided in **Figure 3-24**. First sight glass (HSG0) is right after the 90 degree bend and the distance between each sight glass is increased gradually.

Similar to the bubble velocity measurements obtained at VSG1, high level of fluctuations were observed at HSG0 because of 90 degree bend before its position. However, bubble velocity profile again indicated development at horizontal pipeline, and the profiles tend to agree more with power-law predictions as the positions gets farther from the 90 degree bend, especially at HSG3 (**Figure 4-62**). The universal power-law profiles are well agreed with the bubble velocity measurements at HSG3 when the exponential constant n is 4.

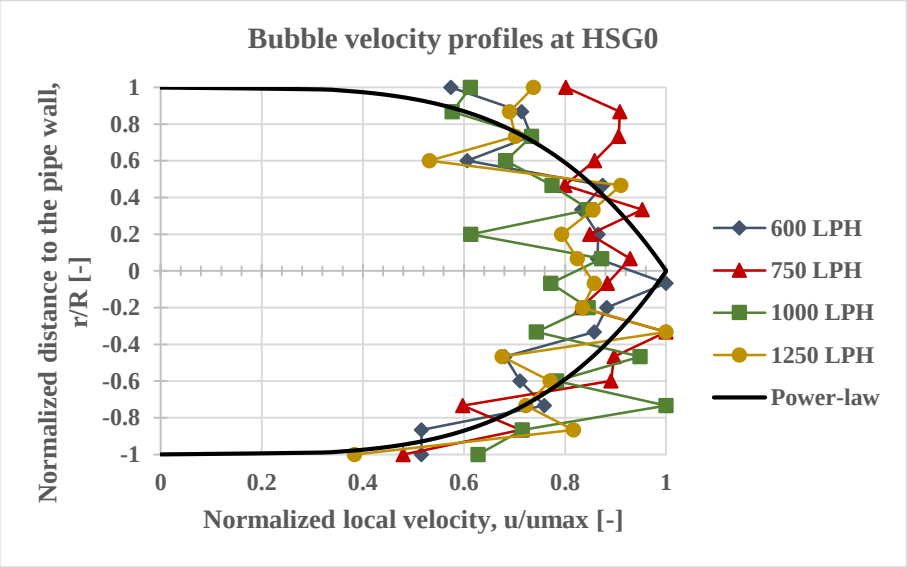

Figure 4-59. Bubble velocity profiles across the pipe section at HSG0.

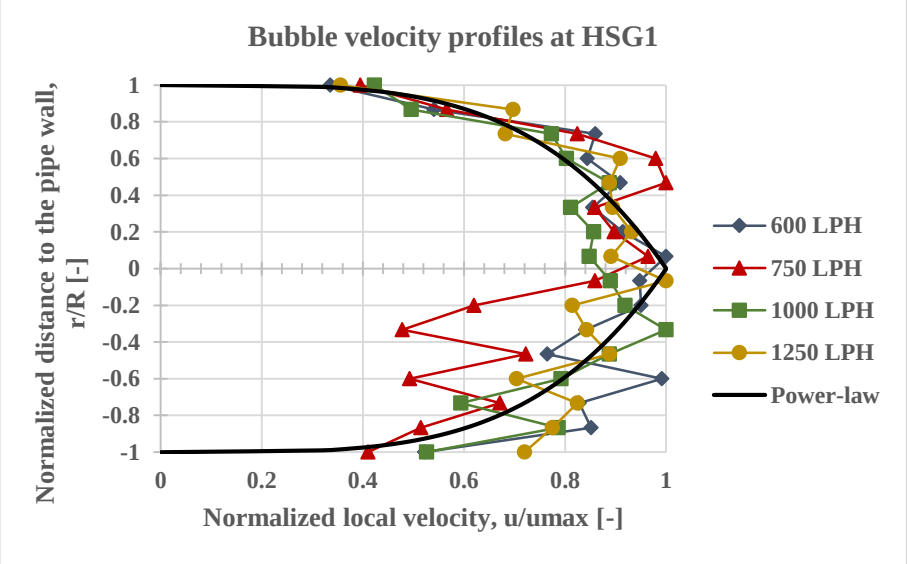

Figure 4-60. Bubble velocity profiles across the pipe section at HSG1.

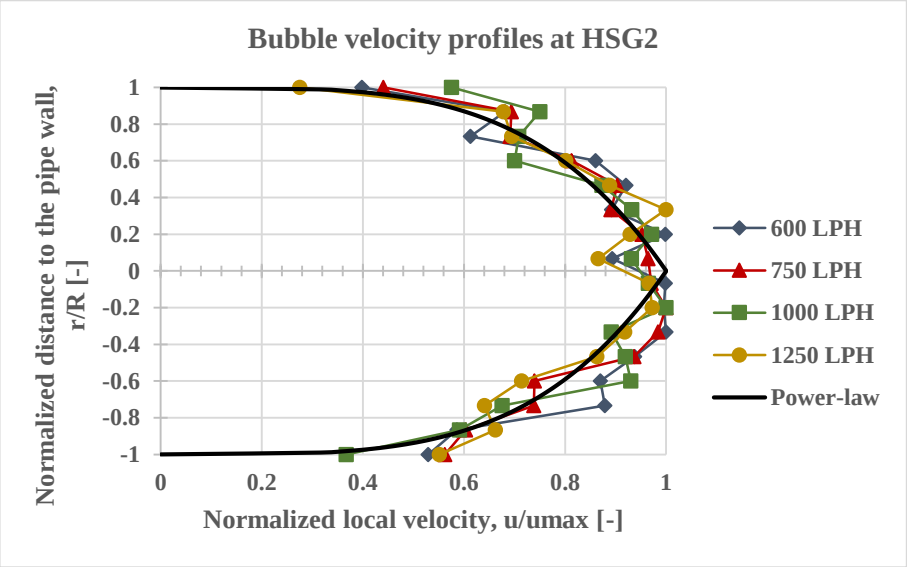

Figure 4-61. Bubble velocity profiles across the pipe section at HSG2.

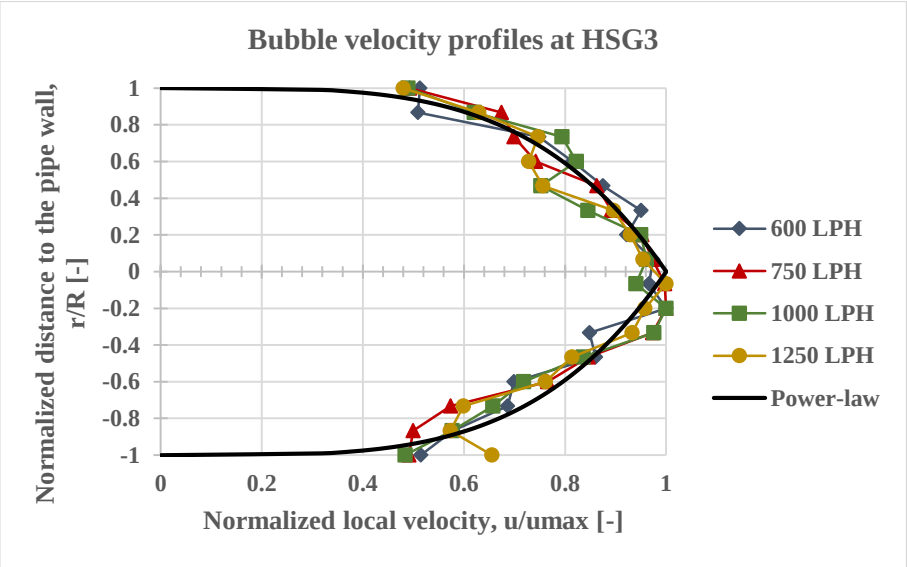

Figure 4-62. Bubble velocity profiles across the pipe section at HSG3.

Overall, bubble velocity measurement implemented in the current research achieved good results and is thought to be a suitable approach to be used in future studies. The analysis was quite uncomplicated and indicates good agreement with the power-law velocity profiles used in single phase flow. It has been concluded that, within the acceptable uncertainty range, simple power-law profiles can be used to predict bubble velocity distribution for bubbly two-phase flows occurring in wet central heating systems. Exponential constant is determined to be 4 in such cases, but further

tests need to be conducted for longer vertical pipes. Moreover, increasing the focal plane number and sample of bubble velocity measurements at each focal plane will give smoother velocity profile curves for further studies.

4.6 Bubble Sizes

Bubble sizes are another important parameter in the study of two-phase flow structures. Bubble sizes directly affect the available surface area for the mass, momentum or energy transfer between phases (Brennen 2005). In this regard, first, experimental results for the bubbles sizes at the boiler exit are presented in **Sections 4.6.1** and **4.6.2**. And afterwards, the factors which may affect bubble size development throughout pipework of central heating systems are discussed and presented in **Sections 4.6.3** and **4.6.4**.

4.6.1 Bubble size prediction at boiler exit

As explained in **Section 4.2,** bubble sizes at the boiler exit were measured at the first focal plane of the VSG1. The data presented here is the same data used in **Section 4.2**. Fsadni et al. (2011) cite bubble detachment prediction model derived by Winterton for finite contact angle and use it to compare experimentally measured bubble diameters at the boiler exit. They also develop an empirical equation to predict bubble sizes at boiler exit, again based on the fundamental study of Winterton. Their empirical equation takes into account the effect of system pressure and heating load on bubble sizes. However, as discussed in **Section 4.2**, experimentally measured bubble diameters do not indicate any change with system parameters, except for flow rate. Therefore, in this section, original bubble size prediction **Equation (4-2)** derived by Winterton for finite contact angle is used to compare the results at different system parameters.

$$\frac{r}{R} = 1.4\left[\frac{F(\theta)}{We}\right]Re^{0.24} \qquad \textbf{(4-2)}$$

Here, r is the bubble radius, R is the radius of the heat exchanger tube ($R = D_h/2$ and D_h is 7.9 mm), $F(\theta)$ is $\sin\theta_0 = (\cos\theta_r - \cos\theta_a)$, We is the Weber number ($We = \rho u^2 D_h/\gamma$), and Re is the Reynolds number ($Re = \rho u D_h/\mu$). Fsadni et al. (2011) argue that there are no available data to predict static contact angles to evaluate $F(\theta)$ for steel surfaces. However, they consider the extreme cases where $\theta_0 = 30°$, $\theta_r = 20°$ and $\theta_a = 40°$. Detailed information regarding the derivation and flow regime limit for utilization of the **Equation (4-2)** can be found in Fsadni et al. (2011).

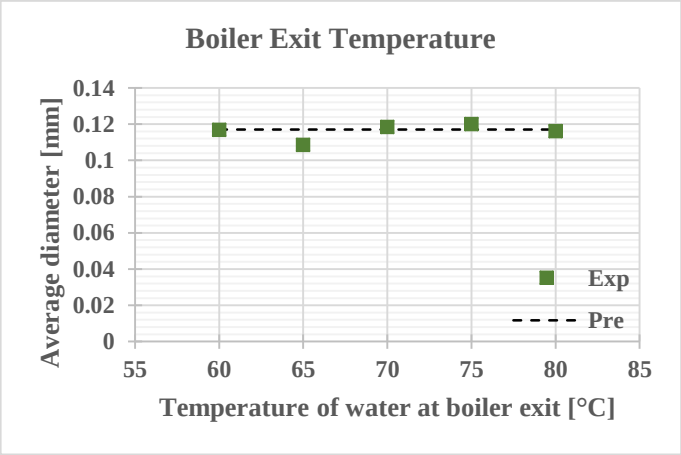

Figure 4-63. Comparison of bubble diameter prediction and experimental results at different temperatures.

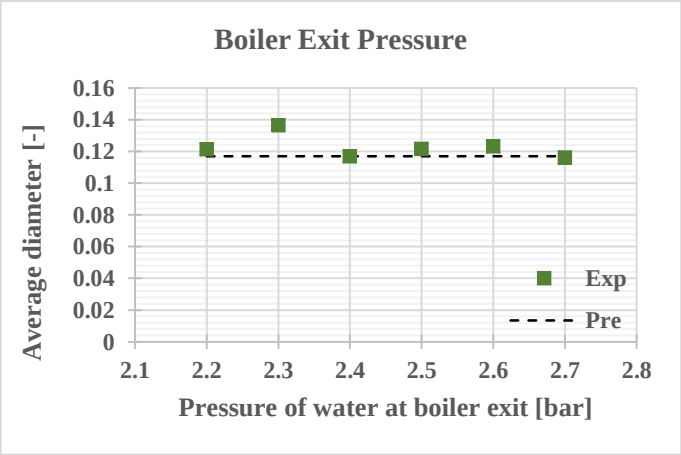

Figure 4-64. Comparison of bubble diameter prediction and experimental results at different pressures.

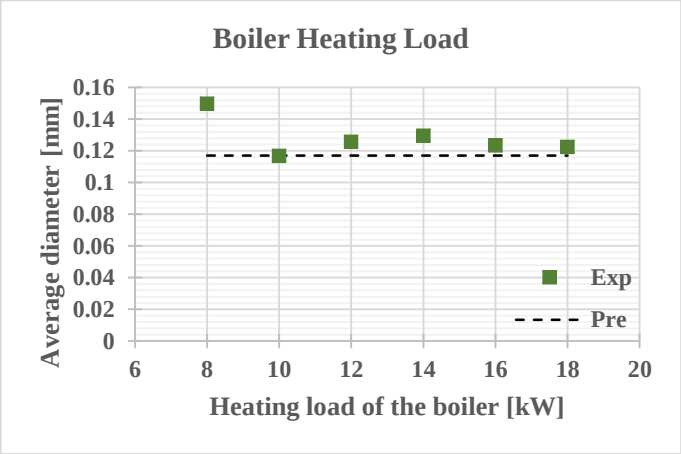

Figure 4-65. Comparison of bubble diameter prediction and experimental results at different heating loads.

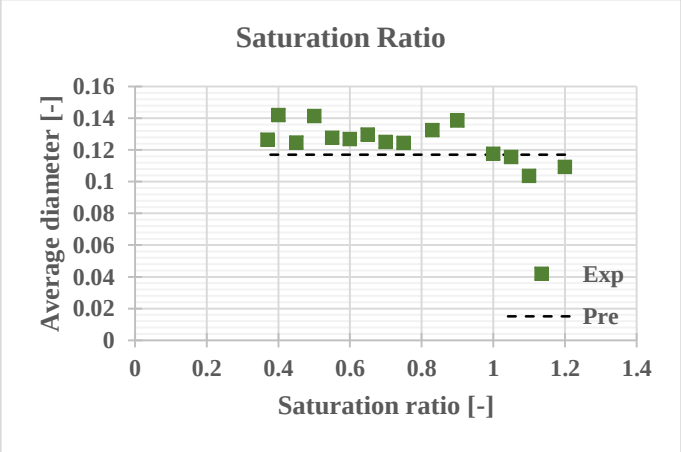

Figure 4-66. Comparison of bubble diameter prediction and experimental results at different saturation ratios.

Figures 4-63 to **4-68** present comparison of the bubble diameter predictions calculated with **Equation (4-2)** and the experimentally measured bubble sizes at the boiler exit. Predicted bubble size for 950 LPH was 0.117 mm, which is very close to the experimentally obtained bubble sizes in the figures, except for the results presented for flow rates (**Figure 4-67**). Experimental results at constant flow rate (**Figures 4-63** to **4-66**) show quasi-constant behaviour throughout the system conditions. This agrees well with the used equation, where bubble detachment size only varies with bulk fluid velocity.

In **Figure 4-67**, predicted bubble diameters and experimentally observed average diameters did not agree with each other. Moreover, because of the reasons discussed

in the **Section 4.2.5,** reduction in average bubble diameter as the flow velocity increases is not clear. Double 90 degree bend before the measurement position is highly effective on the bubble volume and size distributions at VSG1, which is in line with the results in **Section 4.4.1**.

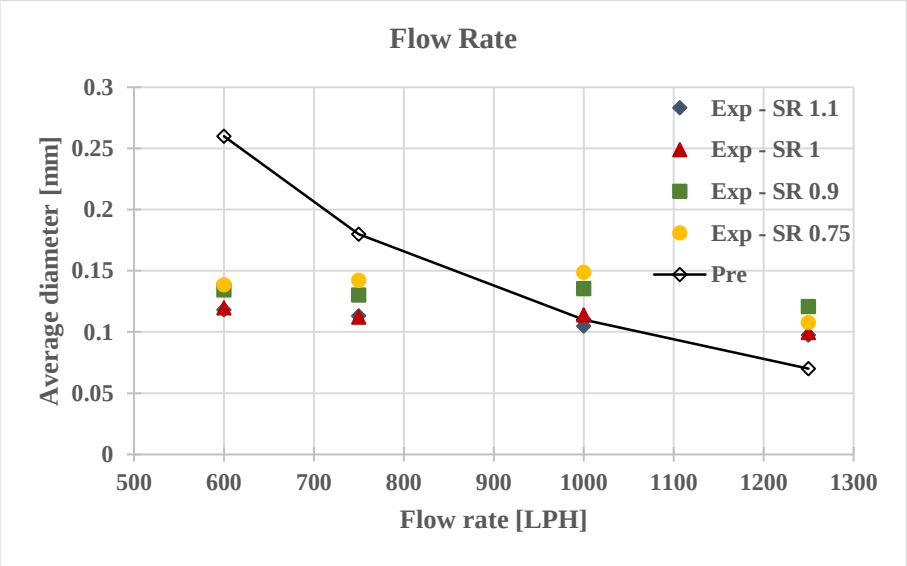

Figure 4-67. Comparison of bubble diameter prediction and experimental results at different flow rates.

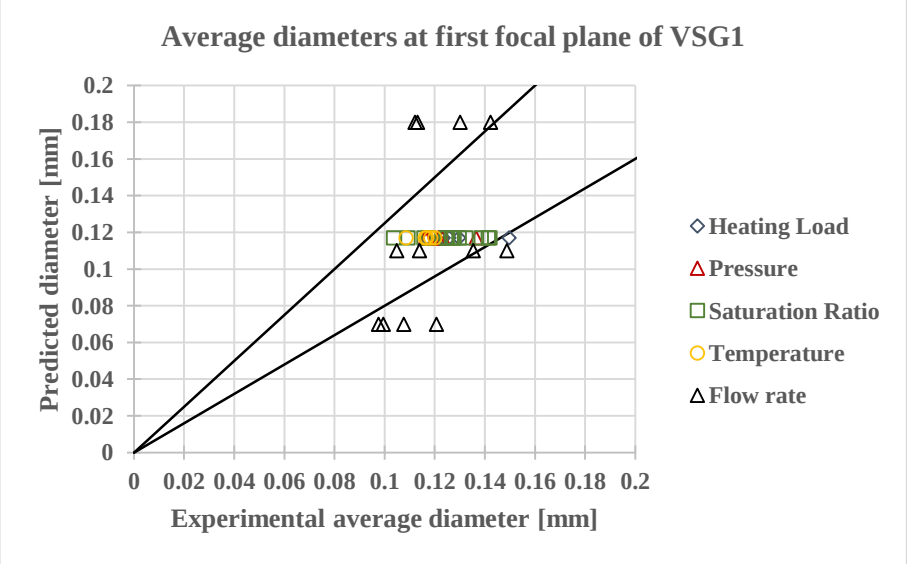

Figure 4-68. Comparison of bubble diameter prediction and experimental results at different system conditions.

Figure 4-68 represents the results and predicted bubble sizes for all of the experimental results conducted at the first focal plane of VSG1. Solid lines represent

the 20% error range between the predicted and the experimented results. Results at constant flow rate (heating load, pressure, saturation ratio, and temperature) fall in the region of 20% error, while most of the experimental results for varied flow rates fall out. This indicates that, bubble detachment prediction provided in **Equation (4-2)** can be used to predict average bubble diameters with an uncertainty level of 20% at measured position provided that utilized conditions are at constant 950 LPH flow rate. However, at different flow rates, this model does not provide reasonable agreement. Therefore, further investigation is needed.

4.6.2 Bubble size distributions at boiler exit

Particle size distribution is an important feature of two-phase flow, where one phase is dispersed into another. There are two types of particle size distributions: monodisperse or polydisperse. Monodisperse is defined as a size distribution where almost all bubbles have similar sizes, whereas, in polydisperse flow, bubble size distributions spread to a large diameter range. In general, if the standard deviation of the particle distribution in a sample is less than 10%, the distribution type can be called monodisperse (Crowe et al. 2012).

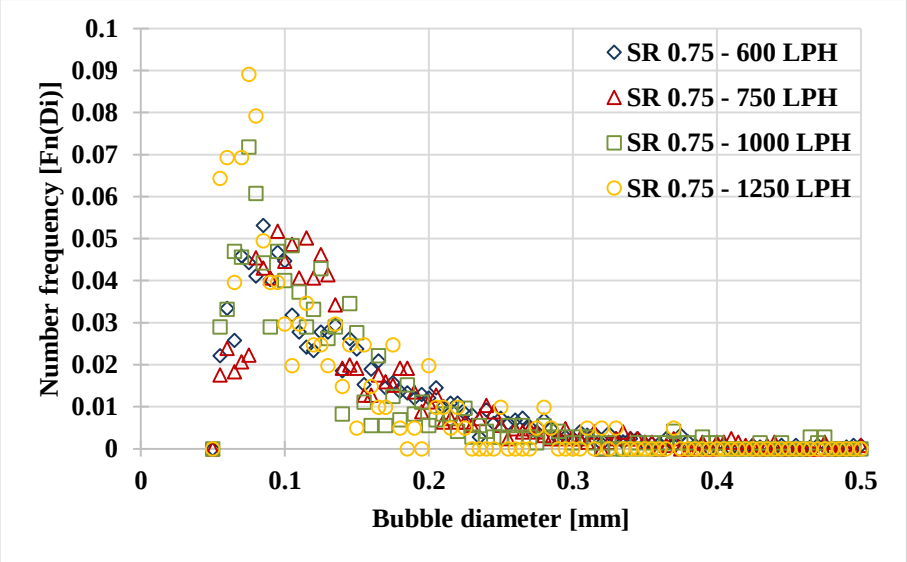

Figure 4-69. Bubble size distributions at VSG1 during saturation ratio 0.75.

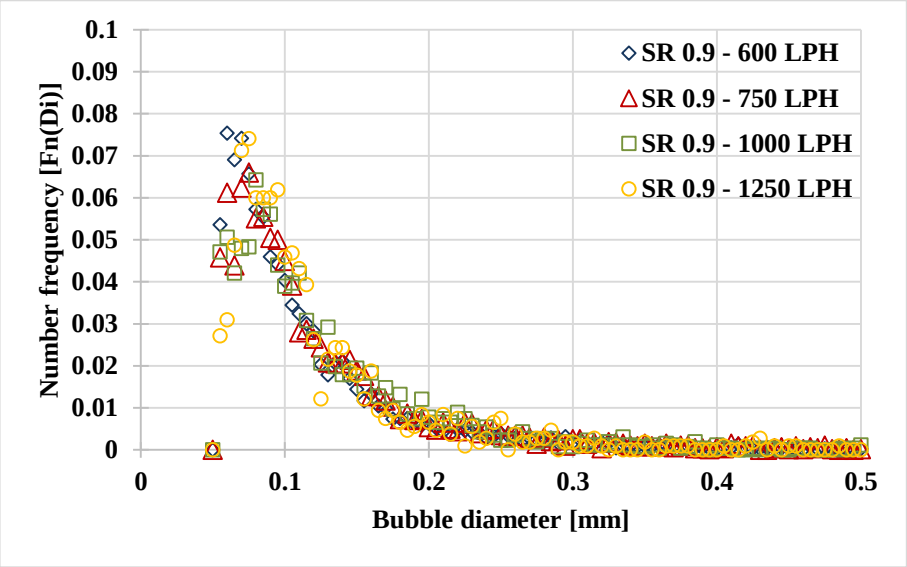

Figure 4-70. Bubble size distributions at VSG1 during saturation ratio 0.9.

Figure 4-69 and **4-70** present the size distributions of the bubble diameters measured at all focal planes of VSG1 during bubble distribution measurements explained in **Section 4.3**. There are two saturation ratios (0.75 and 0.9) and four different flow rates (600, 750, 1000 and 1250). First of all, it is worth mentioning here that standard deviation of all of the data sets in the figures were larger than 10%, which clearly indicates that size distribution is polydisperse. In order to plot these figures, bubble diameters ranging from 0.05 to 0.5 are divided into 0.005 mm intervals. Later, number of bubbles that fall into each bin category is counted and divided to the total number of bubbles in the sample. This operation gave the number frequency of bubbles in each bin category, where the sum of all number frequencies equalled to unity.

At saturation ratio 0.75 (**Figure 4-69**), bubble size distribution shows a sharp increase until 0.08-0.09 mm at the beginning, then reaching an infection point at around 0.1 mm. Later, number frequency at each bin size lowers slowly as the bubble diameters get larger. Similar size distribution profiles are noted at saturation ratio 0.9 (**Figure 4-70**), where inflection point is decreased slightly relative to the distributions at SR 0.75 (to 0.8 - 0.9 mm). However, the distribution profile is more precise compared to the results at saturation ratio 0.75. This shows that, as the

number of bubbles in each sample increases, bubble distribution profiles turn stable, becoming even more pronounced as saturation increases in central heating systems.

There are different kinds of size distribution functions that can be used to represent specific particle size distributions. Two of the most typical ones that are used in particle size investigations are log-normal and rosin-rammler distributions. Log-normal distribution is generally used to define the size of solid particles, whereas, rosin-rammler distribution is commonly used for droplet sizes in sprays (Crowe et al. 2012).

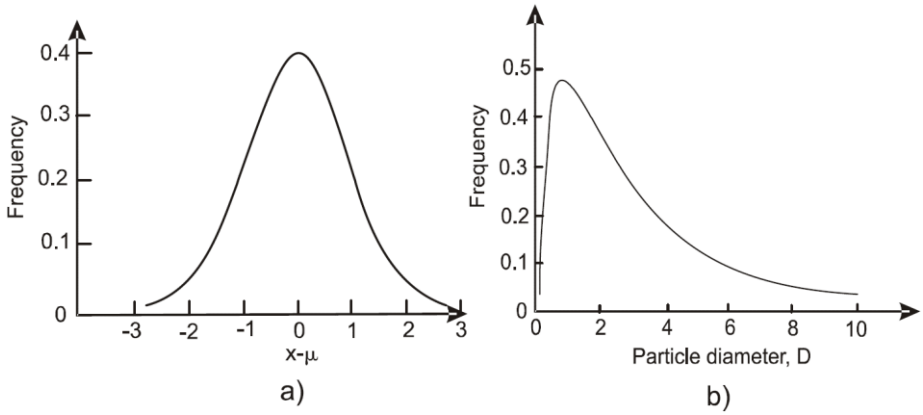

Figure 4-71. Difference between a) Normal Gaussian and b) Log-normal distributions (Crowe et al. 2012).

Figure 4-71 demonstrates the difference between normal and log-normal distributions. It can be clearly seen that log-normal distribution on the right side of the figure is very likely to define the profiles observed in the **Figures 4-69** and **4-70**. Furthermore, Razzaque et al. (2003) also reported that log-normal distribution function can be used to evaluate bubble sizes in two-phase bubbly flow. Therefore, it can be confidently concluded that log-normal frequency distributions can be used to represent bubble size distributions at the boiler exit of the wet central heating systems. **Equation (4-3)** is the log-normal distribution equation noted in Crowe et al. (2012).

$$f_n(D) = \frac{1}{\sqrt{2\pi}\sigma_o} exp\left[-\frac{1}{2}\left(\frac{\ln D - \ln D_{nM}}{\sigma_o}\right)^2\right]\frac{1}{D} \qquad \textbf{(4-3)}$$

where D_{nM} is the median diameter of bubbles in the sample and σ_o is the standard deviations of the bubble sizes.

4.6.3 Break-up and Coalescences

Bubble break-up and coalescences phenomena were assumed to be negligible by Ge et al. (2013) and Fsadni & Ge (2012) while they were modelling dissolution of bubbles in the wet central heating systems pipework. They proposed that small bubble diameters measured in such systems would not lead to any break-up events. Moreover, low void fractions observed throughout the pipeline reduces the possibility of bubble collisions that can lead to coalescences. After reviewing the study of Razzaque et al. (2003), it is thought that the first assumption—bubble break-up, where small bubbles observed in central heating systems will not lead to any breakage event—is reasonable. Because, their theoretical calculations for the maximum bubble diameter that can remain stable in the case of a break-up event is relatively high, compared to the bubbles diameters found in central heating systems. However, second assumption, coalescences phenomenon, is questionable since similar low void fractions were utilized by Razzaque et al. (2003), where they investigated the effect of coalescence on bubble distributions. This indicates that there is a possibility of bubble collision in relatively low void fractions as well, especially at the upper part of the pipe during horizontal flow.

This challenge was overcame after capturing the sequence shown in **Figure 4-72**. Here, the coalescences of two bubbles were filmed at the horizontal pipeline of the test rig. Coalescences of two bubbles is a very fast process, hence, it is very difficult to capture. The sequence was captured at the highest possible frame rate, employed for the bubble velocity measurements explained in **Section 3.5.8**. The sequence was captured during bubble velocity measurements at the first focal plane of horizontal pipe position HSG1. System conditions were typical: boiler exit temperature was 80 °C, pressure was 2.7 bar., flow rate was 1250 LPH, and saturation ratio was around 1.

In the series of frames, it can be clearly observed that two bubbles are approaching to each other and then, colliding to form a bigger new bubble. It is believed that the

sequence demonstrated in **Figure 4-72** provides a strong evidence for the occurrence of bubble coalescences in central heating systems, even when void fractions are relatively low. Therefore, the effects of bubble coalescences during the bubbly pipe flow cannot be neglected and should be taken into account in further investigations.

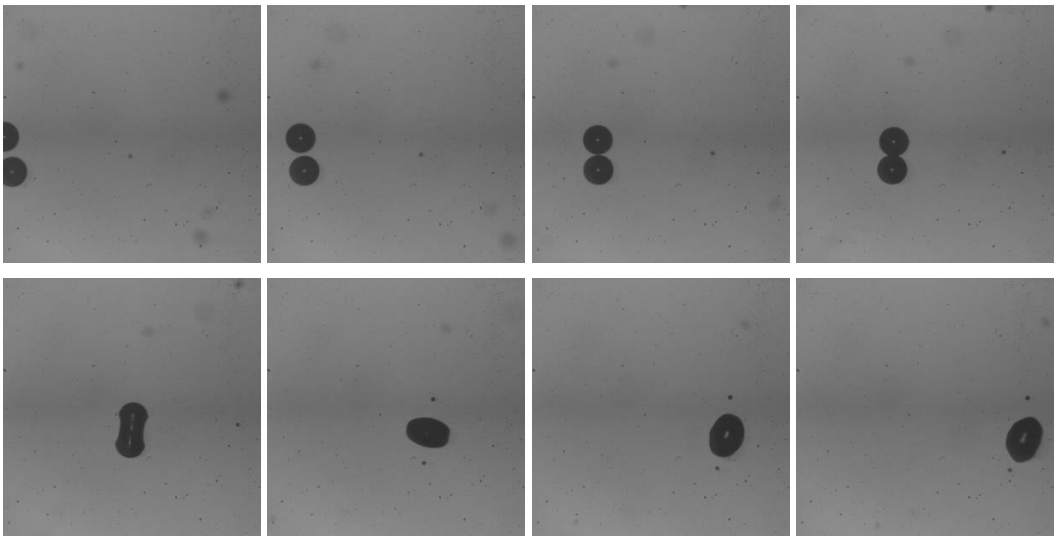

Figure 4-72. Coalescences phenomenon captured during horizontal flow.

The concepts of maximum bubble diameter (d_{max}), that can resist break-up, and minimum bubble diameter (d_{min}), that is stable against coalescences, were reviewed in **Section 2.4.2.3.1**. Theoretical calculations of d_{min} and d_{max} for mobile bubble surfaces provided in **Equations (2-10)** and **(2-14)** were solved for the flow rates utilized in bubble distribution measurements (see **Section 4.3**). **Equations (2-10)** and **(2-14)** were chosen rather than the equations provided for immobile surfaces by Thomas (1981), because there were no surfactants used in the current study. **Table 4-3** and **Figure 4-73** summarize the results of the theoretical calculations of d_{min} and d_{max} for bulk fluid velocities employed during the experiments.

Table 4-3. Theoretical d_{min} and d_{max} calculations.

Flow rate (LPH)	Bulk fluid velocity (m/s)	d_{min}	d_{max}
600	0.531	1.20028	17.79835
750	0.663	0.9545	13.9418
1000	0.884	0.7095	10.15982
1250	1.105	0.5637	7.9485

Calculated d_{min} and d_{max} values presented in **Table 4-3** indicate that bubbly flow in central heating systems are in coalescences dominant regime. Because, most of the bubbles observed right after the boiler, consist of bubbles with smaller diameter than d_{min} (see **Figures 4-69** and **4-70**). Therefore, the expected outcomes is a continuous increase in maximum bubble diameter or at least an increase until maximum bubble dimeter outruns d_{min} as the flow travels through the system pipework. However, steady increase in maximum bubble diameter may continue until it reaches d_{max} and then bubbles bigger than d_{max} will start to break-up to maintain the bubble sizes lower than d_{max}. Moreover, results for d_{max} point out that break-up phenomenon is not likely to happen in such systems because, calculated d_{max} is significantly larger than maximum bubble diameters observed throughout the pipework (see **Figures 4-74**, **4-75**, **4-78** and **4-79**).

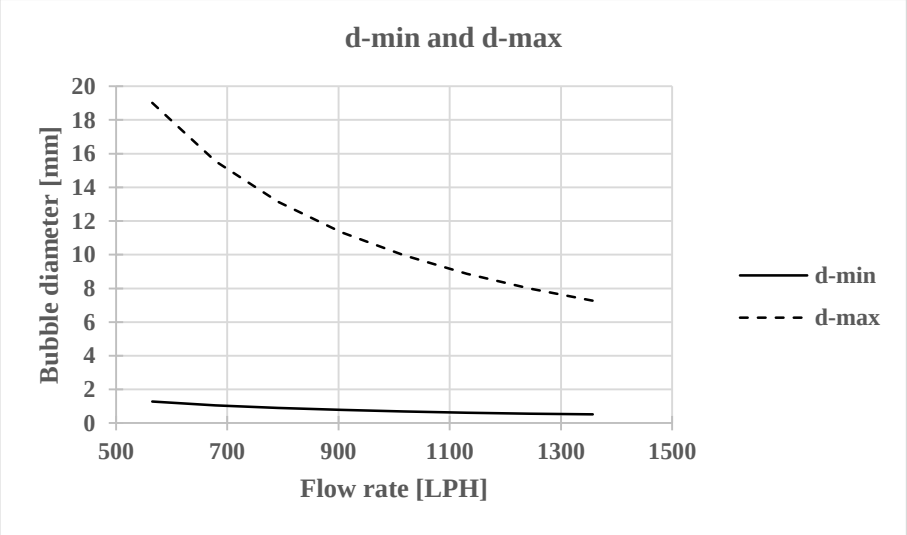

Figure 4-73. Theoretical d_{min} and d_{max} calculations.

Coalescences phenomenon at vertical downward and horizontal flows are presented in terms of maximum bubble diameter observed in each position at two saturation ratios and four different flow rates. Data presented in the following two sections were gathered during bubble distribution measurements demonstrated in **Section 4.3**.

4.6.3.1 Vertical downward flow

Maximum bubble diameters measured at each position on vertical pipeline of the test rig are illustrated in **Figures 4-74** to **4-75**. Y-axes represent the maximum bubble diameter and x-axes the normalized distance to the 90 degree bend, where L/D=7.5 is

VSG1 and L/D=56 is VSG2. Results for saturation ratio 0.75 (**Figure 4-74**) indicate that maximum bubble sizes increase as the flow travels from VSG1 to VSG2, except for the lowest flow rate. At 600 LPH, there is a slight decrease. However, in **Figure 4-75**, increase in maximum bubble diameter occurred at two flow rates, 600 and 1250 LPH, and there is a reduction at 750 and 1000LPH. This was unexpected, therefore, comparison of maximum bubble diameters and theoretical d_{min} calculations is plotted in **Figures 4-76** and **4-77** to better evaluate the effect of coalescences on maximum bubble size.

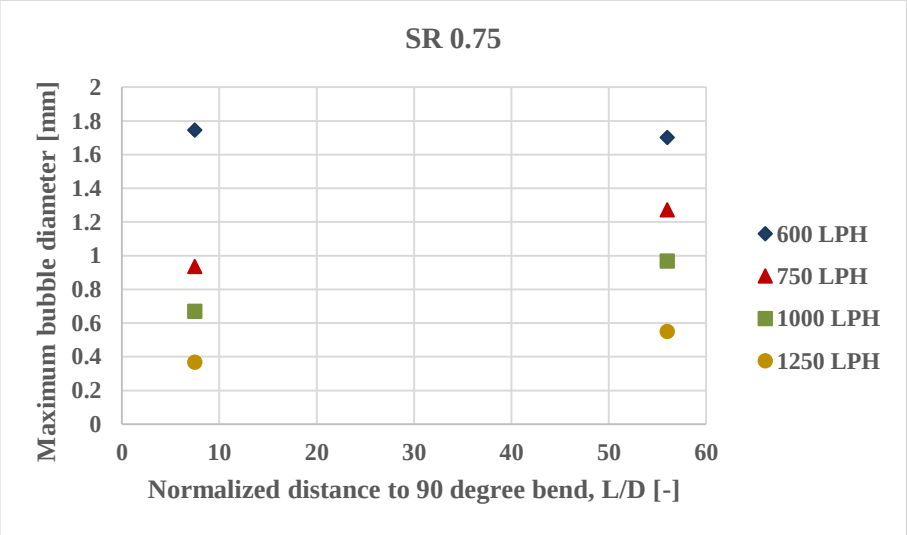

Figure 4-74. Maximum bubble diameters captured on vertical downward flow at saturation ratio 0.75.

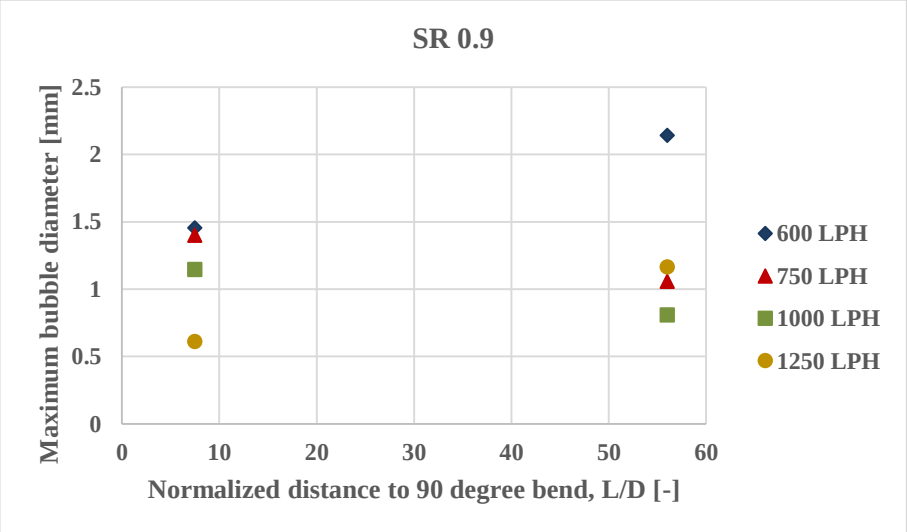

Figure 4-75. Maximum bubble diameters captured on vertical downward flow at saturation ratio 0.9.

Figures 4-76 and **4-77** demonstrate the comparison of maximum bubble diameter and theoretical d_{min} calculations. Y-axis is the maximum bubble diameter and x-axis represents flow rate of the system. **Figure 4-76** gives the results obtained at saturation ratio 0.75. The figure shows that for most of the conditions at VSG1, maximum bubble diameter is lower than the theoretically determined d_{min}, except at the lowest flow rate. At next position (VSG2), maximum bubble diameters increase above d_{min}, which agree well with expectations. Furthermore, maximum bubble diameters at the lowest flow rate are above the theoretical d_{min}, which confirms the fact that coalescence phenomenon becomes more dominant at lower superficial liquid velocities when compared to the higher liquid flow rates (Ishii et al. 2004).

On the other hand, maximum bubble diameters measured at saturation ratio 0.9 (**Figure 4-77**) demonstrates that all of the maximum bubble diameters measured at both positions are above the theoretically determined d_{min}. This indicates that coalescences phenomenon on the vertical pipeline of the test rig becomes pronounced at higher saturation ratios because of the increased bubble numbers. After the comparison of maximum bubble diameters with theoretical calculations (**Figures 4-76** and **4-77**), it is concluded that the unexpected decrease in maximum diameters shown in **Figures 4-74** and **4-75** are reasonable, since the maximum diameters are already above the theoretically calculated d_{min}.

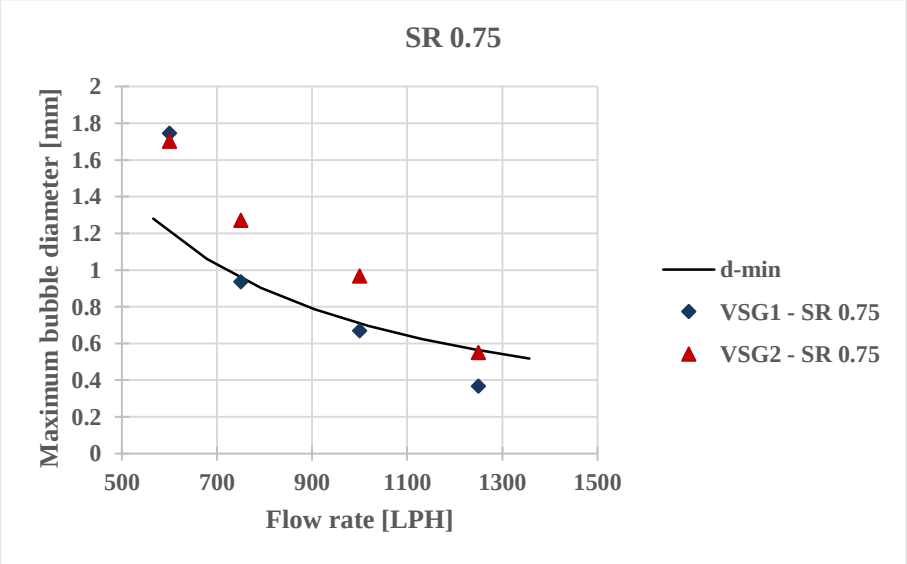

Figure 4-76. Comparison of maximum bubble diameter and theoretical d_{min} calculation at saturation ratio 0.75 during vertical downward flow.

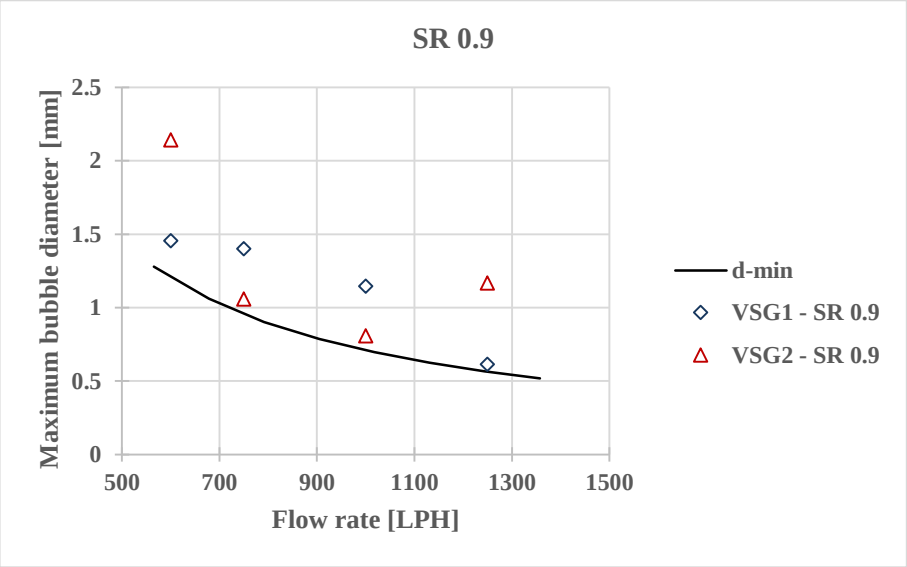

Figure 4-77. Comparison of maximum bubble diameter and theoretical d_{min} calculation at saturation ratio 0.9 during vertical downward flow.

4.6.3.2 Horizontal flow

Maximum bubble diameters measured at each horizontal pipeline position of the test rig are illustrated in **Figures 4-78** and **4-79**. Similar to the figures presented in the previous section, y-axes represent the maximum bubble diameter and x-axes the normalized distances to the 90 degree bend, where L/D=7.5, 28, 74.75, and 139.75 correspond to HGS0, HSG1, HSG2, and HSG3, respectively.

From both **Figures 4-78** and **4-79**, it can be clearly seen that there is a continuous increase in measured maximum bubble diameters as the flow travels from HSG0 to HSG3. This indicates that the increase in bubble diameters is due to the coalescences, since the flow conditions are undersaturated and there is no other possibility for bubble diameters to show this clear ascent. When compared to the vertical downward flow, the effect accentuates at horizontal flow, because bubble accumulation at the upper parts of the pipe increases the collision probability of bubbles. In **Figure 4-78**, there is a sharp increase from the first to the second positions for most of the flow rates, diminishing after the second position, except for the flow rate 750 LPH. It can also be said that growth in maximum bubble diameters becomes more dominant as the flow rates gets lower, similar to previous observations on vertical pipeline. In addition, maximum bubble diameters measured at saturation ratio 0.9 (**Figure 4-79**)

follow similar patterns with the results at SR 0.75. Elevation in maximum bubble diameter becomes more significant due to higher number of bubbles being present at higher saturations, especially at lower flow rates. Additionally, comparison of maximum bubble diameters and theoretical d_{min} calculations for the horizontal pipeline is plotted in **Figures 4-80** and **4-81**.

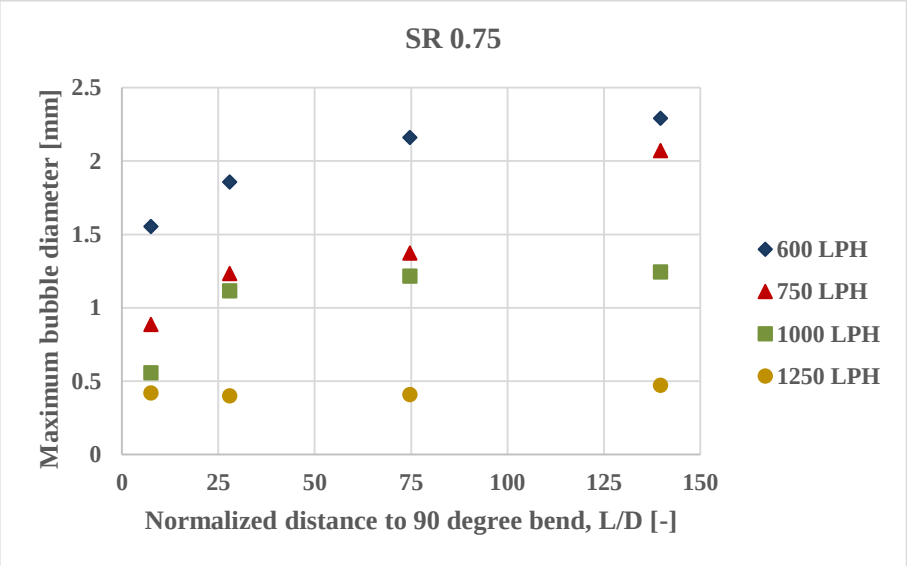

Figure 4-78. Maximum bubble diameters captured on horizontal pipeline at saturation ratio 0.75.

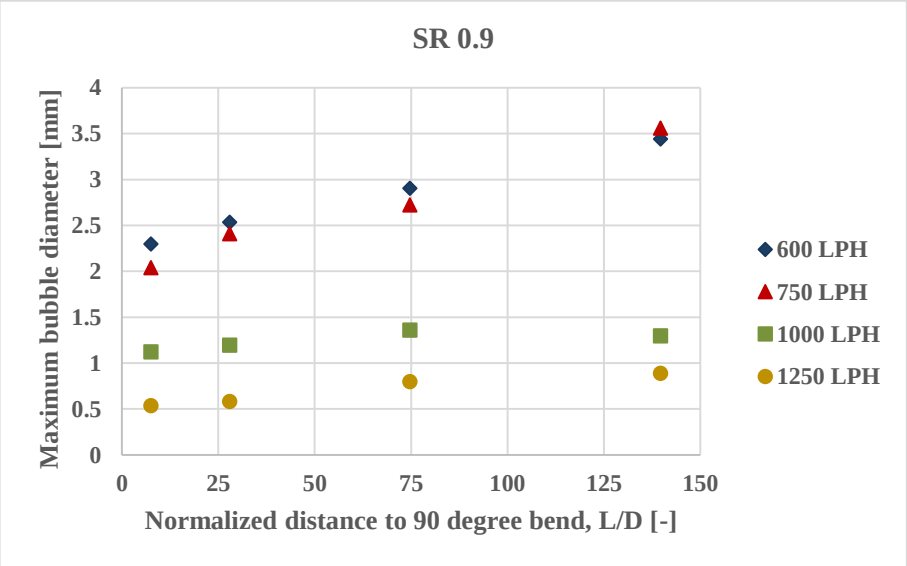

Figure 4-79. Maximum bubble diameters captured on horizontal pipeline at saturation ratio 0.9.

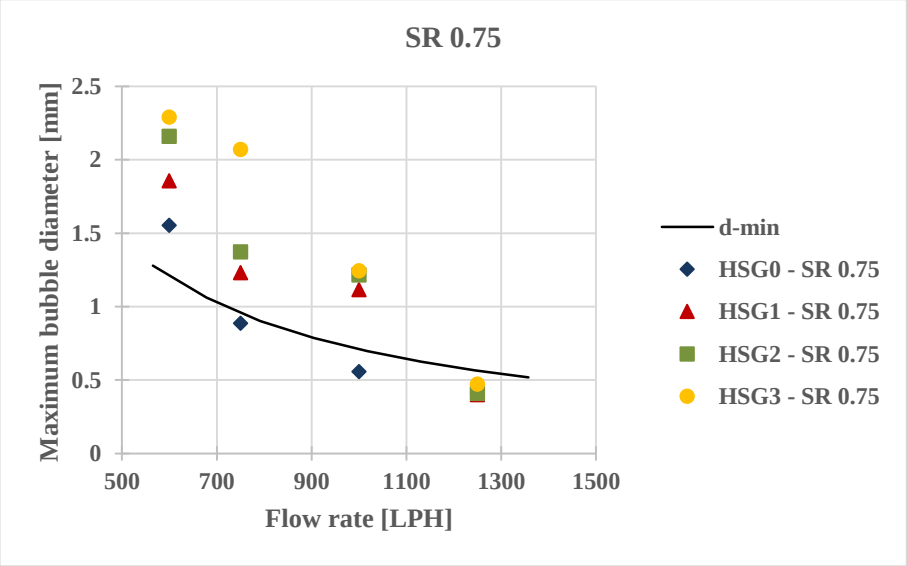

Figure 4-80. Comparison of maximum bubble diameter and theoretical d_{min} calculation at saturation ratio 0.75 during horizontal flow.

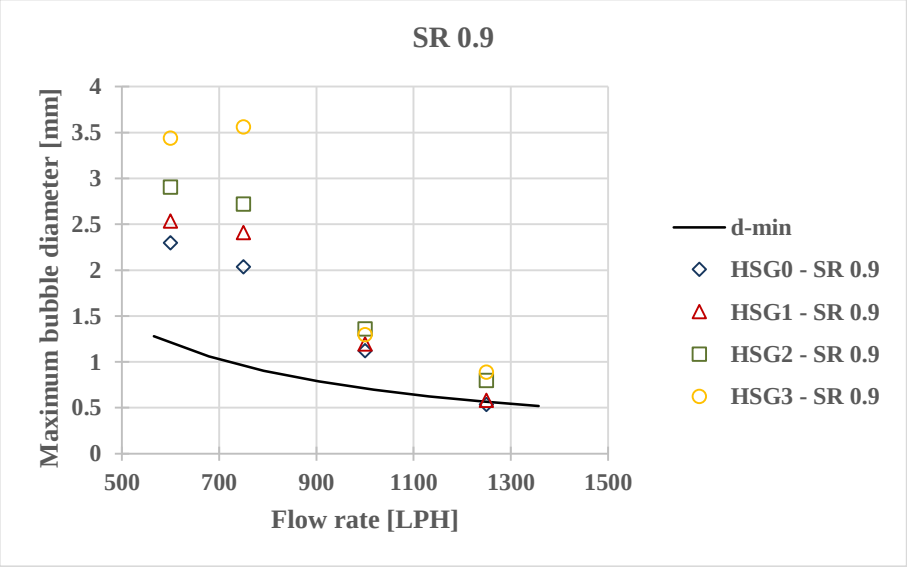

Figure 4-81. Comparison of maximum bubble diameter and theoretical d_{min} calculation at saturation ratio 0.9 during horizontal flow.

Figures 4-80 and **4-81** demonstrate the comparison of maximum bubble diameters and theoretical d_{min} calculations, where y-axes represent the maximum bubble diameter, and x-axes the system flow rate. Results for the saturation ratio 0.75 (**Figure 4-80**) display that, maximum bubble diameters observed at HSG0 is generally below the theoretically calculated d_{min}. Sizes increase above the theoretical limit as the flow travels from HSG0 to HSG3, except at the highest flow rate. At 1250 LPH, maximum bubble

diameters remain under the theoretical limit, indicating that effect of the coalescences diminishes with increasing flow velocity – as noted from the figures presented in previous section. On the other hand, maximum bubble diameters measured at saturation ratio 0.9 (**Figure 4-81**) are above the theoretical limit at all positions, and flowrates are similar to the results obtained at the same saturation on the vertical pipeline. This reveals that maximum bubble diameter is already ahead of theoretical limit before the flow arrives to HSG0 at higher saturation ratio. This is due to the fact that chance of coalescences phenomenon becomes more pronounced at two-phase flow with higher bubble numbers.

Following the evaluation of maximum bubble diameters observed at vertical and horizontal positions on the central heating system, it is concluded that theoretical d_{min} diameter defined in **Equation (2-14)** can be used to determine a limit diameter for the maximum bubble sizes observed throughout the wet central heating systems pipework. In other words, maximum bubble diameters observed after the VSG1 is more likely to have a larger diameter than d_{min} in all cases. Furthermore, under no circumstances, maximum bubble diameters measured during experiments came close to the theoretically defined d_{max}. It is reasoned that pipe lengths investigated in the current study are not sufficient for maximum bubbles to show adequate enlargement, an issue which was also observed by Razzaque et al. (2003). They have investigated pipe lengths as long as 35 m, where d_{max} provided accurate maximum bubble size predictions during turbulent bubble flow. Additional investigations with longer pipes were needed in order to validate whether bubble sizes in wet central heating systems can reach the value of d_{max}.

4.6.4 Dissolution at undersaturated bubbly flow

Dissolution of bubbles in turbulent pipe flows at wet central heating systems' pipeline has been reported by Fsadni & Ge (2012), Fsadni (2012) and Ge et al. (2013) and was discussed in **Section 2.4.2.3.2** of this thesis. More specifically, Fsadni & Ge (2012) and Ge et al. (2013) have evaluated reduction in average bubble diameters along the horizontal pipeline. Additionally, decrease in both volumetric void fraction and average bubble diameters were outlined in Fsadni (2012). In this regard, experiments were conducted at the vertical and horizontal pipeline of the current test rig to test if; 1) the observations of previous reshearchers could be reproduced at higher flow rates, and 2) their dissolution models could be validated under the current study's conditions . The following two sections present the results

of these tests for vertical and horizontal pipelines. Data processed in this section is identical to the data obtained during bubble distribution measurements explained in **Section 4.3**. Cummulative void fractions and average bubble diameters were calculated from focal planes of each position at each system condition given in **Table 4-1**.

4.6.4.1 Vertical downward flow

Vertical downward bubbly flow was measured at two different positions; VSG1 and VSG2 (see **Figure 3-23**). The results of these experiments are presented in **Figures 4-82** to **4-88**. System conditions and procedures followed during the measurements can be found in **Section 4.3.2**. First four figures (**Figures 4-82** to **4-85**) illustrate how cumulative void fraction changes with respect to the captured bubble diameters.

Results at saturation ratio 0.75 are presented in the first two figures for four different flow rates (**Figures 4-82** and **4-83**). In general, it can be noticed that, for all of the bubble sizes, cumulative void fraction calculations at VSG2 is higher than VSG1.. This indicates that bubble volumes tend to increase as the flow travels from VSG1 to VSG2. This was unexpected because the flow was undersaturated, and according to previous studies, bubble should dissolute into liquid, leading to a reduction in volumetric void fraction. On the other hand, cumulative void fraction results shown for the saturation ratio 0.9 (**Figures 4-84** and **4-85**) display that there is a reduction in cumulative void fraction as the flow travels from VSG1 to VSG2. Even though this behaviour agrees with previous observations, due to the dissolution of bubbles, reduction in cumulative void fractions were not obtained at SR 0.75. Dissolution should become pronounced at SR 0.75 because of higher dissolved gas concentration gradient between the bubble boundary and the flowing liquid (Lezhnin et al. 2003).

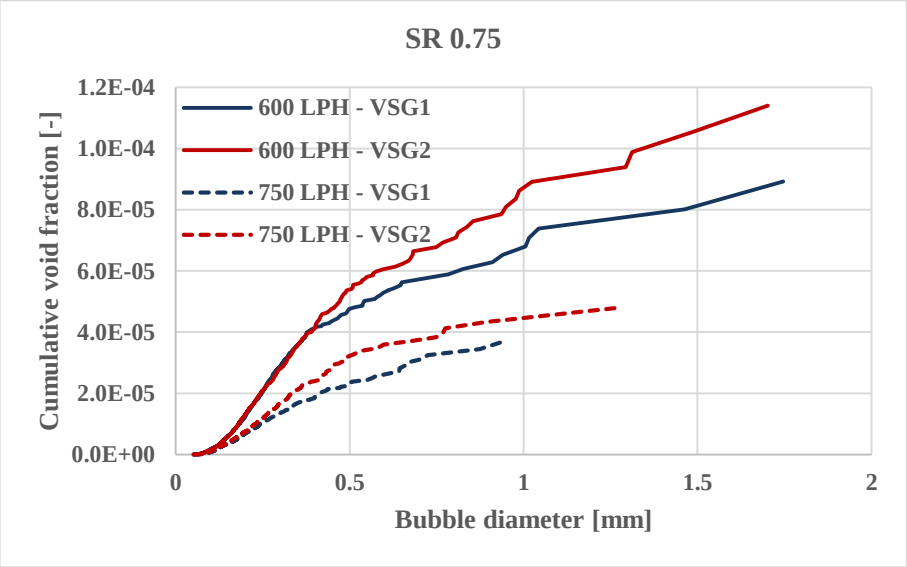

Figure 4-82. Cumulative void fraction vs bubble diameter at vertical downward flow and saturation ratio 0.75.

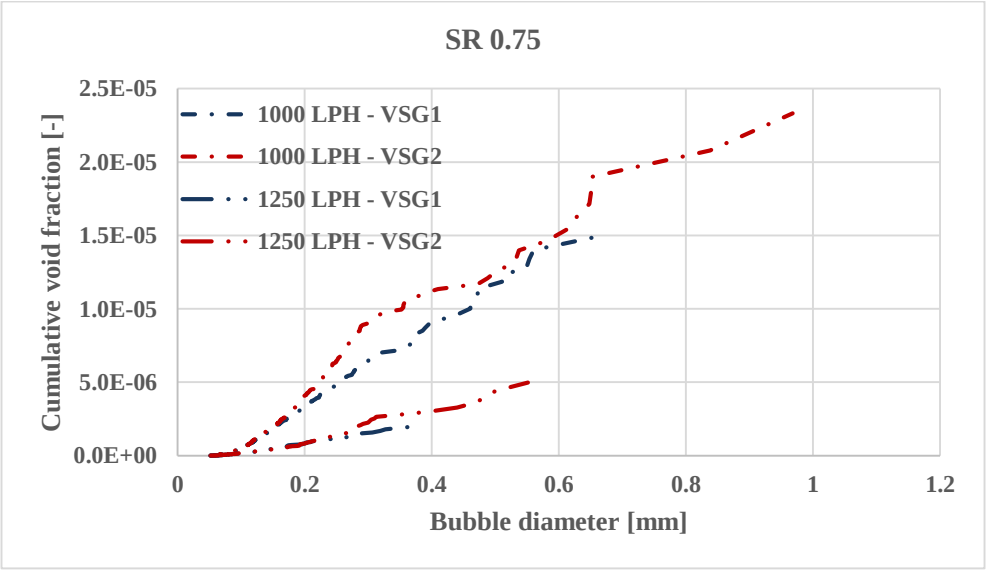

Figure 4-83. Cumulative void fraction vs bubble diameter at vertical downward flow and saturation ratio 0.75.

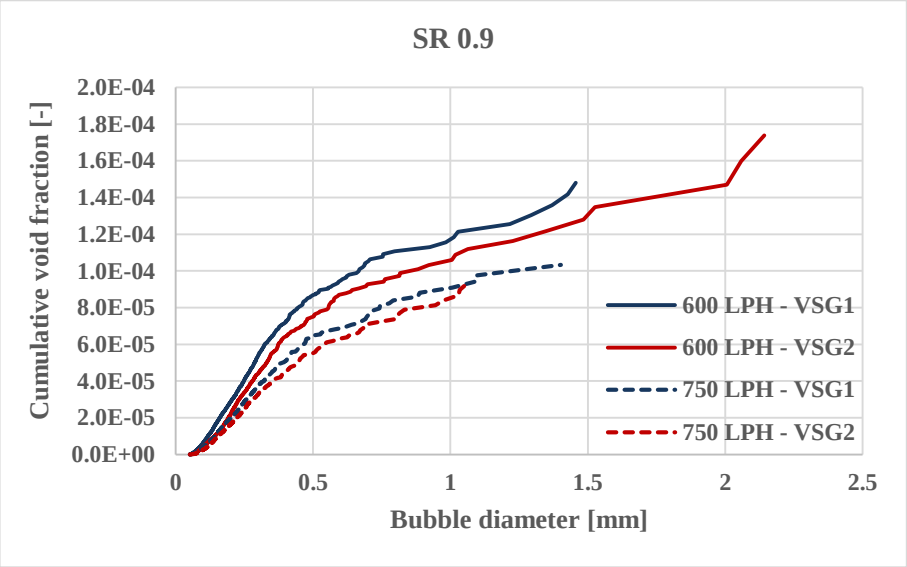

Figure 4-84. Cumulative void fraction vs bubble diameter at vertical downward flow and saturation ratio 0.9.

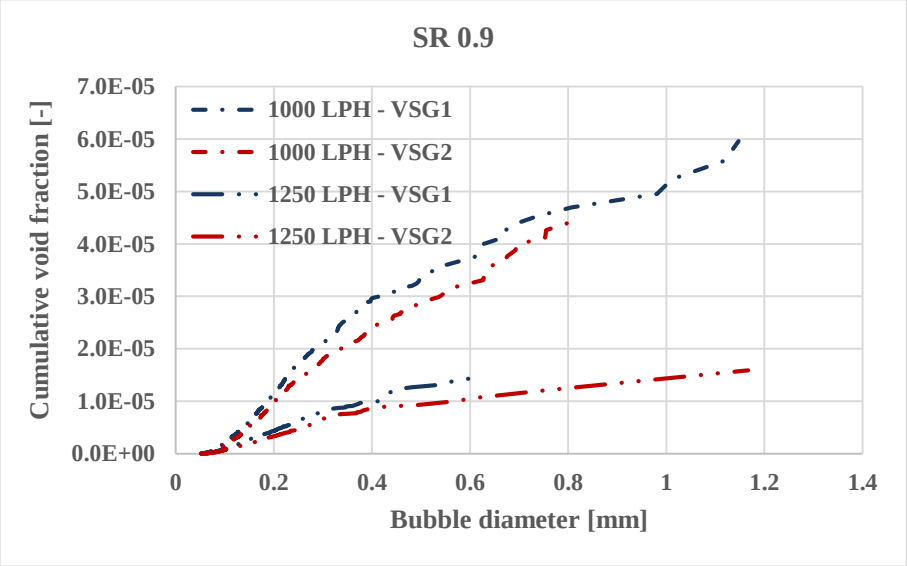

Figure 4-85. Cumulative void fraction vs bubble diameter at vertical downward flow and saturation ratio 0.9.

These abrupt behaviours are attributed to the saturation ratio variation during the filming of the flow. It is very difficult to obtain solid saturation ratios throughout the experiments and saturation ratio slightly increases following the injection of tap water into the system at saturation ratio 0.75. Variation of the system saturation ratio during the filming of flow at two sight glasses can be found in **Appendices 38** to **45**, where it slightly increases at SR 0.75 and decreases at SR 0.9. Increasing saturation

ratio leads to a higher void fraction— as shown in **Section 4.2.4**—therefore, it is concluded that saturation ratio variation is responsible for unexpected behaviours.

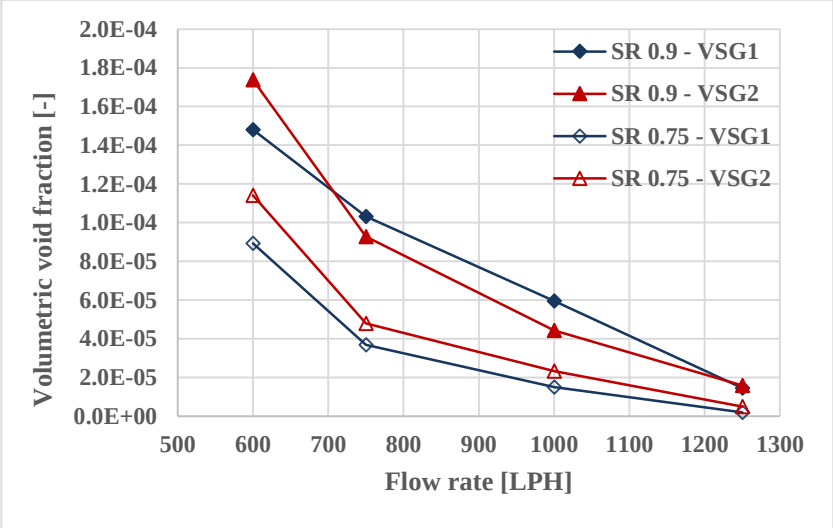

Figure 4-86. Volumetric void fractions at two vertical positions for four different flow rates and saturation ratios 0.75 and 0.9.

Figure 4-86 summarizes the volumetric void fractions observed at each vertical position for all of the saturation ratios and flow rates utilized during the tests. At SR 0.9, volumetric void fractions display a reduction as they travel from VSG1 to VSG2, whereas, there is an elevation in void fraction measurements at saturation ratio 0.75, except for 600 LPH. This is because of the saturation ratio variation discussed previously. The only unexpected behaviour of volumetric void fractions was observed at SR 0.9 for 600 LPH. The evaluation of this specific condition revealed that the increase in volumetric void fraction was due to a significant growth in maximum bubble diameter (see **Figure 4-84**). Additionally, volumetric void fraction decreased as the flow rate increased, reconfirming the conclusions obtained in **Section 4.2.5**.

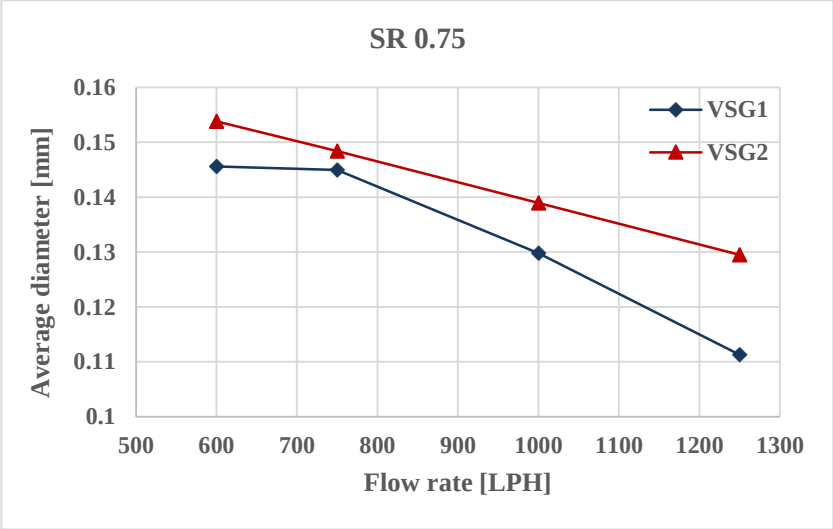

Figure 4-87. Average bubble diameters at two vertical positions for four different flow rates and saturation ratio 0.75.

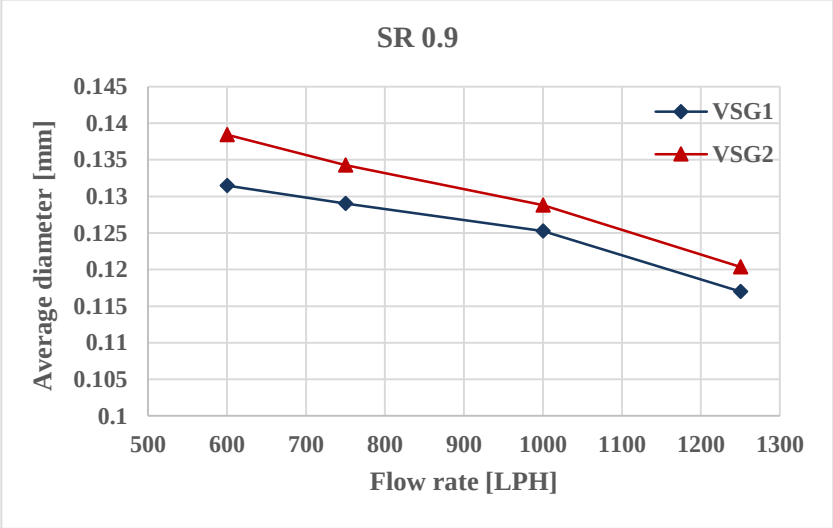

Figure 4-88. Average bubble diameters at two vertical positions for four different flow rates and saturation ratio 0.9.

Figures 4-87 and **4-88** present the average bubble diameters observed at SR 0.75 and 0.9, for four different flow rates. All of the results reveal that average bubble diameters observed at VSG2 are bigger than the ones observed at VSG1. This was attributed to the coalescence effect as discussed in the previous **Section 4.6.3.1**, which leads to an increase in overall bubble diameters, hence, resulting with increased average bubble diameters. Furthermore, average bubble diameter decreases

as the flow rate increases at both saturation ratios, agreeing with the pattern predicted by the bubble detachment model discussed in **Section 4.6.1**.

4.6.4.2 Horizontal flow

Similar to the results presented for vertical downward flow in the previous section, cumulative void fraction change against bubble diameters are plotted in the following **Figures 4-89** to **4-92**. In general, it can be clearly observed that cumulative void fraction calculations at HSG2 are higher than at HSG1 for all of the bubble sizes. This indicates that total bubble volumes increase as the flow travels from HSG1 to HSG2. The effect of variation in saturation ratio observed at vertical downward flow is supressed at horizontal flow. Volumetric void fraction increase at the upper part of pipe was a conclusion derived from the results presented for distribution measurements (see **Sections 4.3.3** and **4.3.4)**. This accumulation leads to an increase in bubble numbers, therefore, to a higher possibility of coalescences to occur (**see Section 4.6.3.2**). Hence, change in bubble volume is dominated by bubble accumulation phenomenon at upper parts of the pipe and coalescences.

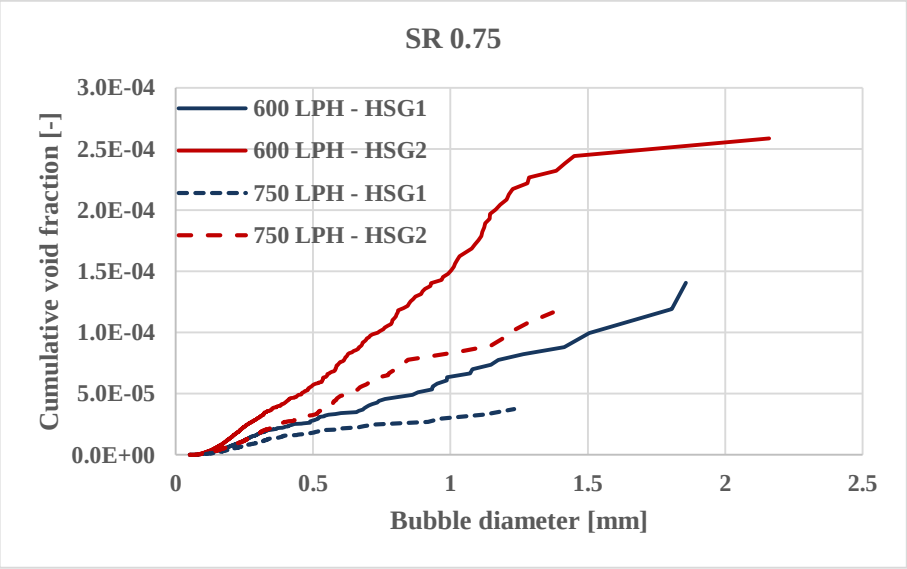

Figure 4-89. Cumulative void fraction vs bubble diameter at horizontal flow and saturation ratio 0.75.

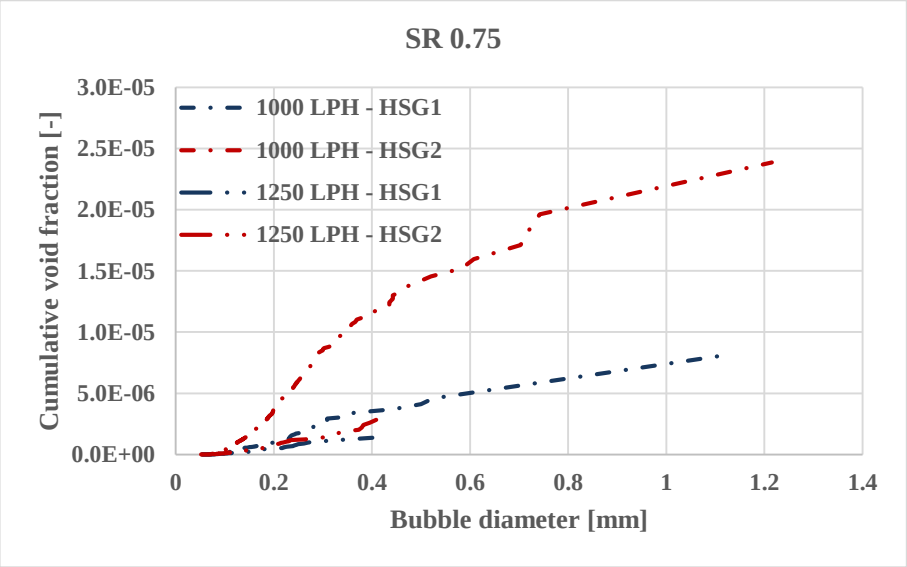

Figure 4-90. Cumulative void fraction vs bubble diameter at horizontal flow and saturation ratio 0.75.

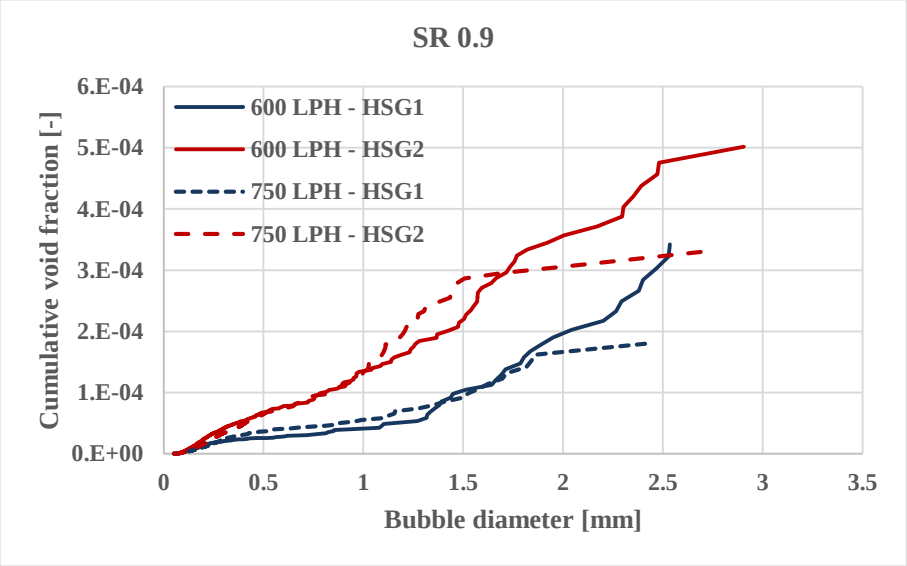

Figure 4-91. Cumulative void fraction vs bubble diameter at horizontal flow and saturation ratio 0.9.

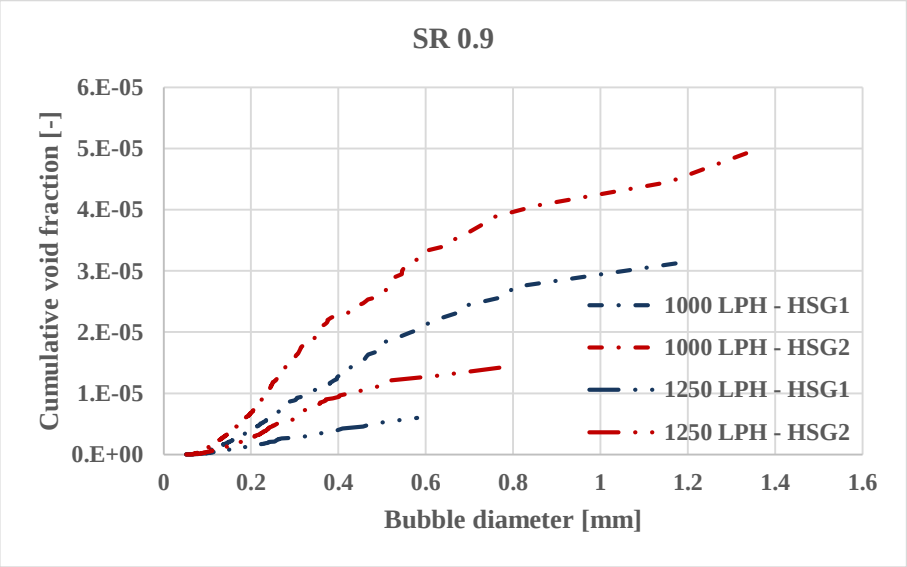

Figure 4-92. Cumulative void fraction vs bubble diameter at horizontal flow and saturation ratio 0.9.

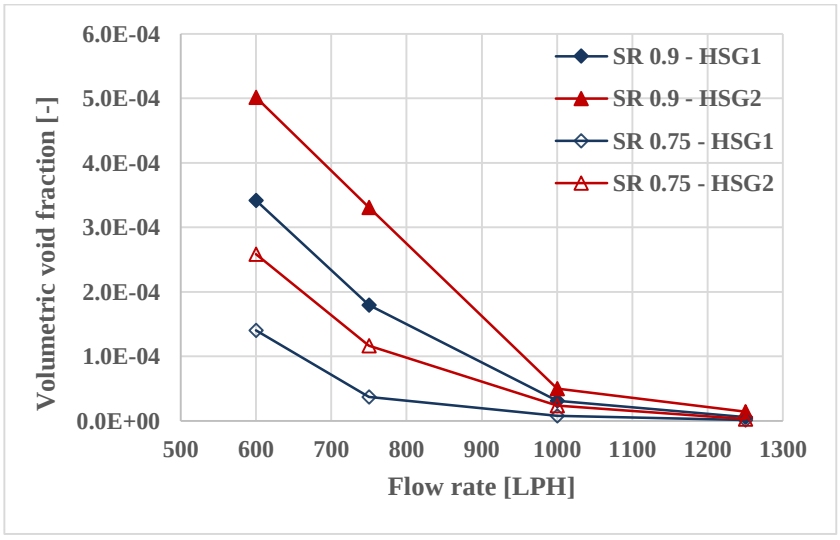

Figure 4-93. Volumetric void fractions at two horizontal positions for four different flow rates and saturation ratios 0.75 and 0.9.

Figure 4-93 summarizes the volumetric void fractions observed at each horizontal position for all of the saturation ratios and flow rates utilized during the tests. In general, all of the data indicate that there is an increase in cumulative void fraction as the flow travels from HSG1 to HSG2. Under no circumstances, Fsadni (2012)'s suggestion that there would be a decrease in void fraction from HSG1 to HSG2, was observed in this study. It is thought that coalescences and bubble development along the axis restrain the dissolution phenomenon, as was the case for cumulative void

fraction. Moreover, similar to the results obtained for vertical flow in the previous section, volumetric void fraction decreases as the flow rate increases, reconfirming the conclusions obtained in **Section 4.2.5**.

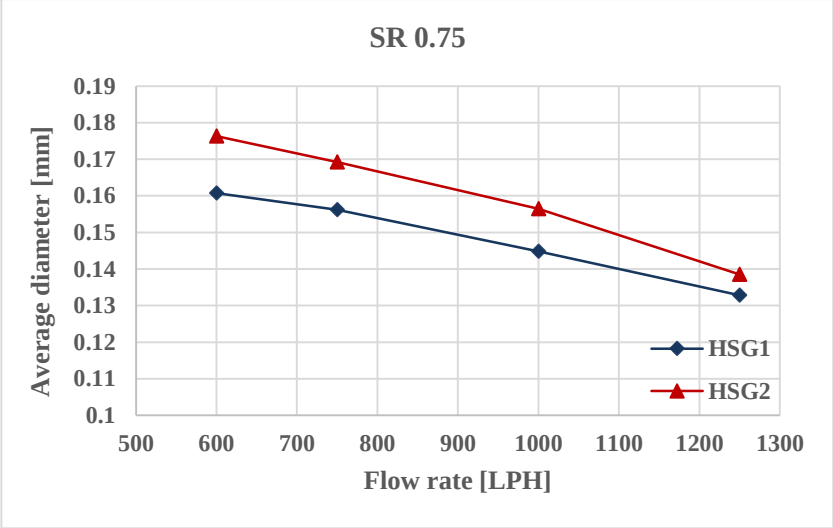

Figure 4-94. Average bubble diameters at two horizontal positions for four different flow rates and saturation ratio 0.75.

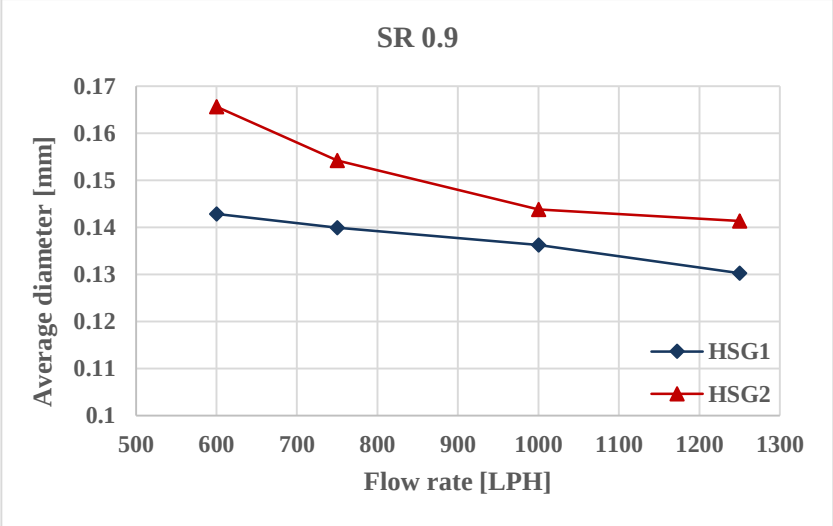

Figure 4-95. Average bubble diameters at two horizontal positions for four different flow rates and saturation ratio 0.9.

Variation of average bubble diameters against flow rates measured at HSG1 and HSG2 are presented in **Figures 4-94** and **4-95**. All of the results indicate that average bubble diameters observed at HSG2 are bigger than at HSG1. This is caused by the coalescence effect discussed in the previous **Section 4.6.3.2**, which leads to

increase in overall bubble diameters, hence, resulting in increased average bubble diameters. Furthermore, average bubble diameters decrease as the flow rate increases at both saturation ratios, which agrees with the pattern defined by the equations for d_{min} and d_{max} as shown in **Figure 4-73**.

4.7 Summary

This chapter presented the results of the experiments conducted to investigate two-phase flow structures occurring in wet central heating systems. Firstly, effects of different parameters on bubble production, void fractions, and average diameters at boiler exit were evaluated. It was shown that bubble production and void fractions increase as the temperature, boiler heating load, and saturation ratio escalate. On the other hand, they reduce when the pressure and flow rate of the system gets higher. Moreover, it was observed that there was not a clear relationship between average bubble diameters and system parameters, except for the system flow rate. It was concluded that bubble sizes at boiler exit were significantly affected by the liquid flow rate, and it was later revealed that average bubble diameters decrease as the flow rate increases.

Secondly, bubble volume distributions across the pipe section at vertical and horizontal pipelines were demonstrated. In general, most noticeable difference between two orientations is the arrangement of bubbles. Bubbles are evenly distributed during vertical flow when compared to horizontal flow, where bubbles tend to flow at the upper parts of the pipe. Bubble distributions at vertical downward flow showed centre-peaked profiles at low flow rates and their distributions levelled as the flow rate increased. Flow rate also affected the bubble distributions at horizontal flow, where bubble arrangement also levelled as the velocity grew. Furthermore, it was shown that bubble distributions were highly affected by obstacles like 90 degree bend, thermocouple or pressure sensors. And, it was observed that axial flow development of bubbly flow was a continuous process and void fraction at the upper part of the pipe increased as the flow travelled through horizontal pipeline.

Thirdly, bubble size distribution across the pipe section showed oscillations right after the double 90 degree bends at vertical downward flow. Size distribution developed along the vertical pipe and became levelled with peak average bubble diameters in the middle. Similarly, size distribution at horizontal flow also showed fluctuation right after 90 degree bend and developed along the horizontal pipe. Size distributions at horizontal flow peaked at the top of the pipe and lessened from top to bottom.

Next, bubble velocity measurements at both vertical and horizontal pipelines of the system were compared with the universal power law profile which defines the fully developed single phase liquid velocity profile. It was concluded that bubble velocity profiles show development along both vertical and horizontal flows and approaches to profiles which can be expressed with power-law.

Finally, experimental results regarding the bubble sizes were demonstrated. Bubble detachment model was compared with experimental results at boiler exit. It was shown that at 950 LPH, bubble detachment model provided predictions with 20% uncertainty. However, it did not provide a reliable prediction when the fluid flow rate varied, indicating that further investigation was necessary. Next, it was observed that bubble size distribution at boiler exit followed log-normal distribution, showing that log-normal distribution function could be used to describe bubble sizes at boiler exit. Coalescences of two bubbles during horizontal flow was captured, emphasizing that the effect of coalescences should not be neglected at low void fractions. It was also found that bubbly flow in central heating systems were in coalescences dominant regime and maximum bubble diameter observed at positions after VSG1 were bigger than theoretically defined d_{min}. Moreover, bubble dissolution effect was not observed in any of the conditions utilized in the present study. The reasons were thought to be the variation saturation ratio and axial flow development of two-phase flow, which supress the effect of dissolution and favours coalescence phenomenon.

CHAPTER 5 COMPUTATIONAL STUDY

5.1 Introduction

Commercially available ANSYS Fluent 14.5 software was utilized to investigate bubble distributions right after the 90 degree bend on horizontal pipeline of the test rig studied in the present work. This chapter provides necessary steps to take regarding these computational analyses. First, **Section 5.2** starts with a brief explanation on how ANSYS Fluent 14.5 works and definition of the physical problem that is desired to be solved. Second, design of the model geometry and mesh of the problem are introduced in **Section 5.3**. Next, solver and physical models, and boundary conditions defined for the problem to simulate turbulent bubbly flow are presented in **Sections 5.4** and **5.5**. In **Section 5.6**, mesh independence analysis is described and results are given in **Section 5.7**. Finally, as a conclusion, a brief summary is given in **Section 5.8**.

5.2 Fluent Software and Physical Problem

Computational fluid dynamics (CFD) is the science of predicting fluid flow, heat and mass transfer, chemical reactions, and related phenomena. In order to achieve this, equations are solved for conservation of mass, momentum, energy etc. It is widely used in studies for new designs, product development, optimization, redesign etc. (Ansys 2015a). In general, CFD codes follow three main steps: pre-processing, solution, and post-processing. Pre-processing stage consists of geometry definition, mesh generation, and determination of appropriate boundary conditions, physical models, and fluid properties. Solution is the step where governing equations are solved by numerical techniques and finally, results of the numerical calculations are visualized and evaluated at post-processing stage (Versteeg & Malalasekera 1995).

Main difference among the available commercial CFD packages is the way they solve the governing equations. There are three main spatial discretisation schemes used to solve these equations: finite difference, finite volume, and finite element methods (Blazek 2001). Advantages of finite volume method against finite difference method are given by Blazek (2001). The writer points out to the fact that discretisation is applied directly in physical space. This eliminates the problems occurring during transformation between coordinate systems which causes difficulties when using finite difference method. Moreover, he notes that finite volume method can be applied on both structured and unstructured meshes which offer flexibility. ANSYS Fluent solver is based on the finite volume method and the computational domain is discretized into a finite set of control volumes. General conservation (transport) equations for mass, momentum, energy, species, etc. were solved on this set of control volumes (Ansys 2013). General form of transport equations can be expressed with **Equation (5-1)**:

$$\int_V \frac{\partial \rho \emptyset}{\partial t} dV + \oint \rho \emptyset \vec{v} \cdot d\vec{A} = \oint \rho \Gamma_\emptyset \nabla_\emptyset \cdot d\vec{A} + \int_V S_\emptyset dV \qquad \textbf{(5-1)}$$

where V is the control volume, ρ is density, $\vec{v}$ is velocity vector, $\vec{A}$ is surface area vector, $\Gamma_\emptyset$ is diffusion coefficient for $\emptyset$, $\nabla_\emptyset$ is gradient of $\emptyset = (\partial\emptyset/x)\hat{\imath} + (\partial\emptyset/y)\hat{\jmath}$ in 2D and $S_\emptyset$ represents source of $\emptyset$ per unit volume. In the equation above, if $\emptyset$ is replaced with corresponding quantities summarized in **Table 5-1**, one can obtain continuity, momentum or energy equations.

Table 5-1. Quantities represent each conservation equations for **Equation (5-1)**

Equation	**Ø**
Continuity	1
X momentum	u
Y momentum	v
Z momentum	w
Energy	h

It is worth mentioning that energy equations will not be solved in the present study since the case is assumed to be isothermal. First term in **Equation (5-1)** is called unsteady term and represents the change rate of ∅ in control volume with respect to time. Second and third terms are called convection and diffusion terms, where they represent net flux of ∅ caused by convection and diffusion, respectively. The last term on the right is called source term which is the net creation rate of ∅ inside the control volume. These partial differential equations are discretized into a system of algebraic equations for the discrete dependent variables like, velocity, pressure, temperature etc. Afterwards, these algebraic equations are numerically solved to obtain solution fields. It is important to note here that control volumes in Fluent are cell-centred, therefore, face values required for convection and diffusion terms in **Equation (5-1)** are acquired by interpolation (Ansys 2015a).

The physical problem that is computationally investigated in the present study is the two-phase bubbly flow along the pipework of wet central heating systems. The main aim of this particular computational research is to investigate the effect of 90 degree bend on void fraction distribution and its development along the pipework. Moreover, distribution patterns obtained from the computational results are compared with the outcomes of the experimental results presented in **Section 4.3**. This provides a way to validate simulations which can be used to predict bubble distribution along the pipework of similar cases where it is difficult to conduct experimental measurements.

As explained in the previous chapters, supersaturated conditions that occur in the primary heat exchanger lead to bubble formation. Afterwards, these bubbles are carried by the flowing liquid and travel along the system pipework causing two-phase bubbly flow. The phenomenon that is simulated in this chapter is not the formation of bubbles but the case where two-phases travel together. It would be interesting to study computationally the formation of the bubbles inside the heat exchanger. However, it was extremely difficult to obtain measurements from the inner sections of the heat exchanger with the equipment used in the experiments. It is also beyond the scope of the present study to investigate bubble formations. Therefore, computational domain is simplified as shown in the next section where

the model geometry includes the vertical and horizontal pipelines that are connected with a 90 degree bend right after the boiler.

Computational domain starts with the vertical section of the test rig right after the boiler and ends with the horizontal pipe section where void fraction of bubbles were experimentally measured at four different positions given in **Figure 3-24**. The beginning of the computational domain was decided to be the first measurement point shown in **Figure 3-23** (VSG1) because void fraction, average bubble diameters and bubble velocity measurements during the experiments can be used as initial conditions. Two-phase flow is assumed to be entering at constant rate of liquid-bubble ratio, fixed average bubble diameter and fixed average bubble velocity which allows one to utilize the experimentally measured void fractions, average bubble diameters and average bubble velocities for each specific set of conditions. Moreover, heat transfer inside the computational domain is assumed to be negligible because of insulations used on the copper pipes. Therefore, energy equation described previously by **Equation (5-1)** and **Table 5-1** are not solved during the computation. Additionally, since experimentally measured velocity profiles and void fraction distributions at VSG1 are fairly uniform, they are both assumed to be uniform across the entrance and they develop as they travel through the model geometry. Velocity on the pipe wall is assumed to be zero which is expressed by the no slip condition. Furthermore, effect of gravity on the phases inside the domain is included in the calculations.

5.3 Model Geometry and Mesh

Horizontal setup of the test rig given in **Figure 3-24** is simplified and 2D model domain is identified as shown in **Figure 5-1** consisting of three bodies. Body 1 is the vertical pipe, Body 2 is the 90 degree bend (see **Appendix 37** for a detailed schematic diagram of the bend) which changes the direction of flow from the vertical pipe to Body 3, the horizontal pipe. Physical model was created by the Model Designer software provided in the ANSYS Workbench. It is necessary to point out that these three parts were created using *Add Frozen* feature and they were unified to create a single part with 3 bodies. This step helps to avoid the creation boundaries

between the bodies, therefore, it eliminates the necessity to define internal boundaries within the domain.

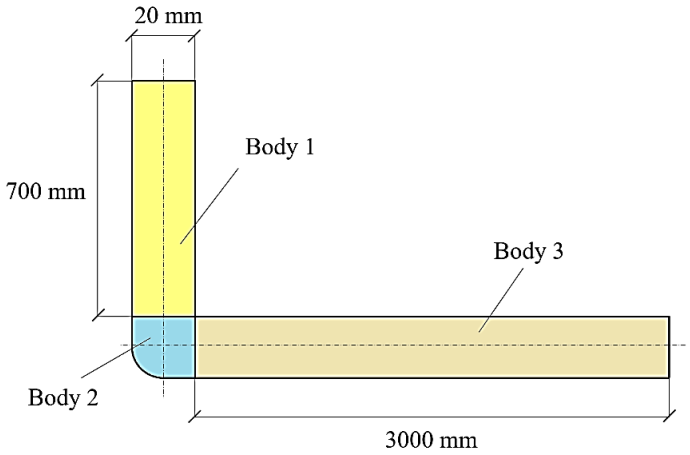

Figure 5-1. Dimensions of model domain.

Model geometry was designed as three bodies in order to better control mesh sizes during the creation of the mesh. Vertical pipe is 700 mm, which is the approximate distance between the VSG1 (**Figure 3-23**) and 90 degree bend before the horizontal pipeline (**Figure 3-24**). Two-phase flow conditions were measured at VSG1 during experiments and it was thought to be the best position to define as the inlet. Moreover, the domain's 3000 mm long horizontal part provides the sufficient length to gather computational results for all of the sight glass positions investigated previously.

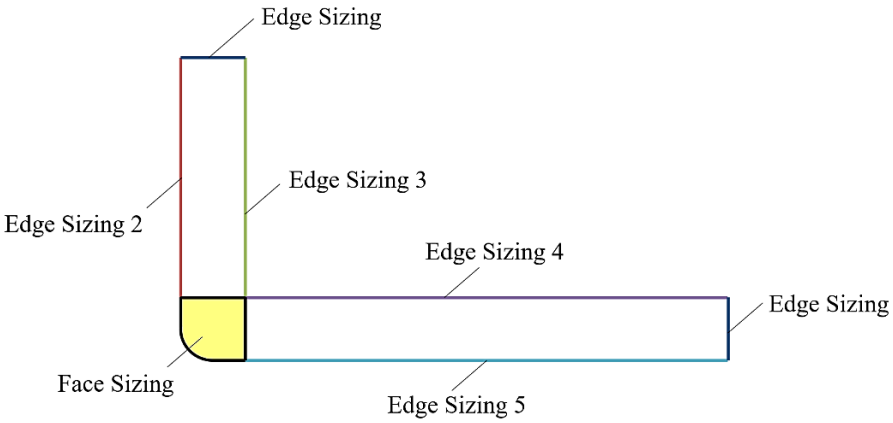

Figure 5-2. Meshing of the computational domain.

After creating the computational domain of the problem, the domain is meshed by the Meshing software provided in the ANSYS Workbench. **Figure 5-2** illustrates the parameters used to create the grid. Borders marked as *Edge Sizing* are set according

to number of divisions, whereas, borders marked with *Edge Sizing 2, 3, 4, 5* and *Face Sizing* were set according to element size. *Mapped Face* meshing feature was employed to Part 1 and 3 of the domain to ensure quadrilateral meshes throughout the geometry. Mapped Face feature cannot be applied to Part 2 because of the curvature. However, mesh sizes at Part 2 are controlled by *Face Sizing* feature, which offers the possibility of more or less same size square quad cells throughout the bend. In addition, *Edge sizing 2, 3, 4* and *5* include bias factor set as level 5 to obtain gradually decreasing mesh sizes from the top to the bottom, and right to the left of the domain. Rectangle meshes on the top and far right side of the domain gradually get smaller towards the 90 degree bend and finally they turn into squares. Screenshots of the mesh geometry was provided in the **Appendices 46** to **48** for further understanding.

Edge sizing and face sizing parameters which control the size of the meshes—and thus the element number in the domain—were changed to create several meshes used in the mesh independence study explained in **Section 5.6**. Moreover, special care was given to create a scalable mesh and maintain the mesh quality within the ranges suggested in Ansys (2015e). The suggested and obtained minimum and maximum mesh qualities from meshes created for the mesh independence test are summarized in **Table 5-2**.

Table 5-2. Suggested and obtained mesh quality criteria.

Mesh metric	Suggested	Obtained minimum	Obtained maximum
Skewness	<0.9	1.3e-10	0.39
Aspect ratio	<100	1	5
Expansion ratio	<1.5	1.05	1.1
Orthogonal quality	>0.1	0.86709	1

5.4 Solver and Physical Models

ANSYS Fluent is launched as double precision with serial processing. Double precision mode provides more accurate results compared to single precision solver, because it stores more decimal places than single precision for each variable (Ansys

2009). Moreover, serial processing is preferred because element numbers employed in the current study are relatively moderate, and solutions showed reasonable convergence times for all of the evaluated cases.

There are two different solver types available to be used by Fluent; pressure and density based solvers. The two types mainly differ from each other in accordance with the way governing equations are solved. Pressure-based solver was the preferred choice of the current study because mixture model was not available with density-based solver. Pressure based solver can be either segregated or coupled, again identified with the sequence of how governing equations are solved. Segregated solver solves the equations one at a time, whereas coupled solver solves all of the equations at the same time. Coupled solver is applicable for most flows and has performance advantages against segregated solver. But it requires 1.5 or 2 times more memory than segregated solver (Ansys 2015c). Despite the latter, it is the chosen solver of the current research because it converges faster than segregated solver.

Absolute velocity formulation was preferred since there is no moving boundary and 2D space option was set as planar which indicates that the problem is 2 dimensional. Gravity term is also included and set as -9.81 m/s^2 on vertical axis of the domain as it plays an important role in determining the distribution of two-phase flow in the horizontal pipeline. The solution was solved as a steady state problem because inlet conditions were assumed to be time independent, and the steady state solver provided sufficient reduction in residuals during the iterations.

As stated previously, mixture model was the preferred one to be used among the three multiphase models available in Fluent. Ansys (2009) suggests mixture model is appropriate for bubbly flows and additionally, with reasonable accuracy, it requires less computational power compared to other models. In addition, mixture model was chosen after considering available experimental data that are suitable for inserting as initial conditions like void fraction, fluid velocity, average bubble diameter and velocities. Moreover, slip velocity and implicit body force formulations are selected to be employed. The bubble velocity measurements obtained from VSG1 during experimental study will be provided as an initial condition at the inlet boundary,

therefore, inclusion of slip velocity calculations are necessary. And implicit body force formulation was also essential, since buoyancy forces dominate bubble arrangements in multiphase flows.

All of the flow conditions studied in this research are in turbulence regime (Re>2300). Therefore, there was a requirement to select a turbulence model from variety of turbulence models available. Realizable K-Epsilon turbulence model was chosen as a viscous model which is recommended for standard cases by Ansys (2015d). Realizable K-Epsilon solves time-averaged Navier-Stokes equations and it is very popular because of its simplicity and low computational power requirements. Mixture drift force was also activated so that effects of slip velocity on governing equations were included. Moreover, enhanced wall treatment for the ε-equation was applied for resolving turbulent boundary layer between the liquid and the wall. Enhanced wall treatment is mesh insensitive and offers flexibility (Ansys 2015d).

As stated previously at the end of **Section 5.2**, field variables that are stored at cell centre must be interpolated to the faces of control volume. In Fluent, there are different interpolation schemes available for each filed variable. **Table 5-3** summarizes each interpolation scheme chosen for each field variable, which in turn were chosen according to the suggestions provided in Ansys (2015c).

Table 5-3. Interpolation schemes selected for each field variable.

Field variable	**Interpolation schemes**
Gradient	Green-gauss node based
Pressure	PRESTO
Momentum	Second order upwind
Volume fraction	QUICK
Turbulent kinetic energy	Second order upwind
Turbulent dissipation rate	Second order upwind

5.5 Fluid Properties and Boundary Conditions

Water and air was added to the materials list of the Fluent software so that they could be chosen later while defining boundary conditions. Temperature of the two-phase flow during bubble distribution measurements at boiler exit was approximately 80 °C, therefore, pre-defined fluid properties (density and viscosity) of selected materials necessitated alteration. Default fluid properties were defined according to 20 °C and they were amended in accordance with the values given in **Table 5-4** for fluids at 80 °C (Perry et al. 1997).

Table 5-4. Properties of fluids used in the simulations.

Material	**Density** (kg/m^3)	**Viscosity** ($kg/m.s$)
Water-liquid	971.21	3.4599e-4
Air	0.99948	2.0947e-5

After adding water and air to the material list, it was necessary to define phases of the multiphase model. Water and air were set as primary and secondary phases. Primary represents continuous phase and secondary is the discrete phase. Moreover, diameter data for the secondary phase was required, therefore, average bubble diameters measured at VSG1 during bubble distribution measurements at saturation ratio 0.9 was supplied as summarized in **Table 5-5**. Similar to the experimental conditions, four different computational cases were defined for four flow rates.

Table 5-5. Data supplied for secondary phase diameter.

Secondary phase	**Parameter**	**Flow Rate (LPH)**			
		600	**750**	**1000**	**1250**
		Case 1	**Case 2**	**Case 3**	**Case 4**
Air	Diameter (m)	0.131e-3	0.129e-3	0.125e-3	0.117e-3

Afterwards, it was necessary to specify information on dependent flow variables at the computational domain. In order to do this, one needed to define boundary conditions which involves: identifying boundary types and locations, and supplying required data depending on type and physical model. Main considerations were

geometry and availability of data. Boundary condition types chosen for the computational domain is illustrated in **Figure 5-3**.

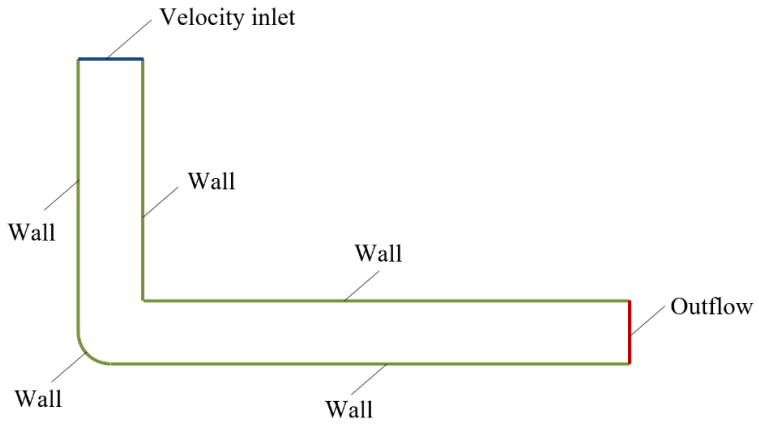

Figure 5-3. Boundary conditions set for the computational domain.

As velocity inlet boundary is the suggested type of inlet to be used for incompressible flows, it was the preferred choice for inlet and Outflow type was chosen for the outlet. Velocity inlet defines the average velocity of fluids, velocity profiles, void fraction and its distribution that enters the computational domain. In this particular case, velocity profile and void fraction profiles are assumed to be uniform across the pipe section. Fluent utilizes velocity components and scalar quantities which were identified to calculate the inlet mass flow rate and momentum fluxes. Outflow type boundary condition treats the flow as if there is zero diffusion flux for all flow variables and ensures that overall continuity is maintained in the domain. And it is usually preferred for the situation where the details of flow velocity and pressure are unknown before the calculations and it is suitable for fully developed flows. Rest of the boundaries were left as Wall type, which was default and they are used to bound fluid. Boundary conditions at wall were kept as default: they were predefined as stationary wall for wall motion and shear condition for no slip (Ansys 2015b).

Table 5-6. Data supplied for velocity inlet.

Phase	Parameter	Flow Rate (LPH)			
		600	**750**	**1000**	**1250**
		Case 1	**Case 2**	**Case 3**	**Case 4**
Water	Velocity (m/s)	0.531	0.663	0.884	1.105
Air	Velocity (m/s)	0.493	0.584	0.855	1.010
	Volume fraction (-)	1.48e-4	1.03e-4	5.96e-5	1.45e-5

Only data needed for the chosen boundary conditions were for velocity inlet (summarized in **Table 5-6** for four different cases). Data given in the table was acquired during experimental study as explained previously. Moreover, turbulence specification method was chosen as intensity and hydraulic diameter. And they were set to %5 and 0.02 m, respectively for all of the cases. %5 turbulent intensity is recommended in Ansys (2015d) for nominal turbulence through a circular inlet.

5.6 Mesh Independence Test

Mesh independence test is a crucial part of computational studies because it ensures that the obtained solution is reliable and does not calculate different results as the mesh gets denser. Solutions become more accurate as the mesh density increases, however, it is important to prevent over-meshing which may require enormous amount of computational power (Ansys 2015e). Basically, it is the process of obtaining optimum mesh for a specific problem and solution. In this regard, six different meshes were created using the settings summarized in **Table 5-7**. Data in the table represent the values supplied to Meshing software (see **Section 5.3)**. Furthermore, table includes number of nodes and elements for each resultant mesh.

These six different meshes were then computed with the settings and initial conditions provided previously. Boundary conditions identified for case 4 (1250 LPH) were utilized for all of the meshes in order to compare their outcomes with each other. Fluent requires all solution variables to be initialized before starting iterations. Therefore, hybrid initialization was used to solve potential equations.

Residuals for governing equations were monitored throughout the iterations and criteria limit for converged solution was set to 1e-5, which offers high accuracy. Moreover, average void fraction calculation at the outlet was monitored to make sure that the calculated value for void fraction stabilizes at a single value at the end of iterations. Screenshots which display typical change in residuals of governing equations and average void fraction against each iteration are provided in **Appendices 49** and **50**. Calculations were completed at the iteration numbers provided in the table below.

Table 5-7. Mesh parameters to create meshes used in mesh independence test.

Ratio	1	1.6	2	3.2	4	5
	Mesh 1	**Mesh 2**	**Mesh 3**	**Mesh 4**	**Mesh 5**	**Mesh 6**
Edge Sizing	5	8	10	16	20	25
Edge Sizing 2 to 5	1.0e-2	6.25e-3	5.0e-3	3.125e-3	2.5e-3	2.0e-3
Face Sizing	4.0e-3	2.5e-3	2.0e-3	1.25e-3	1e-3	8e-4
Number of nodes	2248	5395	8227	20344	31393	48554
Number of elements	1869	4789	7471	19135	29883	46668
Iteration number	107	115	136	198	239	446

After the calculations were completed, 10 points with 2 mm intervals were defined inside the computational domain. They correspond to a line at the centre position of HSG3 given in **Figure 3-24** (2795 mm to the bend). Void fraction data at each point for each mesh was gathered and then distribution profiles were compared to each other (see **Appendices 51** to **55**). After evaluating the change in void fraction profile as the mesh density increases, it has been decided that the solution will be mesh independent subsequent to mesh 4. Therefore, mesh 4 was used for all of the 4 cases given in **Table 5-6**. Moreover, three different convergence criteria limits (1e-3, 1e-4 and 1e-5) for residuals of governing equations were tested to make sure that results obtained with 1e-5 limit is accurate. Three different limits were tested using mesh 4 and it has been concluded that 1e-5 provides accurate calculations since the distribution profile does not vary after the criteria limit 1e-4 (See **Appendices 56** and **57**).

5.7 Results

Results of the computational analysis are presented in the following section. Computational analysis were run four times with the settings and conditions provided in the previous section for four cases (see **Tables 5-5** and **5-6**). Firstly, contour plots of air void fraction throughout the computational domain is demonstrated. Secondly, void fraction distributions, which correspond to the sight glass positions used in experiments (see **Figure 3-24**), were plotted against pipe depth for four different cases. Finally, void fraction distributions were reorganized so that profile development along the axial direction could be revealed.

5.7.1 Contours plots of air void fraction throughout the computational domain

Computational domain designed in the current study is relatively large and it is not convenient to illustrate contour plots of the whole domain at once. Therefore, four different sections on the horizontal pipeline were determined to be closed-up as shown in **Figure 5-4**. *Section 1* is at the 90 degree bend and the rest of the sections were chosen in a way to allow a clear observation of development of void fractions.

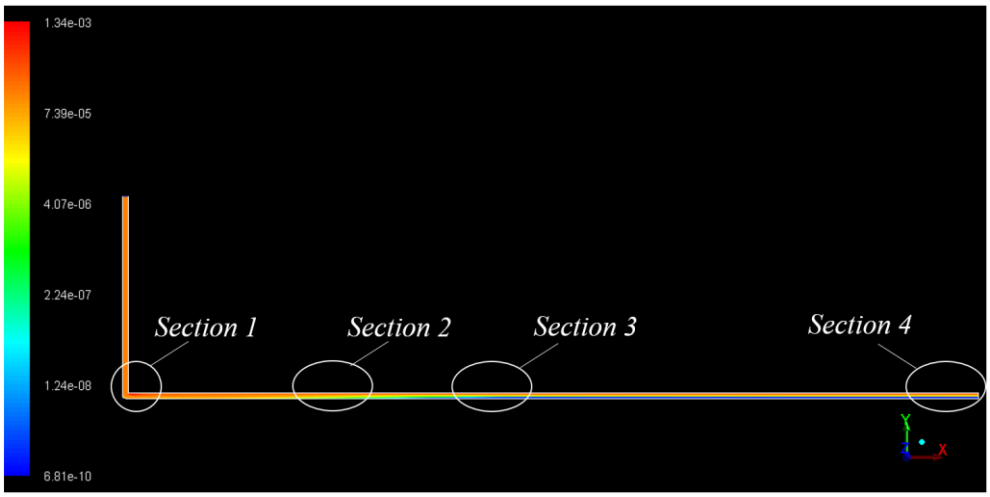

Figure 5-4. Positions of closed-up sections to show contour plots of air void fraction.

Contour plots of void fraction for four cases are more or less identical. For this reason, results from case 1 is presented in the following figures. **Figure 5-5** is the

close-up view of *Section 1* and displays the change in void fraction contours at the 90 degree bend. Void fractions at vertical pipe was levelled across the pipe section. However, an increase in air void fractions at the upper part of the pipe can be clearly seen right after the 90 degree bend. This is because of the 90 degree bend effect on flow structure, where liquid velocity at the bottom part of the pipe increases and pushes the air phase to the upper wall. Increase in mixture velocity at the bottom part of the pipe at *Section 1* can be noted from the velocity vector plots provided in **Appendix 58**. Moreover, contours of the turbulence kinetic energy are given in **Appendix 59**, which indicates that turbulences increase at the upper part of the pipe, closer to the 90 degree bend and diminish as the measurement position becomes remote. This is another evidence that higher turbulence levels closer to the 90 degree bend can lead to the fluctuations observed in void fraction and bubble size distributions encountered during experimental measurements.

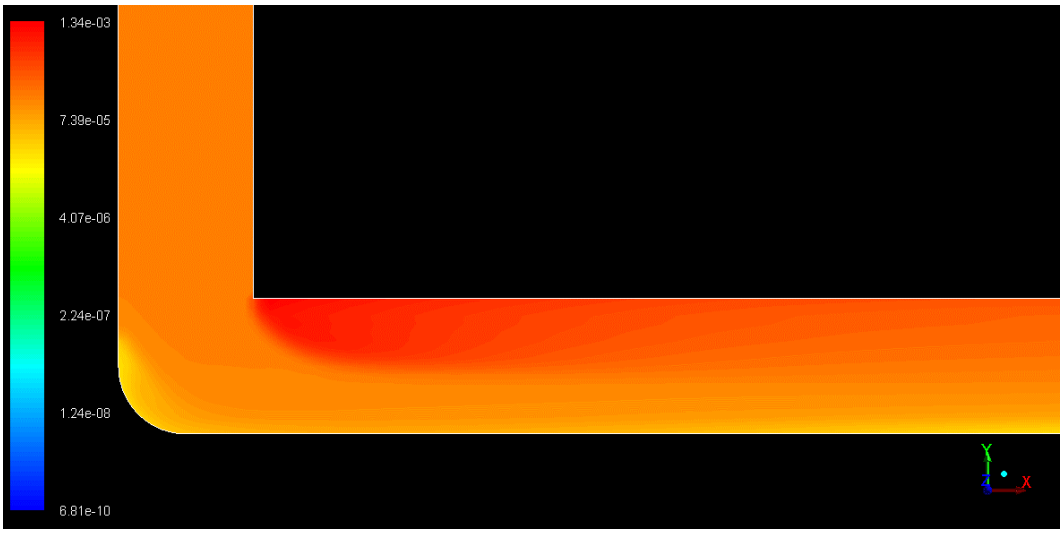

Figure 5-5. Contour plots of air void fraction at *Section 1* in **Figure 5-4**.

Furthermore, flow separation phenomenon occurs right after the bend, which is a well-known subject in fluid dynamics. Basically, when flow arrives at a sharp step, it tends to detach from the wall boundary and reattaches after some length, depending on flow velocity and step geometry (Singh et al. 2011). Detachment of flow from the wall boundary can be seen from the velocity vector plot given in **Appendix 58**. In the figure, velocity vectors close to the upper wall after the bend are directed against the flow direction which indicates separation. Later, these velocity vectors shift their direction back to the flow direction at a certain length, called the reattachment length.

In our case, where the flow contains two-phases, air phase substitutes this detached region and shows an increase in the void fraction.

In addition, effect of secondary flow on phase distributions during bubbly flow was investigated experimentally by Yadav, Worosz, et al. (2014). They investigated the development of bubble flow structure from a pipeline, where vertical upward flow was directed to horizontal flow through a 90 degree elbow. They observed that secondary flow causes bubbles to gather at two distinct regions perpendicular to the flow direction. This leads to bimodal void fraction distributions across the pipe section at horizontal direction, and uniform void fraction distributions at vertical direction, rather than typically top peaked profiles observed during horizontal flow. Bubbles tend to accumulate towards the centre of the secondary flow vortices right after the bend and typical top peaked profiles starts to appear as the effect of secondary flow diminishes far from the bend. This can also be used to explain increasing void fraction at the upper part of the pipe right after the bend. Position of the secondary flow centre (**Appendix 58**), corresponds to the highest air void fractions seen in **Figure 5-5**. After the peaked void fractions occur right after the 90 degree bend, contours of void fractions indicate development. Contours become uniform, similar to the void fractions observed at vertical pipe as travelled farther away from the bend.

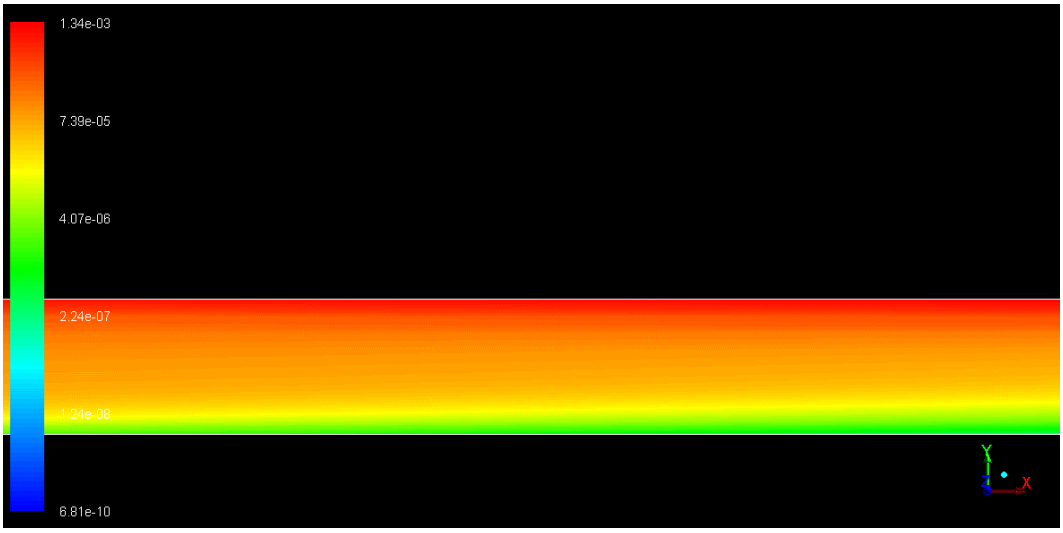

Figure 5-6. Contour plots of air void fraction at *Section 2* in **Figure 5-4**.

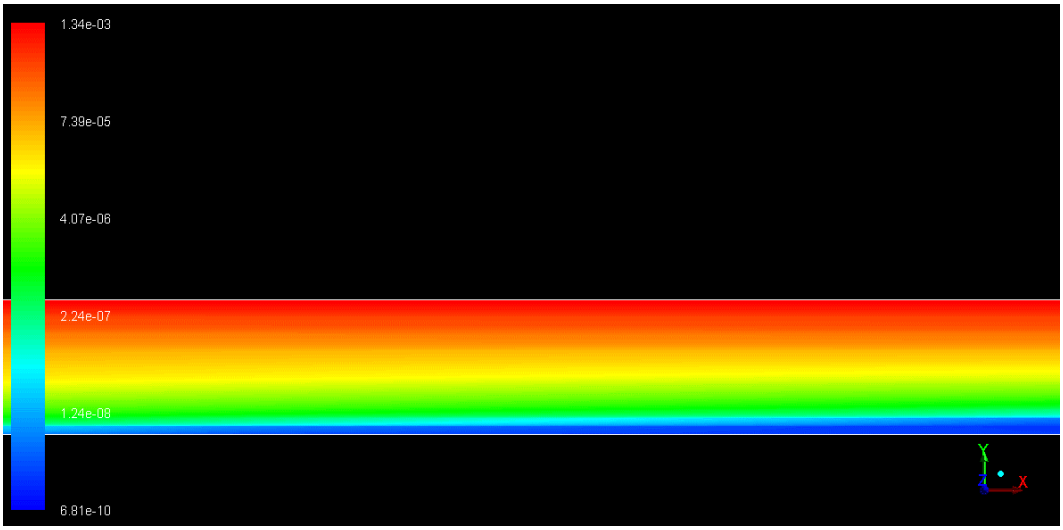

Figure 5-7. Contour plots of air void fraction at *Section 3* in **Figure 5-4**.

Figure 5-8. Contour plots of air void fraction at *Section 4* in **Figure 5-4**.

Rest of the close-up positions (*Section 2*, *3* and *4*) are illustrated in **Figures 5-6** to **5-8**. In general, void fraction contours develop back to typical top peaked profiles observed during horizontal flow following the uniform distribution observed at end of *Section 1*. Air void fractions at the upper part of the pipe increase steadily, whereas, void fractions at the bottom decreases as the flow travels from the bend to the outlet because of the buoyancy forces.

5.7.2 Bubble distributions across the pipe section

Air void fraction distribution calculations were gathered from the lines created in the computational domain which corresponds to the centre of each sight glass position shown in **Figure 3-24**. Later, they were plotted against normalized distance to the pipe wall similar to figures presented for the experimentally measured local void fractions. The following four **Figures 5-9** to **5-12** represent the results obtained from each position for four different cases where 0.531, 0.663, 0.884 and 1.105 m/s corresponds to the experimental flow rates 600, 750, 1000 and 1250 LPH.

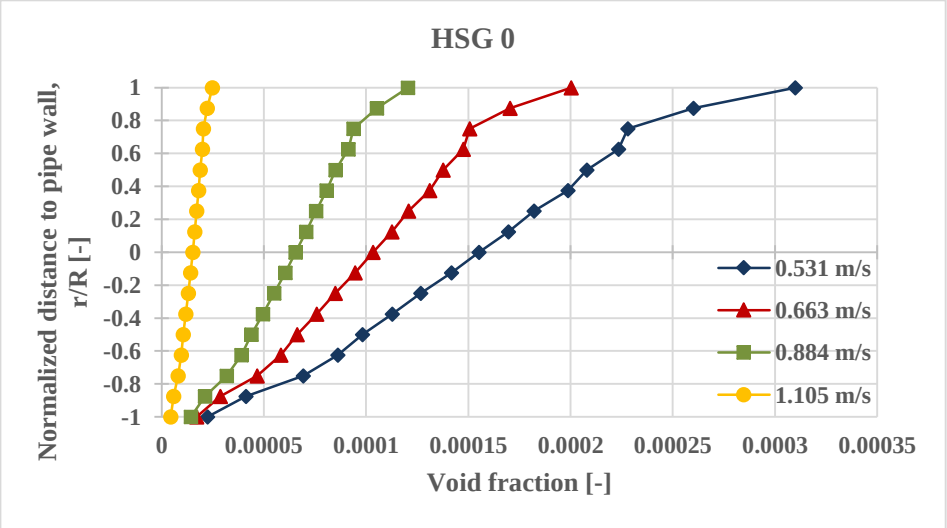

Figure 5-9. Computational results of bubble distribution at HSG0.

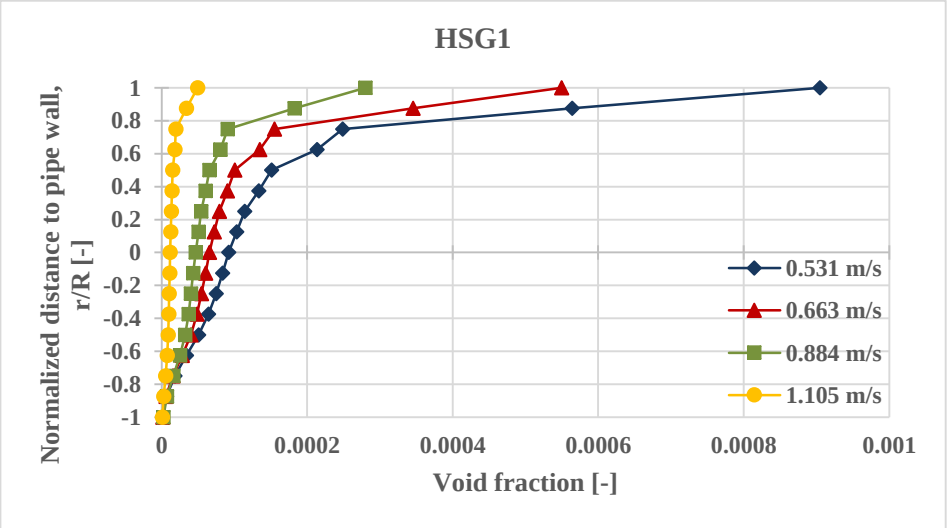

Figure 5-10. Computational results of bubble distribution at HSG1.

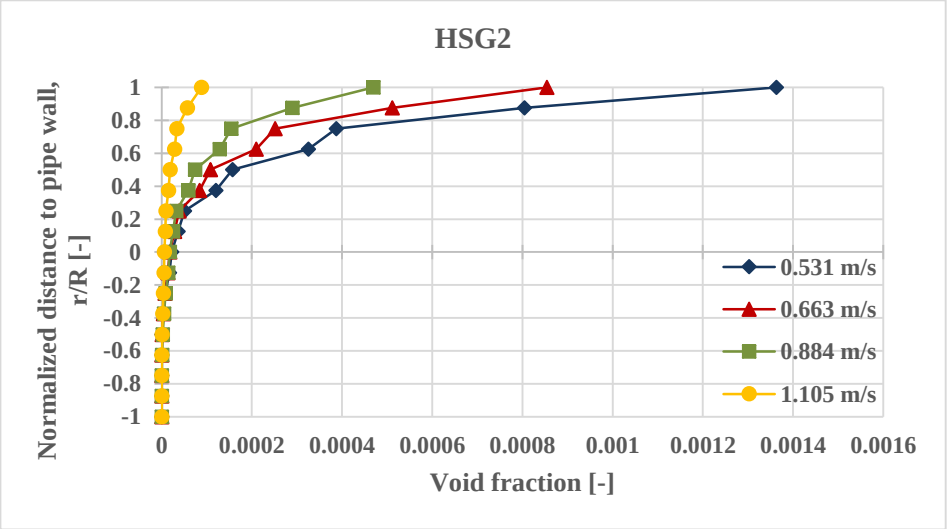

Figure 5-11. Computational results of bubble distribution at HSG2.

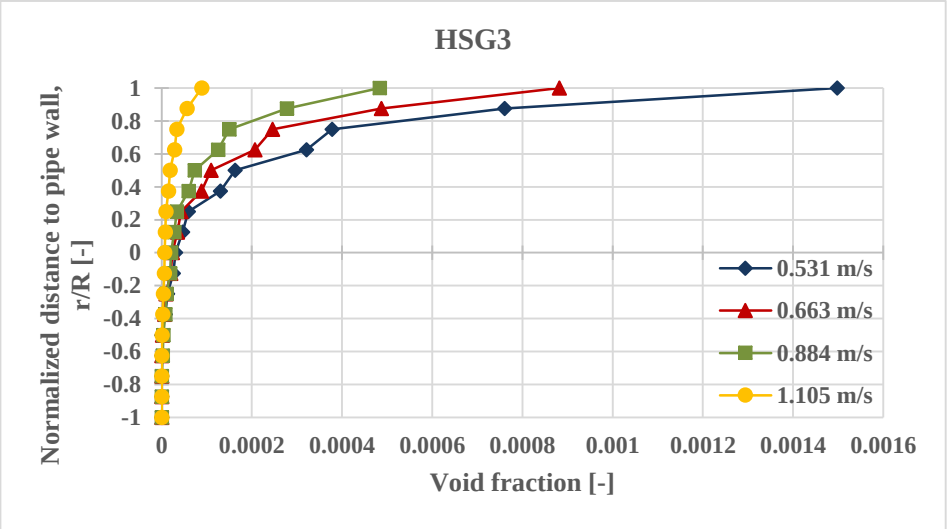

Figure 5-12. Computational results of bubble distribution at HSG3.

In general, void fractions at the upper part of the pipe are higher than void fractions at the bottom, and they become more uniform as the flow velocity increases. These behaviours agree well with the observations of previous researchers discussed in **Section 2.4.2.1.2** and also with the distribution profiles measured experimentally during the current study at the horizontal pipeline (see **Section 4.3.3**). Furthermore, levelling of distribution profiles becomes pronounced as the measurement positions approach to the bend which indicates that the 90 degree bend is responsible for this behaviour. Same conclusion on the 90 degree bend effect was observed during experiments as mentioned previously.

5.7.3 Bubble distribution development along the horizontal pipeline

The data that was processed to plot figures in the previous section were reorganized and plotted in a way to allow the development of void fraction profiles. Each figure (**Figures 5-13** to **5-16**) presents the change in void fraction profile along the horizontal pipeline for each flow velocity.

In general, there is no significant difference between the developments of void fraction distributions for four cases. However, axial flow development is clearly seen in all the figures. Profiles are levelled at HSG0 and they develop as they travel farther away from the bend. It is also important to note that, void fractions at the upper part of the pipe increases from HSG0 to HSG3 and vice-versa occurs at the bottom of the pipe. This indicates that axial development along the horizontal axis is a continuous process, as reported by previous researchers discussed in **Section 2.4.2.1.2**. Similar observations were obtained from the experimental results as well, presented in **Section 4.3.4**.

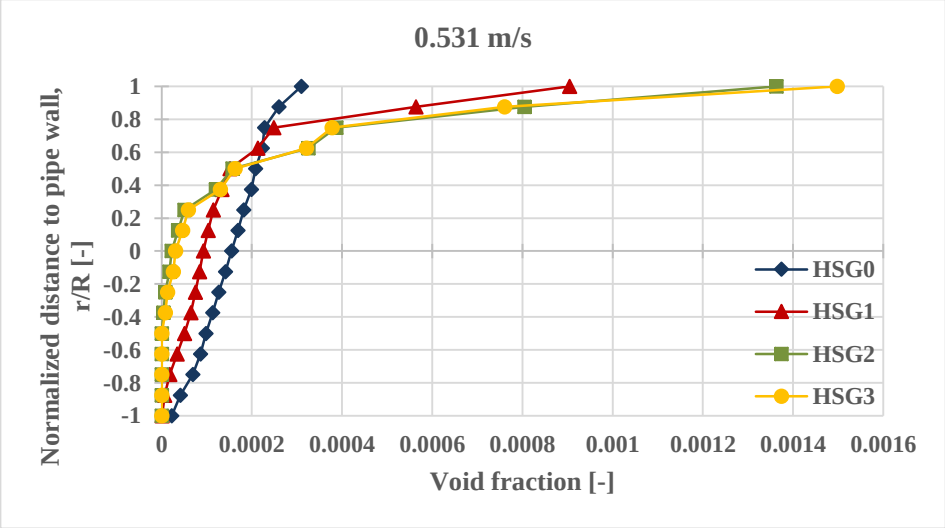

Figure 5-13. Computational results for bubble distribution development at 0.531 m/s.

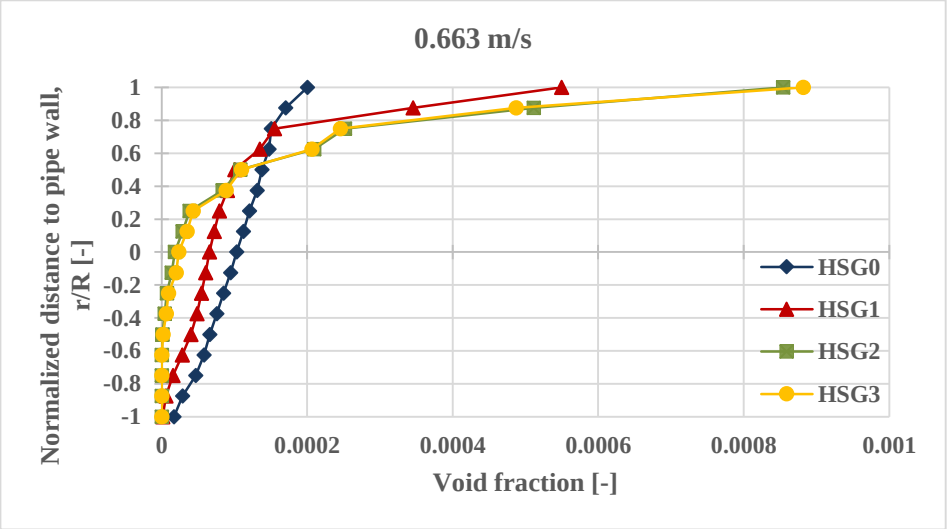

Figure 5-14. Computational results for bubble distribution development at 0.663 m/s.

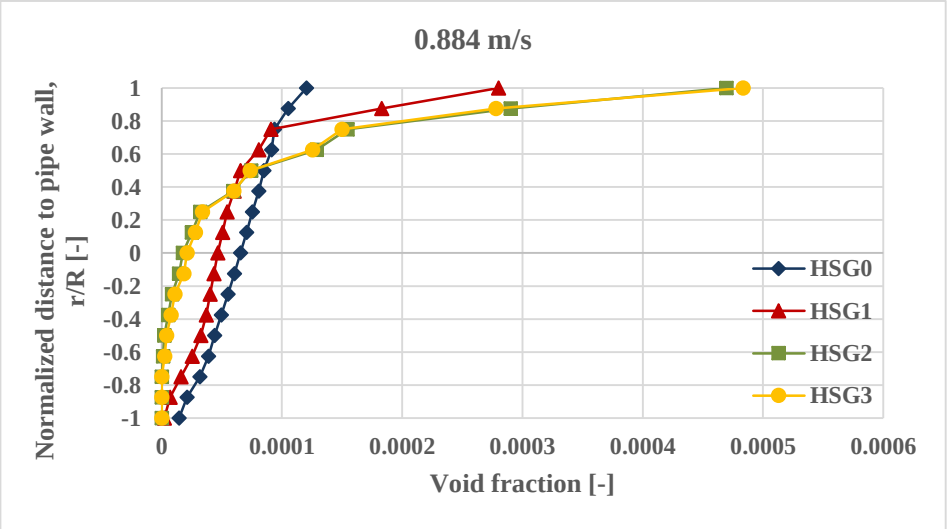

Figure 5-15. Computational results for bubble distribution development at 0.884 m/s.

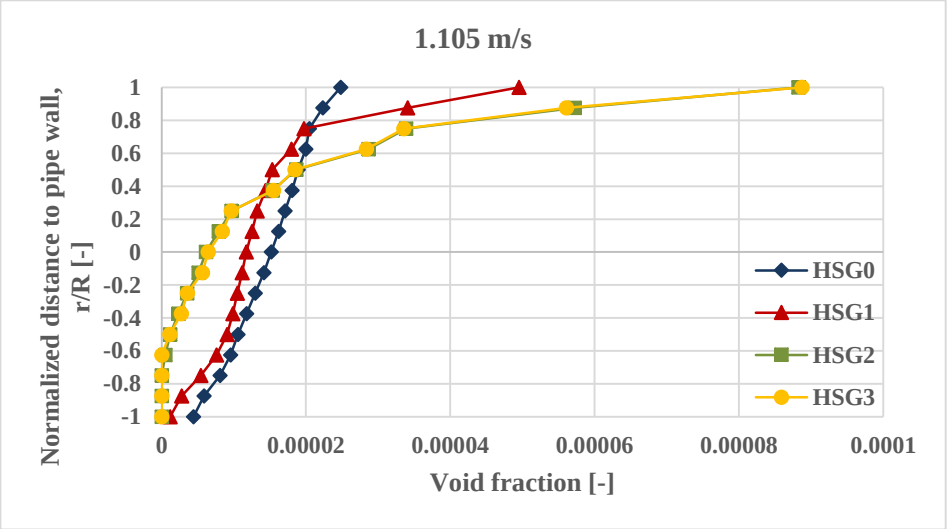

Figure 5-16. Computational results for bubble distribution development at 1.105 m/s.

5.8 Summary

To summarize, this section presented the computational study conducted to investigate bubble distributions that can occur in wet central heating systems. The case where downward flow was directed to horizontal flow with a 90 degree bend was the main consideration since the experimental measurements were conducted on a similar setup. A brief introduction to how CFD works and all of the necessary information to replicate the simulations were provided. In general, computational results agreed well with the observations reported in the literature and also with the conclusions reached from the experiments of this study. Main conclusions can be summarized in three sentences. First, the 90 degree bend is responsible for the levelling of void fractions at HSG0. Second, the 90 degree bend effect becomes pronounced as the fluid velocity increases, and finally, axial development of void fraction profiles is a continuous process.

CHAPTER 6 CONCLUSIONS AND RECOMMENDATIONS FOR FUTURE WORK

Investigation of two-phase flow structures throughout a typical wet central heating system was carried out at the experimental facility located in Brunel University London, UK. This project was a continuation of a preceding research, therefore, the experimental facility was modified in order to concord to the aims of the current project. In this regard, LabVIEW software used by the previous researcher to monitor experimental conditions throughout the test rig was altered to achieve online monitoring of the saturation ratio of the system. Sight glasses were reconfigured based on the previous design, and plastic compression fittings were installed at frequently altered positions on the test rig to minimize damage. Additionally, an extra pump was installed to the primary loop to enable higher flow rates than the previous study.

Similarly, photographic bubble measurement technique developed previously was improved to provide repeatability and accuracy. Camera and light positions with specific lens setups were determined and presented in detail to help future studies in replicating comparable image qualities. Comparable image quality is important in obtaining reliable results from the image processing technique since it identifies bubble diameters in the two-phase flow. Previously developed image processing routine by the software company was also improved according to the images obtained with light, camera, and lens settings determined for this study. Furthermore, an accurate depth of field measurement technique was developed to enhance the actual void fraction calculations. Finally, frame independence tests were employed to ensure that sufficient amount of samples were captured to produce reliable data.

Later, series of experiments were conducted at vertical and horizontal pipelines of the modified and improved test rig. Conclusions of the experimental results can be summarized as follows.

Firstly, effect of system parameters (temperature, pressure, heating load, and saturation ratio) on bubble production rates, void fractions, and average bubble diameters at the boiler exit were investigated. The results showed that bubble production and void fractions increase as the temperature, boiler heating load, and saturation ratio escalate. On the other hand, they reduce when the pressure and flow rate of the system gets higher. Moreover, it was observed that there was not a clear relationship between average bubble diameters and system parameters, except for the system flow rate. It was concluded that bubble sizes at boiler exit were significantly affected by the liquid flow rate, and this was later supported by the fact that average bubble diameters decrease as flow rate increases.

Secondly, bubble volume distributions across the pipe section was investigated at vertical downward flow and horizontal pipeline of the test rig. Most noticeable difference between two orientations is the arrangement of bubbles. Bubbles are evenly distributed during vertical flow when compared to horizontal flow, where bubbles tend to flow at the upper parts of the pipe. Bubble distributions at vertical downward flow showed centre-peaked profiles at low flow rates and their distributions levelled as the flow rate increased. Flow rate also affected the bubble distributions at horizontal flow, where bubble arrangement also levelled as velocity grew. Furthermore, it was shown that bubble distributions were highly affected by obstacles like the 90 degree bend, thermocouple or pressure sensors. And, it was observed that axial flow development of bubbly flow was a continuous process and void fraction at the upper part of the pipe increased as the flow travelled through horizontal pipeline.

Thirdly, bubble size distributions across the pipe section was investigated at vertical downward flow and horizontal pipeline of the test rig. Bubble size distribution across the pipe section showed oscillations right after the double 90 degree bends at vertical downward flow. Size distribution developed along the vertical pipe and became levelled with peak average bubble diameters in the middle. Similarly, size

distribution at horizontal flow also showed fluctuation right after the 90 degree bend and developed along the horizontal pipe. Size distributions at horizontal flow peaked at the top of the pipe, and lessened from top to bottom.

Fourthly, a bubble velocity measurement technique was employed by tracking a single bubble through the sample volume with high shutter speed. Bubble velocity measurements were carried out at both vertical and horizontal pipelines of the system. Later, results of these measurements were compared with the universal power law profile, which defines the fully developed single phase liquid velocity profile. It was concluded that bubble velocity profiles show development along both vertical and horizontal flows and approach to profiles which can be expressed with power-law.

Lastly, bubble detachment model proposed by Winterton was compared with experimental results at boiler exit. It was shown that at 950 LPH, bubble detachment model provided predictions with a 20% uncertainty. However, it did not provide a reliable prediction when the fluid flow rate varied, indicating that further investigation was necessary. Next, it was observed that bubble size distribution at the boiler exit followed a log-normal distribution, showing that log-normal distribution function could be used to describe bubble sizes at boiler exit. Coalescence of two bubbles during the horizontal flow was captured, emphasizing that the effect of coalescences should not be neglected at low void fractions. It was also found that bubbly flow in central heating systems were in coalescence dominant regime and maximum bubble diameter observed at positions after VSG1 were bigger than theoretically defined d_{min}. Moreover, bubble dissolution effect was not observed in any of the conditions utilized in the present study. The reasons were thought to be the variation saturation ratio and axial flow development of two-phase flow, which supress the effects of dissolution and favours coalescences phenomenon.

Following, a computational study was carried out to investigate bubble distribution variations when the vertical downward bubbly flow is directed to a horizontal pipe through a typical 90 degree bend used in domestic central heating systems. Main conclusions can be summarized as follows:

- 90 degree bend is responsible for the levelling of void fractions at HSG0.

- 90 degree bend effect becomes pronounced as fluid velocity increases.
- Axial development of void fraction profiles is a continuous process.

After evaluating conclusions from the experimental results and computational study regarding the effect of the 90 degree bend on void fraction distributions, it was concluded that employed physical model and solver settings in ANSYS Fluent 14.5 can be used to predict bubble distribution developments throughout the central heating systems pipework.

According to the experience acquired from experimental and computational investigations, following recommendations can be made for future studies:

- Even though current sight glass design offers effective filming of the two-phase flow, a new sight glass design can be developed. This will facilitate to reduce the effects of transition from circular to quadratic cross section, in order to achieve more accurate measurements. Moreover, it would be wise to consider a new design which can easily be assembled and reassembled. By doing so, glasses will be cleaned more efficiently.
- Image analysis software requires an enhancement since the processing time for each set of 2000 frames necessitated approximately 30 mins. This can quickly add up to an enormous amount of time if several focal planes and different positions are included in the measurements. The author believes that this problem can be handled more effectively by using the latest version of the current software or employing Matlab Software as an image processing tool, which offers higher processing speeds.
- Microsoft excel was used while processing the data from image analysis. This again required excessive amount of work since several focal planes and positions were involved in the study. Such a workload can easily lead to human errors during processing. In order to overcome these undesirable situations and improve the efficiency and accuracy of the data processing stage, a software with a more flexible programming capability can be employed. Matlab Software can be used as such since it offers algorithm implementation of and data plotting. Moreover, image and data processing

can be performed simultaneously in Matlab Software, which would save enormous amount of time.

- In the current study, the camera was moved with an adjustable slider by rotating a screw using an Allen key, making the process prone to human errors. An automatic traverse mechanism can be designed and employed to reduce this risk. Moreover, distances determined for the bubble measurement equipment were measured by a steel ruler, which may also involve human error. More accurate distance measurements can help to improve the accuracy of the measurements. Automatic traverse mechanism and more accurate distance measurements can both lead to a more accurate depth of field determination, and thus, to more precise void fraction calculations.
- The dissolved gas concertation measurement device used in the current study requires a 15 or 20 mins time frame to respond to the changes in system conditions. Therefore, a different dissolved gas concentration measurement requiring less response time can be considered for usage in future studies.

All in all, the writer anticipates that this research will contribute to future studies which aim to investigate innovative ways of improving the efficiency of central heating systems. It is the author’s wish that studies like this proliferate in the near future, in order to advance our understanding on the subject and provoke scientific curiosity for the improvement of human conditions.

REFERENCES

Andreussi, P., Paglianti, A. & Silva, F.S., 1999. Dispersed bubble flow in horizontal pipes. *Chemical Engineering Science*, 54, pp.1101–1107.

Angeli, P., 2014. *Multiphase flow fundamentals-Lecture Notes*,

Anon, 2009. *A Dictionary of Physics* 6th ed., Oxford University Press.

Anon, Depth of field. Available at: http://en.wikipedia.org/wiki/Depth_of_field [Accessed April 29, 2015].

Anon, 2011. *Great Britian's housing energy fact file*,

Anon, 2010. *The building regulations 2010*, UK.

Ansys, 2009. *ANSYS Fluent 12.0 User's Guide*, USA: ANSYS Inc.

Ansys, 2013. *ANSYS Fluent Theory Guide*, USA: ANSYS Inc.

Ansys, 2015a. Lecture 2: Introduction to the CFD methodology.

Ansys, 2015b. Lecture 3: Cell zone and boundary conditions.

Ansys, 2015c. Lecture 5: Solver settings.

Ansys, 2015d. Lecture 7: Turbulence modeling.

Ansys, 2015e. Lecture 9: Best practice guidelines.

Battino, R. & Clever, H.L., 1966. The solubility of gases in liquids. *Chemical Reviews*, 66(4), pp.395–463.

Battino, R., Rettich, T. & Tominaga, T., 1984. The solubility of nitrogen and air in liquids. *Journal of physical and …*, 13(2), pp.563–600.

Bearings, S., 2010. *AISI 52100 Chrome Steel Data Sheet*, Lancashire.

Bernardin, J.D. & Mudawar, I., 2002. A Cavity Activation and Bubble Growth Model of the Leidenfrost Point. *Journal of Heat Transfer*, 124(5), p.864.

Bevington, P.R. & Robinson, D.K., 2003. *Data Reduction and Error Analysis for the Physical Sciences* Third Edit., London: McGraw-Hill.

Bhagwat, S.M. & Ghajar, A.J., 2012. Similarities and differences in the flow patterns and void fraction in vertical upward and downward two phase flow. *Experimental Thermal and Fluid Science*, 39, pp.213–227.

Blazek, J., 2001. *Computational fluid dynamics: Principles and applications*, London: Elsevier Science Ltd.

Bottin, M. et al., 2014. Experimental investigation of a developing two-phase bubbly flow in horizontal pipe. *International Journal of Multiphase Flow*, 60, pp.161–179.

Bowers, P.G. et al., 1995. Supersaturation Limit for Homogeneous Nucleation of Oxygen Bubbles in Water at Elevated Pressure: "Superhenry's Law." *Omega*, 99, pp.9632–9637.

Brennen, C.E., 2005. *Fundamentals of multiphase flows*, Cambridge: Cambridge University Press.

De Chant, L.J., 2005. The venerable 1/7th power law turbulent velocity profile: a classical nonlinear boundary value problem solution and its relationship to stochastic processes. *Applied Mathematics and Computation*, 161(2), pp.463–474.

Chisholm, D., 1983. *Two-phase flow in pipelines and heat exchangers*, Essex: Longman Group Limited.

Clever, H.L. & Battino, R., 1975. The solubility of gases in liquids. In M. R. J. Dack, ed. *Solutions and solubilities*. London, pp. 379–443.

Coleman, H.W. & Steele, W.G., 1999. *Experimental and uncertainty analysis for engineers*, New York: Wiley.

Crowe, C.T. ed., 2006. *Multiphase flow handbook*, London: Taylor&Francis.

Crowe, C.T. et al., 2012. *Multiphase flows with droplets and particles* 2nd ed., London: Taylor&Francis Group.

Curry, B., 2001. *Copper tubes in domestic heating systems*, Hertfordshire.

Danckwerts, P. V., 1970. *Gas-liquid reactions*, London: McGraw-Hill.

Devereux, M.G. & Lee, W.T., 2011. Mathematical modelling of bubble nucleation in stout beers and experimental verification. In *Proceedings of the World Congress on Engineering*. pp. 160–164.

Divinis, N. et al., 2006. Lateral motion and interaction of gas bubbles growing over spherical and plate heaters. *Microgravity - Science and Technology*, 18(3-4), pp.204–209.

Divinis, N. et al., 2005. Self-similar growth of a gas bubble induced by localized heating: The effect of temperature-dependent transport properties. *Chemical Engineering Science*, 60(6), pp.1673–1683.

Drew, D. a. & Lahey, R.T., 1982. Phase-distribution mechanisms in turbulent low-quality two-phase flow in a circular pipe. *Journal of Fluid Mechanics*, 117, p.91.

Druck, 2010. *PTX 7500 series*, Leicester.

Ekambara, K. et al., 2012. CFD Modeling of Gas-Liquid Bubbly Flow in Horizontal Pipes: Influence of Bubble Coalescence and Breakup. *International Journal of Chemical Engineering*, 2012, pp.1–20.

Ekambara, K. et al., 2008. CFD simulation of bubbly two-phase flow in horizontal pipes. *Chemical Engineering Journal*, 144(2), pp.277–288.

Enríquez, O.R. et al., 2013. Growing bubbles in a slightly supersaturated liquid solution. *Review of Scientific Instruments*, 84.

Feynman, R., 1994. Atoms in motion. In *Six easy pieces*. New York: Addison-Wesley, pp. 1–15.

Frolich, P.K. et al., 1931. Solubilities of gases in liquids at high pressure. *Industrial & Engineering Chemistry*, 23(5), pp.548–550.

Fsadni, A. & Ge, Y., 2014. Bubble shape and breakage events in a vertical pipe at the boiler flow line. *EPJ Web of Conferences*, 64, pp.02029–1–6.

Fsadni, A. & Ge, Y.T., 2013. Two-phase distribution in the vertical flow line of a domestic wet central heating system. *EPJ Web of Conferences*, 45, pp.01030–1–6.

Fsadni, A.M., 2012. *The fundamentals of two-phase flow in wet domestic central heating systems*. Brunel Univeristy.

Fsadni, A.M. & Ge, Y., 2012. Micro bubble formation and bubble dissolution in domestic wet central heating systems. *EPJ Web of Conferences*, 25, pp.01016–1–16.

Fsadni, A.M., Ge, Y.T. & Lamers, A.G., 2012. Bubble nucleation on the surface of the primary heat exchanger in a domestic central heating system. *Applied Thermal Engineering*, 45-46, pp.24–32.

Fsadni, A.M., Ge, Y.T. & Lamers, A.G., 2011a. Experimental analysis of two-phase flow in domestic central heating systems – micro bubble characteristics. In *Multiphase flow*. Southamptom: WIT press, pp. 165–176.

Fsadni, A.M., Ge, Y.T. & Lamers, A.G., 2011b. Measurement of bubble detachment diameters from the surface of the boiler heat exchanger in a domestic central heating system. *Applied Thermal Engineering*, 31, pp.2808–2818.

Galbraith, W., 1955. The Optical Measurement of Depth. *Quarterly Journal of Microscopical Science*, 96(part 3), pp.285–288.

GE, 2007. *ELSV-60 Watt Metal-Halide source*, England.

Ge, Y.T., Fsadni, A.M. & Wang, H.S., 2013. Bubble dissolution in horizontal turbulent bubbly flow in domestic central heating system. *Applied Energy*, 108, pp.477–485.

Gerrard, W., 1976. *Solubility of gases and liquids : a graphic approach*, London: Plenum Press.

Govier, G.W. & Aziz, K., 1972. *The flow of comples mixtures in pipes*, New York: Van Nostrand Reinhold Company.

Groundfos, 2009. *Groundfos data sheet UPS Solar*, Denmark.

Groundfos, 2012. *Groundfos selectric/super selectric*, England.

Groundfos, 2004. *Pump Handbook*, Bjerringbro.

Haoues, L., Olekhnovitch, A. & Teyssedou, A., 2008. Influence of the void fraction profile on the distribution parameter C0 for a bubbly gas–liquid flow in a horizontal round pipe. *Nuclear Engineering and Design*, 238(4), pp.1155–1158.

Haoues, L., Olekhnovitch, A. & Teyssedou, A., 2009. Numerical study of the influence of the internal structure of a horizontal bubbly flow on the average void fraction. *Nuclear Engineering and Design*, 239(1), pp.147–157.

Harvey, A., 1996. Semiempirical correlation for Henry's constants over large temperature ranges. *AIChE journal*, 42(5), pp.1491–1494.

Henry, W., 1802. Experiments on the quantity of gases absorbed by water, at different temperatures, and under different pressures. *Philosophical Transactions of the Royal Society of London*, 93, pp.29–42.

Hibiki, T. et al., 2005. Axial development of interfacial structure of vertical downward bubbly flow. *International Journal of Heat and Mass Transfer*, 48(3-4), pp.749–764.

Hibiki, T. et al., 2004. Structure of vertical downward bubbly flow. *International Journal of Heat and Mass Transfer*, 47(8-9), pp.1847–1862.

Ishii, M. et al., 2004. Interfacial structures and interfacial area transport in downward two-phase bubbly flow. *International Journal of Multiphase Flow*, 30(7-8), pp.779–801.

Iskandrani, a. & Kojasoy, G., 2001. Local void fraction and velocity field description in horizontal bubbly flow. *Nuclear Engineering and Design*, 204(1-3), pp.117–128.

Jones, S.F., Evans, G.M. & Galvin, K.P., 1999. Bubble nucleation from gas cavities — a review. *Advances in Colloid and Interface Science*, 80, pp.27–50.

Karapantsios, T.D. et al., 2008. Nucleation, growth and detachment of neighboring bubbles over miniature heaters. *Chemical Engineering Science*, 63(13), pp.3438–3448.

Kashinsky, O.N. & Randin, V.V., 1999. Downward bubbly gas–liquid flow in a vertical pipe. *International Journal of Multiphase Flow*, 25(1), pp.109–138.

Keller, 2009. *Highly precise pressure transmitters*, Germany.

Kern, W.F. & Bland, J.R., 1938. *Solid Mensuration: with Proofs*, London: Chapman&Hall Limited.

Kim, S. et al., 2007. Geometric effects of 90-degree Elbow in the development of interfacial structures in horizontal bubbly flow. *Nuclear Engineering and Design*, 237(20-21), pp.2105–2113.

Kocamustafaogullari, G. & Huang, W.D., 1994. Internal structure and interfacial velocity development for bubbly two-phase flow. *Nuclear Engineering and Design*, 151(1), pp.79–101.

Kocamustafaogullari, G., Huang, W.D. & Razi, J., 1994. Measurement and modeling of average void fraction, bubble size and interfacial area. *Nuclear Engineering and Design*, 148(2-3), pp.437–453.

Kocamustafaogullari, G. & Wang, Z., 1991. An experimental study on local interfacial parameters in a horizontal bubbly two-phase flow. *International Journal of Multiphase Flow*, 17(5), pp.553–572.

Krichevsky, I. & Kasarnovsky, J., 1935. Thermodynamical calculations of solubilities of nitrogen and hydrogen in water at high pressures. *Journal of the American Chemical Society*, 57(11), pp.2168–2171.

Lemlich, R. ed., 1972. *Adsorptive bubble separation techniques*, London: Academic Press Inc.

Levy, S., 1999. *Two-phase flow in complex systems*, New York: John Wiley&Sons Inc.

Lezhnin, S. et al., 2003. Dissolution of air bubbles in a turbulent water pipeline flow. *Heat Mass Trans.*, 39(5-6), pp.483–487.

Litremeter, 2010. *500 series flowmeter specification sheet*, England.

Liu, S. & Li, D., 1999. Drop coalescence in turbulent dispersions. *Chemical Engineering Science*, 54, pp.5667–5675.

Loeffler, A., 2011. *Tech tip #38*, Oklahoma.

Markham, A. & Kobe, K.A., 1941. The solubility of gases in liquids. *Chemical Reviews*, 28(3), pp.519–588.

MediaCybernetics, 2010. *Image-Pro Plus Start-Up Guide*, Bethesda.

Melvin, M., 2005. *How to use system-head curves*, Indianapolis.

Moffat, R.J., 1988. Describing the uncertainties in experimental results. *Experimental Thermal and Fluid Science*, 1(1), pp.3–17.

Nassar, A.B., 1994. Apparent depth. *The Physics Teacher*, 32(9), pp.526–529.

NI, 2008. *User guide and pecifications NI cDAQ-9172*, UK.

Oshinowo, T. & Charles, M.E., 1974. Vertical two-phase flow part I. Flow pattern correlations. *The Canadian Journal of Chemical Engineering*, 52(1), pp.25–35.

Ottochemie, 2013. *Technical datasheet Otto Primer 1216*, Germany.

Ottochemie, 2014. *Technical Datasheet OTTOSEAL S28*, Germany.

Perry, R.H., Green, D.W. & Maloney, J.O. eds., 1997. *Perry's chemical engineers' handbook* 7th ed., London: McGraw-Hill.

Phantom, 2007. *Phantom v5.1 data sheet*, USA.

Prausnitz, J.M., Lichtenthaler, R.N. & de Azevedo, E.G., 1999. Solubilities of gases in liquids. In N. R. Amundson, ed. *Molecular thermodynamics of fluid-phase equilibria*. New Jersey: Prentice-Hall, pp. 595–631.

Prodanovic, V., Frase, D. & M., S., 2002. Bubble behavior in subcooled flow boiling of water at low pressures and low flow rates. *International Journal of Multiphase Flow*, 28, pp.1–19.

Rahman, M. a., Heidrick, T. & Fleck, B. a., 2009. A Critical Review of Advanced Experimental Techniques to Measure Two-Phase Gas/Liquid Flow. *The Open Fuels & Energy Science Journal*, 2(1), pp.54–70.

Rawle, A.F., 2014. Representative sampling – another Cinderella of particle size analysis. *Procedia Engineering*, 00(MAY 2014), pp.1–7.

Razzaque, M.M. et al., 2003. Bubble size in coalescence dominant regime of turbulent air–water flow through horizontal pipes. *International Journal of Multiphase Flow*, 29(9), pp.1451–1471.

Reid, R.C., Prausnitz, J.M. & Bruce, E.P., 1986. Solubilities of gases in liquids. In *The properties of gases and liquids*. London: McGraw-Hill, pp. 332–337.

Research, V., 2007. *The CINE File Format*, New Jersey.

RS, 2010. *Data sheet mineral insulated thermocouple with standard plug*, England.

Rubin, M.B. & Noyes, R.M., 1987. Measurements of Critical Supersaturation for Homogeneous Nucleation of Bubbles. *The Journal of Physical Chemistry*, 91(15), pp.4193–4198.

Schott, 2012. *Schott borofloat 33 data sheet*, Germany.

Sear, R.P., 2007. Nucleation: theory and applications to protein solutions and colloidal suspensions. *Journal of Physics: Condensed Matter*, 19(3), p.033101.

Shedd, T.A., 2005. General model for estimating bubble dissolution and droplet evaporation times. *Journal of Micro/Nanolithography, MEMS, and MOEMS*, 4(3), p.033004.

Singh, A., Paul, A. & Ranjan, P., 2011. Investigation of reattachment length for a turbulent flow over a backward facing step for different step angle. *International Journal of Engineering, Science and Technology*, 3(2), pp.84–88.

Speedfit, 2015. *The push-fit solution for plumbing and heating systems*, London.

Spirotech, 2013. *Automatic air vents for heating, cooling and process sytems*, Helmond.

Talanquer, V. & Oxtoby, D.W., 1995. Nucleation of bubbles in binary fluids. *The Journal of Chemical Physics*, 102(5), pp.2156–2164.

Talley, J.D. & Kim, S., 2010. Horizontal bubbly flow with elbow restrictions: Interfacial area transport modeling. *Nuclear Engineering and Design*, 240(5), pp.1111–1120.

Thomas, R.M., 1981. Bubble coalescence in turbulent flows. *International Journal of Multiphase Flow*, 7(6), pp.709–717.

Usui, K. & Sato, K., 1989. Vertically Downward Two-Phase Flow, (I). *Journal of Nuclear Science and Technology*, 26(7), pp.670–680.

Vaillant, 2008. Instructions for installation and servicing ecoTEC. *Vaillant Ltd*.

Versteeg, H.K. & Malalasekera, W., 1995. *An introduction to computational fluid dynamics: The finite volume method*, New York: Longman scientfic & Technical.

Walski, T., Hartell, W. & Wu, Z., 2010. Developing system head curves for closed systems. *Journal / American Water Works Association*, 102(9), pp.84–89.

Wang, S.K. et al., 1987. 3-D turbulence structure and phase distribution measurements in bubbly two-phase flows. *International Journal of Multiphase Flow*, 13(3), pp.327–343.

Watten, B.J. & Smith, D.R., 1997. Continuous Monitoring of Dissolved Oxygen and Total Dissolved Gas Pressure Based on Head-Space Partial Pressures. *Journal Of The World Aquaculture Society*, 28(4), pp.316–333.

Wiebe, R., Gaddy, V. & Heins, C.J., 1934. The solubility of nitrogen in water at 50, 75 and 100 from 25 to 1000 atmospheres. *Journal of the American Chemical Society*, 55(3), pp.947–953.

Wisniak, J., Apelblat, A. & Segura, H., 2006. The solubility of gases in liquids. *Physics and Chemistry of Liquids*, 34(3), pp.125–153.

Yadav, M., Talley, J.D. & Kim, S., 2010. Comparison of Local Interfacial Structures Around 90 and 45-Degree Elbows in Horizontal Bubbly Flows. *Journal of Fluids Engineering*, 132(11), p.111302.

Yadav, M.S., Worosz, T., et al., 2014. Characterization of the dissipation of elbow effects in bubbly two-phase flows. *International Journal of Multiphase Flow*, 66, pp.101–109.

Yadav, M.S., Kim, S., et al., 2014. Experiments on geometric effects of 90-degree vertical-upward elbow in air water two-phase flow. *International Journal of Multiphase Flow*, 65, pp.98–107.

Yang, X. & Thomas, N.H., 1998. Prediction of Void Fraction and Velocity Profiles of Bubbly Flows in Vertical Pipes. *Chemical Engineering Communications*, 163(1), pp.145–176.

Yeoh, G.H., Cheung, S.C.P. & Tu, J.Y., 2012. On the prediction of the phase distribution of bubbly flow in a horizontal pipe. *Chemical Engineering Research and Design*, 90(1), pp.40–51.

Yoshida, Y. et al., 1998. Distribution of void fraction in bubbly flow through a horizontal channel : Bubbly boundary layer flow , 2nd report. *J Mar Sci Technol*, 3, pp.30–36.

APPENDICES

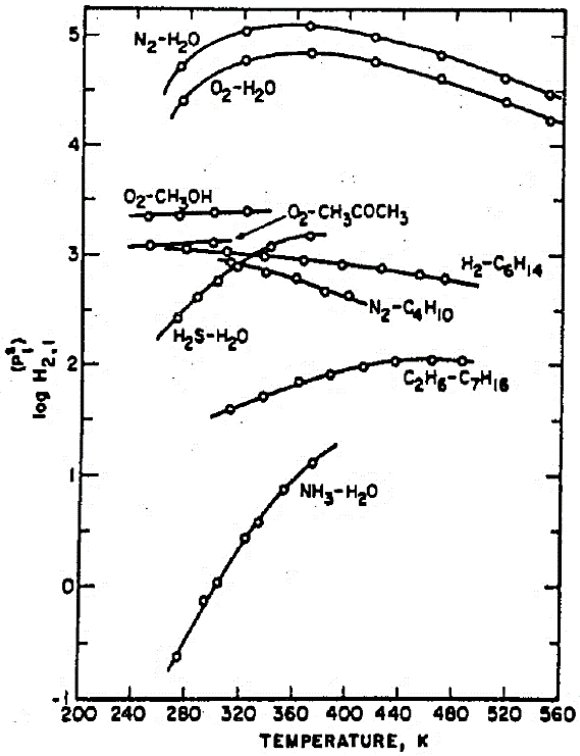

Appendix 1. Variation of Henry's constant with temperature for different solute-solvent pairs (Prausnitz et al. 1999).

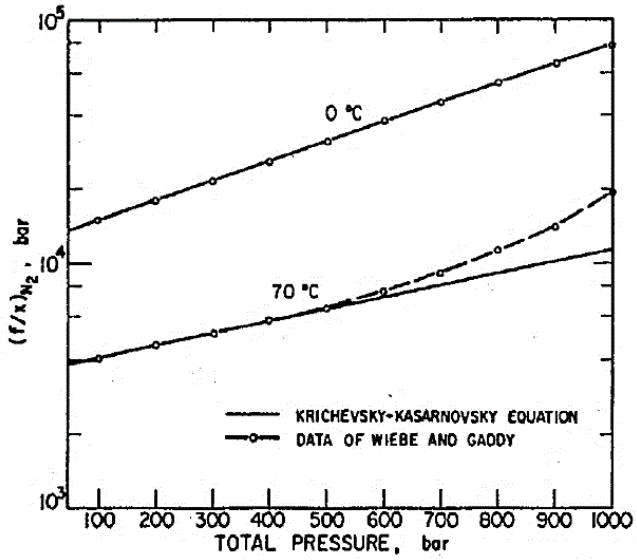

Appendix 2. Limit of Krichevsky-Kasarnovsky equation for nitrogen in liquid ammonia (Prausnitz et al. 1999).

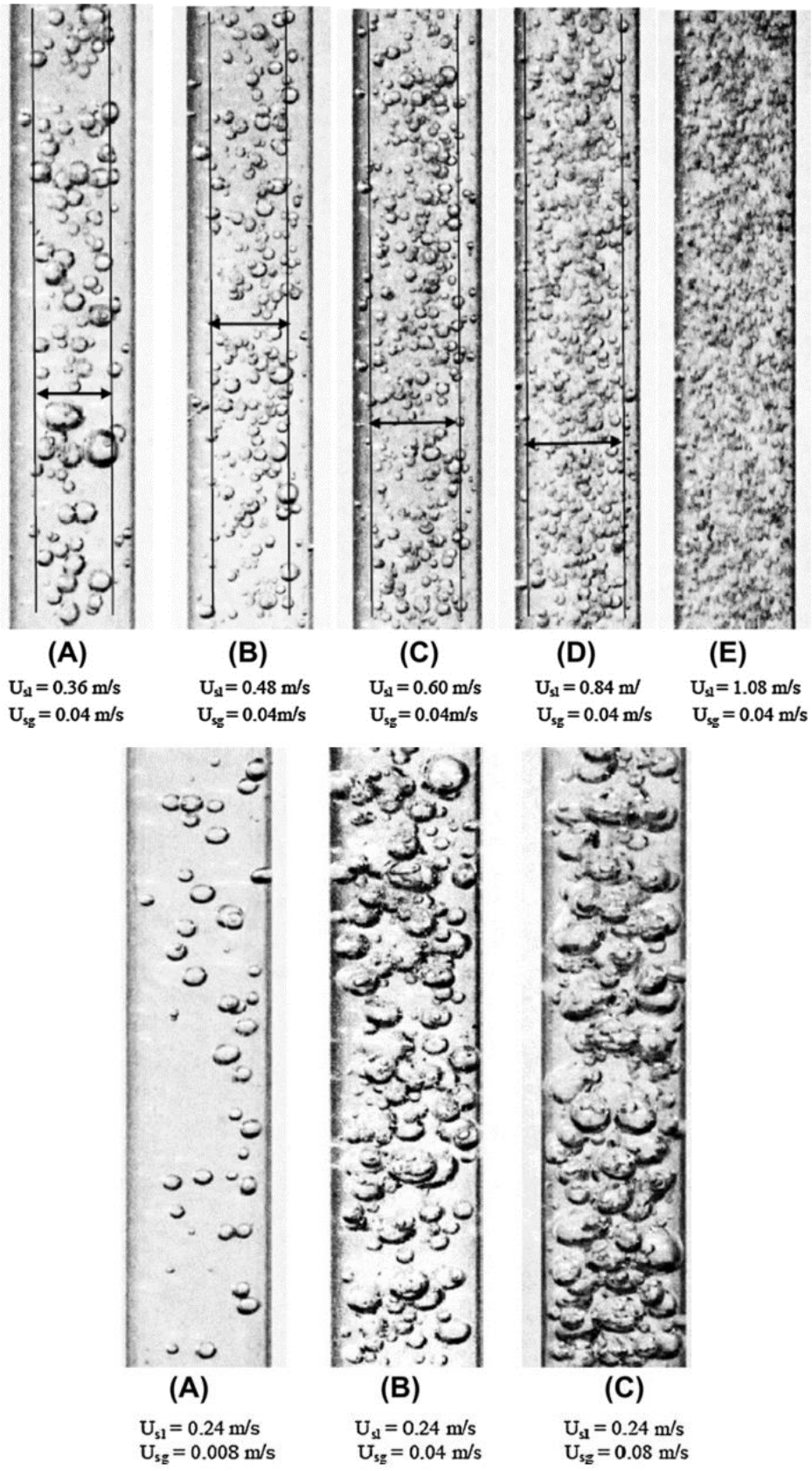

Appendix 3. Effect of liquid and gas superficial velocities on downward bubble flow (Bhagwat & Ghajar 2012).

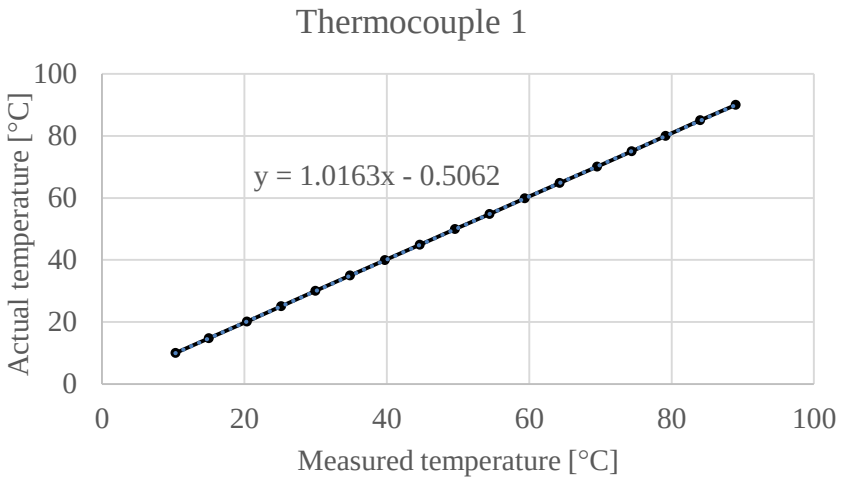

Appendix 4. Calibration curve for thermocouple 1.

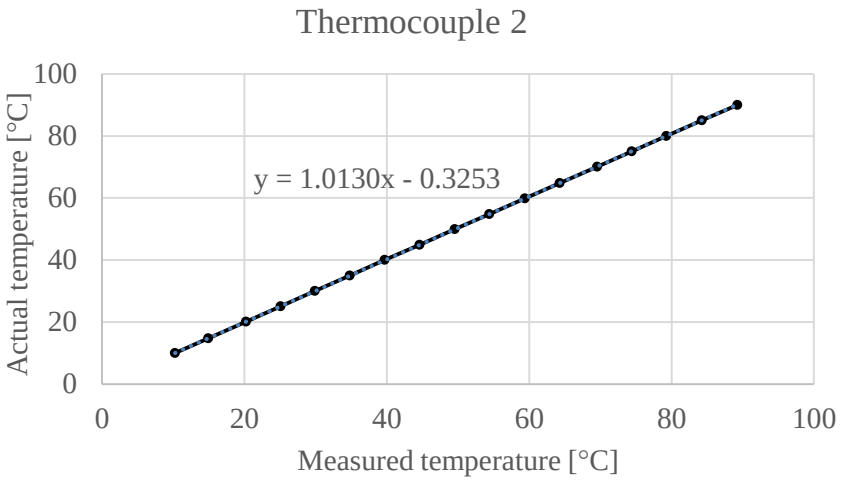

Appendix 5. Calibration curve for thermocouple 2.

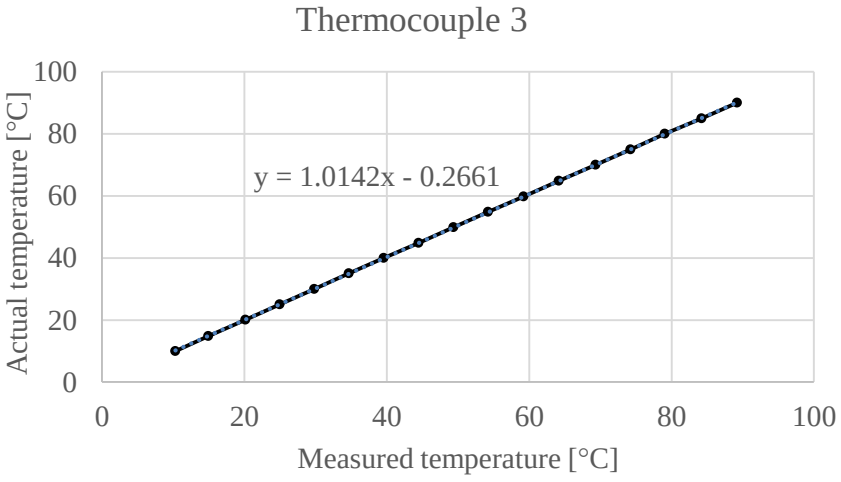

Appendix 6. Calibration curve for thermocouple 3.

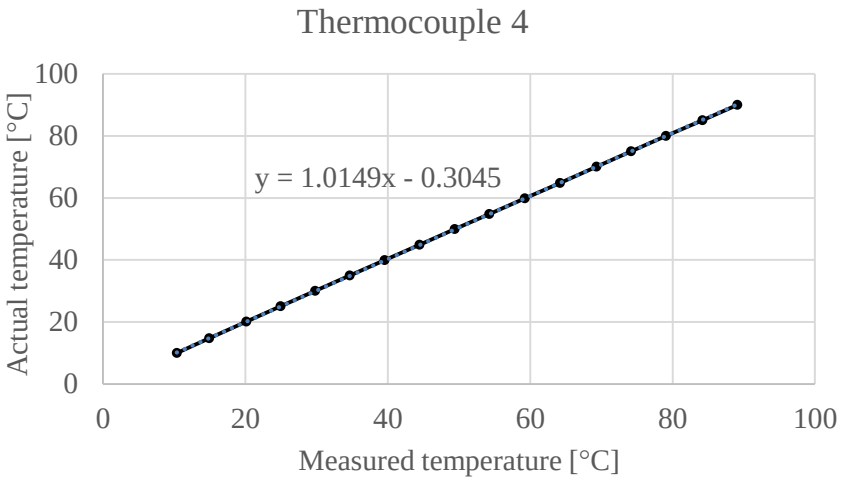

Appendix 7. Calibration curve for thermocouple 4.

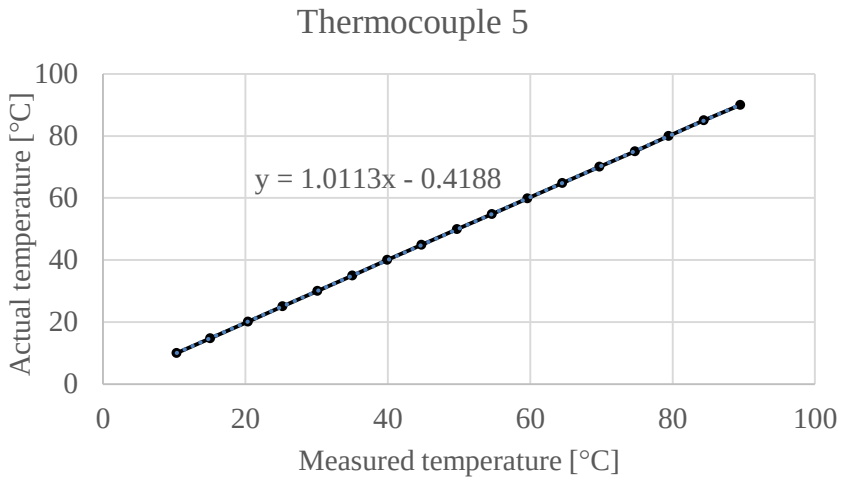

Appendix 8. Calibration curve for thermocouple 5.

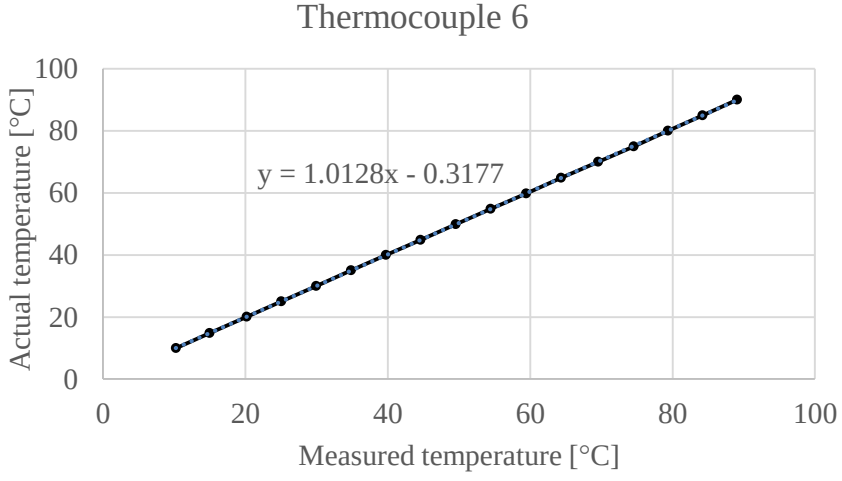

Appendix 9. Calibration curve for thermocouple 6.

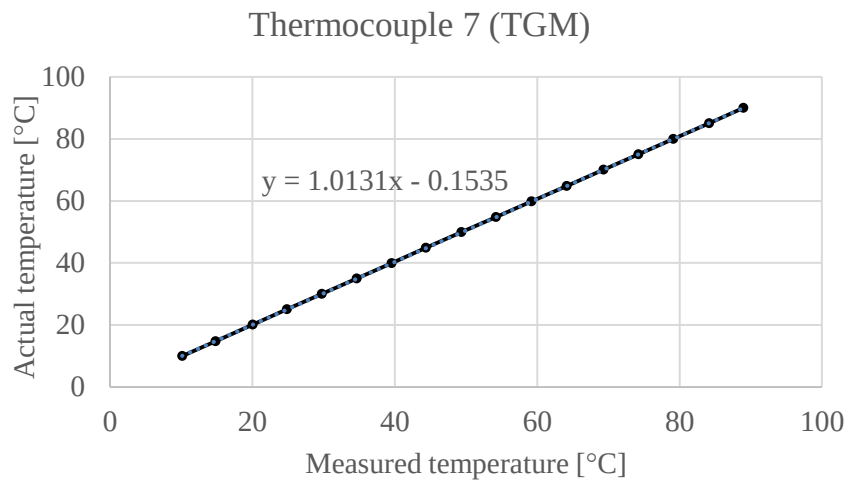

Appendix 10. Calibration curve for thermocouple 7 (TGM).

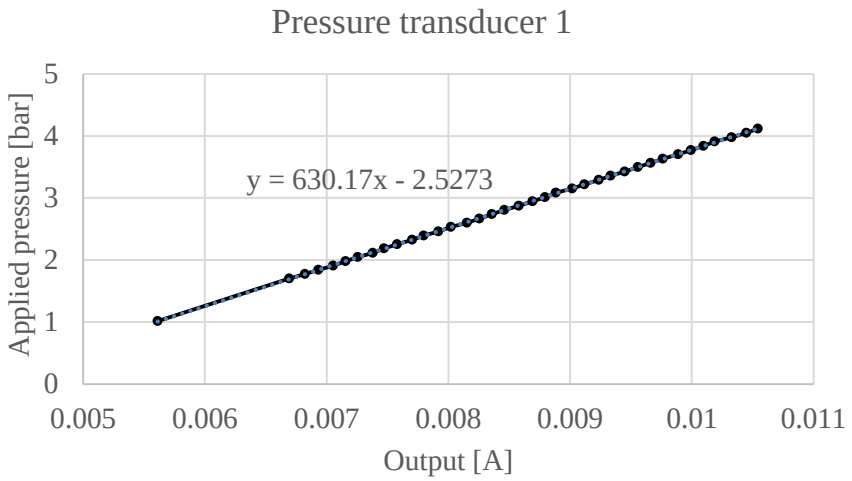

Appendix 11. Calibration curve for pressure transducer 1.

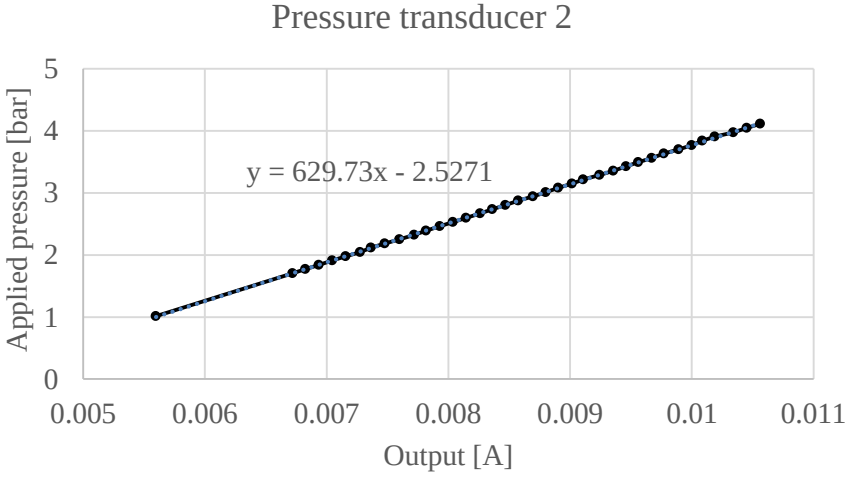

Appendix 12. Calibration curve for pressure transducer 2.

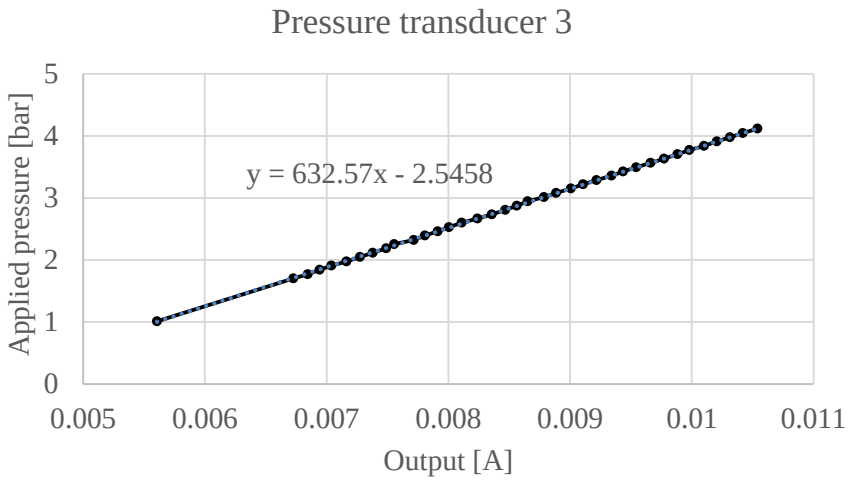

Appendix 13. Calibration curve for pressure transducer 3.

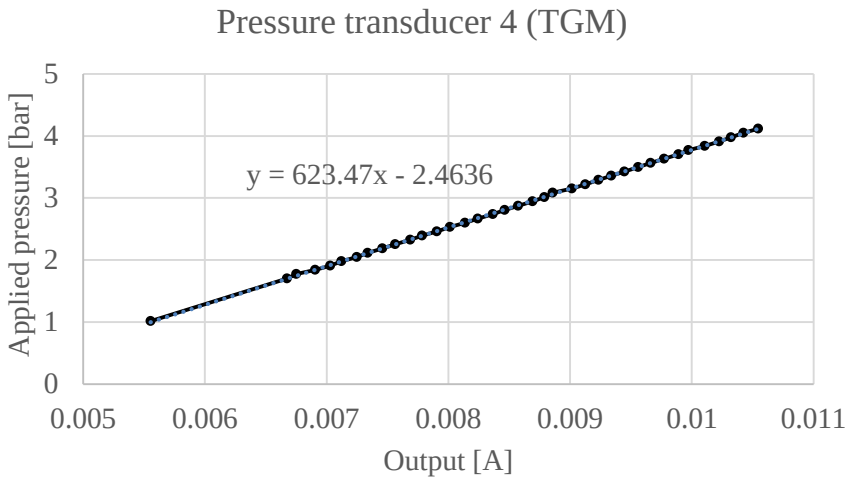

Appendix 14. Calibration curve for pressure transducer 4 (TGM).

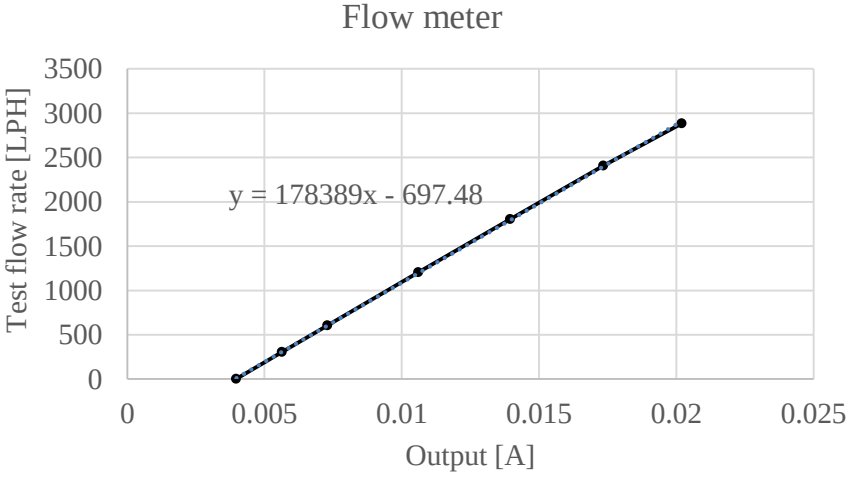

Appendix 15. Calibration curve for flow meter.

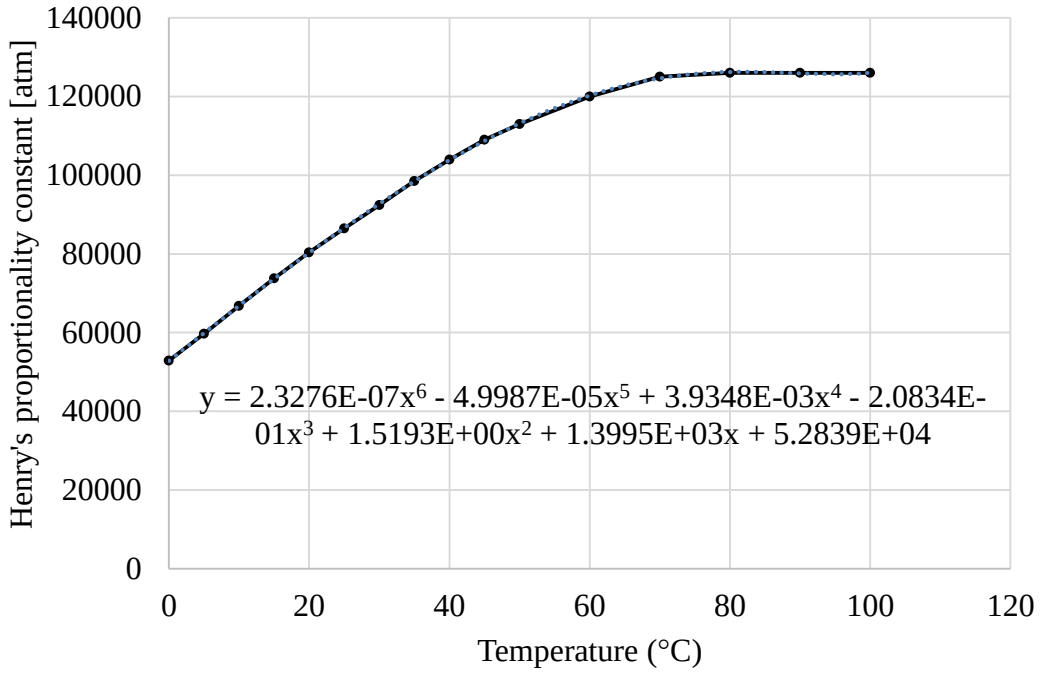

Appendix 16. Correlation used to calculate proportionality constant.

*Source: Perry et al. (1997)

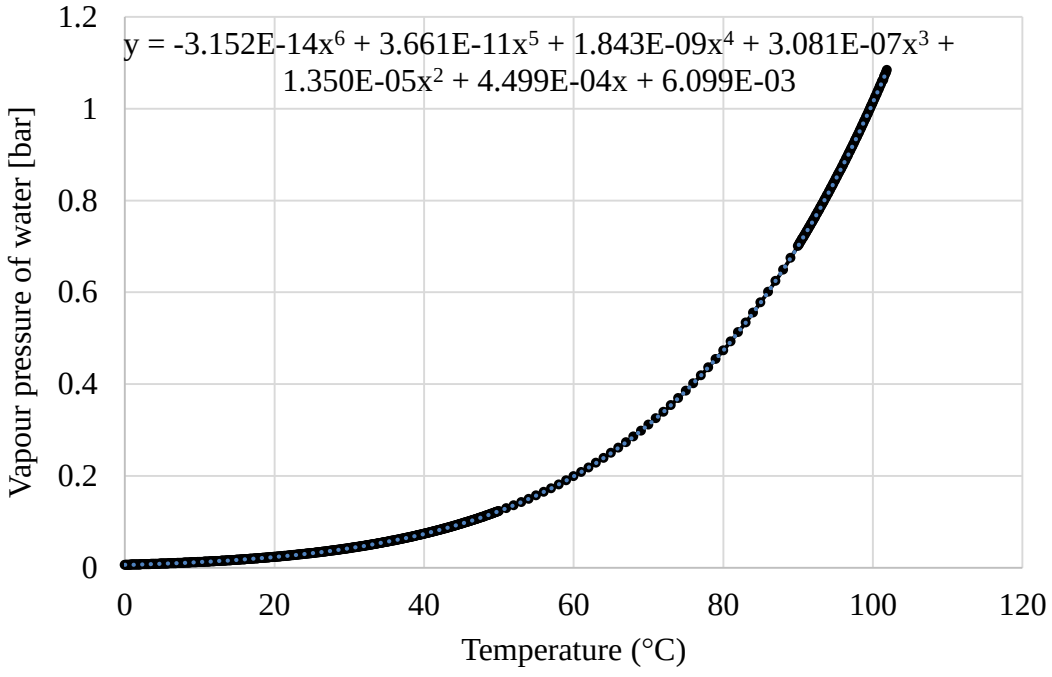

Appendix 17. Correlation used to calculate vapour pressure of water.

*Source: Perry et al. (1997)

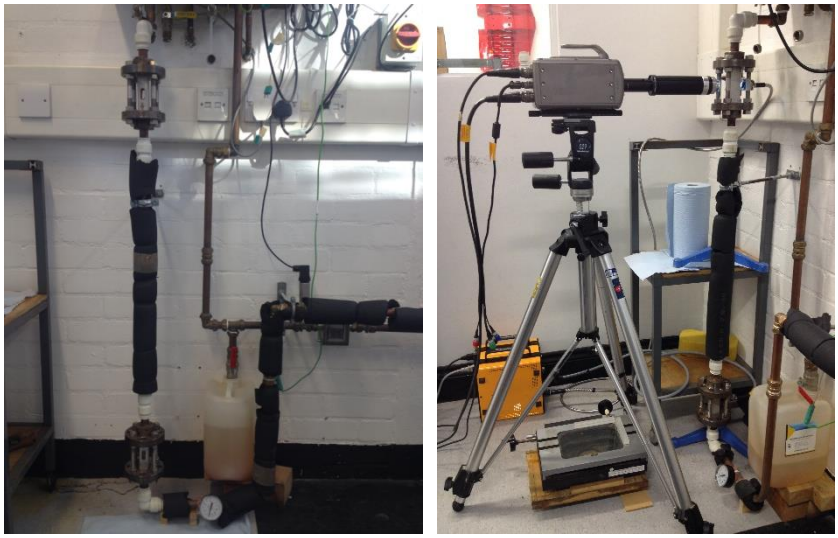

Appendix 18. The vertical setup.

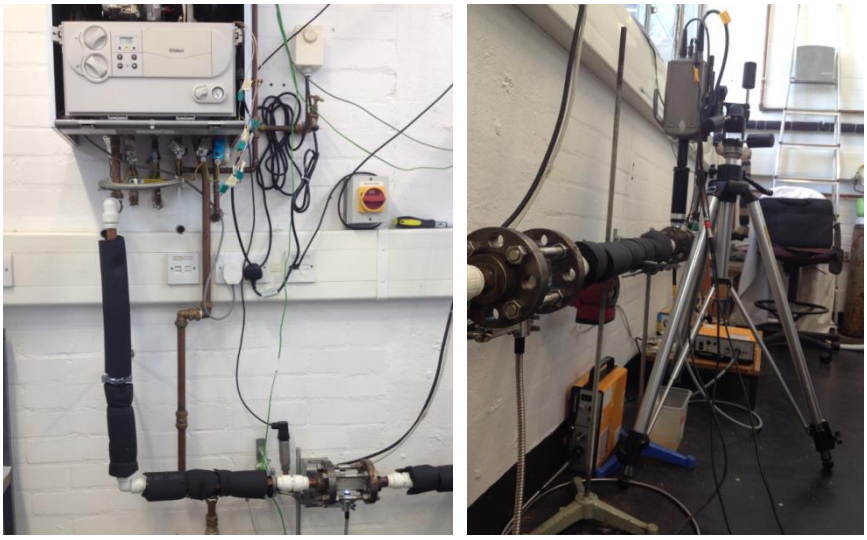

Appendix 19. The horizontal setup.

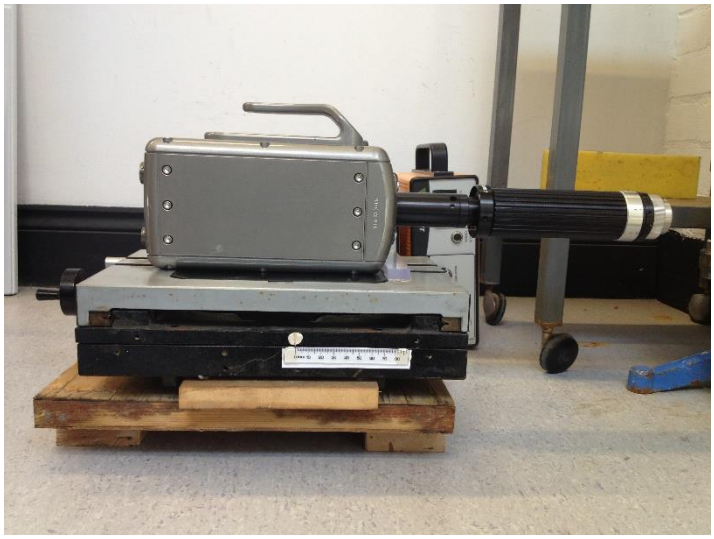

Appendix 20. 2-way slider used for the measurements at VSG2.

Appendix 21. A level ruler used to verify axes of camera setup and sight glasses.

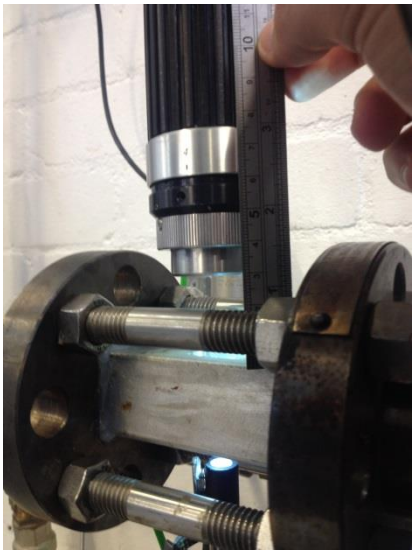

Appendix 22. 150mm stainless steel ruler used to measure camera and light distances.

Appendix 23. Ruler on the adjustable slider.

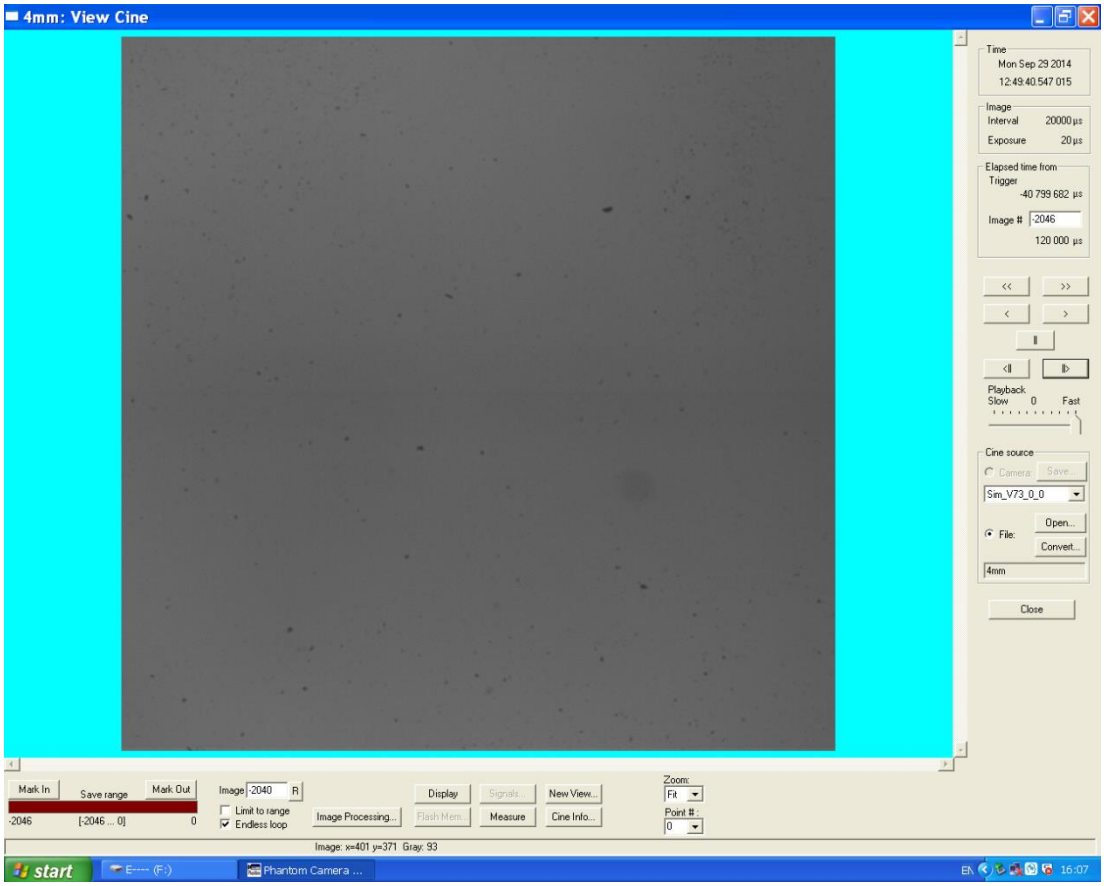

Appendix 24. Monitoring with Phantom Camera Controller (Gray intensity value is at the bottom of the user interface).

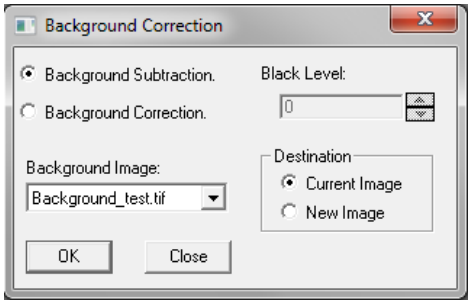

Appendix 25. Background correction.

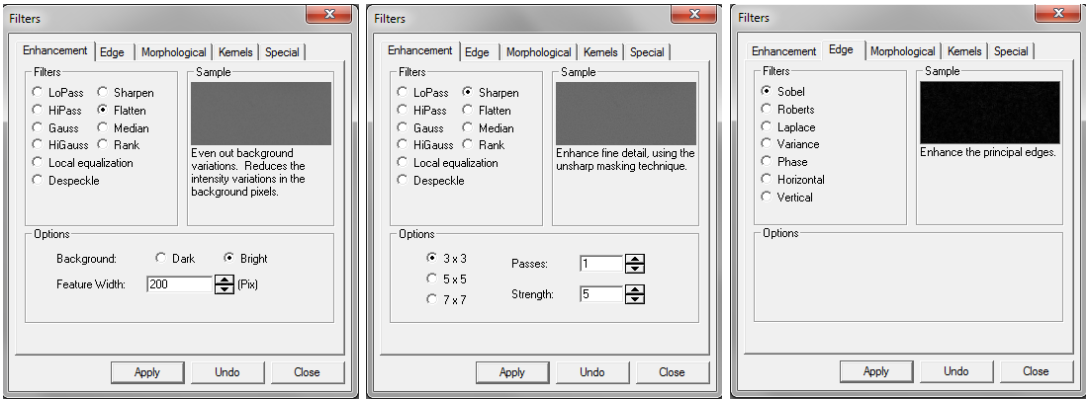

Appendix 26. Settings used in filters.

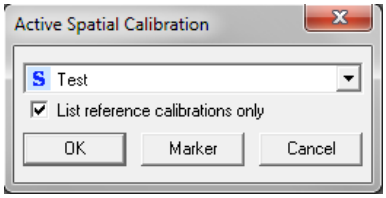

Appendix 27. Calibration selection.

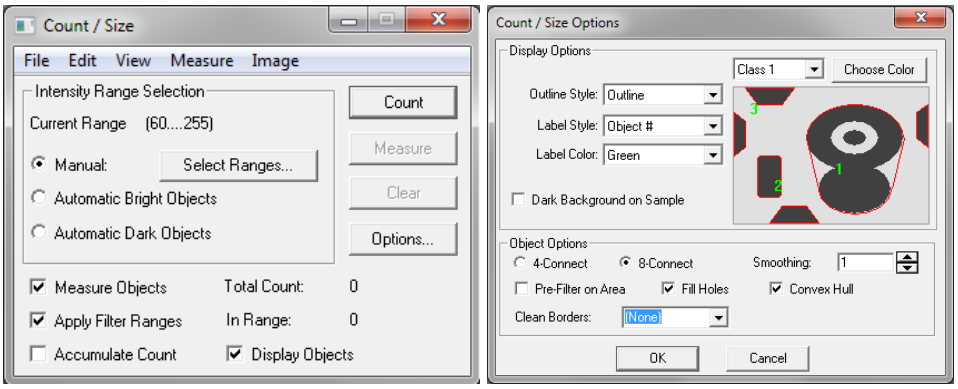

Appendix 28. Count/size menu and options used.

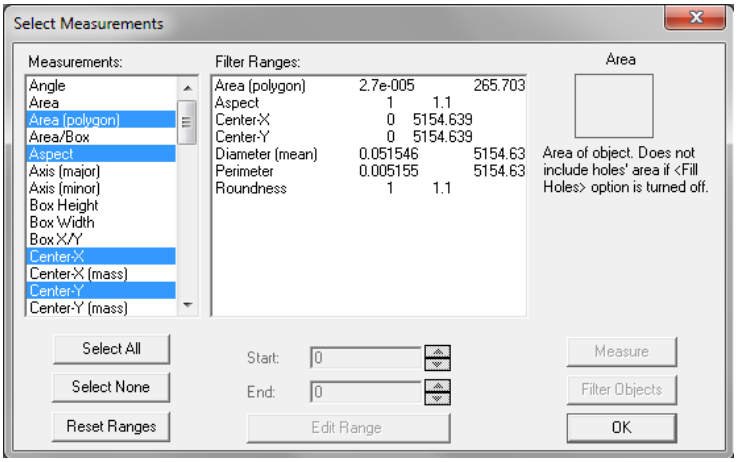

Appendix 29. Measurement selection.

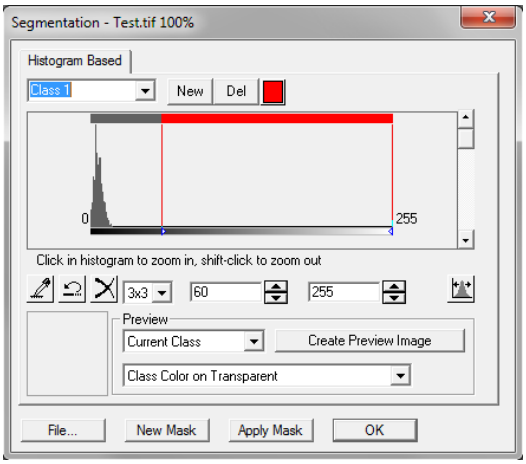

Appendix 30. Manual intensity range selection.

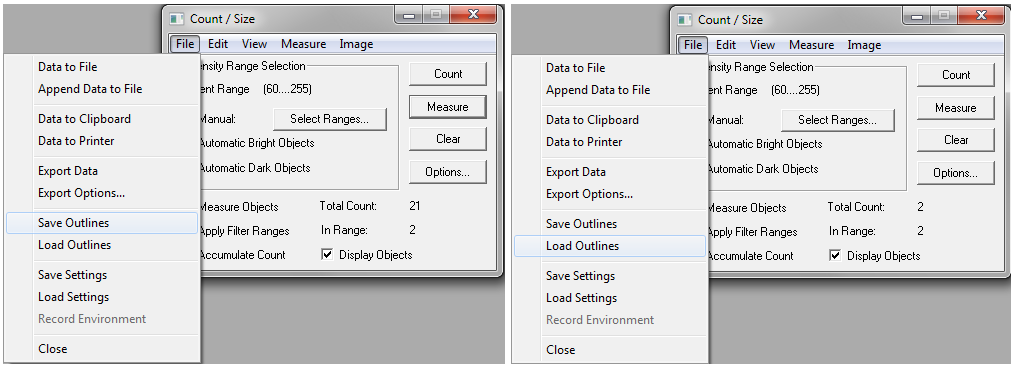

Appendix 31. Saving and loading outlines.

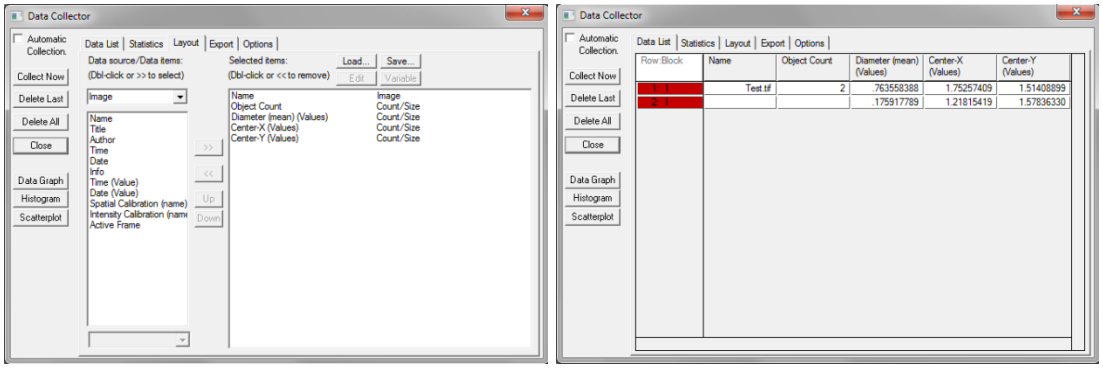

Appendix 32. Data collector feature.

```
Sub ProcessDirectory()
' Scan through and process all files in a directory
    Dim IName As String*255
    Dim fName As String
    Dim workStr As String
    Dim docID As Integer
    ' Make certain we have a reasonable starting point. This code is only executed the first run
    ' after macro compilation. If you have a desired standard starting point, initialize the
    ' directory search here.
    If gDirStart = "" Then
        gDirStart = "C:\"
    End If
    ' Get a file name in the desired directory
    workStr = GetFilePath("", "*", gDirStart, _
       "Select a file in the desired directory", 0)
    ' Check to make certain the user did not cancel
    If workStr = "" Then
        Exit Sub
    End If
    ' Close all open images prior to processing (this can be removed if desired)
    ret = IpAppCloseAll()
    ' Extract the directory name from the full file name
    gDirStart = Left(workStr, InStrRev(workStr, "\"))
    ' Clear the output for work purposes
    DebugClear
    ret = IpOutputClear()
    ' Call a setup routine ***
    ' Insert your setup call here
    ' Look for standard files, no directories or system files. See the 'Dir' command help for details
    fName = Dir(gDirStart + "*.*", 32)
    While fName <> ""
        ' Print out the file name and its attributes
        Debug.Print GetAttr(gDirStart + fName); " "; fName
        ' Load the image
        docID = IpWsLoad(gDirStart + fName, "")
        ' Don't process if there is a failure loading
        If docID >= 0 Then

            ' Call processing routine here ***

                ' Edited by the Ali Shefik

                ' Background Correction
                ret = IpWsLoad("C:\Users\sefik\Desktop\Image Processing\Background_test.tif","tif")
                ret = IpOpShow(3)
                ret = IpAppSelectDoc(0)
                ret = IpOpBkgndSubtract(1, 0)
                ret = IpOpShow(2)
                ret = IpAppSelectDoc(1)
                ret = IpDocClose()
                ret = IpAppSelectDoc(0)

                ' Filter Application
                ret = IpFltShow(1)
                ret = IpFltFlatten(0, 200)
                ret = IpFltSharpen(3, 5, 1)
                ret = IpFltSobel()

                ' Calibration Selection
                ret = IpSCalSelect("Test")

                ' Count and Size Menu
                ret = IpSCalShowEx(SCAL_DLG_SELECT, SCAL_HIDE)
                ret = IpBlbShow(1)

                    ' Measurement Filters
                    ret = IpBlbEnableMeas(BLBM_AREA, 0)
                    ret = IpBlbEnableMeas(BLBM_MEANFERRET, 1)
                    ret = IpBlbEnableMeas(BLBM_ASPECT, 1)
                    ret = IpBlbEnableMeas(BLBM_ROUNDNESS, 1)
                    ret = IpBlbEnableMeas(BLBM_PERIMETER, 1)
                    ret = IpBlbEnableMeas(BLBM_AREAPOLY, 1)
                    ret = IpBlbSetFilterRange(BLBM_MEANFERRET, 10, 1000000.0)
                    ret = IpBlbSetFilterRange(BLBM_ROUNDNESS, 1.0, 1.1)
                    ret = IpBlbSetFilterRange(BLBM_ASPECT, 1.0, 1.1)
```

```
                ' Segmentation
                ret = IpSegShow(1)
                ret = IpSegShow(1)
                ret = IpSegShow(1)
                ret = IpSegSetRange(0, 60, 255)
                ret = IpSegPreview(CURRENT_C_T)
                ret = IpSegSetRange(0, 60, 255)
                ret = IpSegShow(0)

                ' Count and Measurement
                ret = IpBlbCount()
                ret = IpBlbMeasure()
                ret = IpBlbUpdate(0)

                ' Saving Outline
                ret = IpBlbSaveOutline("C:\Image Pro Macro Files\bubles.scl")

                ' Undo Filters
                ret = IpWsUndo(0)
                ret = IpFltShow(0)

                ' Loading Outline
                ret = IpBlbLoadOutline("C:\Image Pro Macro Files\bubles.scl")

            ' Data Collection
            ret = IpDcShow(3)
            ret = IpDcSelect("Image", "Name", 0)
            ret = IpDcSelect("Count_Size", "Count", 0)
            ret = IpDcSelect("Count_Size", "BLBM_MEANFERRET", 0)
            ret = IpDcSelect("Count_Size", "BLBM_CENTRX", 0)
            ret = IpDcSelect("Count_Size", "BLBM_CENTRY", 0)
            ret = IpDcShow(1)
            ret = IpDcSet(DC_AUTO, 0)
            ret = IpDcUpdate(DC_FETCH)

            ' Snap Image with its Measurement Overlays
            ret = IpSnap()

            ' Close Unneccesary Windows
            ret = IpAppSelectDoc(0)
            ret = IpDocClose()

            ' Save Processed Image with its Measurement Overlays as a New File
            ret = IpAppSelectDoc(1)
            ret = IpWsSaveAs(gDirStart + fName + "_processed.tif", "TIF")

            ' Close Unneccesary Windows
            ret = IpBlbShow(0)
            ret = IpDocClose()
            ret = IpIOvrShow(0)
            ret = IpAnShow(0)

            'End of User Editing

        ' The document ID and file name are sent here in Case the processing routine needs them.
        DoStuff docID, gDirStart + fName
        ' Close the initial image
        ret = IpAppSelectDoc(docID)
        ret = IpDocClose()
    Else
        Debug.Print "Error loading "; gDirStart + fName
    End If
    ' Get the next file name
    fName = Dir()
Wend
' Call a finish routine ***
' Insert your code here.
' Let the user know that we've finished
ret = IpMacroStop("All images in directory processed.", MS_MODAL)
End Sub
```

Appendix 33. Macro used to process all of the images in the directory.

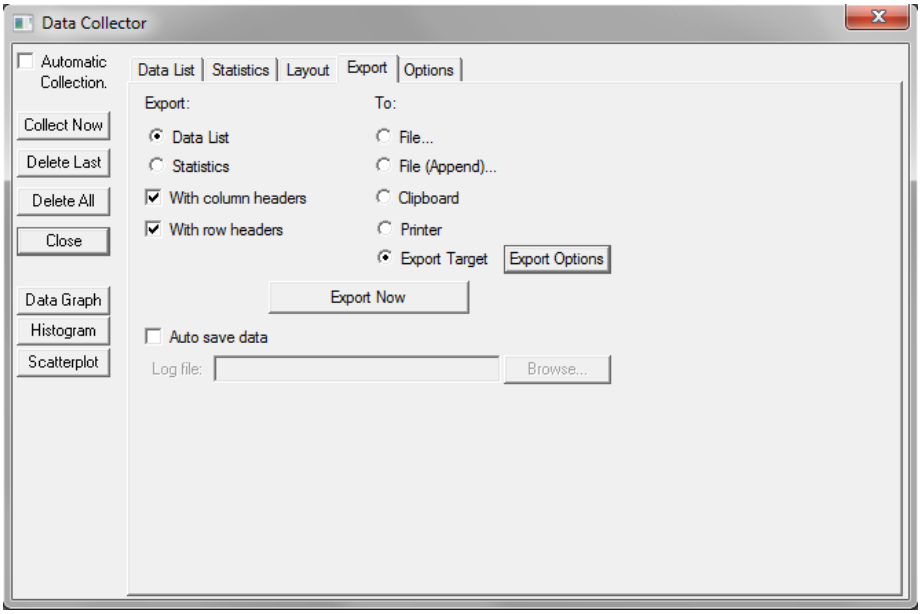

Appendix 34. Exporting data with data collector feature.

Appendix 35. Original picture of sand particles used in DOF determination.

Appendix 36. Allen key used to move the camera with 0.3125 mm intervals.

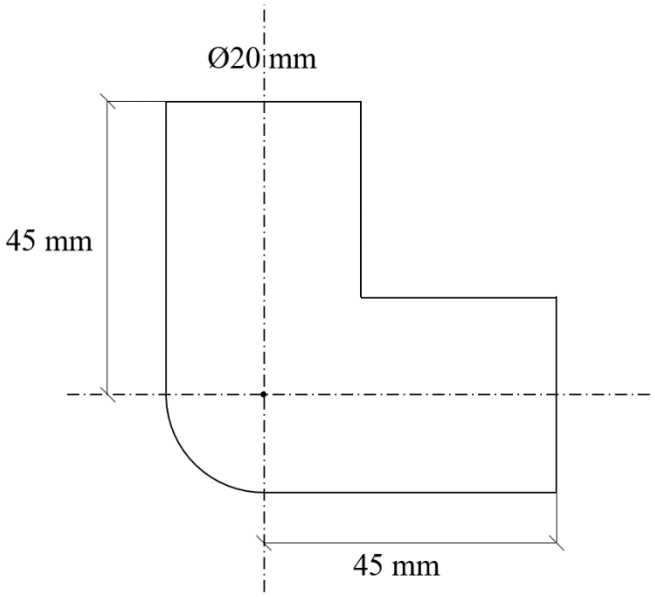

Appendix 37. Schematic diagram of inner structure of 90 degree bend used in the study.

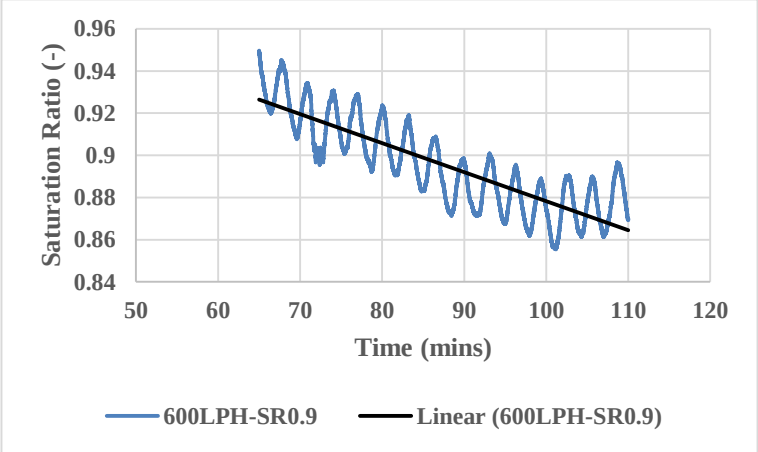

Appendix 38. Saturation ratio variation during bubble dissolution measurements at 600LPH for saturation ratio 0.9.

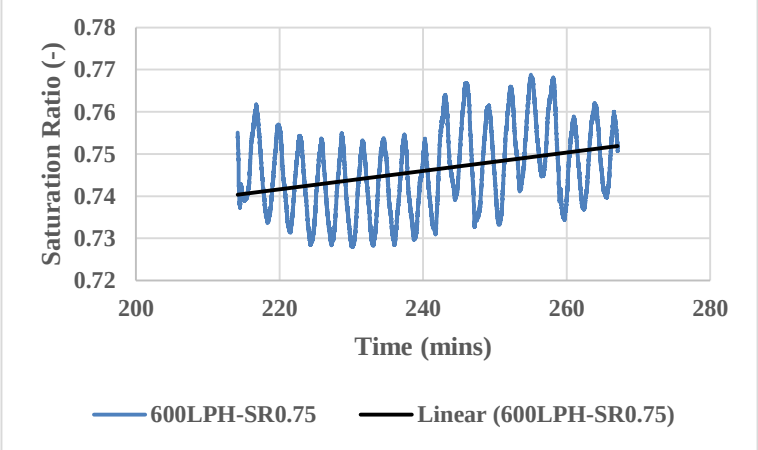

Appendix 39. Saturation ratio variation during bubble dissolution measurements at 600LPH for saturation ratio 0.75.

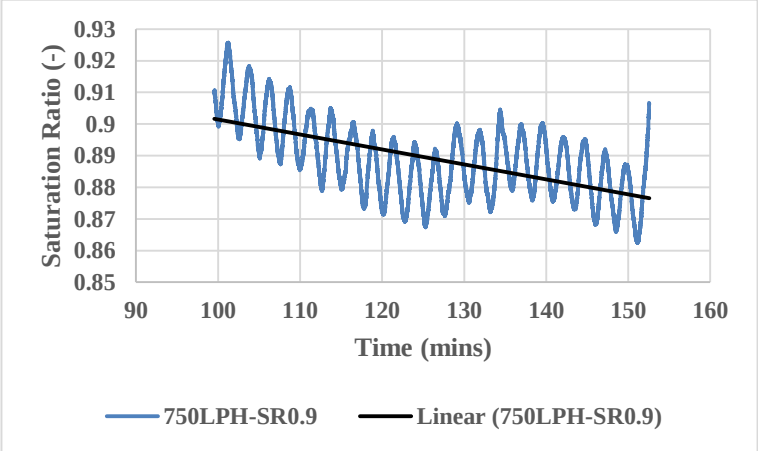

Appendix 40. Saturation ratio variation during bubble dissolution measurements at 750LPH for saturation ratio 0.9.

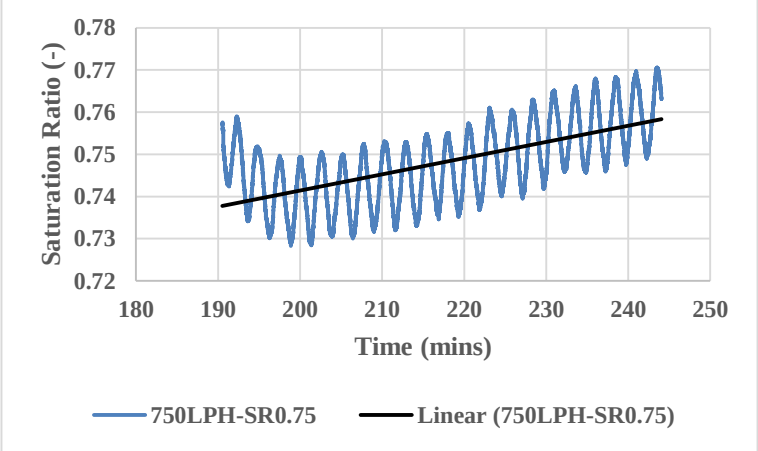

Appendix 41. Saturation ratio variation during bubble dissolution measurements at 750LPH for saturation ratio 0.75.

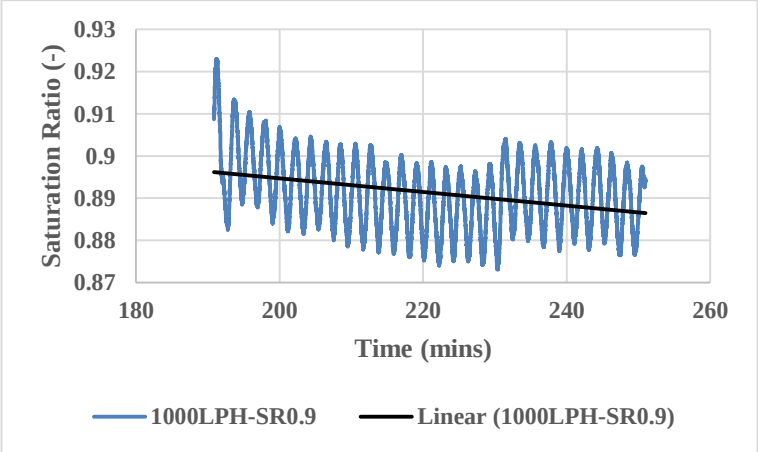

Appendix 42. Saturation ratio variation during bubble dissolution measurements at 1000LPH for saturation ratio 0.9.

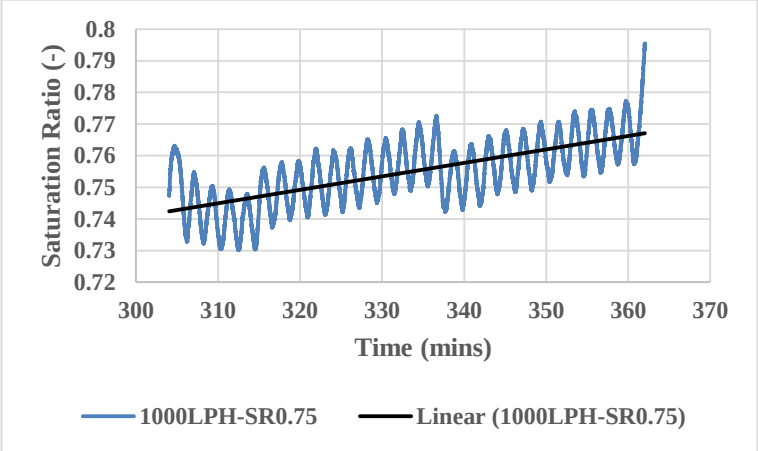

Appendix 43. Saturation ratio variation during bubble dissolution measurements at 1000LPH for saturation ratio 0.75.

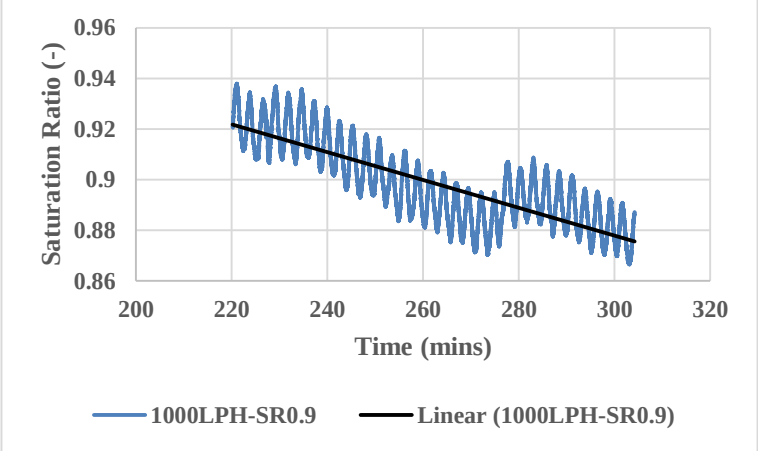

Appendix 44. Saturation ratio variation during bubble dissolution measurements at 1250LPH for saturation ratio 0.9.

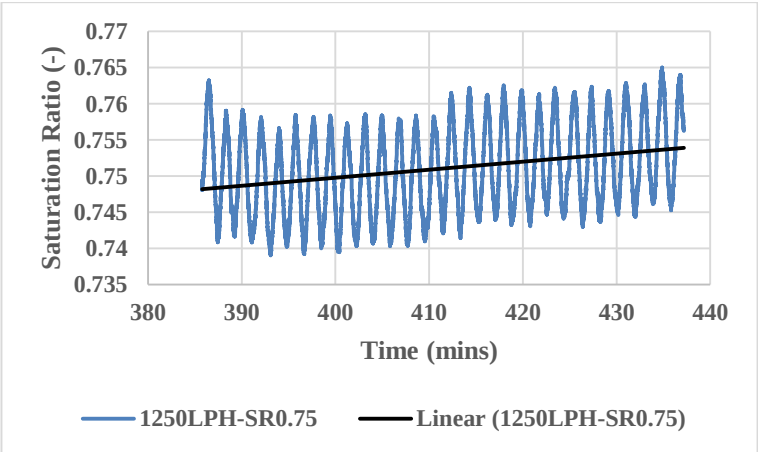

Appendix 45. Saturation ratio variation during bubble dissolution measurements at 1250LPH for saturation ratio 0.75.

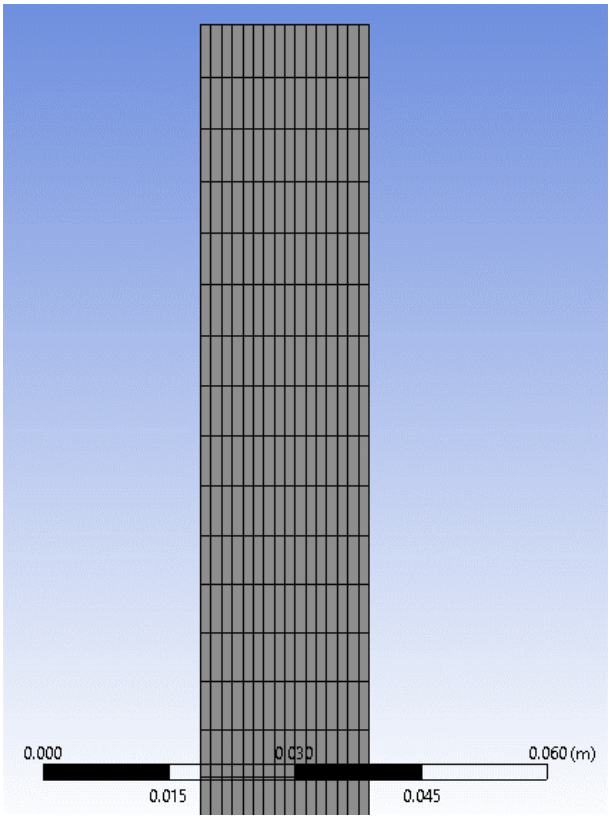

Appendix 46. Mesh details at top of the vertical pipeline.

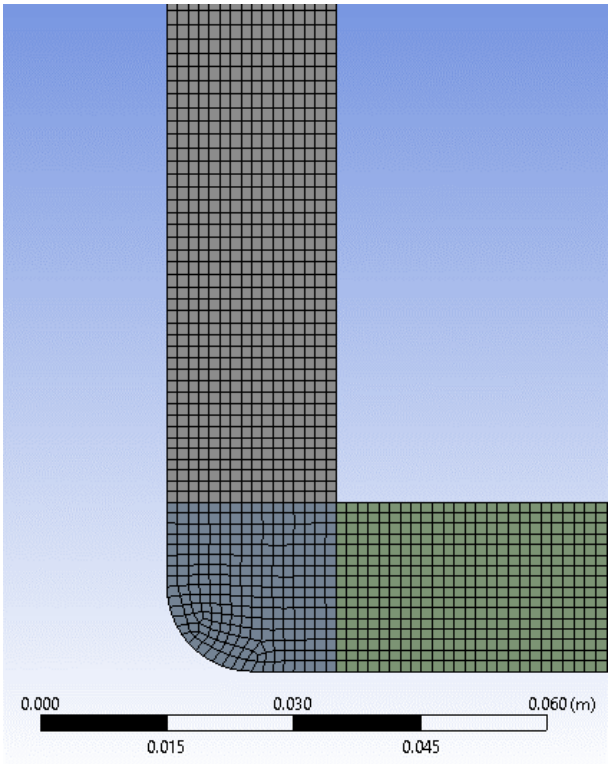

Appendix 47. Mesh details at the 90 degree bend

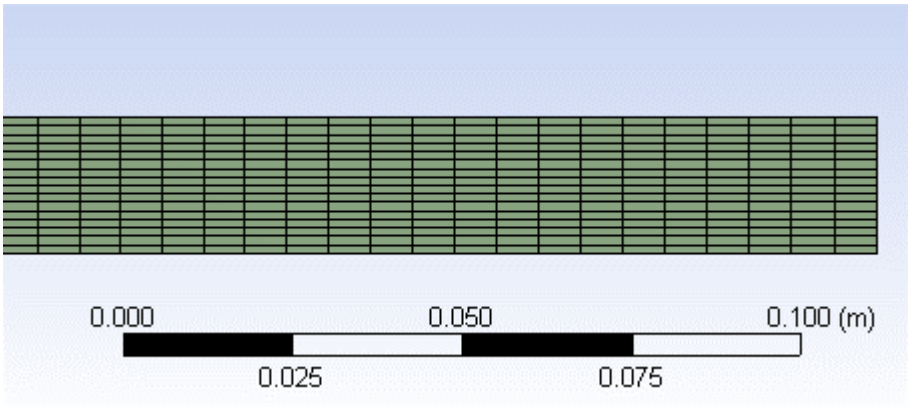

Appendix 48. Mesh details at the end of horizontal pipeline.

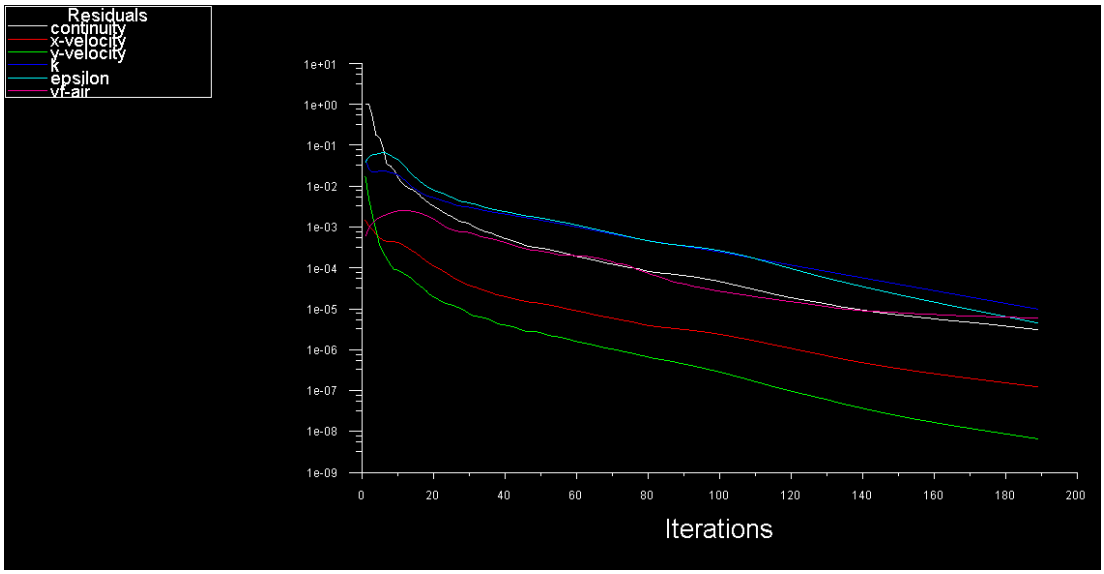

Appendix 49. Residuals monitoring for governing equations.

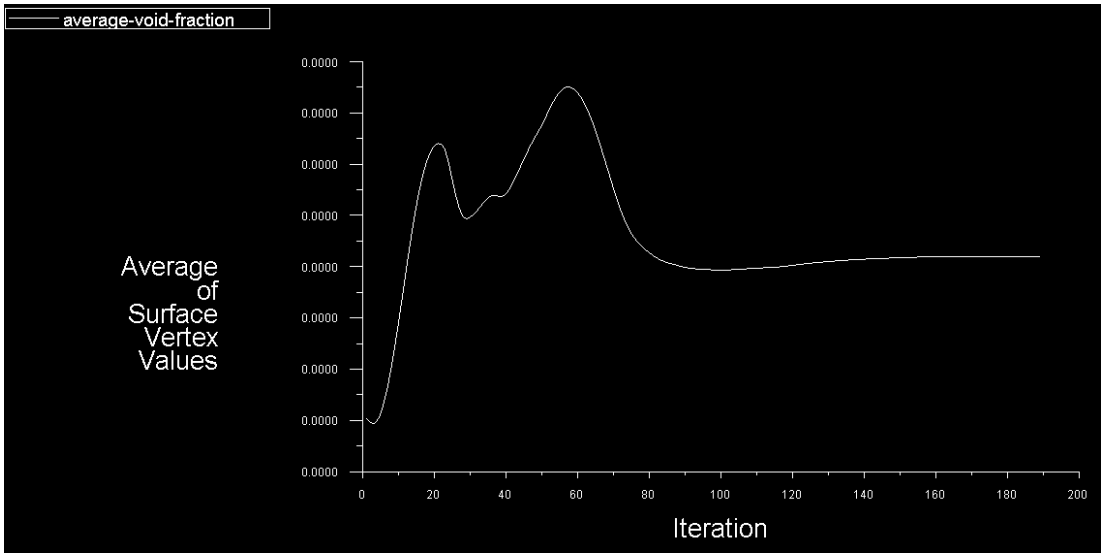

Appendix 50. Average void fraction monitoring at outlet.

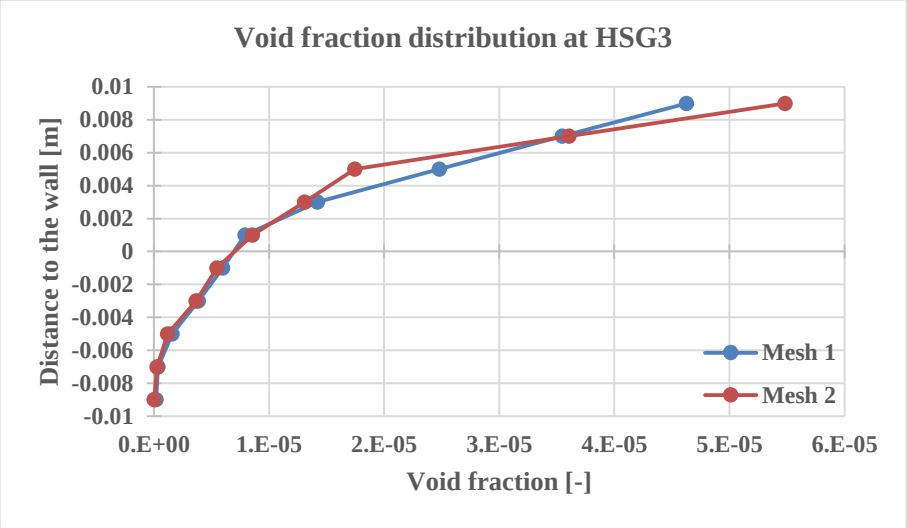

Appendix 51. Void fraction distribution comparison between mesh 1 and 2.

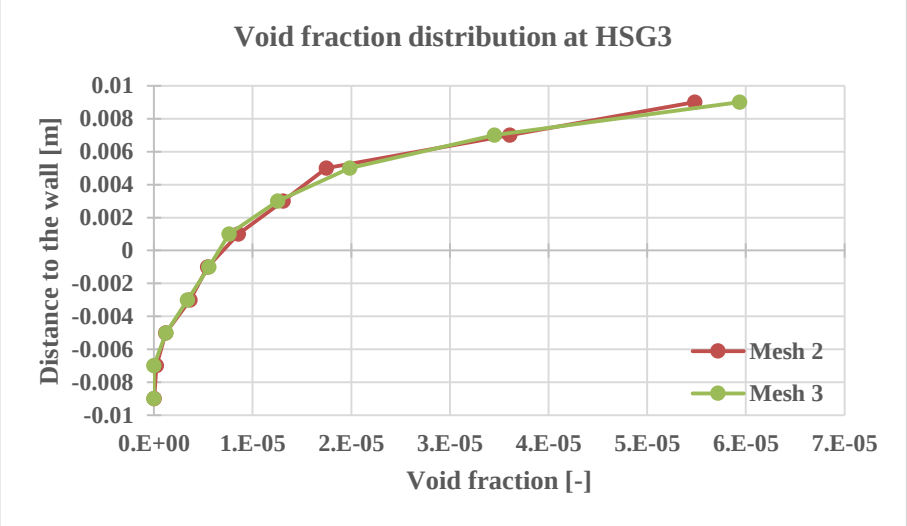

Appendix 52. Void fraction distribution comparison between mesh 2 and 3.

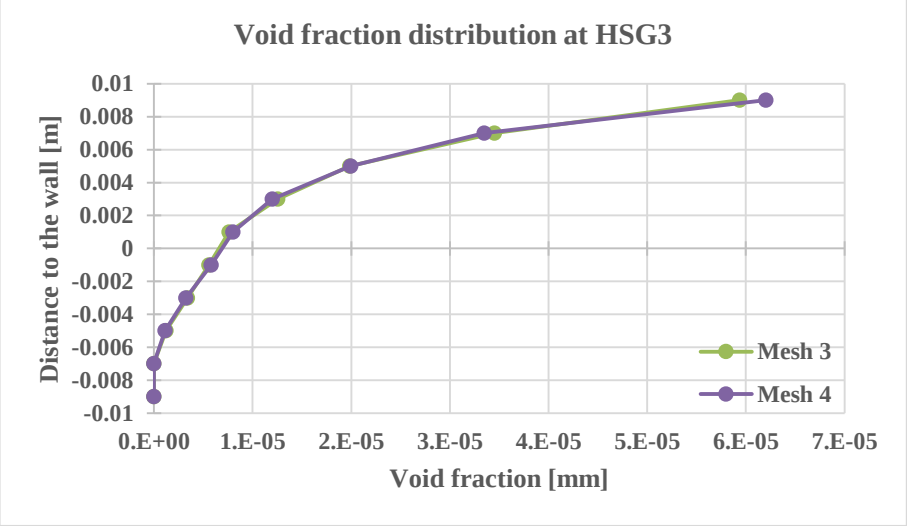

Appendix 53. Void fraction distribution comparison between mesh 3 and 4.

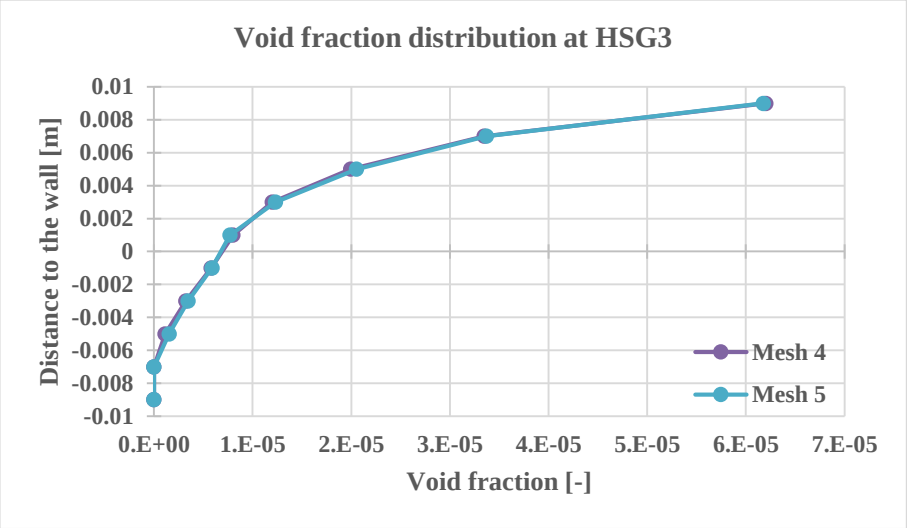

Appendix 54. Void fraction distribution comparison between mesh 4 and 5.

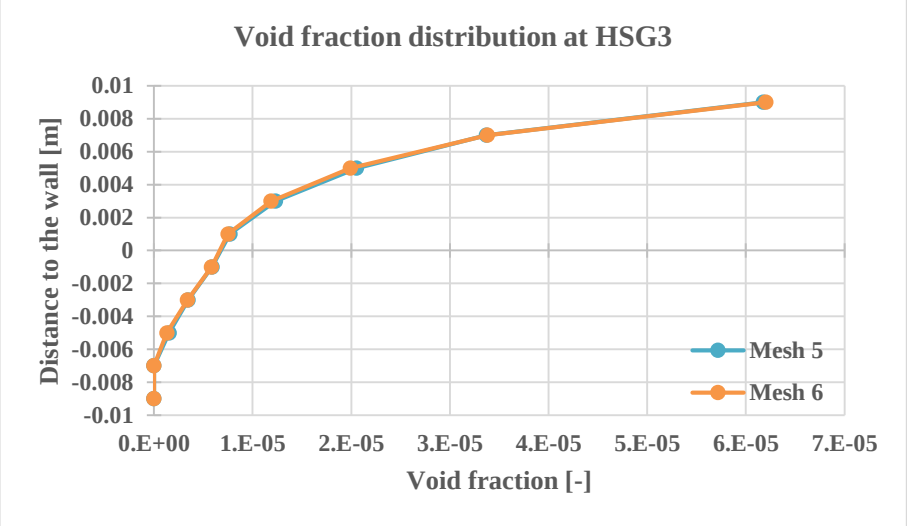

Appendix 55. Void fraction distribution comparison between mesh 5 and 6.

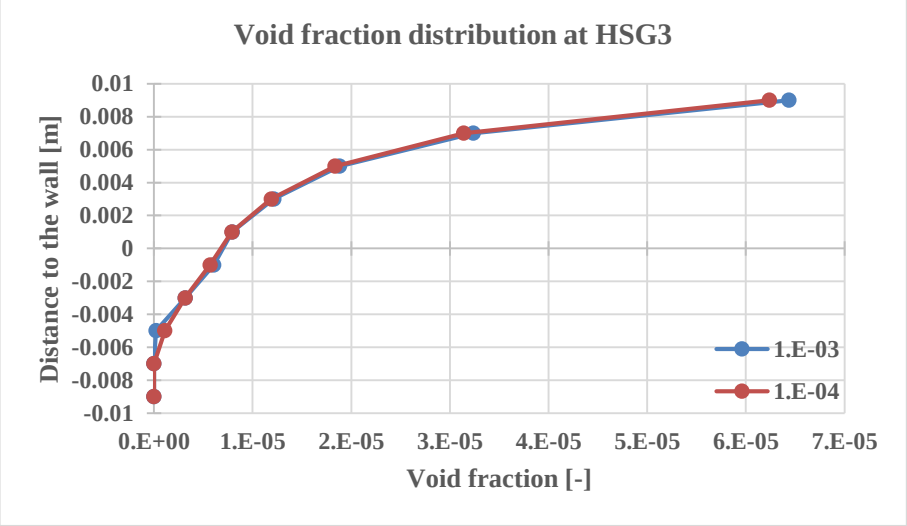

Appendix 56. Distribution profiles with convergence criteria 1e-3 and 1e-4 for mesh 4.

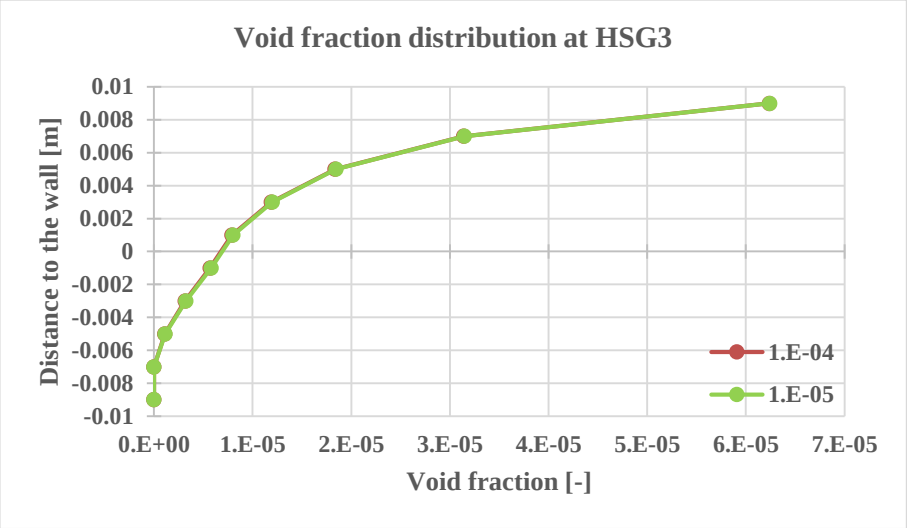

Appendix 57. Distribution profiles with convergence criteria 1e-4 and 1e-5 for mesh 4.

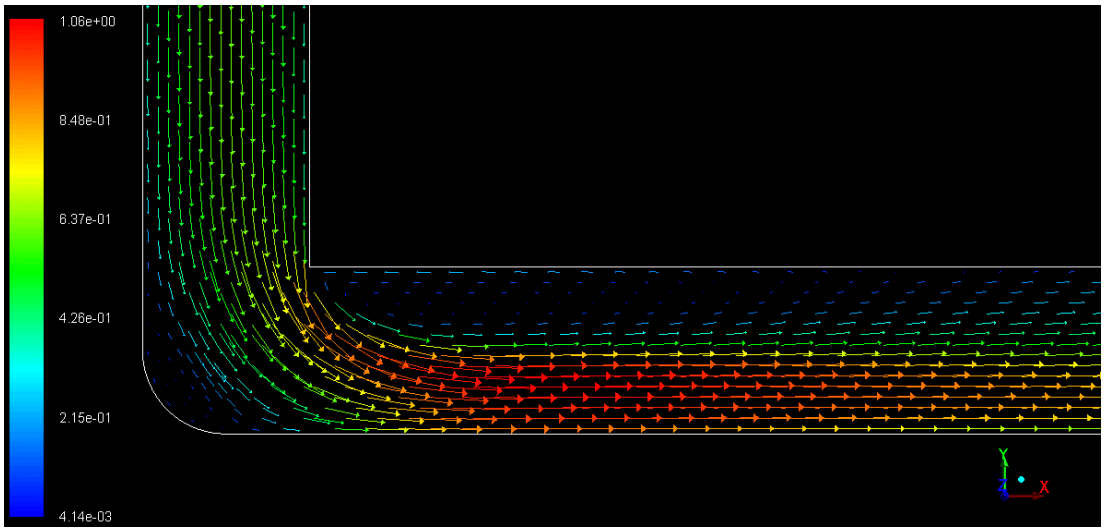

Appendix 58. Vector plots of velocities after the 90 degree bend.

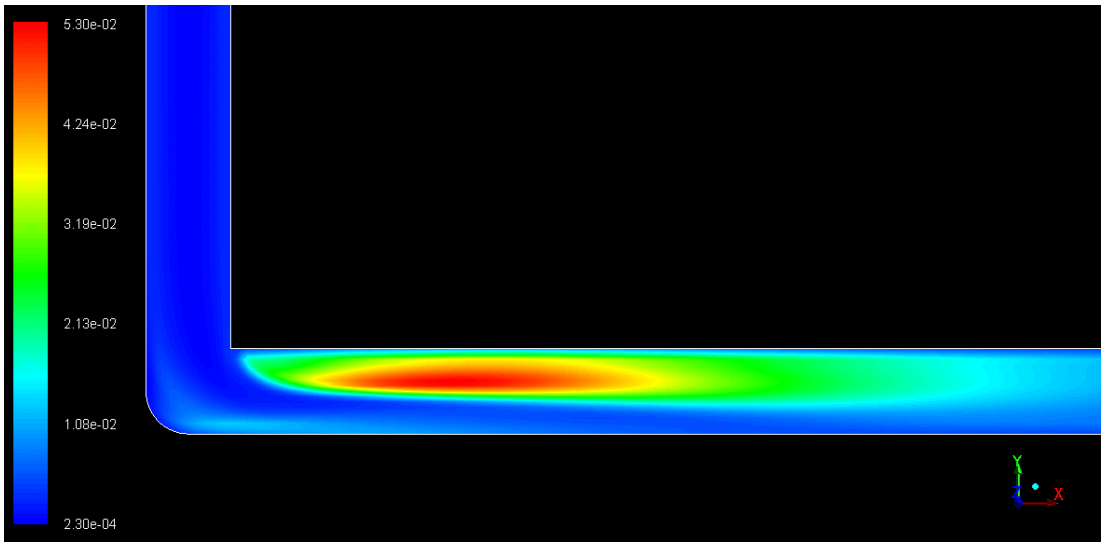

Appendix 59. Contours of turbulence kinetic energy after 90 degree bend.